



# Mechanical Instabilities of Soft Materials: Creases, Wrinkles, Folds, and Ridges

## Citation

Jin, Lihua. 2014. Mechanical Instabilities of Soft Materials: Creases, Wrinkles, Folds, and Ridges. Doctoral dissertation, Harvard University.

## Permanent link

<http://nrs.harvard.edu/urn-3:HUL.InstRepos:13064983>

## Terms of Use

This article was downloaded from Harvard University's DASH repository, and is made available under the terms and conditions applicable to Other Posted Material, as set forth at <http://nrs.harvard.edu/urn-3:HUL.InstRepos:dash.current.terms-of-use#LAA>

## Share Your Story

The Harvard community has made this article openly available.  
Please share how this access benefits you. [Submit a story](#).

[Accessibility](#)

**Mechanical Instabilities of Soft Materials:**

**Creases, Wrinkles, Folds, and Ridges**

A dissertation presented

by

**Lihua Jin**

to

The School of Engineering and Applied Sciences

in partial fulfillment of the requirements

for the degree of

Doctor of Philosophy

in the subject of

Engineering Sciences

Harvard University

Cambridge, Massachusetts

August, 2014

© 2014 – Lihua Jin

All rights reserved

# **Mechanical Instabilities of Soft Materials: Creases, Wrinkles, Folds, and Ridges**

## **Abstract**

Subject to a sufficiently large compression, materials may undergo mechanical instabilities of various types. When the material is homogeneous, creases set in. When the material is a bilayer consisting of a stiff thin film on a thick compliant substrate, wrinkles set in. Creases are localized self-contact regions with large strain deviating from the smooth state, while wrinkles are undulations finite in space with infinitesimal strain deviating from the smooth state. After the formation of wrinkles, if the compression further increases, wrinkles double their period and form localized folds. If the substrate is subject to a sufficiently large pre-tension, wrinkles transit to ridges. This thesis explores different types of mechanical instabilities: creases, wrinkles, folds, and ridges.

We start with studying creases in different materials. Soft tissues growing under constraint often form creases. We adopt the model of growth that factors the deformation gradient into a growth tensor and an elastic deformation tensor, and show that the critical conditions for the onset of creases take a remarkably simple form. We then perform simulations to explore creases in strain-stiffening materials. For a solid that stiffens steeply at large strains, as the compression increases, the surface is initially smooth, then forms creases, and finally becomes smooth again. For a solid that stiffens steeply at small strains,

creases never form for all levels of compression. In order to better control the formation and disappearance of creases, we design a soft elastic bilayer with same moduli of the film and substrate but the substrate pre-compressed, and show that the bilayer can snap between the flat and creased states reproducibly with tunable hysteresis in a large strain range. We also show that an interface between two soft materials can form creases under compression.

We then investigate the critical conditions for the onset of wrinkles and creases in bilayers with arbitrary thicknesses and moduli of the two layers, and show several new types of bifurcation behavior when the film and substrate have comparable moduli and thicknesses. We study the effect of substrate pre-stretch on post-wrinkling bifurcations, and show that pre-tension stabilizes wrinkles while pre-compression destabilizes wrinkles. When the pre-compression is sufficiently large, ‘chaotic’ morphologies emerge. When the pre-tension is sufficiently large, we realize ridge localizations and networks under an equi-biaxial compression, and study the mechanics of ridge formation and propagation.

# Table of Contents

<b>Title Page</b> .....	<b>i</b>
<b>Copyright Page</b> .....	<b>ii</b>
<b>Abstract</b> .....	<b>iii</b>
<b>Table of Contents</b> .....	<b>v</b>
<b>Acknowledgements</b> .....	<b>x</b>
<b>Chapter 1 Introduction</b> .....	<b>1</b>
1.1 Mechanical instabilities .....	1
1.2 Wrinkles and linear perturbation analysis .....	2
1.3 Creases .....	4
1.4 Folds and ridges .....	6
1.5 Outline of this thesis .....	8
<b>Chapter 2 Creases in soft tissues generated by growth</b> .....	<b>10</b>
2.1 Introduction .....	10
2.2 Growth model .....	12
2.3 Critical condition for the initiation of creases due to growth .....	14
2.4 Tissue growing in a rigid shell .....	15
2.5 Tissue growing outside a rigid core .....	18
2.6 Number of deep creases .....	21
2.7 Summary .....	23
<b>Chapter 3 Smoothing creases on surfaces of strain-stiffening materials</b> .....	<b>24</b>

3.1	Introduction .....	24
3.2	Strain-stiffening materials .....	27
3.3	Creases .....	30
3.4	Wrinkles .....	35
3.4.1	Two states with small difference in deformation gradient and pressure .....	35
3.4.2	Represent general solutions using functions of complex variables .....	36
3.4.3	Critical condition for the onset of wrinkles .....	39
3.5	Summary .....	42
<b>Chapter 4 Controlled formation and disappearance of creases .....</b>		<b>44</b>
4.1	Introduction .....	44
4.2	Subcritical creases .....	45
4.3	Methods .....	49
4.3.1	Sample preparation .....	49
4.3.2	Measurement of viscoelastic properties .....	50
4.3.3	Optical and confocal microscope imaging .....	51
4.3.4	Numerical analysis .....	51
4.4	Results .....	53
4.5	Summary .....	62
<b>Chapter 5 Creases on the interface between two soft materials .....</b>		<b>64</b>
5.1	Introduction .....	64
5.2	Analysis and simulations .....	66
5.2.1	Interfacial creases under applied strain .....	66

5.2.2	Interfacial creases under both applied strain and pre-strains .....	74
5.3	Linear perturbation analysis for the onset of interfacial wrinkles .....	78
5.4	Experimental results .....	81
5.5	Experimental methods .....	83
5.5.1	Experiment with hydrogels confined in a glass slit .....	83
5.5.2	Experiment with thin layers of gels on a glass substrate .....	84
5.6	Summary .....	86
<b>Chapter 6</b>	<b>The formation of wrinkles or creases in bilayers .....</b>	<b>87</b>
6.1	Introduction .....	87
6.2	Linear perturbation analysis for wrinkles .....	90
6.2.1	Governing equations and their incremental forms .....	90
6.2.2	Eigenvalue problem .....	92
6.2.3	Critical condition for the onset of wrinkles .....	95
6.3	Subcritical and supercritical creases .....	99
6.4	Diagram of wrinkles and creases .....	103
6.5	Summary .....	107
<b>Chapter 7</b>	<b>Role of substrate pre-stretch in post-wrinkling bifurcations .....</b>	<b>109</b>
7.1	Introduction .....	109
7.2	Methods .....	112
7.2.1	Experimental setup .....	112
7.2.2	Experimental details .....	113
7.2.3	Finite element simulations .....	115

7.3	Results .....	116
7.3.1	Effect of substrate pre-stretch on period doubling .....	116
7.3.2	Chaotic period multiplication under large substrate pre-compression .....	121
7.4	Summary .....	131
<b>Chapter 8 Ridge localizations and networks under equi-biaxial loading .....</b>		<b>133</b>
8.1	Introduction .....	133
8.2	Experimental results .....	135
8.3	Finite element simulations .....	142
8.4	Summary .....	147
<b>Chapter 9 Mechanics of ridge formation and propagation .....</b>		<b>149</b>
9.1	Introduction .....	149
9.2	Formation and propagation of ridges .....	151
9.2.1	Static force-displacement method .....	153
9.2.2	Pseudo-dynamic loading-unloading method .....	158
9.2.3	Verification of the two methods .....	163
9.3	Deformation mechanism and geometry of ridges .....	165
9.4	Summary .....	172
<b>Chapter 10 Conclusions .....</b>		<b>174</b>
<b>Bibliography .....</b>		<b>178</b>
<b>Appendix .....</b>		<b>205</b>
Appendix A	Supporting information for Chapter 3 .....	205
A.1	Implementation of the Gent material in ABAQUS .....	205

A.2 Tangent moduli $\mathbf{C}$ and matrices $\mathbf{A}$ , $\mathbf{Q}$ and $\mathbf{L}$ of the Gent materials .....	206
Appendix B Explicit expression of matrix $\mathbf{A}$ in Chapter 6 .....	208
Appendix C Supporting information for Chapter 8 .....	209
C.1 Methods .....	209
C.2 Supplementary figures .....	211

## **Acknowledgements**

First and foremost, I would like to bring my heartiest gratitude to my PhD advisor Professor Zhigang Suo. Zhigang is such an enthusiastic scientist, encouraging mentor and enlightening teacher. I first met Zhigang at Tongji University in 2008 when I was still a master student back in China. Zhigang's talk was extremely illuminative so that I immediately had the desire to pursue my PhD with him at Harvard. Luckily I was admitted. In the past five years, I learned from Zhigang in every of our meetings. He has tremendous knowledge in mechanics, but can express things in the simplest ways. His incredible inspiration and constant supports keep me making progress. I enjoy taking Zhigang's courses and love reading his class notes. He always has the magic to make the classes full of fun and infect everybody in the classroom with the excitement, but at the same time, gives us deep understandings and insight to the problems. Zhigang sets the best role model in my research career.

I am also deeply grateful to Professor Ryan Hayward at University of Massachusetts Amherst. Most part of my thesis is based on a close collaboration with his group. We have kept regular Skype meetings in the past three years. His group works on the experimental side of the projects, and I work on theories. Their beautiful experimental results keep inspiring new theories and understandings. When our theories predict new phenomena, they can quickly design experiments and produce the observations. Although as an experimentalist, Ryan thinks deeper than theoreticians and understands all the details of the projects. His critical questions in the meetings are always helpful to improve the theories.

I have had the great honor to work with Professor John Hutchinson during my PhD. I was the teaching fellow in one of his classes, wrote several papers with him, and took a research class from him, in which we discussed Koiter's post-buckling analysis. John is one of the most celebrated scholars in the field of mechanics. Although he has been retired, he can not stop working on mechanics. John is always supportive and inspiring. His pet phrase is 'Jesus, how interesting'. I can not imagine how many young researchers he has encouraged in his career for longer than five decades. I want to express my gratitude and respect to Professor John Hutchinson.

I also want to thank my committee members, Professor James Rice, Professor Katia Bertoldi, Professor Lakshminarayanan Mahadevan and Professor Shmuel Rubinstein, for their suggestions and comments to my research. Jim is another of the most celebrated scholars in mechanics. It is fabulous for me to read his achievements more than 45 years ago in textbooks, but at the same time, to knock at his door and discuss with him face to face. Jim is a devoting teacher. He teaches subjects widely from mathematics to fluid dynamics, from solid mechanics to geophysics. I was amazed in his classes how things become equally simple to him as long as they can be described by equations. Katia is an expert on finite element analysis, and I learned a lot from her class on the finite element method. Most part of my thesis was done based on the finite element analysis. Therefore, whenever I got frustrated by the divergence of my simulations, I turned to Katia. Katia is always helpful on improving my skills of finite element analysis. Maha is the person who created the field of crease instability, which sets the stage of most of my thesis work. Maha is such a knowledgeable scientist, and he works on almost everything. His critical questions and comments in talks and seminars

always inspire me to think and to better understand. I thank Shmuel for allowing and guiding me to do experiments in his lab. He is an encouraging teacher, and I enjoyed all the discussions with him.

I am grateful to Professor Noel Holbrook and Doctor Fulton Rockwell for leading me to the new field of plants. I started to discuss with them in my first year in the United States. My English was not good enough, not to mention English terminology of plants. They were so kind and patient to go through the basic concepts and phenomena in plants with me, and introduced me to interesting mechanics problems in plants. I fell in love with plants then, and will keep an eye on those problems in the future.

I am thankful to my other collaborators. Lots of ideas were brought together and achievements were realized through the interactions with them. They are Dr. Dayong Chen (who did the experiments in Chapter 4 and 5) and Anesia Auguste (who did the experiments in Chapter 7) at Umass Amherst; Dr. Atsushi Takei (who did the experiments in Chapter 8) at University of Tokyo; Dr. Jia Liu, Prof. Bozhi Tian, Prof. Charles Lieber, Dr. Ramses Martinez, Prof. George Whitesides, Prof. Adam Abate, Lloyd Han, Prof. David Weitz., Prof. Shengqiang Cai, Jiawei Yang, Dr. Pengfei Wang, Dr. Jiangshui Huang, Prof. David Clarke, Dian Yang, Rajiv Desai, Prof Neel Joshi, and Prof. David Mooney at Harvard.

I have also had chances to interact with a number of other distinguished professors at Harvard and took their classes. I want to thank Prof. Joost Vlassak, Prof. Michael Brenner, Prof. Frans Spaepen, and Prof. Joanna Aizenberg. They are always kind and open, and welcome questions. I would also like to thank SEAS academic computing office for their help on computation softwares.

It is joyful to work with people in Zhigang's group. I want to thank all those great friends: Prof. Nanshu Lu, Prof. Xuanhe Zhao, Dr. Yuhang Hu, Prof. Kejie Zhao, Dr. Matt Pharr, Prof. Jeong-Yun Sun, Prof. Jian Zhu, Prof. Rui Huang, Prof. Tiefeng Li, Dr. Christoph Keplinger, Prof. Keith Choon Chiang Foo, Dr. Laurance Brassart, Prof. Adrian Koh, Dr. Tongqing Lu, Prof. Ronghou Xia, Widusha Illeperuma, Qihan Liu, Jianyu Li, Chao Chen, Ruobing Bai, Philipp Rothemund, Yecheng Wang, Jianguo Li, Weiss Francois, Zhengjin Wang, Jingda Tang, Liwu Liu, Huiming Wang and Xin Lan.

I also got lots of helps on finite element analysis from people in Katia's group. I would like to thank Prof. Jongmin Shim, Dr. Sung Hoon Kang, Sicong Shan, Jia Liu, Pai Wang and Sahab Babae.

I also want to extend my gratitude to other folks in SEAS and friends: Dr. Olga Dudchenko, Dr. Zhiyan Wei, Dr. Xi Yao, Dr. Hongyan Yuan, Dr. Laura Adams, Dr. Liheng Cai, Dr. Xinfeng Quan, Dr. Evan Hohlfeld, Omer Gottesman, especially my office mates, Miriam Huntley, Michael Chemama, Dr. Elizabeth Chen, and my roommates, Jingyi Yu, Yingjun Liu.

Finally, I would bring my deepest gratitude to my parents. They have given me unconditional love, deep care, constant supports and tremendous understandings. Without those, I can never go so far on my own.

# Chapter 1

## Introduction

### 1.1 Mechanical instabilities

Mechanical instabilities are ubiquitous in nature and daily life [1-4]. Instabilities can form due to various loadings, such as compression, constrained swelling or differential growth. When the loading is small, the surface of the material keeps smooth. However, when the loading reaches a critical value, the smooth state loses stability, and the total energy of the material is minimized by forming instability patterns. Figure 1.1 shows instabilities in a (a) brain, (b) plant and (c) curtain.

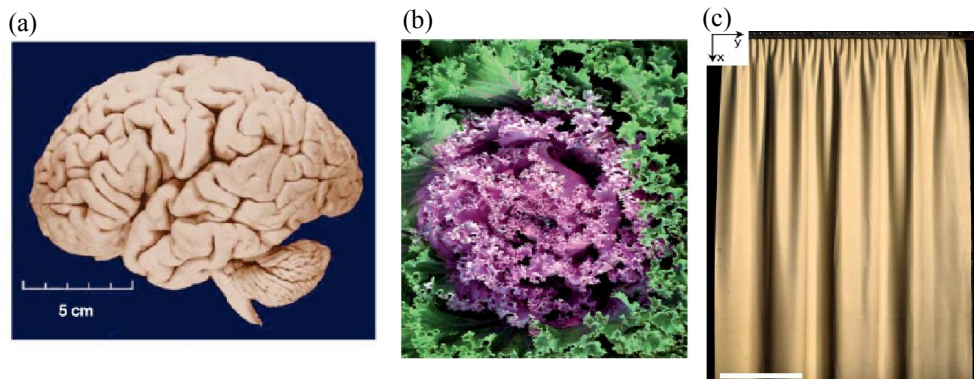


Figure 1.1 Instabilities are ubiquitous in nature and daily life. They are observed in a (a) brain [3], (b) plant [1], and (c) curtain [2].

In the engineering field, mechanical instabilities used to be thought as modes of failure, for example, buckling of undersea pipes [5], MEMS [6], and composite materials [7]. However, now people exploit the variety applications of mechanical instabilities [8-12]. Especially, the elastic character of soft materials makes it possible to repeatedly cycle

between the smooth state and the instability patterns. People use instabilities to fabricate stretchable electronics [13-18] and microfluidics [19-21], measure material properties [14, 22-26], self-assemble particles [27, 28], align cells [29, 30], reversibly tune adhesion [31-33], wettability [34-37], friction [38], surface chemistry [39] and optical properties [37, 40-43].

Mechanical instabilities play significant roles in biological systems [44-49], for example in fingerprint formation [50], embryo invagination [51], gut development [52-55], brain morphogenesis [56-58], tumor growth [59] and mucus folding [60-63]. The morphology of viruses [64], plants [65-72] is also related to mechanical instabilities generated by differential growth or differential swelling.

This thesis studies different types of mechanical instabilities in soft materials: creases, wrinkles, folds and ridges. Soft materials are usually much more stretchable than stiff materials, which makes it possible to access new modes of instabilities. Creases [73], folds [74] and ridges [75] are highly nonlinear modes of instabilities, and they were all identified in the last several years. The following sections provide an introduction to the different types of instabilities.

## **1.2 Wrinkles and linear perturbation analysis**

When a bilayer structure with a stiff thin film on a compliant thick substrate is compressed to a critical load, wrinkles set in to release stress (Figure 1.2). Wrinkles form periodically in a finite space (Figure 1.2a). The wavelength of wrinkles is determined by a balance between the deformation of the substrate, which favors short wavelengths, and the

bending of the film, which favors long wavelengths [76-79]. When the loading is uniaxial, parallel wrinkles form perpendicular to the compression direction (Figure 1.2b) [80]. When the loading is biaxial, complex modes of wrinkles, such as herringbone (Figure 1.2c), checkerboard and hexagonal, are observed [81-86]. People also studied wrinkles formed under tensile stretching [87-90], shearing [91, 92] and bending [93, 94].

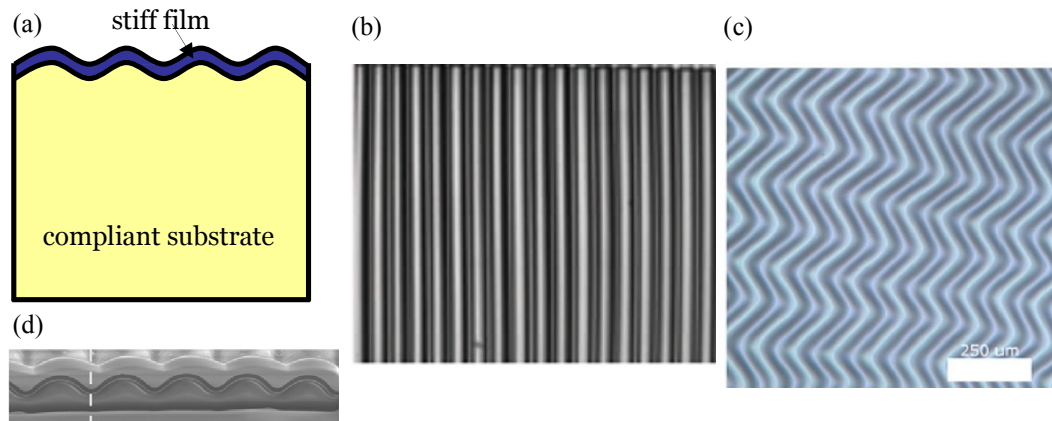


Figure 1.2 Wrinkle instability. (a) A schematic of wrinkles. (b) Top view of parallel wrinkles formed under a uniaxial compression [80]. (c) Top view of herringbone mode of wrinkles formed under an equi-biaxial compression [82]. (d) Cross-section view of parallel wrinkles [95].

Wrinkles have infinitesimal strain deviating from the smooth state and the cross-sections of wrinkles form smooth undulation (Figure 1.2d). Therefore, a linear perturbation analysis can be used to predict the critical loading condition and wavelength of wrinkles [75, 85, 96-99]. A linear perturbation analysis formulates an incremental boundary value problem with the flat state as a reference, and the onset of wrinkles corresponds to the existence of a non-trivial solution to the incremental boundary value problem, which is an eigenvalue problem. Biot used this method to study the surface instability of a hyperelastic half space [97] and interfacial instability of two hyperelastic half spaces [100]. Modeling both the film and substrate as linear elastic materials, and considering the thin film as a von Karman plate under the assumption that the film thickness is much smaller than the

wavelength of wrinkles, people further developed nonlinear theories of wrinkles [76-79, 101-104], which can not only predict the initiation of wrinkles, but also growth of wrinkles under small strains.

### **1.3 Creases**

Using a linear perturbation analysis on a semi-infinite neo-Hookean material in compression, Biot predicted five decades ago that the free surface of an elastomeric half space would become unstable to the formation of sinusoidal waves upon a critical strain of 0.46 under plane strain condition [97]. However, Biot's prediction was challenged by experimental results. Gent and Cho bent a rubber block and observed sharp creases on the surface at a critical strain of 0.35 [105].

Hohlfeld [73] and Hohlfeld and Mahadevan [106] showed that Biot's solution and creases are two distinct instabilities. Biot linearized the boundary value problem around a state of finite homogeneous deformation, and his solution corresponds to a smooth, wavy surface (i.e., wrinkles) of small strain relative to the homogeneous state. By contrast, a crease is a localized, self-contact region of large strain relative to the homogeneous state (Figure 1.3). A crease has a sharp tip, and the cross-section of a crease (Figure 1.3d) looks very different from that of a wrinkle (Figure 1.2d). Hohlfeld [73] and Hohlfeld and Mahadevan [106] simulated creases numerically, and found creases set in at a critical strain of 0.354, which agrees well with the experimental observation of Gent and Cho [105]. The critical strain for the onset of creases has since been obtained by several other approaches of numerical analysis [107-111].

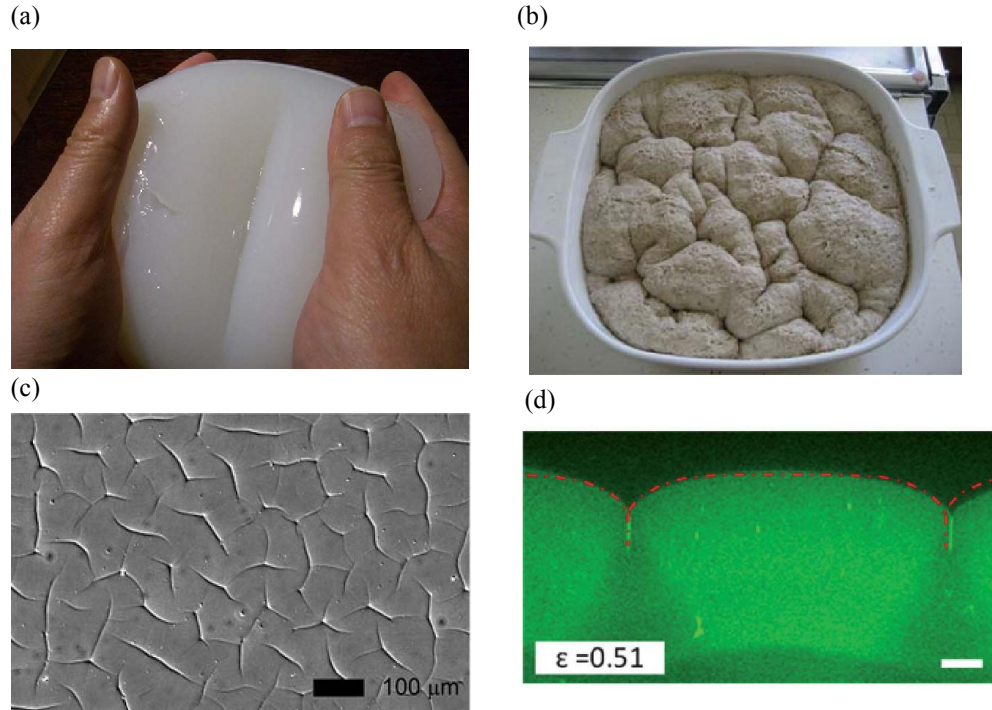


Figure 1.3 Crease instability. (a) Crease of Liangfen, a starch gel, due to bending [107]. (b) Creases of rising dough due to the constraint of the bowl [108]. (c) Creases of a swelling gel due to the constraint of the substrate [112]. (d) Cross-section view of creases [113].

No evidence exists that Biot's smoothly wavy surfaces have ever been observed experimentally on homogeneous elastic blocks under compression. Creases, however, have been observed routinely on elastic blocks compressed by various means, including mechanical forces [99, 105, 113-116], constrained swelling [112, 117-129], temperature change [39], electric fields [130-135], and light [136]. Creases have been studied in soft tissues [48, 58, 60]. Creases have been related to the Schallamach waves arising during the frictional sliding of a rubber against a rigid surface [137], and to the osmotic collapse of a water-filled cavity in a hydrogel [108].

Surface energy adds a barrier to the nucleation of creases, and makes nucleation defect-sensitive [119, 138]. When the loading is an electric field, either creases or wrinkles may form depending on the value of the elastocapillary number [132]. For a layer of finite

thickness with a traction-free bottom surface, creases on the top surface are subcritical—that is, as the applied compressive strain increases and then decreases, creases form and disappear with hysteresis [139]. Creases can also form on the interface between two elastic solids [140]. Applications of creases have been explored, including the use of creases to control chemical patterns [39, 136], enzymatic activity [39], cellular behavior [141], adhesion [142], and biofouling [143].

#### **1.4 Folds and ridges**

A bilayer with a stiff thin film on top of a compliant thick substrate can form wrinkles, if it is compressed to a critical value. If the compression is further increased sufficiently, a secondary bifurcation can happen. The secondary bifurcation varies depending on the details of the substrate.

When there is no mismatch stress between the film and substrate, localized folds can form when the bilayer is compressed far beyond the onset of wrinkles (Figure 1.4) [74, 95, 144-148]. Wrinkles lose their initial periodicity through the emergence of sub-harmonic modes due to nonlinear contributions to the elastic response of the substrate [145, 149]. Typically, a progression from wrinkles to a period-doubled state is observed, followed by a period-quadrupled state, and finally the formation of self-contacting folds [95, 145, 147]. The emergence of sub-harmonic spatial modes in this context is analogous to appearance of temporal sub-harmonics for a non-linear oscillator [145].

Localized folds can be controlled by the patterns of the substrate [150], and are also observed when the substrate is a viscous fluid (Figure 1.4a) [74, 151, 152] or an elastic foam

[153]. Theoretical studies on fold instability were conducted analytically [74, 145, 149, 154] and numerically [75, 95]. Geometric patterns in biological interfaces are often far from idealized sinusoidal wrinkles, but more look like folds. Examples include thread filaments used by mussel shellfish to adhere to rocks, inner arterial wall and lung surfactants [144].

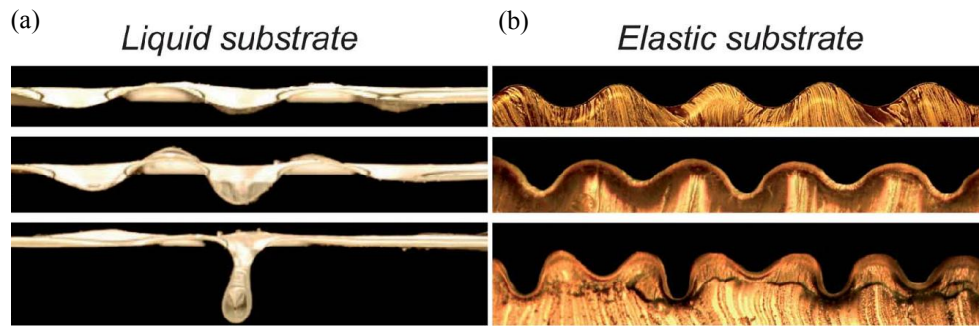


Figure 1.4 Fold instability. (a) Progression of the folds with increase of strain from top to bottom when the substrate is a viscous liquid [74, 147]. (b) Progression of the folds with increase of strain from top to bottom when the substrate is an elastic solid [147].

However, if the substrate is highly pre-stretched, localized ridge instability, instead of fold, forms as the secondary bifurcation [75, 99, 155-157]. One in every several wrinkles grows to large amplitude to form ridges, and leave the neighboring wrinkles flattened (Figure 1.5). Although both folds and ridges are localized, their morphologies look very different. Folds grow inwards and fold up the surface, while ridges grow outwards and lift up the surface (Figure 1.5). If the substrate is not pre-stretched, folds form as a secondary bifurcation from wrinkles [145]; if the substrate is pre-tensioned mildly, wrinkles can sustain larger compression without a secondary bifurcation and form a shape with high aspect ratio [158]; if the pre-tension is large enough, ridges form at a relatively small compressive strain [75, 99, 155-157]. All these various behavior can be explained by the highly nonlinear elasticity of the substrate [155]. A pre-tension of the substrate favors the occurrence of outward deflections of the surface, while a pre-compression favors inward deflections [155].

Ridge instability was first observed and predicted by a numerical simulation [75], and then was realized in experiments [99, 155-157]. Large aspect ratio of the ridge instability facilitates its applications in reversible wettability tuning and stem cells alignment [156].

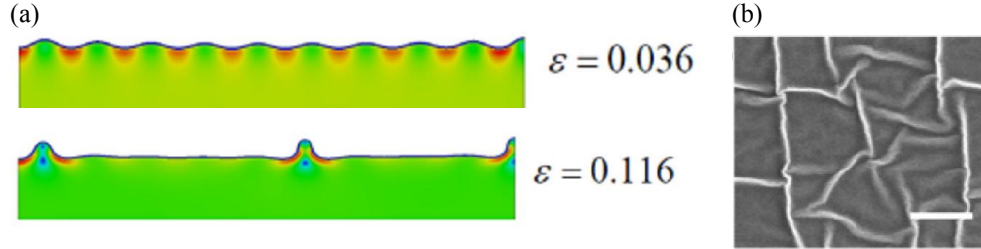


Figure 1.5 Ridge instability. (a) Simulation result showing the cross-section view of a secondary bifurcation from wrinkles to ridges [75]. (b) Experimental results showing the top view of ridges [156].

## 1.5 Outline of this thesis

This thesis studies the different types of mechanical instabilities: creases, wrinkles, folds, and ridges. In Chapter 2, we model growth in soft tissues and study creases generated by growth analytically and numerically. In Chapter 3, we perform numerical simulations to examine initiation and evolution of creases in strain-stiffening materials. In Chapter 4, we design a soft elastic bilayer to better control the formation and disappearance of creases based on a joint experimental and theoretical study. In Chapter 5, we perform simulations and experiments to show that an interface between two soft materials can form creases under compression. In Chapter 6, we investigate the critical conditions for the formation of wrinkles and creases in bilayers with arbitrary thicknesses and moduli of the two layers. In Chapter 7, we explore the effect of pre-stretch in the substrate on the post-wrinkling bifurcations in bilayers experimentally and theoretically. In Chapter 8, we experimentally realize the ridge localizations and networks by incremental release of the equi-biaxial

pre-stretch in the substrate with a microfluidic device, and theoretically simulate ridges and obtain the critical conditions for the formation of ridges. In Chapter 9, we perform numerical simulations to analyze the mechanics of ridge formation and propagation. Chapter 10 provides conclusions of this thesis.

## Chapter 2

### Creases in soft tissues generated by growth

#### 2.1 Introduction

Soft tissues often grow under constraint. For example, many tubular organs—arteries, airways, esophagi and intestines—grow under the constraint of a stiffer tissue, the smooth muscle [62, 159]. Some tumors grow under the constraint of necrotic cores [160]. Even in the absence of any stiff tissues, soft tissues develop internal constraint when the growth is inhomogeneous [161]. Constrained growth can cause the soft tissues to undulate and fold. These mechanical instabilities have physiological and pathological consequences [50, 51, 60, 65, 160, 162, 163]. When the smooth muscle of airways shortens, the mucosa folds and obstructs the airways; the amount of obstruction increases in asthma due to the thickening of the airway walls [162, 163]. Buckling can enable the invagination of embryos [51], and the primordial development of sunflowers [65]. Fingerprint patterns can result from the buckling of the layer of basal cells of the fetal epidermis [50]. The shape of a tumor can indicate its type [160].

Figure 2.1 illustrates several ubiquitous patterns of instability. For a soft material covered with a stiff thin layer, compression beyond a critical level leads to wrinkles [81]. Further compression will turn some of the wrinkles into folds [74, 95]. For a soft material not covered with a stiff layer, however, compression beyond a critical level leads to creases, without forming wrinkles first [106-109, 112, 113, 164]. While the wrinkles keep the surface

of the material locally smooth, the folds and creases cause the surface to self-contact. The tip of a fold remains open due to the bending rigidity of the stiff layer, but the tip of a crease is sharp.

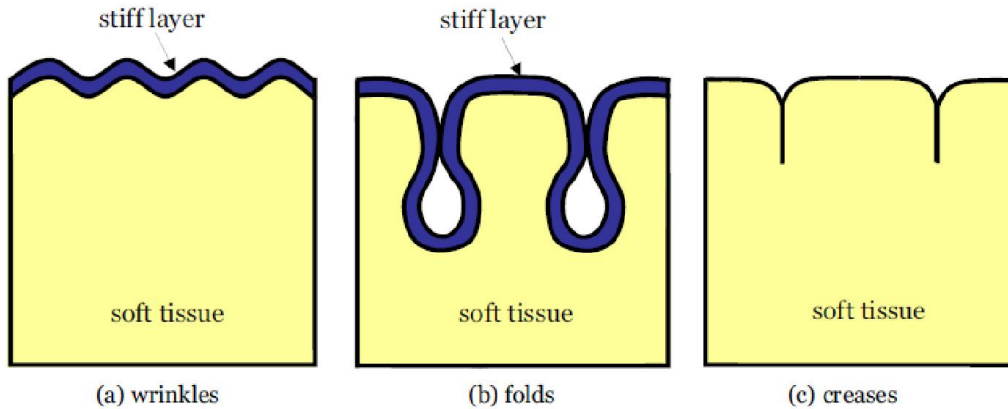


Figure 2.1 Schematic illustrations of three ubiquitous patterns of mechanical instability.

The onset of wrinkles corresponds to superposing a field of strain infinitesimal in amplitude, but finite in space. By contrast, the onset of creases corresponds to superposing a field of strain finite in amplitude, but infinitesimal in space. Consequently, the critical condition for the onset of wrinkles can be determined by a classical linear perturbation analysis, while the critical condition for the onset of creases cannot. Several recent papers have studied creases in soft materials caused by external forces [106-109, 113, 164].

This chapter studies creases in tissues undergoing constrained growth. We show that the critical conditions for the onset of the growth-induced creases take a remarkably simple form. The critical conditions are illustrated with tubes of tissues growing either inside a rigid shell or outside a rigid core. Furthermore, deep creases in a tube are simulated by using the finite-element method, and the number of creases is estimated by minimizing the free energy.

## 2.2 Growth model

As illustrated in Figure 2.2, we adopt a well-known model of growth [165]. A tissue is taken to be stress-free before the growth. An unconstrained and homogeneous growth changes the size of the tissue, but does not induce any stress. The stress-free growth is characterized by a growth tensor,  $\mathbf{G}$ , which maps any vector in the tissue in the stress-free state to a vector in the tissue after the growth by a stretch and a rotation. To model the constrained and inhomogeneous growth, we think of the tissue as many small elements, and name each element by its coordinate  $\mathbf{X}$  when the tissue is in the stress-free state. The growth of the element is characterized by a growth tensor  $\mathbf{G}(\mathbf{X})$ , which may vary from one element to another. If only the stress-free growth tensor were considered, the neighboring elements would not fit together after the growth, but would have gaps or overlaps [166]. This incompatible, stress-free state after the growth is illustrated in Figure. 2.2 To make the elements compatible with one another, and to satisfy the constraint imposed by surrounding stiff tissues, each element deforms, which is characterized by a deformation tensor,  $\mathbf{A}(\mathbf{X})$ . The multiplication of the growth tensor and the deformation tensor gives the deformation gradient [165]:

$$\mathbf{F} = \mathbf{A}\mathbf{G} . \tag{2.1}$$

As illustrated in Figure. 2.2,  $\mathbf{G}(\mathbf{X})$  maps the tissue from the stress-free state before the growth to the stress-free state after the growth,  $\mathbf{A}(\mathbf{X})$  maps the tissue from the stress-free state after the growth to the stressed state after the growth, and the deformation gradient  $\mathbf{F}(\mathbf{X})$  maps the tissue from the stress-free state before the growth to the stressed state after the growth. While both  $\mathbf{G}(\mathbf{X})$  and  $\mathbf{A}(\mathbf{X})$  may be incompatible, their multiplication  $\mathbf{F}(\mathbf{X})$

is compatible [166, 167].

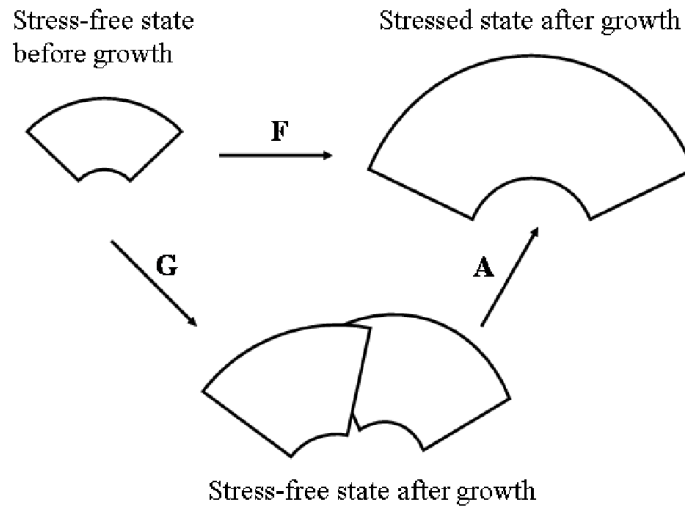


Figure 2.2 A model of the growth of a tissue identifies three states: the stress-free state before the growth, stress-free state after the growth, and the stressed state after the growth. Mapping from one state to another is accomplished by three tensors: the growth tensor  $\mathbf{G}$ , the deformation tensor  $\mathbf{A}$ , and the deformation gradient  $\mathbf{F}$ , which are related to each other by  $\mathbf{F} = \mathbf{A}\mathbf{G}$ .

The deformation gradient relates to the field of displacement in the usual way. Let an element of the tissue occupy a place of coordinate  $\mathbf{X}$  when the tissue is in the stress-free state before the growth, and move to a place of coordinate  $\mathbf{x}$  when the tissue is in the stressed state after the growth. The field of displacement in the tissue is represented by the function  $\mathbf{x}(\mathbf{X})$ . The constraint of the surrounding stiff tissues can be imposed by prescribing the values of the function  $\mathbf{x}(\mathbf{X})$  for the elements of the tissue on the boundary. The deformation gradient is defined as

$$F_{iK} = \partial x_i(\mathbf{X}) / \partial X_K. \quad (2.2)$$

We adopt the simplest version of the model, in which the field of the growth tensor  $\mathbf{G}(\mathbf{X})$  is prescribed and is independent of the stress in the tissue. Furthermore, the deformation is assumed to be elastic and incompressible,  $\det(\mathbf{A})=1$ . The elasticity of the

tissue is assumed to be neo-Hookean and isotropic, so that the elastic energy of the tissue is

$$\Pi = \int \frac{\mu}{2} [\text{tr}(\mathbf{A}^T \mathbf{A}) - 3] \det(\mathbf{G}) dV, \quad (2.3)$$

where  $\mu$  is the shear modulus. The integral extends over the volume of the tissue in the stress-free state before the growth, and  $\det(\mathbf{G})$  is the volume after the growth divided by that before the growth. If the body is subject to mechanical forces, the potential energy of the forces need be added to (2.3). The total free energy is minimized subject to the constraint  $\det(\mathbf{A}) = 1$  and the boundary conditions of  $\mathbf{x}(\mathbf{X})$ .

### 2.3 Critical condition for the initiation of creases due to growth

Before creases set in, the surface of the tissue is smooth, and every element on the surface is in a well-defined state of strain. When the state of strain of an element reaches a critical condition, a crease sets in at this element—that is, the onset of each crease is autonomous [106-108]. For a neo-Hookean material subject to external forces, the critical conditions for the onset of creases have been calculated for general states of strain [107]. We now apply these conditions to tissues growing under constraint. Within the model of growth illustrated in Figure 2.2, the stress is developed in going from the stress-free state after the growth to the stressed state after the growth. Consequently, the critical conditions for the onset of creases obtained in [107] should be applied to the elastic deformation tensor  $\mathbf{A}(\mathbf{X})$ .

For an element  $\mathbf{X}$  on the surface of the tissue, the three eigenvalues of  $\mathbf{A}^T \mathbf{A}$  are denoted by  $\alpha_1^2, \alpha_2^2, \alpha_3^2$ —that is,  $\alpha_1, \alpha_2, \alpha_3$  are the principal elastic stretches. The surface of the tissue is assumed to be traction free, so that the direction normal to the surface is a principal direction of the stress tensor and, for a material of isotropic elasticity, is also a

principal direction of the elastic deformation tensor. The other two principal directions are tangential to the surface of the tissue. We label the direction normal to the surface as direction 3, and the other two principal directions as directions 1 and 2. The critical condition for the onset of a crease normal to direction 1 is

$$\alpha_3 / \alpha_1 = 2.4, \quad (2.4)$$

while the critical condition for the onset of a crease normal to direction 2 is

$$\alpha_3 / \alpha_2 = 2.4. \quad (2.5)$$

The value 2.4 was obtained for the incompressible neo-Hookean material by finite element calculation in [107], in which the critical condition for the onset of crease is defined as the condition when the elastic energy of creased state equals the smooth state. Creases will form first in the direction with the lower value in  $\alpha_1$  and  $\alpha_2$ . If  $\alpha_1 = \alpha_2$ , creases may form in any direction inside the surface.

## 2.4 Tissue growing in a rigid shell

We next illustrate the critical conditions with examples. Figure 2.3 shows a tube of a tissue growing in a rigid shell. In the stress-free state before the growth, the tube is of radii  $A$  and  $B$ . In the stressed state after the growth, the tube is of radii  $a$  and  $B$ . The rigid shell constrains the growth, and the soft tissue is perfectly bonded to the rigid shell, so that after the growth the outer radius and the length of the tube remain unchanged. Since the length of the tube is large compared to the radii, we assume that the tissue deforms under the plane-strain conditions. The growth tensor is assumed to be of the form  $\mathbf{G} = \text{diag}[g_r, g_\theta, g_z]$ , where  $g_r, g_\theta, g_z$  are the growth ratios in the radial, circumferential, and longitudinal

directions of the tube. The growth is taken to be homogeneous, so that  $g_r, g_\theta, g_z$  are constant independent of the position in the tissue.

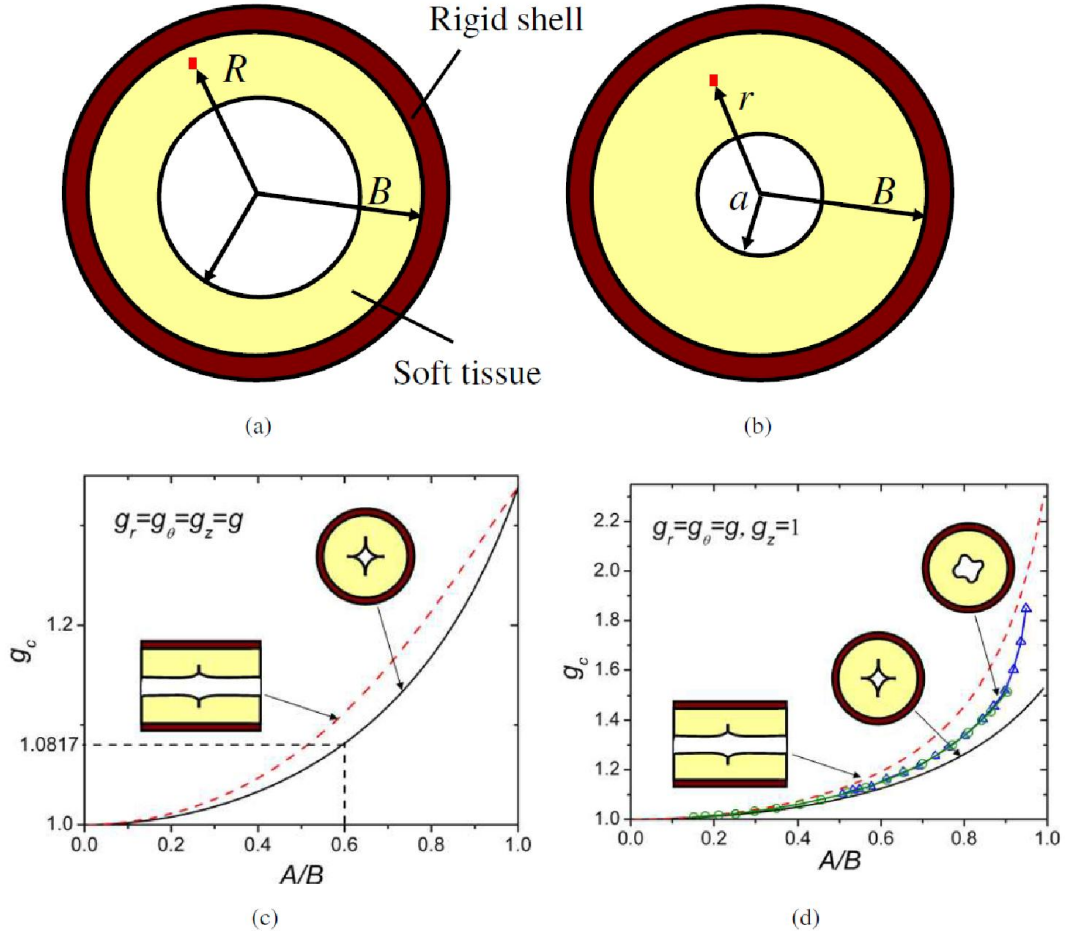


Figure 2.3 A tube of a tissue grows inside a rigid shell. (a) The stress-free state before the growth. (b) The axisymmetric stressed state after the growth. The critical growth ratio for the onset of creases as a function of  $A/B$  for (c) isotropic growth and (d) an example of anisotropic growth. The solid lines are for circumferential creases, and the dashed lines are for longitudinal creases. In (d) the line with circles and triangles are the critical conditions for the onset of wrinkles. For the isotropic growth (c), when  $A/B = 0.6$ , the critical growth ratio is  $g_c = 1.0817$ .

Prior to the onset of creases, the growth causes the tube to undergo axisymmetric deformation. Consider an element of the tissue, at distance  $R$  from the axis of the tube in the stress-free state before the growth. In the stressed state after the growth, the element moves to a place at distance  $r$  from the axis of the tube. The function  $r(R)$  specifies the field of

displacement. Because the elastic deformation is taken to be incompressible, the increase in the volume of the tube is entirely due to the growth. Consider an annulus between the radii  $B$  and  $R$  in the stress-free state before the growth, and between the radii  $B$  and  $r$  in the stressed state after the growth. The growth increases the volume of the annulus by factor  $g_r g_\theta g_z$ , so that

$$B^2 - r^2 = g_r g_\theta g_z (B^2 - R^2). \quad (2.6)$$

This expression specifies the field of displacement, the function  $r(R)$ . To prevent the tissue from interpenetrating after the growth, we require that  $a > 0$ . Inserting this condition into (6), we obtain that  $B^2 > g_r g_\theta g_z (B^2 - A^2)$ . The deformation gradient takes the form  $\mathbf{F} = \text{diag}[\lambda_r, \lambda_\theta, \lambda_z]$ , with the principal stretches being  $\lambda_r = g_r g_\theta g_z / \lambda_\theta$ ,  $\lambda_\theta = r / R$ , and  $\lambda_z = 1$ . The elastic deformation tensor takes the form  $\mathbf{A} = \text{diag}[\alpha_r, \alpha_\theta, \alpha_z]$ , with the principal elastic stretches being  $\alpha_r = \lambda_r / g_r$ ,  $\alpha_\theta = \lambda_\theta / g_\theta$ ,  $\alpha_z = \lambda_z / g_z$ .

Following (2.4) and (2.5), the critical condition for the onset of circumferential creases is  $\alpha_r / \alpha_\theta = 2.4$  at the surface of the tube  $R = A$ , or

$$g_\theta^2 g_z^2 / \left( \frac{B^2}{A^2} - g_r g_\theta g_z \left( \frac{B^2}{A^2} - 1 \right) \right) = 2.4. \quad (2.7)$$

The critical condition for the onset of longitudinal creases is  $\alpha_r / \alpha_z = 2.4$  at the surface of the tube  $R = A$ , or

$$g_\theta g_z^2 / \sqrt{\frac{B^2}{A^2} - g_r g_\theta g_z \left( \frac{B^2}{A^2} - 1 \right)} = 2.4. \quad (2.8)$$

In the limit  $A/B \rightarrow 0$ , any growth  $g_r g_\theta g_z > 1$  will cause very large compressive elastic strain at the inner surface of the tube, so that the critical condition for the onset of creases is  $g_r g_\theta g_z = 1$ . In the limit  $A/B \rightarrow 1$ , the tube behaves like a flat layer constrained by

a rigid substrate, so that the critical condition for the onset of the circumferential creases is  $g_\theta^2 g_z = 2.4$ , and the critical condition for the onset of the longitudinal creases is  $g_\theta g_z^2 = 2.4$ .

For isotropic growth,  $g_r = g_\theta = g_z = g$ , Figure. 2.3c plots the critical growth ratio  $g_c$  for the onset of creases as a function of  $A/B$ . The solid curve represents the critical condition for the onset of circumferential creases, and the dashed curve represents the critical condition for the onset of longitudinal creases. For both types of creases,  $g_c = 1$  in the limit  $A/B \rightarrow 0$ , and  $g_c = \sqrt[3]{2.4}$  in the limit  $A/B \rightarrow 1$ . Between the two limits, the growth ratio needed to initiate the circumferential creases is less than that needed to initiate the longitudinal creases.

As an example of anisotropic growth, consider the growth ratios  $g_r = g_\theta = g$  and  $g_z = 1$ . Figure 2.3d plots the critical growth ratio  $g_c$  for the onset of creases as a function of  $A/B$ . In the limit  $A/B \rightarrow 1$ ,  $g_c = \sqrt{2.4}$  for the onset of the circumferential creases and  $g_c = 2.4$  for the onset of the longitudinal creases. In this example, the growth needed to initiate the circumferential creases is less than that needed to initiate the longitudinal creases. Also included in Figure 2.3d are the critical conditions for the onset of circumferential wrinkles obtained by the linear perturbation analysis (circles from [159] and triangles from [168]). A comparison of these results in Figure 2.3d indicates that the circumferential creases will set in, rather than the circumferential wrinkles.

## 2.5 Tissue growing outside a rigid core

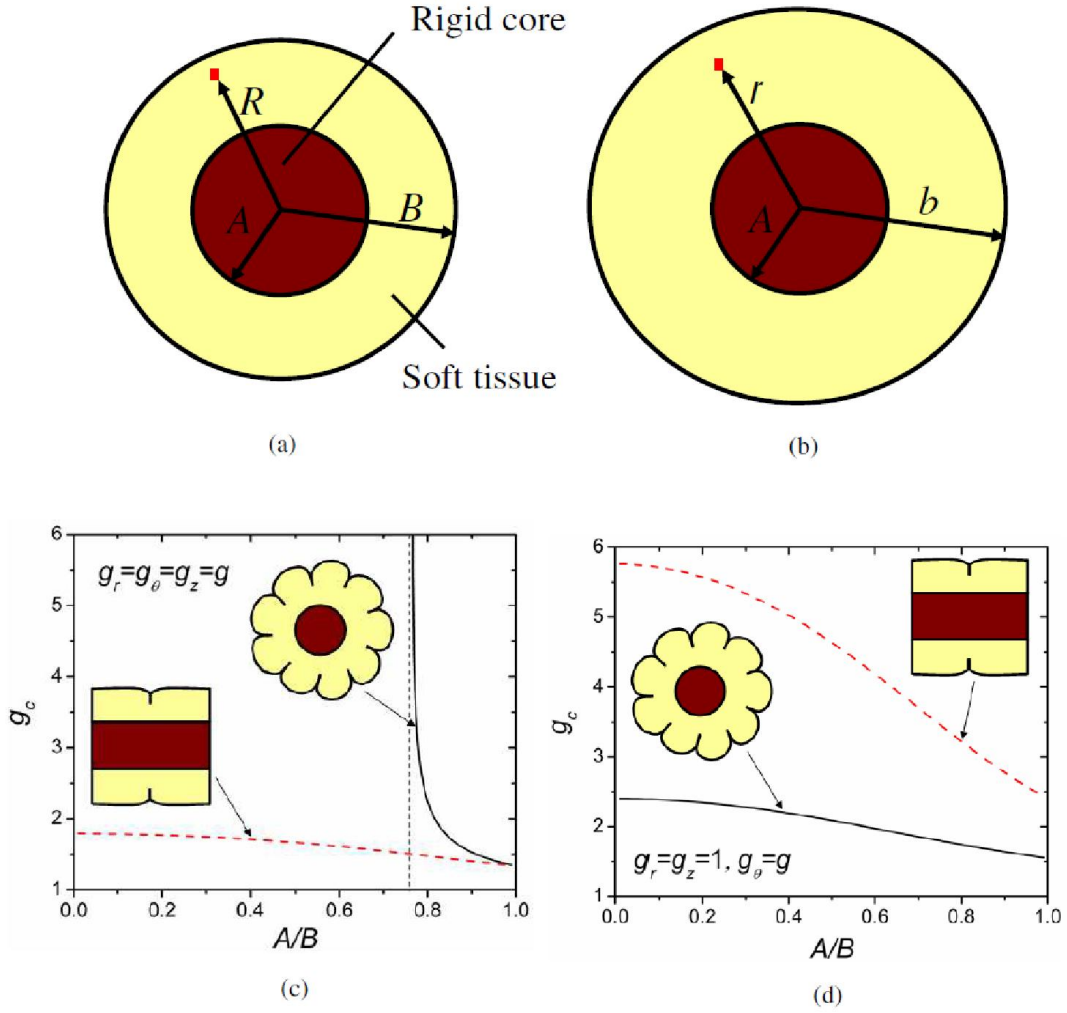


Figure 2.4 A tube of a tissue grows outside a rigid core. (a) The stress-free state before the growth. (b) The axisymmetric stressed state after the growth. The critical growth ratio for the onset of creases as a function of  $A/B$  for (c) isotropic growth and (d) an example of anisotropic growth. The solid lines are for circumferential creases, and the dashed lines are for longitudinal creases.

Figure 2.4 illustrates a tube of a tissue growing outside a rigid core. The tube is of radii  $A$  and  $B$  in the stress-free state before the growth, and is of radii  $A$  and  $b$  in the stressed state after the growth. Prior to the onset of creases, the growth causes axisymmetric deformation in the tube. The field of deformation  $r(R)$  is determined by

$$r^2 - A^2 = g_r g_\theta g_z (R^2 - A^2) . \quad (2.9)$$

The critical condition for the onset of circumferential creases on the outer surface of the tube

is

$$g_\theta^2 g_z / \left( \frac{A^2}{B^2} - g_r g_\theta g_z \left( \frac{A^2}{B^2} - 1 \right) \right) = 2.4. \quad (2.10)$$

The critical condition for the onset of longitudinal creases on the outer surface of the tube is

$$g_\theta g_z^2 / \sqrt{\frac{A^2}{B^2} - g_r g_\theta g_z \left( \frac{A^2}{B^2} - 1 \right)} = 2.4. \quad (2.11)$$

In the limit  $A/B \rightarrow 0$ , the rigid core becomes a thin needle, and the critical conditions for the onset of the circumferential and longitudinal creases become  $g_\theta/g_r = 2.4$  and  $\sqrt{g_\theta g_z^3/g_r} = 2.4$ . In the limit  $A/B \rightarrow 1$ , the tube behaves like a flat layer constrained by a rigid substrate, which has been discussed above.

For the isotropic growth  $g_r = g_\theta = g_z = g$ , Figure 2.4c plots the critical level of growth  $g_c$  for the onset of creases as a function of  $A/B$ . The critical condition for the onset of circumferential creases can only be satisfied when  $A/B > \sqrt{7/12}$ . Below this value, the rigid core does not provide sufficient constraint to cause circumferential creases on the outer surface of the tube. At all values of  $A/B$ , longitudinal creases will set in before circumferential creases. By contrast, in the case of anisotropic growth,  $g_r = g_z = 1$ ,  $g_\theta = g$ , circumferential creases can form in the entire range of  $A/B$ , and can form before longitudinal creases, Figure 2.4d. In [122], the swelling of a gel under constraint was studied in the similar geometry. When the core is much stiffer than the swelling gel, sharp creases were observed in the gel. The linear perturbation analysis in [122] assumed infinitesimal strains from the smooth state, and corresponds to an analysis of wrinkling. By contrast, our analysis based on the result of nonlinear finite element method allows large strains from the smooth state, and corresponds to creases.

## 2.6 Number of deep creases

Because the state of strain is invariant everywhere on the surface of the tube under the axisymmetric deformation, every point on the surface reaches the critical condition to initiate a crease simultaneously. Consequently, the condition for the onset of creases does not determine the number of creases in a tube. In order to determine the number of creases, we go beyond the initiation of the creases and analyze deep creases. The analysis is carried out by using the commercial finite-element software ABAQUS, in which the growth of soft tissues can be simulated by thermal expansion. Plane strain conditions are assumed. Symmetry is assumed such that if the number of creases is  $N$ , we only need to simulate one part of the tube within angle  $\pi/N$ . Following [113], we prescribe the nucleus of a crease by placing a defect, a quarter of a circle with small radius, on the surface of the tube. To eliminate the effect of the defect, its size is made much smaller than the thickness of the tube. At the same time, to resolve the field close to the defect, the size of the elements close to the defect is made much smaller than the size of the defect. The surface of the tube is allowed to self-contact.

As an example, consider a tube of a tissue growing inside a rigid shell, with  $A/B=0.6$ . The growth is taken to be isotropic, and the elasticity neo-Hookean. The finite-element calculation determines the free energy per unit thickness of the tube as a function of the growth ratio,  $\Pi(g)$ . The free energy per thickness of the axisymmetric deformation without creases can be calculated analytically, according to (2.3):

$$\Pi_0 = \frac{\mu\pi g}{2} \left[ B^2(1-g^3) \log \frac{g^3(A^2 - B^2) + B^2}{A^2} + (2g^3 + 1 - 3g^2)(B^2 - A^2) \right]. \quad (2.12)$$

Figure 2.5 shows the ratio  $\Pi/\Pi_0$  as a function of the growth ratio  $g$  for several cases of

prescribed numbers of defects. When  $g$  is small,  $\Pi/\Pi_0 = 1$ , and the defects do not cause the surface to self-contact and become creased. Beyond a critical value  $g_c = 1.085$ , however,  $\Pi/\Pi_0 < 1$ , and the defects cause the surface to self-contact and become creased. This critical value is consistent with the analytical prediction for the onset of creases  $g_c = 1.0817$  as shown in Figure 2.3c. Right after the initiation, individual creases do not interact, so that more creases can release more energy. With the further growth, the creases deepen and interact with one another. As shown in Figure 2.5, the energy in the tube with seven creases is lowest when  $g < 1.1033$ . After that the tube with six creases has the lowest energy until  $g = 1.1291$ , and then the tube with five creases has the lowest energy. Figure 2.6 shows the creased states of the tube with different prescribed numbers of creases at different growth ratios. The color indicates the value of the von Mises stress.

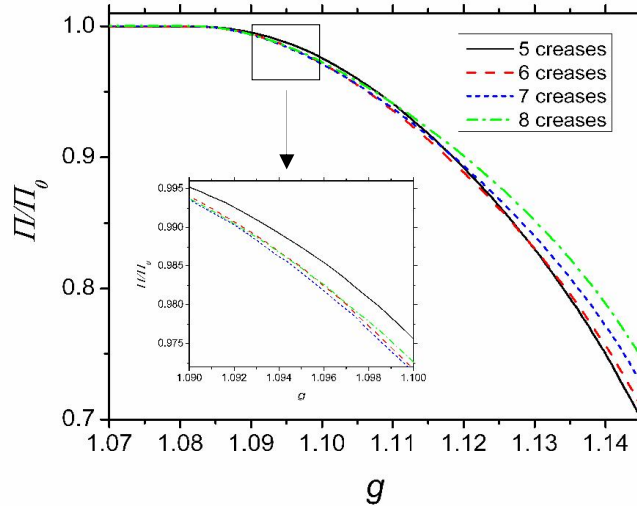


Figure 2.5 For a tube of a tissue growing inside a rigid shell, the ratio of the elastic energy of the creased state to that of the axisymmetric state,  $\Pi/\Pi_0$ , is plotted as a function of the growth ratio,  $g$ . The inset enlarges the squared region.

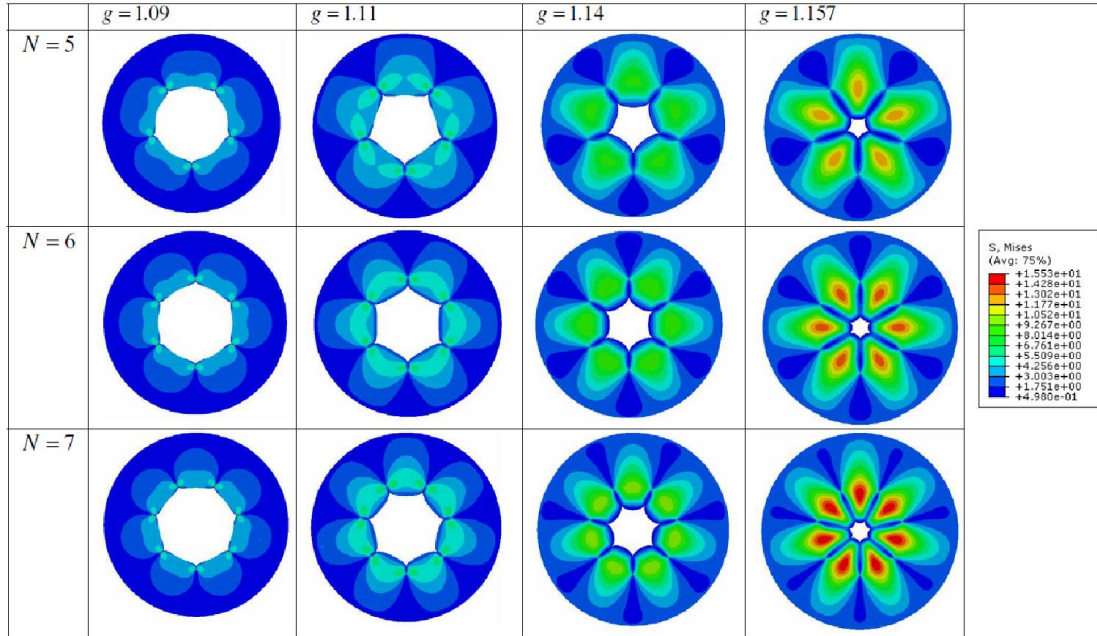


Figure 2.6 Deep creases develop from the surface of a tube of a tissue growing inside a rigid shell. Different numbers of creases are prescribed. The color indicates the level of the von Mises stress.

## 2.7 Summary

In summary, we obtain the critical conditions for the onset of creases caused by constrained growth. The critical conditions are illustrated with tubes of soft tissues growing under the constraint of either rigid outer shells or rigid inner cores. By comparing with the critical conditions for the onset of wrinkles, we show that creases are preferred type of instability. Deep creases are simulated by using the finite-element method. The number of deep creases in a tube may be determined by minimizing the free energy.

## Chapter 3

# Smoothing creases on surfaces of strain-stiffening materials

### 3.1 Introduction

Biot analyzed an elastic block compressed under the plane strain conditions (Figure 3.1a, b), and predicted that the flat surface of the block was unstable when the compression reached a critical strain of 0.46 [97]. This theoretical prediction remained unchallenged until Gent and Cho noted its disagreement with their experimental finding that the surface formed creases at a critical strain of 0.35 [105]. Hohlfeld and Mahadevan showed that Biot's solution and creases are two distinct instabilities, and that creases set in at a critical strain of 0.35 [73, 106]. Biot linearized the boundary-value problem around a state of finite homogeneous deformation, and his solution corresponds to a smooth, wavy surface (i.e., wrinkles) of small strain relative to the homogeneous state (Figure 3.1c). By contrast, a crease is a localized, self-contact region of large strain relative to the homogeneous state (Figure 3.1d). The critical strain for the onset of creases has since been obtained by several other approaches of numerical analysis [107-111]. Furthermore, Hohlfeld mapped the onset of a crease to the coexistence of two scale-invariant states [169]. A post-bifurcation analysis of Cao and Hutchinson showed that Biot's solution is unstable [164].

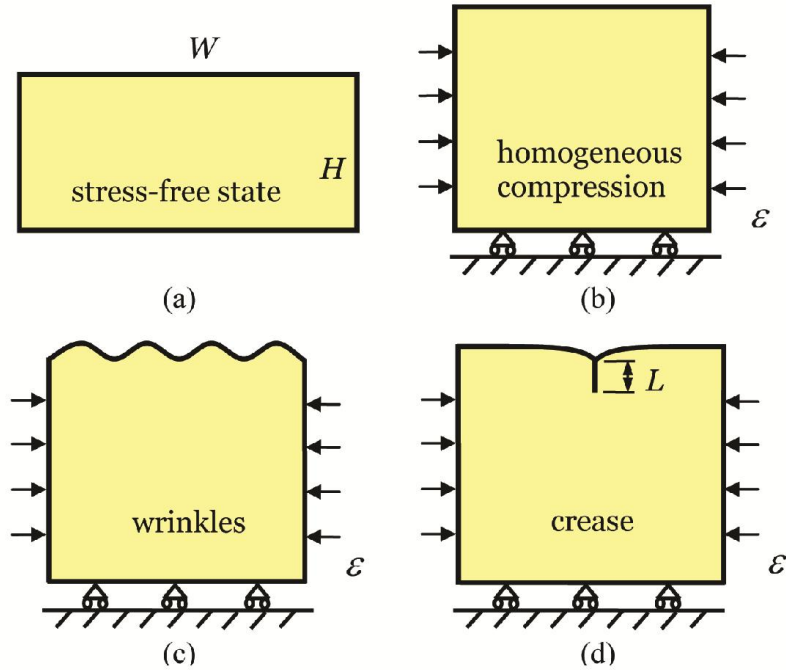


Figure 3.1 (a) In the stress-free state, a block of elastic material is of width  $W$  and height  $H$ . Under compression the material may deform in several ways. (b) The block undergoes homogeneous compression. (c) The surface forms wrinkles. (d) The surface forms a crease of crease depth  $L$ . The applied strain  $\epsilon$  is defined by the compressive displacement divided by the initial width of the block.

No evidence exists that Biot’s smoothly wavy surfaces have ever been observed experimentally on homogeneous elastic blocks under compression. Creases, however, have been observed routinely on elastic blocks [39, 99, 105, 112-118, 120-128, 130-136]. Creases have been studied in soft tissues [48, 58, 60]. Creases have been related to the Schallamach waves arising during the frictional sliding of a rubber against a rigid surface [137], and to the osmotic collapse of a water-filled cavity in a hydrogel [108]. Creases can also form on the interface between two elastic solids [140]. Applications of creases have been explored, including the use of creases to remove control chemical patterns [39, 136], enzymatic activity [39], cellular behavior [141], adhesion [142], and biofouling [143].

Although wrinkles have never been observed experimentally on large homogeneous elastic blocks under compression, many factors affect the behavior of creases, and may even

promote the formation of wrinkles. Surface energy adds a barrier to the nucleation of creases, and makes nucleation defect-sensitive [119, 138]. When the loading is an electric field, wrinkles may form when the elastocapillary effect is strong enough [132]. For a layer of finite thickness with a traction-free bottom surface, creases on the top surface are subcritical—that is, as the applied compressive strain increases and then decreases, creases form and disappear with hysteresis [139]. For a stiff film on a soft substrate under compression, the film forms periodic wrinkles at a small strain [81]. As the strain increases, the wrinkles double their period, and ultimately lead to deep folds [74]. When the film and the substrate have comparable moduli, the transitions between creases, wrinkles and folds become complex [99, 170]. Complex behavior also occurs in a solid of gradient modulus [171, 172]. If the substrate is pre-compressed, creases are subcritical, and form and disappear with hysteresis [173].

Biot's original analysis, as well as much of the subsequent theoretical work, represents the elastic solid by the neo-Hookean model. This model describes elastomers of long polymer chains well, but is inadequate when materials stiffen steeply. A soft biological tissue, for example, is usually a composite of a compliant matrix and stiff fibers [174]. When the tissue is under a small strain, the matrix carries much of the load, but the fibers are not tight, so that the tissue is soft. As the strain increases, the fibers gradually tighten and rotate to the loading direction, so that the tissue stiffens steeply. As another example, an elastomer is a three-dimensional network of long and flexible polymer chains [175]. When the elastomer is under no stress, the chains undergo thermal motion and coil. When the elastomer is subject to moderate strains, the chains uncoil and the stress-strain relation of

the elastomer is well represented by the neo-Hookean model, which is derived under the assumption of Gaussian chains. When the chains become nearly straight, however, they no longer obey the Gaussian statistics, and the stress-strain curve rises steeply and deviates significantly from the neo-Hookean model. Destrade et al. analyzed the onset of wrinkles on the surface of a bending block [94]. They showed that when the material stiffens at a relatively small strain, the critical strain for the onset of wrinkles differs significantly from that of a neo-Hookean material. These authors, however, did not consider the formation of creases.

In this chapter, we represent a strain-stiffening material by using the Gent model [176], and study the initiation and development of creases by using a finite element method. For a solid that stiffens at large strains, as the compression increases, the surface is initially smooth, then forms creases, and finally becomes smooth again. For a solid that stiffens at small strains, creases will never form and the surface remains smooth for all levels of compression. We also study the condition for the onset of wrinkles by using linear perturbation. If a strain-stiffening material does become unstable under compression, we find that creases—rather than wrinkles—will form.

### **3.2 Strain-stiffening materials**

We list the equations that govern the boundary-value problems of finite elasticity [177]. A body deforms in space from the stress-free state to a current state. In the body, a material particle is at spatial location  $\mathbf{X}$  in the stress-free state, and is at spatial location  $\mathbf{x}$  in the current state. The function  $\mathbf{x}(\mathbf{X})$  describes the deformation of the body from the

stress-free state to the current state. The deformation gradient is

$$F_{iK} = \frac{\partial x_i(\mathbf{X})}{\partial X_K}. \quad (3.1)$$

Let  $s_{iK}$  be the nominal stress. The balance of forces requires that

$$\frac{\partial s_{iK}}{\partial X_K} = \mathbf{0}. \quad (3.2)$$

The balance of forces also requires that

$$s_{iK} N_K = T_i, \quad (3.3)$$

where  $N_K$  is the unit vector normal to a small flat region in the body in the stress-free state, and  $T_i$  is the nominal traction (i.e., the force applied on the region in the current state divided by the area of the region in the stress-free state).

The body is made of an elastic material, taken to be incompressible,

$$\det(\mathbf{F}) = 1. \quad (3.4)$$

The density of the Helmholtz free energy is a function of the deformation gradient,  $\psi(\mathbf{F})$ .

The equation of state is

$$s_{iK} = \frac{\partial \psi(\mathbf{F})}{\partial F_{iK}} - \Pi H_{iK}, \quad (3.5)$$

where  $\mathbf{H} = \mathbf{F}^{-T}$ , and  $\Pi$  is a hydrostatic pressure to be determined by the boundary-value problem. When the material undergoes a rigid-body rotation, the free energy is invariant, so that  $\psi$  depends on  $\mathbf{F}$  through the Green deformation tensor  $\mathbf{F}^T \mathbf{F}$ . This dependence, together with (3.5), implies the balance of moments acting on any small part of the body,

$$s_{iK} F_{jK} = s_{jK} F_{iK}.$$

Following Gent [176], we model strain-stiffening materials by using the free energy function

$$\psi = -\frac{\mu}{2} J_{\text{lim}} \log\left(1 - \frac{J_1}{J_{\text{lim}}}\right). \quad (3.6)$$

The Gent model represents the magnitude of deformation by a single scalar,  $J_1 = F_{iK} F_{iK} - 3$ . The model has two material parameters,  $\mu$  and  $J_{\text{lim}}$ . In the limit of small deformation,  $J_1/J_{\text{lim}} \rightarrow 0$ , the Gent model recovers the neo-Hookean model  $\psi = \mu J_1/2$ , with  $\mu$  being the shear modulus. In the limit of large deformation,  $J_1/J_{\text{lim}} \rightarrow 1$ , the free energy diverges and the stress-strain curve turns vertical. The parameter  $J_{\text{lim}}$  represents the limiting deformation. The stress-strain relation of the Gent materials is

$$s_{iK} = \frac{\mu}{1 - J_1/J_{\text{lim}}} F_{iK} - \Pi H_{iK}. \quad (3.7)$$

For a block in a state of homogeneous, plane-strain deformation, when the width changes by a factor of  $\lambda$ , the height changes by a factor of  $\lambda^{-1}$ , and the deformation gradient is

$$\mathbf{F} = \begin{bmatrix} \lambda & 0 & 0 \\ 0 & 1 & 0 \\ 0 & 0 & \lambda^{-1} \end{bmatrix}. \quad (3.8)$$

The nominal stress in the direction of compression is

$$s = \frac{\mu(\lambda - \lambda^{-3})}{1 - (\lambda^2 + \lambda^{-2} - 2)/J_{\text{lim}}}. \quad (3.9)$$

In obtaining (3.9), we have used the traction-free boundary condition  $s_{33} = 0$ , which gives  $\Pi = \mu\lambda^{-2}/(1 - (\lambda^2 + \lambda^{-2} - 2)/J_{\text{lim}})$ . Define the compressive strain by  $\varepsilon = 1 - \lambda$ . For a given value of  $J_{\text{lim}}$ , the stress-strain curve turns vertical at a limiting strain  $\varepsilon_{\text{lim}}$  (Figure 3.2a). The limiting strain increases with  $J_{\text{lim}}$  (Figure 3.2b).

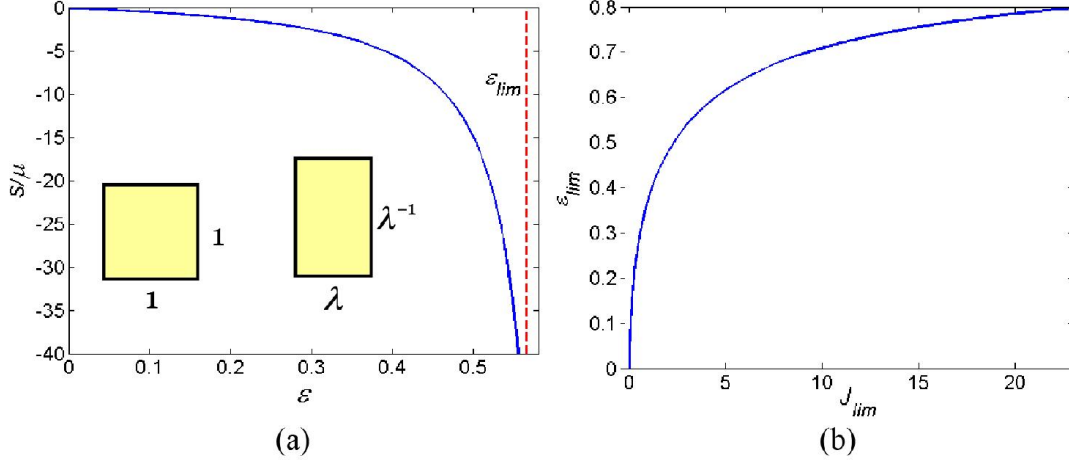


Figure 3.2 The Gent model characterizes a strain-stiffening material with two parameters:  $\mu$  and  $J_{lim}$ . (a) The compressive stress-strain curve for a Gent material with  $J_{lim} = 4.5$ . A unit cube is compressed under the plane strain condition, with the width changing by a factor of  $\lambda$ , the height changing by a factor of  $\lambda^{-1}$ . The compressive strain is defined by  $\varepsilon = 1 - \lambda$ , and the stress  $s$  is normalized by  $\mu$ . The stress-strain curve turns vertical at the limiting strain  $\varepsilon_{lim}$ . (b) The limiting strain  $\varepsilon_{lim}$  increases with  $J_{lim}$ .

### 3.3 Creases

We study the initiation and development of creases by using the finite element software ABAQUS. We implement the Gent model by writing a user-defined subroutine UMAT (Appendix A.1). We assume that surface of the solid forms a periodic array of creases, and one period of the solid is a block of width  $W$  and height  $H$  in the stress-free state (Figure 3.1a). The width  $W$  of the block is assumed to be 3.5 times of the height  $H$  of the block, a ratio that is representative of experimental observations [113]. Taking advantage of the symmetry of a crease, we only simulate one half of the block. We fix the horizontal position of the mid-plane of the block, compress the block under the plane strain conditions by prescribing horizontal displacement on the edge of the block, and fix the vertical position of the bottom plane of the block (Figure 3.1d). To break the translational symmetry, we place a quarter of a

small circle on the surface as a defect. The size of the defect is much smaller than the length scale of the problem,  $H$ . In the vicinity of the defect, we resolve the field by using meshes much smaller than the size of the defect.

Our calculation shows that, as the applied compressive strain increases, the surface is initially flat, then forms a crease, and finally becomes flat again. This surprising sequence of development is understood by inspecting the distribution of deformation in the block at several values of the applied compressive strain (Figure 3.3). Here the particular sequence is calculated using a Gent material with  $J_{\text{lim}} = 4.5$ . The colors correspond to the values of the scalar measure of deformation,  $J_1$ . Recall that the free energy density  $\psi$  is a monotonic function of  $J_1$ . At  $\varepsilon = 0.351$ , the surface of the block is flat and the deformation in the block is homogeneous (Figure 3.3a). A crease initiates at the critical strain  $\varepsilon = 0.396$ . After the crease sets in, the deformation becomes inhomogeneous. The formation of the crease reduces deformation in a T-shaped region close to the surface and in the region underneath the tip of the crease (Figure 3.3b). However, in a wing-shaped regions on the two sides near the tip of the crease (in green), the deformation exceeds the applied deformation. The two effects—the reduced deformation in the T-shaped region and the increased deformation in the wing-shaped region—compete. The combination of these two effects guarantees that the total energy of the creased state is lower than the flat state. Self-contact of the surface starts to form when the crease initiates, and the crease first grows deeper as the applied strain  $\varepsilon$  increases. However, the wing-shaped region also grows larger (Figure 3.3c). Due to the strain-stiffening effect, the energy penalty in the wing-shaped region may increase faster than the energy reduction in the T-shaped region. When  $\varepsilon = 0.498$ , the crease depth is

maximal (Figure 3.3c). With the further increase of  $\varepsilon$ , the penalty of forming a deep crease is so high that the crease starts to smoothen instead. When  $\varepsilon = 0.556$ , both the crease depth and penalty region become smaller (Figure 3.3d). When  $\varepsilon = 0.579$ , the surface becomes nearly flat again, and the value of  $J_1$  in the whole block of material is close to  $J_{lim}$  (Figure 3.3e). Interestingly, similar smoothening and disappearance of ridge instability was also predicted in strain-stiffening Arruda-Boyce materials with a small stretch limit [155].

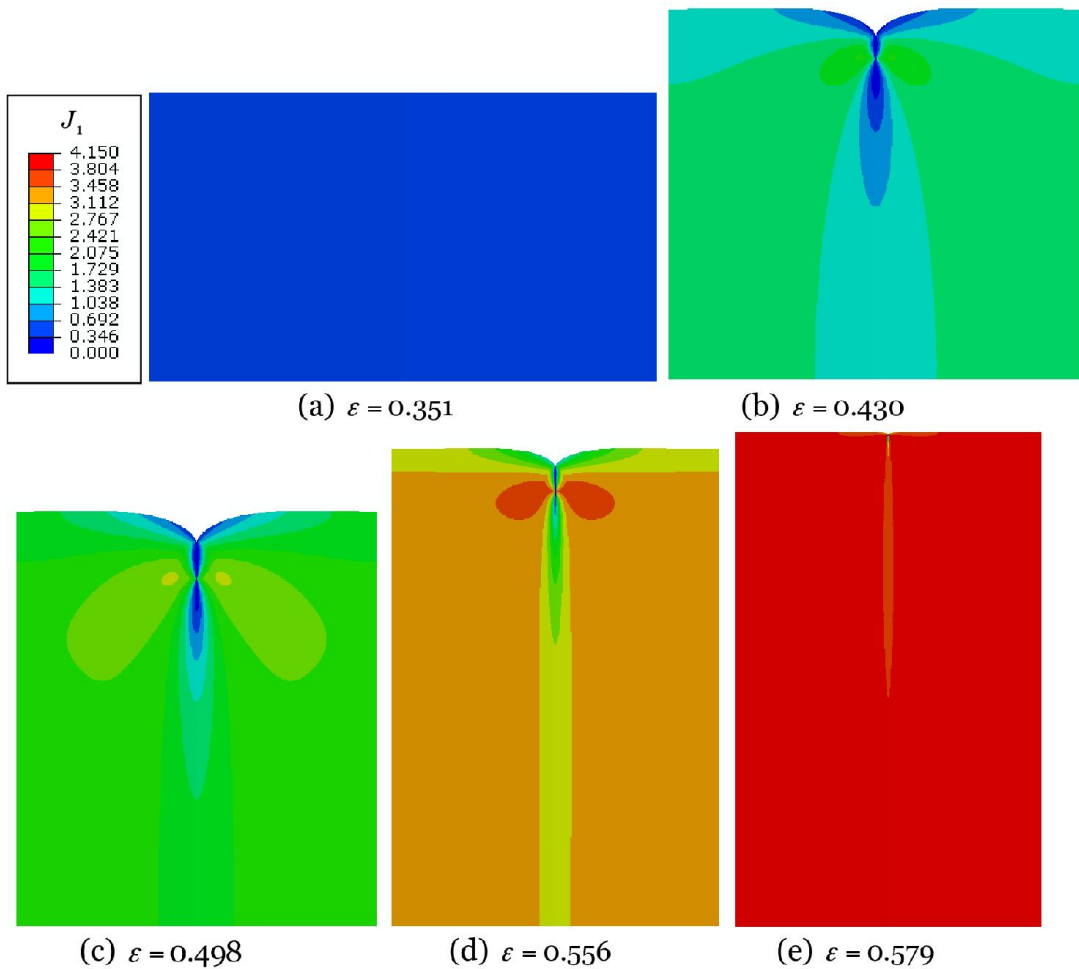


Figure 3.3 As the applied strain  $\varepsilon$  increases, the surface is initially flat, then forms a crease, and finally becomes flat again. The calculation is carried out with a Gent material of  $J_{lim} = 4.5$ . (a)-(e) correspond to states at increasing levels of applied strain. The colors represent the scalar measure of the deformation,  $J_1$ .

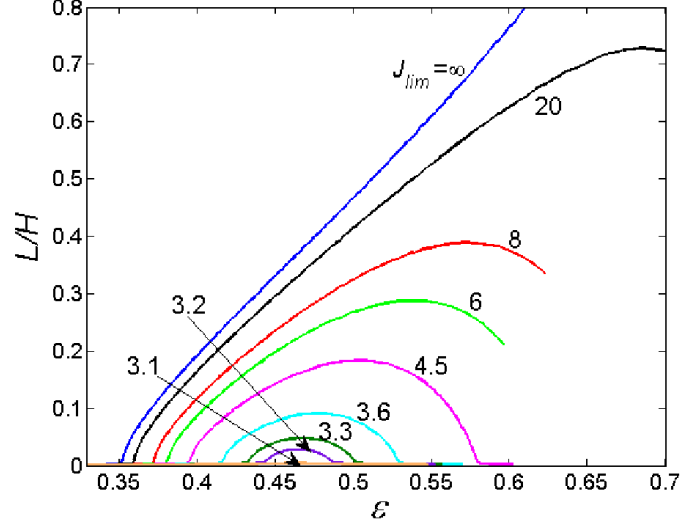


Figure 3.4 The normalized crease depth  $L/H$  as a function of the applied strain  $\varepsilon$ . When  $J_{lim} \rightarrow \infty$ , the Gent model recovers the neo-Hookean model, and the crease initiates when  $\varepsilon$  reaches around 0.354. With the decrease of  $J_{lim}$ , the critical strain for the onset of the crease increases, and the crease disappears when the applied strain is large enough. When  $J_{lim}$  is below about 3.1, no crease forms at any strain.

We plot the bifurcation diagram by using the applied strain  $\varepsilon$  as the control variable, and the normalized crease depth  $L/H$  as a proxy for the state of the block (Figure 3.4). For a Gent material of  $J_{lim} = 4.5$ , the crease depth first grows larger as the strain  $\varepsilon$  increases. The crease depth reaches the maximal at the strain of  $\varepsilon = 0.498$ . With further increase of the strain  $\varepsilon$ , the crease depth starts to decrease, and the crease is smoothed. At strain  $\varepsilon = 0.579$ , the crease depth becomes zero again, and the crease disappears. The dependence of the normalized crease depth  $L/H$  on strain  $\varepsilon$  for other  $J_{lim}$  is also plotted in Figure 3.4. For large values of  $J_{lim}$ , the limiting stretches are large, so that the mesh near the tip of the crease distorts severely. The computation remains stable to a larger applied strain as we refine the mesh further, but the computation will be extremely expensive to reach the disappearance of the creases. Therefore, we only included the results that show the clear growth and smoothing of creases. When  $J_{lim} \rightarrow \infty$ , the material recovers the

neo-Hookean material. The crease depth  $L/H$  is zero until a crease sets in at strain around 0.354. Then the crease depth  $L/H$  monotonically increases with  $\varepsilon$ . For finite  $J_{lim}$ , the creases always smoothen at some finite strain. With the decrease of  $J_{lim}$ , the critical strain for the onset of crease increases. At the same time, the strain for the disappearance of crease decreases with the decrease of  $J_{lim}$ . When  $J_{lim} \leq 3.1$ , creases are completely suppressed.

The conditions for the onset and disappearance of creases depend on the value of  $J_{lim}$  (Figure 3.5). The lower part of the curve corresponds to the strain for the initiation of the crease, and the upper part of the curve corresponds to the strain for the disappearance of the crease. No crease forms when  $J_{lim} \leq 3.1$ . Creases can only form in the region enclosed by the curve. The window of strain for the existence of creases decreases with the decreases of  $J_{lim}$ .

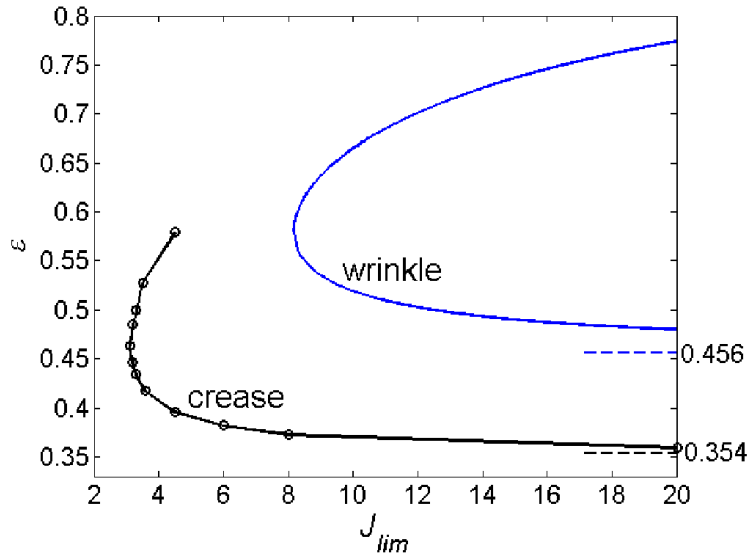


Figure 3.5 The critical strains for the initiation and disappearance of a crease as a function of  $J_{lim}$ . The circles represent the results of finite element simulations. Also plotted are the critical conditions for the formation of wrinkles predicted by a linear perturbation analysis.

### 3.4 Wrinkles

When a body of a Gent material is compressed, will the flat surface of the body form wrinkles instead of creases? To answer this question, we determine the critical condition for the onset of wrinkles, and compare the condition with that for the onset of creases. We perturb the homogeneous state with a field of small, inhomogeneous strain. We look for the condition under which the homogeneous deformation bifurcates into the inhomogeneous state. This bifurcation corresponds to the onset of wrinkles (Figure 3.1c). The inhomogeneous field is governed by linear partial differential equations. Their general solutions under the plane strain conditions can be represented by functions of complex variables [178]. We solve the field using a method of functions of a single complex variable [179]. The Stroh formalism has been used to perform linear perturbation analysis by many authors [94, 127, 180].

#### 3.4.1 Two states with small difference in deformation gradient and pressure

For a body made of an incompressible material, specified by a free energy function  $\psi(\mathbf{F})$  and a set of boundary conditions, we ask if the body can be in two distinct states. A standard method to answer this question exists if the difference between the two states is restricted to be small in deformation gradient and pressure. Represent one state by functions  $\mathbf{x}^o(\mathbf{X})$  and  $\Pi^o(\mathbf{X})$ , and the other state by functions  $\mathbf{x}(\mathbf{X})$  and  $\Pi(\mathbf{X})$ . Define the difference of the two fields by the functions

$$\tilde{\mathbf{x}} = \mathbf{x}(\mathbf{X}) - \mathbf{x}^o(\mathbf{X}), \quad (3.10)$$

$$\tilde{\Pi} = \Pi(\mathbf{X}) - \Pi^\circ(\mathbf{X}). \quad (3.11)$$

Similarly write the difference in deformation gradient, stress and traction as  $\tilde{\mathbf{F}} = \mathbf{F} - \mathbf{F}^\circ$ ,

$$\tilde{\mathbf{s}} = \mathbf{s} - \mathbf{s}^\circ \quad \text{and} \quad \tilde{\mathbf{T}} = \mathbf{T} - \mathbf{T}^\circ.$$

The two states both satisfy (3.1)-(3.5), giving the equations that govern the difference between the two states:

$$\tilde{F}_{iK} = \frac{\partial \tilde{x}_i(\mathbf{X})}{\partial X_K}, \quad (3.12)$$

$$\frac{\partial \tilde{s}_{iK}}{\partial X_K} = \mathbf{0}, \quad (3.13)$$

$$\tilde{s}_{iK} N_K = \tilde{T}_i, \quad (3.14)$$

$$H_{iK}^\circ \tilde{F}_{iK} = \mathbf{0}, \quad (3.15)$$

$$\tilde{s}_{iK} = C_{iKjL}(\mathbf{F}^\circ) \tilde{F}_{jL} - H_{iK}^\circ \tilde{\Pi}, \quad (3.16)$$

where  $\mathbf{H}^\circ = (\mathbf{F}^\circ)^{-T}$ , and the fourth order tensor of tangent moduli is

$$C_{iKjL}(\mathbf{F}^\circ) = \left[ \frac{\partial^2 \psi(\mathbf{F})}{\partial F_{iK} \partial F_{jL}} \right]_{\mathbf{F}=\mathbf{F}^\circ} + \Pi H_{iL}^\circ H_{jK}^\circ. \quad (3.17)$$

In obtaining (3.15)-(3.17), we have assumed that the differences in the deformation gradient and in the pressure between the two states are small enough to allow the Taylor expansion around the state  $\mathbf{F}^\circ$  and  $\Pi^\circ$ . This assumption is valid when the other state represented by  $\mathbf{x}(\mathbf{X})$  and  $\Pi(\mathbf{X})$  corresponds to wrinkles, but not creases. Given the state represented by  $\mathbf{x}^\circ(\mathbf{X})$  and  $\Pi^\circ(\mathbf{X})$ , (3.12)-(3.17) define a boundary-value problem that governs the incremental state  $\tilde{\mathbf{x}}(\mathbf{X})$  and  $\tilde{\Pi}(\mathbf{X})$ .

### 3.4.2 Represent general solutions using functions of complex variables

We further assume that the state represented by  $\mathbf{x}^o(\mathbf{X})$  and  $\Pi^o(\mathbf{X})$  is a homogeneous deformation, so that  $C_{iKjL}$  is a tensor of the same value for all material particles in the body. A combination of (3.12), (3.13) and (3.16) gives that

$$C_{iKjL} \frac{\partial^2 \tilde{x}_j(\mathbf{X})}{\partial X_L \partial X_K} - H_{iK}^o \frac{\partial \tilde{\Pi}(\mathbf{X})}{\partial X_K} = \mathbf{0}. \quad (3.18)$$

A combination of (3.12) and (3.15) gives that

$$H_{iK}^o \frac{\partial \tilde{x}_i(\mathbf{X})}{\partial X_K} = \mathbf{0}. \quad (3.19)$$

Equations (3.18) and (3.19) are linear, homogeneous, constant-coefficient, partial differential equations that govern the incremental deformation  $\tilde{\mathbf{x}}(\mathbf{X})$  and incremental pressure  $\tilde{\Pi}(\mathbf{X})$ .

In the stress-free state, the body fills a half space below the plane  $X_3 = 0$ . Because the incremental field is governed by linear equations, wrinkles of arbitrary shape can be represented by a linear superposition of Fourier components. Each Fourier component correspond to a field invariant in a direction lying in the  $(X_1, X_2)$ . We make this direction coincide with the axis  $X_2$ . Consequently, the state is represented by functions of two variables,  $\tilde{\mathbf{x}}(X_1, X_3)$  and  $\tilde{\Pi}(X_1, X_3)$ .

We now adopt the method of Stroh [178] to obtain the general solution to equations (3.18) and (3.19). Write both  $\tilde{\mathbf{x}}(X_1, X_3)$  and  $\tilde{\Pi}(X_1, X_3)$  in terms of a function of a single variable:

$$\tilde{\mathbf{x}}(X_1, X_3) = \mathbf{A}f(z), \quad (3.20)$$

$$\tilde{\Pi}(X_1, X_3) = Qf'(z). \quad (3.21)$$

Here  $z = X_1 + pX_3$ ,  $f(z)$  is an analytical function, and  $f'(z) = df(z)/dz$ . The quantities  $p$ ,  $Q$  and  $A_j$  are determined as follows.

Substituting (3.20) and (3.21) into (3.18) and (3.19), we obtain that

$$\left(C_{i_1 j_1} + p(C_{i_1 j_3} + C_{i_3 j_1}) + p^2 C_{i_3 j_3}\right) A_j - (H_{i_1}^0 + p H_{i_3}^0) Q = 0, \quad (3.22)$$

$$(H_{j_1}^0 + p H_{j_3}^0) A_j = 0. \quad (3.23)$$

These are four linear, homogeneous algebraic equations for  $A_1, A_2, A_3$  and  $Q$ , corresponding to an eigenvalue problem. Non-trivial solution exists if and only if

$$\det \mathbf{M} = 0, \quad (3.24)$$

where

$$\begin{aligned} M_{ij} &= C_{i_1 j_1} + p(C_{i_1 j_3} + C_{i_3 j_1}) + p^2 C_{i_3 j_3}, \\ M_{i_4} &= -H_{i_1}^0 - p H_{i_3}^0, M_{4j} = H_{j_1}^0 + p H_{j_3}^0, M_{44} = 0, \end{aligned} \quad (3.25)$$

with  $i = 1, 2, 3$  and  $j = 1, 2, 3$ .

Although  $\mathbf{M}$  is a four-by-four matrix, we note that  $\det \mathbf{M}$  is a sixth-order polynomial of  $p$ . A real-valued  $p$  would correspond to body waves and spread the incremental field in the entire body. Here we look for surface waves, and assume that all roots of (3.24) are complex-valued  $p$ . Because the coefficients of the sixth-order polynomial are real-valued, the six roots of the polynomials form three complex conjugates. We label the three roots with positive imaginary part by  $p_\alpha$  ( $\alpha = 1, 2, 3$ ), and their complex conjugates by  $\bar{p}_\alpha$ . We label the corresponding quantities solved from the eigenvalue problem by  $(A_{1\alpha}, A_{2\alpha}, A_{3\alpha}, Q_\alpha)$  and  $(\bar{A}_{1\alpha}, \bar{A}_{2\alpha}, \bar{A}_{3\alpha}, \bar{Q}_\alpha)$ . For each value of  $\alpha$ , the quantities  $(\bar{A}_{1\alpha}, \bar{A}_{2\alpha}, \bar{A}_{3\alpha}, \bar{Q}_\alpha)$  can be normalized by an arbitrary complex number.

Let  $z_\alpha = X_1 + p_\alpha X_3$ , and  $f_1(z_1), f_2(z_2), f_3(z_3)$  be three arbitrary analytical functions. The functions  $\tilde{\mathbf{x}}(X_1, X_3)$  and  $\tilde{\Pi}(X_1, X_3)$  are real-valued. The general solution to (3.18) and (3.19) is a linear superposition of the three analytical functions:

$$\tilde{x}_i = \sum_{\alpha=1}^3 A_{i\alpha} f_{\alpha}(z_{\alpha}) + \sum_{\alpha=1}^3 \bar{A}_{i\alpha} \overline{f_{\alpha}(z_{\alpha})}, \quad (3.26)$$

$$\tilde{\Pi} = \sum_{\alpha=1}^3 Q_{\alpha} f'_{\alpha}(z_{\alpha}) + \sum_{\alpha=1}^3 \bar{Q}_{\alpha} \overline{f'_{\alpha}(z_{\alpha})}. \quad (3.27)$$

We use the Greek letter  $\alpha$  for the summation over a non-tensor suffix and explicitly indicate the summation.

Substituting (3.26) and (3.27) into the equation of state (3.16), we obtain the incremental nominal stress  $\tilde{s}_{iK}$ :

$$\tilde{s}_{i3} = \sum_{\alpha=1}^3 L_{i\alpha} f'_{\alpha}(z_{\alpha}) + \sum_{\alpha=1}^3 \bar{L}_{i\alpha} \overline{f'_{\alpha}(z_{\alpha})}, \quad (3.28)$$

$$\tilde{s}_{i1} = -\sum_{\alpha=1}^3 L_{i\alpha} p_{\alpha} f'_{\alpha}(z_{\alpha}) - \sum_{\alpha=1}^3 \bar{L}_{i\alpha} \bar{p}_{\alpha} \overline{f'_{\alpha}(z_{\alpha})}, \quad (3.29)$$

where

$$L_{i\alpha} = (C_{i3j1} + p_{\alpha} C_{i3j3}) A_{j\alpha} - H_{i3} Q_{\alpha}. \quad (3.30)$$

For the incompressible Gent material, the tangent moduli  $C_{iKjL}$  and the components of the matrices  $A_{i\alpha}$ ,  $Q_{\alpha}$  and  $L_{i\alpha}$  are given in Appendix A.2.

### 3.4.3 Critical condition for the onset of wrinkles

The Stroh representation involves three complex variables. We now derive the critical condition for the onset of wrinkles using the method of a single complex variable [179]. Let  $z$  be a complex variable of the form  $z = X_1 + qX_3$ , with  $q$  being an arbitrary complex number with a positive imaginary part. Observe that at the surface of the body,  $X_3 = 0$ , the complex variable  $z$  coincides with  $z_1$ ,  $z_2$  and  $z_3$  defined above. Write

$$\mathbf{f}(z) = [f_1(z), f_2(z), f_3(z)]^T. \quad (3.31)$$

Once we obtain  $\mathbf{f}(z)$  for any  $z$ , we can replace  $z$  with  $z_1, z_2$  and  $z_3$ , and use  $f_1(z_1)$ ,  $f_2(z_2)$  and  $f_3(z_3)$  to describe the wrinkled state.

The surface of the body ( $X_3 = 0$ ) is traction-free, so that (3.28) reduces to

$$\mathbf{L}\mathbf{f}'(X_1) + \bar{\mathbf{L}}\bar{\mathbf{f}}'(X_1) = \mathbf{0}. \quad (3.32)$$

This equation sets the boundary condition for the function  $\mathbf{f}(z)$ . The boundary-value problem is solved as follows. Assume that the material occupies the lower half plane ( $X_3 \leq 0$ ). Because no singularity is present in the material,  $\mathbf{L}\mathbf{f}'(z)$  is a function analytic in the lower half plane. Consequently,  $\bar{\mathbf{L}}\bar{\mathbf{f}}'(z)$  is a function analytic in the upper half plane. By the theorem of analytic continuation, the boundary condition (3.32) requires that both functions be analytic in the entire plane [181]. The wrinkles are disturbance localized on the surface of the gel, so that the analytic functions vanish as  $|z| \rightarrow \infty$ . The only function analytic in the entire plane and vanishing as  $|z| \rightarrow \infty$  is the function being zero everywhere. Consequently, the solution to the boundary-value problem (3.32) is

$$\mathbf{L}\mathbf{f}'(z) = \mathbf{0}. \quad (3.33)$$

Equation (3.33) is an eigenvalue problem. A nontrivial solution of  $\mathbf{f}'(z)$  exists if and only if

$$\det \mathbf{L} = 0. \quad (3.34)$$

For the in-plane deformation of a Gent material, a combination of (3.34) and (A.16) in Appendix A.2 gives the critical condition for the onset of wrinkles. The determinant of  $\mathbf{L}$  is a purely imaginary number. Figure 3.6 plots  $\det \mathbf{L} (J_{\text{lim}} - J_1)^2 / \mu^2 J_{\text{lim}}^2 i$  as a function of the applied strain. As  $J_{\text{lim}}$  increases, the curves approach the behavior of the limiting case for the neo-Hookean materials,  $J_{\text{lim}} \rightarrow \infty$ . When  $J_{\text{lim}} \rightarrow \infty$ , the solution  $\varepsilon = 0.456$  recovers

the Biot condition for the onset of wrinkles in a neo-Hookean material. When  $J_{\text{lim}} > 8.169$ , there are two admissible solutions. When  $J_{\text{lim}} = 8.169$ , equation (3.34) has a unique solution  $\varepsilon = 0.580$ . When  $J_{\text{lim}} < 8.169$ , equation (3.34) has no solution, i.e. no wrinkles are predicted by the linear perturbation method.

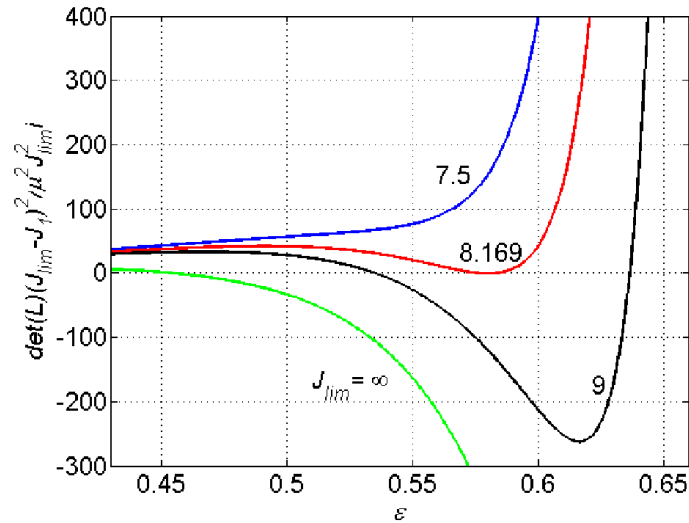


Figure 3.6 The critical strains for wrinkles are determined by  $\det \mathbf{L} = 0$ . Plotted here are  $\det \mathbf{L} (J_{\text{lim}} - J_1)^2 / \mu^2 J_{\text{lim}}^2 i$  as a function of the applied strain  $\varepsilon$  for different values of  $J_{\text{lim}}$ . When  $J_{\text{lim}} \rightarrow \infty$ , the solution  $\varepsilon = 0.456$  recovers the Biot condition for the onset of wrinkles in a neo-Hookean material. When  $J_{\text{lim}} > 8.169$ ,  $\det \mathbf{L}$  becomes zero at two values of the applied strain. When  $J_{\text{lim}} = 8.169$ ,  $\det \mathbf{L} = 0$  has a single solution  $\varepsilon = 0.580$ . When  $J_{\text{lim}} < 8.169$ ,  $\det(\mathbf{L})$  cannot reach zero at any applied strain.

The critical conditions for the formation of wrinkles obtained by the linear perturbation analysis are compared with those of creases (Figure 3.5). As  $J_{\text{lim}}$  decreases, the branch of smaller strains increases, but the branch of larger strains decreases. Observe that creases always form at a smaller strain than wrinkles. Thus, neither branch of wrinkles can be realized. Creases, rather than wrinkles, should be observed in the Gent materials.

Once the critical strain is determined by (3.34), the eigenvector is

$$\begin{bmatrix} e_1 \\ e_3 \end{bmatrix} = \begin{bmatrix} 1 \\ -L_{11}/L_{13} \end{bmatrix}. \quad (3.35)$$

Consequently, the field of the wrinkled state is determined by  $f'_1(z_1) = w(z_1)$  and  $f'_3(z_3) = -(L_{11}/L_{13})w(z_3)$ , where  $w(z)$  is an arbitrary scalar-valued function.

### 3.5 Summary

In this chapter, we study the initiation and development of creases in strain-stiffening materials. As a result, strain-stiffening effect raises the critical strain for crease initiation and smoothens creases when the compressive strain is large enough. When the strain-stiffening effect is strong enough, creases can be completely suppressed. As a comparison, we also study the initiation of wrinkles in strain-stiffening materials by the linear perturbation method under Stroh formalism. The classical Stroh formalism is extended for incompressible materials. Our calculations show that creases always form at a lower strain than wrinkles, and should be observed.

The stretchability of soft tissues varies with age, pathology, humidity, as well as the type of tissues. Tendons and ligaments can be uniaxially stretched to a strain of around 15% [182], cartilage 120% [182], skins 110% [183], and aorta 100% [182]. These values correspond to  $J_{\text{lim}} = 0.06, 2.75, 2.36$  and  $2.00$ , respectively. These small values of  $J_{\text{lim}}$  suggests that strain-stiffening effect can play a significant role to suppress the formation of creasing in these soft tissues.

For polymers, the limiting stretch can be estimated as  $\sqrt{n}$ , with  $n$  being the number of monomers between two crosslinkers. The value of  $n$  can be as small as several or

as large as thousands, and  $J_{\text{lim}}$  can be correspondingly tuned by changing the crosslink density. The value of  $J_{\text{lim}}$  can also be tuned by mixing polymers of different kinds. It is hoped that our theoretical prediction of the smoothening and suppressing of creases can soon be demonstrated experimentally.

## Chapter 4

# Controlled formation and disappearance of creases

### 4.1 Introduction

While elastic instabilities, such as buckling of a column or wrinkling of a sheet, have long been regarded as modes of failure in architectural structures [184], electromechanical systems [6], and composite materials [7], they have increasingly been exploited for a variety of applications [13, 20, 22, 27, 28, 81, 185-187]. An example of recent interest is the formation of surface creases when a soft elastic material is compressed beyond a critical value [106, 107, 112, 138]. Creases may look superficially like cracks, since both correspond to sharp, singular features. A significant difference, however, can be readily appreciated and will have practical implications. While repeated opening and closing of cracks often leads to fatigue and catastrophic failure, the elastic character of creases makes it possible to cycle a soft material repeatedly between flat and creased states without inducing damage.

The formation of creases corresponds to a pronounced change of state, reminiscent of a phase transition. This change of state has recently been used to connect diverse stimuli to multiple functions. Crease-inducing stimuli include temperature [39], light [136] and electric fields [134, 188]. Functions enabled by the formation of creases include the control of chemical patterns [39, 136], enzymatic activity [39], cellular behavior [141], and adhesion [142]. Each of these applications depends on how creases form and disappear. For a planar surface under in-plane compression, the creasing instability is supercritical, where creases

appear and disappear at the same critical strain, with no hysteresis [107]. In practice, however, surface tension provides a small energy barrier against creasing, thus leading to nucleation and growth of shallow, but finite-depth, creases at small over-strains beyond the critical value [138]. It is tantalizing to imagine devices that exploit snapping creases, in a way analogous to other snap-through instability used to trigger giant deformation between bistable states [186, 187]. Unfortunately, the challenges associated with controlling this barrier, and the related presence of adhesion within the self-contacting creases [138], have led to widely varying degrees of hysteresis in different material systems [105, 114, 119-121] complicating the application of creases.

In this chapter, we describe a strategy to create bistable flat and creased states, and to switch between the two states repeatedly, with hysteresis, at reproducible strains. We pre-compress a thick substrate, and then attach a thin film on top of the substrate. When we further compress the substrate-film bilayer, the difference in compression between the two layers defines an elastic energy barrier that separates the flat state from a state with deep creases that penetrate into the substrate. We use a combination of experiments and calculations to show that this approach yields well-defined bistable states, connected by a snap-through instability. The strains at which the creases form and disappear are tunable over a large range, through the pre-compression of the substrate and the relative thickness of the film.

## **4.2 Subcritical creases**

The formation of creases can be either a supercritical or subcritical bifurcation. We

sketch the bifurcation diagrams using the applied strain  $\varepsilon$  as the control parameter, and the depth of crease  $d$  as an indicator of state (Figure 4.1). The depth of a crease  $d$  is defined as the distance between the uppermost point on the free surface and the bottom of the self-contacting region. For each type of bifurcation, a compressed solid has two branches of equilibrium states: the flat and the creased states. In the bifurcation diagram, the branch of flat states corresponds to the horizontal axis  $d = 0$ , while the branch of creased states corresponds to a curve with  $d > 0$ . In the supercritical bifurcation, the creased branch is a monotonic function. When  $\varepsilon$  exceeds a critical value  $\varepsilon_c$ , the flat surface forms creases. The depth of the creases  $d$  is infinitesimal initially, and then increases gradually as  $\varepsilon$  increases. When  $\varepsilon$  is reduced, the creases disappear at the same critical strain  $\varepsilon_c$ , with no hysteresis. By contrast, in the subcritical bifurcation, the creased branch is not a monotonic function. When the applied compressive strain exceeds the strain  $\varepsilon_f$ , the flat state becomes unstable, but no creased state of small depth exists; rather, the flat surface snaps forward to a state with creases of finite depth  $d_f$ . When the applied compressive strain is reduced, the depth of the creases decreases gradually initially and then, at a finite depth  $d_b$  and strain  $\varepsilon_b$ , the creased surface snaps backward to the flat state. That is, the switching between the flat and the creased state is hysteretic.

We can also describe the subcritical bifurcation by sketching the change in elastic energy  $\Delta E$  to form creases as a function of the depth of the creases  $d$  (Figure 4.1c). A minimum energy corresponds to a stable equilibrium state, and a maximum energy corresponds to an unstable equilibrium state. The shape of the energy landscape depends on the applied compressive strain  $\varepsilon$ . At a very small strain,  $\varepsilon < \varepsilon_b$ , creases of any depth raise

the energy, and the flat state is stable. At a very large strain,  $\varepsilon > \varepsilon_F$ , the flat state is unstable, and a creased state is stable. At an intermediate strain,  $\varepsilon_B < \varepsilon < \varepsilon_F$ , the energy landscape has two local minima, one corresponding to a flat state, and the other to a creased state. Between the snap-forward strain  $\varepsilon_F$  and the snap-backward strain  $\varepsilon_B$  lies the Maxwell strain  $\varepsilon_M$ , at which the two energy minima are equal. The flat state has a lower energy than the creased state when  $\varepsilon_B < \varepsilon < \varepsilon_M$ , and the opposite is true when  $\varepsilon_M < \varepsilon < \varepsilon_F$ .

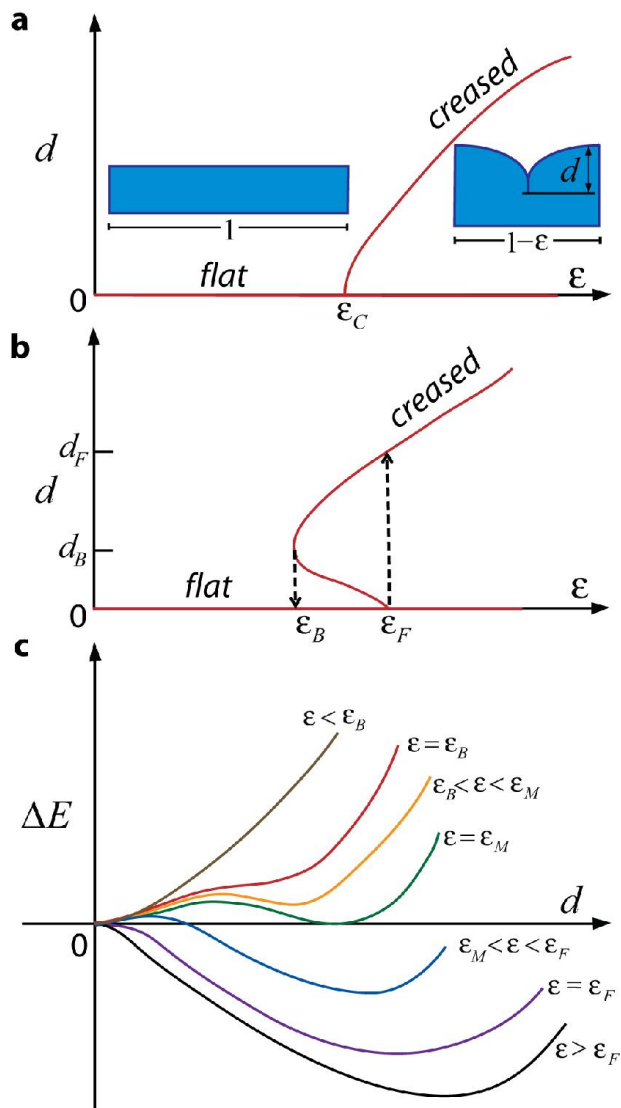


Figure 4.1 Supercritical and subcritical creases. Bifurcation diagrams for (a) supercritical and (b) subcritical creases. (c) Energy landscape corresponding to the subcritical bifurcation diagram.

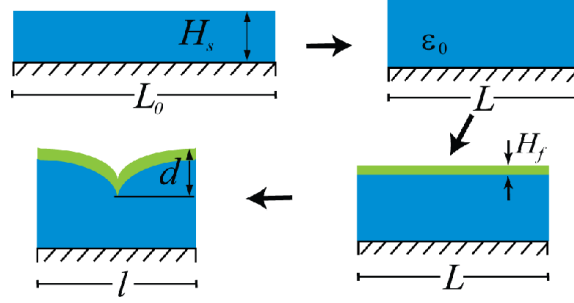


Figure 4.2 Experimental setup. A mounting layer is stretched to length  $L_0$ , and a substrate of undeformed thickness  $H_s$  is attached over the mounting layer. The mounting layer is partially relaxed to length  $L$ , and a film of undeformed thickness  $H_f$  is attached over the substrate. The mounting layer is further relaxed to length  $l$ .

We design a system capable of tunable hysteresis of creases by using a multilayer setup (Figure 4.2). We stretch a mounting layer to a length  $L_0$ , and attach a substrate of undeformed thickness  $H_s = 200 \mu\text{m}$ . We then partially relax the mounting layer to a length  $L$ , which compresses the substrate to a pre-strain  $\epsilon_0 = 1 - L/L_0$ . On the pre-strained substrate we attach a film of undeformed thickness  $H_f = 4 \mu\text{m}$ . When we relax the mounting layer to a length  $l$ , the film is under a compressive strain of  $\epsilon = 1 - l/L$ . Both the film and substrate are poly (dimethyl siloxane) (PDMS; Sylgard 184, Dow Corning) elastomers of the same composition (40 : 1 base : crosslinker by weight), and thus possess identical elastic properties in the undeformed state (shear modulus  $G = 16 \text{ kPa}$ ). The mounting layer is a much stiffer and thicker PDMS slab ( $G = 260 \text{ kPa}$ ), which keeps the bottom boundary of the substrate nearly planar while enabling the application of large compressive strains. All experiments are conducted with the surface submerged under an aqueous solution containing  $0.5 \text{ mg/mL}$  3-[hydro(polyethyleneoxy) propyl] heptamethyltrisiloxane (Gelest), which greatly reduces both surface tension (to  $\sim 0.8 \text{ mN/m}$ ) and self-adhesion [138], minimizing the importance of these effects compared to elasticity.

As a result, the hysteresis arises predominantly from the elastic barrier due to the differential strain between the thin film and substrate, rather than the small residual surface energy and adhesion in the self-contacting region.

## **4.3 Methods**

We use a combination of experiments and simulations to realize and study the subcritical creases, and demonstrate its controllable hysteresis.

### **4.3.1 Sample preparation**

All experiments are performed on bilayers supported on a pre-stretched elastic ‘mounting layer’. The film layer and substrate layer consist of Sylgard 184 (Dow Corning) PDMS, while the mounting layer is prepared using a custom PDMS formulation from Gelest Inc. The mounting layer is prepared by first thoroughly mixing part A containing 99.997% fumed silica reinforced vinyl terminated PDMS (DMS-V31S15, Gelest Inc.) and 0.003% platinum catalyst (SIP6831.2) and part B containing 90% vinyl terminated PDMS (DMS-V31) and 10% trimethylsiloxy terminated methylhydrosiloxane-dimethylsiloxane copolymer (HMS-301) by a weight ratio 3 to 1. The mixture is then degassed, spread onto a silicon wafer, and cured at 120 °C for 8 h to yield a PDMS film with a thickness of ~1-1.2 mm. This PDMS film is then cut into 0.8 cm × 2 cm slabs and the shear modulus is determined by tensile experiments to be 260 kPa. This custom formulation of PDMS provides larger accessible pre-stretch in the mounting layer (up to 250%) without fracture, while maintaining a modulus substantially above that of the substrate and film. The substrate layer

is prepared by spin coating degassed Sylgard 184 40:1 (by weight) base : crosslinker mixture onto a polystyrene support at 360 rpm for 120 s. After being cured at 70 °C for 1 h, the substrate layer is bonded to the mounting layer by spinning coating an adhesive layer of uncured 40:1 PDMS at 1200 rpm for 120 s and subsequently crosslinking this layer at 70 °C for 8 h prior to releasing pre-stretch in the mounting layer. Combining the pre-cured film with the adhesive layer gives rise to the substrate layer with an initial thickness of ~200  $\mu\text{m}$ . Then the polystyrene is detached and the PDMS substrate layer is put under uniaxial compression ( $\epsilon_0$ ) by partially releasing pre-stretch. The top film is a Sylgard 184 40:1 PDMS film with a thickness of ~4  $\mu\text{m}$  by spinning at 7000 rpm for 120 s. The top film is first partially cured at 70 °C for 15 min and then attached to the pre-compressed substrate; bonding between the layers is achieved by subsequently fully curing the film at 70 °C for 8 h. The lateral dimensions of the sample are at least 50 times as large as the combined thickness of the film and substrate, and thus in the central region of the film (where all measurements are conducted), the stress within each layer should be nearly uniform along the thickness direction.

#### **4.3.2 Measurement of viscoelastic properties**

To measure the viscoelastic properties of our samples, compression stress relaxation experiments are conducted on Sylgard 184 40:1 PDMS cylinders with 12.5 mm in diameter and 15 mm in height molded in a syringe by fully curing at 70 °C for 8 h. The compression stress relaxation experiments are performed on an Instron 5800 compression test machine with 50 N loading cell by first loading the cylinder to a compressive strain of 0.45 with a

strain rate  $0.05 \text{ min}^{-1}$ , and then tracking the compressive stress relaxation over 1 h while holding at this strain. Fitting the stress relaxation curve with exponential decay function gives rise to the characteristic viscoelastic time  $\tau = 1100 \text{ s}$ .

### 4.3.3 Optical and confocal microscope imaging

Over the strains of interest ( $\varepsilon = 0.42 - 0.48$  for loading and  $\varepsilon = 0.48 - 0.35$  for unloading), deformation is performed slowly by applying an incremental changes in strain of  $\sim 0.01$  every 30 min, while the formation/disappearance of creases is monitored *in situ* using an upright optical microscope (Zeiss AxioTech Vario) in bright field reflection mode. Mechanical perturbation is performed with the sample held at a fixed strain by gently poking the surface with a rounded glass micropipette prepared by pulling a heated glass pipette until break and then forging the tip with a torch.

For laser scanning confocal microscopy (Zeiss 510 META), the top film is labeled by incorporating a small amount of fluorescent monomer ( $4.5 \mu\text{g}$  fluorescein-o-acrylate per 1 g PDMS). The sample surface is immersed in a refractive index matched fluid of 72% by weight glycerol and 28% water [138].

### 4.3.4 Numerical analysis

We use finite-element software ABAQUS to simulate snapping creases in a bilayer film-substrate structure subject to uniform external compression with the substrate under pre-strain. Both the film and the substrate are modeled as incompressible neo-Hookean materials. We write a user-defined material subroutine UMAT for the substrate to include

the pre-strains in the free energy function. In order to break the translational symmetry, a small defect ( $10^{-4}$  times the total thickness  $H_f + H_s$  in size) is prescribed on the surface, and a crease will form on the position of the defect when the critical strain is reached. To eliminate the effect of the defect, its size is set much smaller than the thickness of the film. At the same time, to resolve the field close to the defect, the size of the elements close to the defect is made much smaller than the size of the defect. The spacing of the creases is prescribed as 2.5 times of the total thickness of the film and substrate, which is similar to the experimental observations. Symmetry is assumed so that only half of a crease is simulated. Riks method based on arclength continuation is used to solve the boundary value problem so that not only the stable solutions, but also the unstable solutions can be captured. After the onset of a crease, the crease tip folds up and forms self-contact. The combination of the Riks method and contact makes the convergence of the simulation hard. A thick layer with extremely low shear modulus (1/100 of the film and substrate shear modulus) is added on the top of the film to prevent self-contact. The top boundary of the extremely compliant layer is constrained to be flat so that instability cannot form there, but can only form on the interface between the film and the extremely compliant layer. As shown in [140], when the modulus of the top layer is much smaller than that of the film and substrate, the result of the interfacial crease asymptotically approaches that of a surface crease. In order to realize the uniaxial compression condition as in the experiment by a 2D simulation, we model an axisymmetric ring under uniaxial compression parallel to the symmetry axis. The radius of the ring has to be much larger than its thickness so that the curvature of the ring can be neglected. Element type CAX8H is used.

## 4.4 Results

We use reflected light optical microscopy to obtain top-view images *in situ* while relaxing the mounting layer (Figure 4.3a). The substrate is under pre-strain  $\varepsilon_0 = 0.15$ . When the film is compressed, the flat surface snaps forward into the state of deep creases at a strain of  $\varepsilon_F = 0.45$ . Notably, the value of snap-forward strain  $\varepsilon_F$  is very close to the anticipated value of 0.44, i.e., the critical strain for creasing of the film, since the barrier due to surface tension here is very low, and hence even small defects are sufficient to enable creases to nucleate. As compressive strain is further increased, additional deep creases nucleate and grow on the surface, eventually packing into a quasi-periodic array, as seen in Figure 4.3a, panel iii. The tendency of creases to adopt an average spacing proportional to the layer thickness, but without well-defined periodicity, is well known [113], and results from the difficulty of sliding creases laterally across the surface to adjust the crease locations initially defined by the nucleation and growth process. Once the quasi-periodic array is established, further compression causes the crease spacing to be reduced in an affine manner, i.e., such that the spacing between creases follows  $\alpha(H_f + H_s)(1 - \varepsilon)$ . Here, we measure a value of  $\alpha$  that ranges from 1.9-2.8 between neighboring creases. Thus, we adopt a typical value of  $\alpha = 2.5$  for the numerical simulations. When the compressive strain is reduced below the snap-backward strain, the surface becomes flat again. No scars or other visible signs of the creases remain.

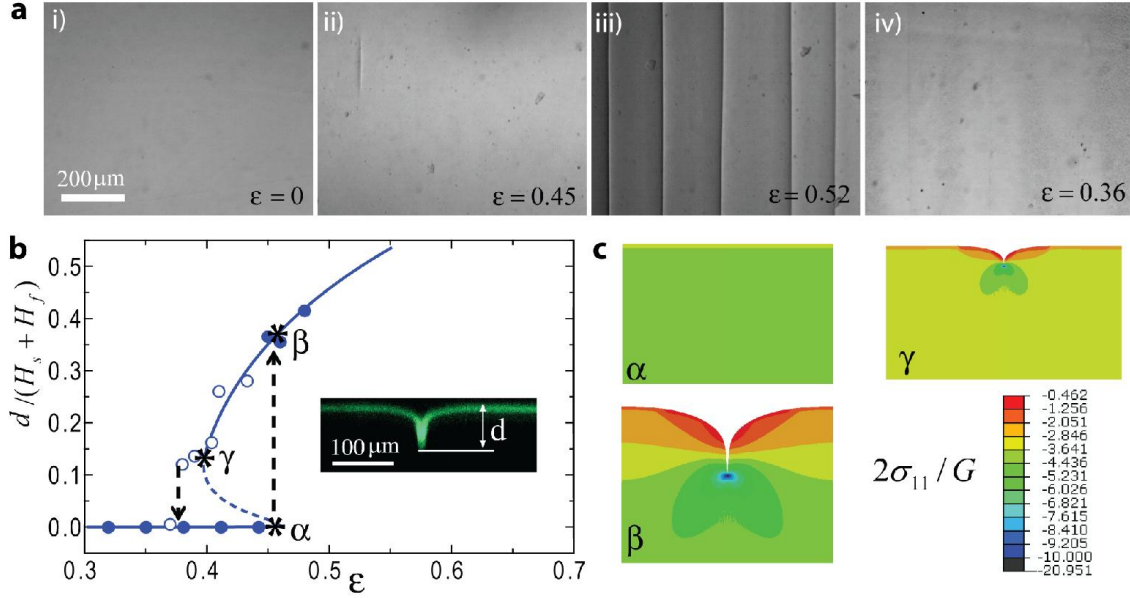


Figure 4.3 Hysteresis of creases. The substrate is pre-compressed by a strain of  $\varepsilon_0 = 0.15$ , and the film-substrate bilayer is then subjected to an additional compressive strain  $\varepsilon$ . (a) Optical microscopy images show that (i) the surface is flat at  $\varepsilon = 0$ , (ii) snaps into creases at  $\varepsilon = 0.45$ , (iii) forms an array of creases at larger compressive strains, and (iv) becomes flat at  $\varepsilon = 0.36$ . (b) Normalized crease depth as a function of the strain applied to the bilayer. The lines are predictions from the finite element method, with the solid line being the stable solution and the dashed line the unstable solution. The dots are experimental results, with the solid dots being on the snap-forward path and the open dots on the snap-backward path. The inset shows the confocal cross-section at a strain of  $\varepsilon = 0.46$ . (c) Cross-sections (with only the top 2/3 simulation volume shown) generated from finite element simulation showing the distribution of normalized true stress in the compression direction ( $2\sigma_{11} / G$ ) at three different strains: right before snap-forward ( $\alpha$ ), right after snap-forward ( $\beta$ ), and right before snap-backward ( $\gamma$ ), as indicated in (b) with star symbols.

We use finite-element software ABAQUS to simulate the formation of creases. To construct the entire branch of ceased states, namely, both the stable and unstable equilibrium states, we use the Riks method of arclength continuation [189]. Due to the combination of the Riks method and issues associated with self-contact, the simulation often does not converge. To enable these calculations, we therefore place a much softer material on top of the film, which prevents surface self-contact and facilitates convergence of the simulation. As the modulus of this top layer is made much smaller than that of the film and substrate, the result will asymptotically approach that for a free surface [140]. As an example,

we present the bifurcation diagram for the case  $\varepsilon_0 = 0.15$  and  $H_f / (H_s + H_f) = 0.02$  (Figure 4.3b) obtained using this method. Also shown are cross-sections with the contour plots of the normalized true stress in the compression direction generated from the simulation (Figure 4.3c). The snap-forward strain is set by the condition to form a crease in the film, which should be the same as the critical strain for a crease to form in a homogeneous material under uniaxial compression,  $\varepsilon_F = 0.44$  [107]. The result calculated here,  $\varepsilon_F = 0.46$ , is slightly higher than this value, reflecting the small influence of the soft material placed above the film. We focus on the case that the film is much thinner than the substrate,  $H_f \ll H_s$ . The equilibrium depth of this crease will be set by the substrate thickness—that is  $d_F$  is a fraction of  $H_s$ . Over some intermediate range of strains, two (meta-)stable states exist, one corresponding to a flat surface ( $d = 0$ ), and the other to a deep crease. In this regime, the film remains below the critical strain for creasing, and hence a shallow crease with  $d \ll H_f$  raises the elastic energy, while the substrate is above the critical strain, and hence a deeper crease that penetrates into the substrate with  $d \gg H_f$  can lower the elastic energy.

To provide a detailed comparison with these predictions, we use laser scanning confocal microscopy (LSCM) to characterize the cross-sections of the samples. The film is stained with fluorescein [138], and the deep crease is clearly visible (Figure 4.3b inset). Experiments show that upon loading (solid symbols) the surface remains flat until a strain of  $\varepsilon = 0.45$  before forming creases. Just beyond this point, a normalized crease depth of  $d_F / (H_s + H_f) = 0.36$  is measured, clearly indicating that the creases extend a distance many times the film thickness into the substrate. These values are in good agreement with

numerical predictions. As mentioned above, the snap-forward strain  $\varepsilon_F$  obtained by the finite element simulations is around 0.46, which is slightly above the anticipated value of 0.44, due to the addition of the extremely compliant layer to help the numerical convergence. The snap-forward strain  $\varepsilon_F = 0.45$  observed in experiments also represents a slight overestimate due to the small remaining barrier from surface tension.

Upon subsequently reducing the strain (open symbols), the creases become shallower, reaching a limiting depth of  $d_B = 0.12(H_f + H_s)$  before undergoing a discontinuous snap-through transition back to the flat state at value of  $\varepsilon_B = 0.38$ . The experimental results and numerics show good agreement, although the measured values of  $\varepsilon_B$  are slightly lower than the predictions. In the simulations, the snap back strain  $\varepsilon_B$  is slightly overestimated due to the soft layer placed above the film. We also suspect that the experimental value of  $\varepsilon_B$  may be reduced slightly due to a small amount of adhesion of the surface within the self-contacting region. Nevertheless, bistability between flat and creased states, and a well-defined window of hysteresis are clearly developed by applying a compressive pre-strain to a soft substrate underlying a soft film.

Our experimental measurements show that the snap-forward and snap-backward strains are reproducible (Figure 4.4). The measured values of  $\varepsilon_F$  and  $\varepsilon_B$  remain unchanged over several cycles within the precision of our measurements, once again indicating that no permanent scarring or damage to the material has occurred. The inset images in Figure 4.4 show the first cycle (a and b) and the third cycle (c and d) switching between creased states and flat states. During the third cycle, the sample is left creased (image c) for 2-3 days prior to snapping back at the same strain, indicating that even

long-term aging does not damage the material. However, the creases do form at the same locations during each cycle, presumably due to the heterogeneities in the film that consistently serve as nucleation sites [119].

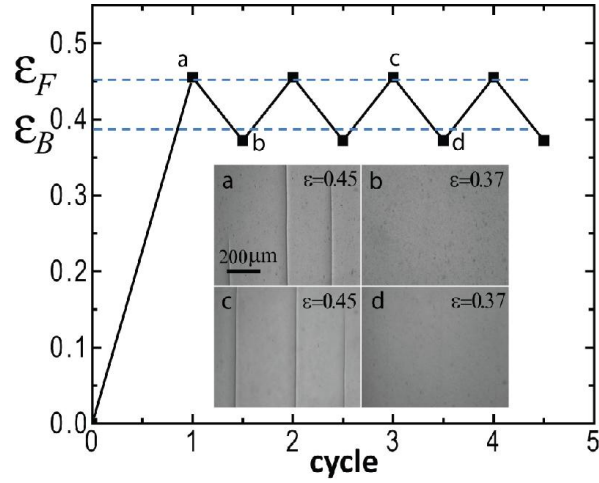


Figure 4.4 Switching between flat and creased states. The sample is switched between flat and creased states by cyclically increasing and decreasing the strain. The dots are experimental data. The dashed lines are the snap-forward strain  $\epsilon_F$  and snap-backward strain  $\epsilon_B$  calculated using the finite element method. The optical images show the surface in four states.

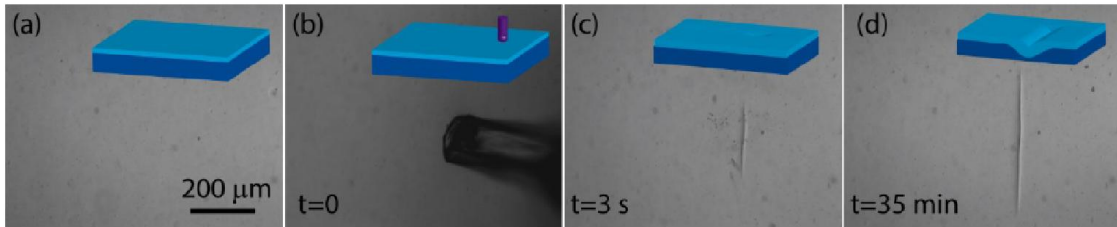


Figure 4.5 In the strain range of  $\epsilon_M < \epsilon < \epsilon_F$ , flat surface is metastable against mechanical perturbation. (a) When the substrate is subject to a pre-strain of  $\epsilon_o = 0.15$  and the bilayer is subject to an additional compressive strain of  $\epsilon = 0.42$ , between the Maxwell strain and the snap-forward strain, the flat surface is metastable. (b) A gentle poke overcomes the energy barrier and (c) the flat surface locally snaps into a deep crease. (d) The deep crease propagates at both ends and crosses the entire surface of the sample over time.

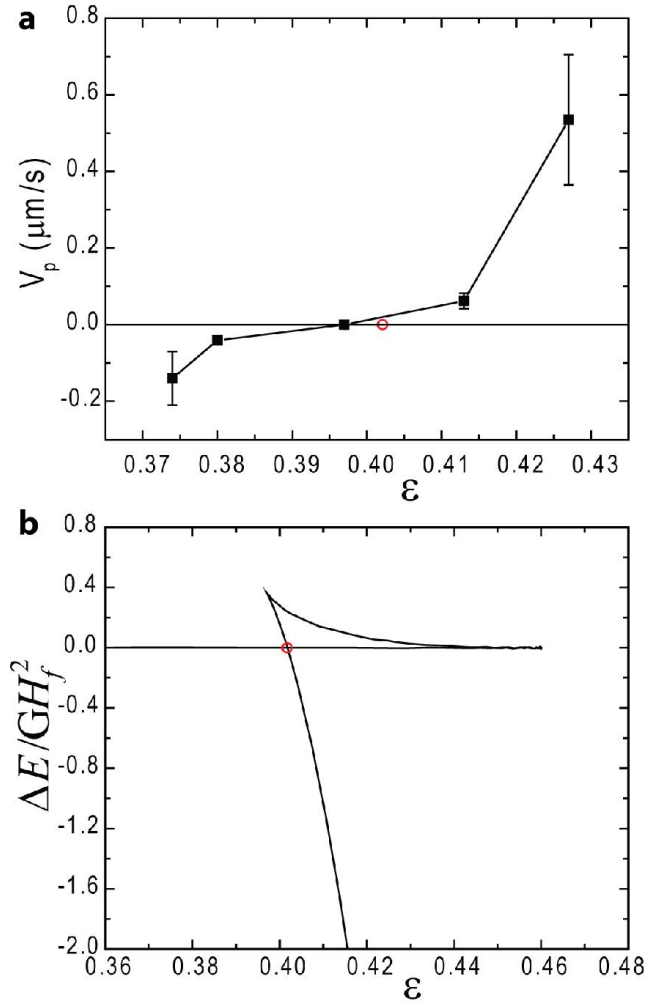


Figure 4.6 The zero-speed strain and the Maxwell strain. (a) The speed at which an isolated crease propagates or retracts is measured experimentally as a function of the applied strain. The interpolated zero-speed strain is  $\epsilon = 0.397 \pm 0.005$ , which is close to the Maxwell strain  $\epsilon_M = 0.402$  calculated using the finite element method (indicated by the red open circle). (b) The energy difference between creased and flat states as a function of the applied strain is calculated using the finite element analysis. The Maxwell strain is the strain where creased state has the same energy as flat state (indicated by the red open circle).

When the applied strain lies between the Maxwell strain  $\epsilon_M$  and the snap-forward strain  $\epsilon_F$ , the flat state is metastable against the formation of creases, and hence it should be possible to mechanically perturb the surface to overcome the elastic energy barrier and drive the formation of a deep crease. Figure 4.5 shows just this behavior on the surface of a bilayer with  $\epsilon_0 = 0.15$  and  $\epsilon = 0.42$  gently poked with a glass micropipette. Initially, a crease

forms rapidly, and only in the vicinity of the perturbation. However, since the crease is lower in energy than the flat state, this localized crease spreads laterally, or “channels”, slowly from both ends over time. While this local snapping is fast, propagation of the short deep crease is slow. On the contrary, if the applied strain is below  $\varepsilon_B$ , the flat surface is the global energy minimum and should be stable against perturbations. For bilayer with  $\varepsilon_0 = 0.15$  and  $\varepsilon = 0.37$ , while poking with a glass micropipette induces formation of a transient crease, the flat state is quickly recovered.

This behavior allows us to experimentally determine the Maxwell strain, where the crease propagation speed should vanish, which is otherwise difficult to measure. As in Figure 4.5, an isolated crease is formed first by poking the surface of a sample compressed to  $\varepsilon_M < \varepsilon < \varepsilon_F$ . The compressive strain is then reduced stepwise and the crease propagation velocity characterized at each step. As plotted in Figure 4.6a, the growth velocity decreases as the applied strain is lowered, due to the reduction in the driving force for growth (i.e., the difference in elastic energy between the flat and creased states), just as in channeling of cracks [190]. When the strain is reduced to the Maxwell strain, the crease ceases to propagate, and ultimately begins to retract from both ends with further decreases in strain. In Figure 4.6b, we plot the normalized energy difference between the creased state and the flat state obtained by simulations. The shallow crease solution always has higher energy than the flat state, while the deep crease solution has energy lower than the flat state when the strain is higher than the Maxwell strain. The predicted Maxwell strain, defined as the strain when the flat state and the deep creased state have the same elastic energy, is denoted by red open circles in Figure 4.6a and 4.6b. When  $\varepsilon_0 = 0.15$  and  $H_f/(H_f + H_s) = 0.02$ , the

Maxwell strain is predicted as  $\varepsilon_M = 0.402$ , while the measured value is  $\varepsilon_M = 0.397 \pm 0.005$ , very close to the prediction. However, we note that the predicted Maxwell strain is for periodic creases, while the measured Maxwell strain is for an isolated crease, thus the two should not agree perfectly. While the kinetics of crease channeling remain under study, we

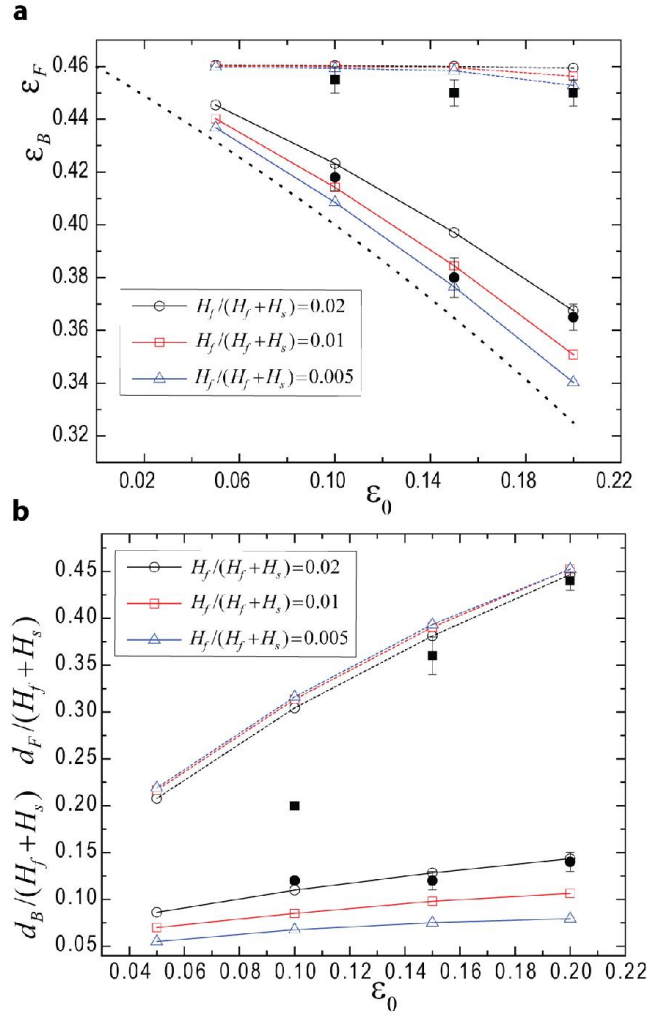


Figure 4.7 Tunable hysteresis of creases. (a) Snap-forward and snap-backward strains as a function of pre-strain for different thickness ratios. The black dotted line indicates the relationship  $\varepsilon_B = (\varepsilon_F - \varepsilon_0)/(1 - \varepsilon_0)$  between snap-forward strain  $\varepsilon_F$  and snap-backward strain  $\varepsilon_B$ , expected in the limit of vanishing film thickness. (b) Snap-forward and snap-backward crease depths as a function of pre-strain for different thickness ratios. Dashed lines (snap-forward) and solid lines (snap-backward) are calculated using the finite element method. The black solid symbols (squares for snap-forward and circles for snap-backward) are experimental results for thickness ratio  $H_f/(H_f + H_s) = 0.02$ , in good agreement with numerical results.

note that the slow propagation speeds of  $0.54 \mu\text{m/s}$  to  $-0.14 \mu\text{m/s}$  (Figure 4.6a), likely reflect the viscoelastic relaxation of material elements near the front of the propagating crease, in a similar fashion as for propagating cracks [191].

We use finite element simulations to characterize how the hysteresis of creases depends on the level of pre-strain and the thickness ratio of the film and substrate (Figure 4.7). The snap-forward strain  $\varepsilon_F$  has no dependence on either quantity, as it is simply determined by the stability of the film against forming a shallow crease. In contrast, the snap-backward strain  $\varepsilon_B$  increases with  $H_f/(H_f+H_s)$  but decreases with  $\varepsilon_0$ . Snapping back is determined by the difference between the energy reduction in the substrate and the energy increase in the film in the deep creased state with respect to the flat state. When the pre-strain  $\varepsilon_0$  is larger, the energy reduction in the substrate in the deep creased state is bigger and hence the snap-backward strain  $\varepsilon_B$  is lower. When  $\varepsilon_0$  is smaller, the snap-backward strain gets closer to the snap-forward strain  $\varepsilon_F$  and converges to  $\varepsilon_F$  when  $\varepsilon_0=0$ . In the limit of vanishing film thickness, the snap back strain  $\varepsilon_B$  should correspond to the point where the strain in the substrate drops to the critical strain for creasing. This would lead to the relationship  $\varepsilon_B = (\varepsilon_F - \varepsilon_0)/(1 - \varepsilon_0)$ , as plotted in Figure 4.7a (black dotted line). When the thickness ratio  $H_f/(H_f+H_s)$  is larger, the energy increase in the film in the deep creased state is bigger and the snap back strain is higher. The snap-forward depth  $d_F$  is primarily set by the thickness and strain of the substrate. Hence,  $d_F$  is almost independent of the film thickness but increases with the pre-strain  $\varepsilon_0$ . However, the snap back depth  $d_B$  increases with the film thickness, for similar reasons as the effect on  $\varepsilon_B$  described above. The snap back depth  $d_B$  also increases with the pre-strain  $\varepsilon_0$ , since the

depth of the crease increases with the strain in the substrate. With the decrease of  $\varepsilon_0$ ,  $d_F$  gets closer to  $d_B$ . Finally both converge to 0 when  $\varepsilon_0 = 0$ , and the instability becomes supercritical with no hysteresis. In the current study, we only consider pre-strains  $\varepsilon_0 \leq 0.2$ , because larger pre-strains yield wrinkles at strain smaller than  $\varepsilon_F$ . However, we note that reducing the modulus of the film below that of the substrate allows the pre-strain  $\varepsilon_0$  to be tuned over a larger range. We also include in Figure 4.7 the corresponding experimental results for the thickness ratio studied,  $H_f / (H_f + H_s) = 0.02$ , which show rather good agreement with numerical results. These results provide detailed guidelines for fine-tuning both the extent of the hysteresis window in strain, as well as the amplitudes of both the snap-in and snap-out transitions.

## 4.5 Summary

In this chapter, we have described a robust method for controlling the hysteretic behavior of surface creases through application of compressive pre-strain to the substrate of a soft bilayer. Over a well-defined range of strain, the system shows kinetic bistability between flat and deep creased states with snap-through transitions between these states at either extreme. Surfaces can be repeatedly snapped forward and backward between these states with little variation, and in good agreement with the predictions from numerical analysis. We anticipate that the greatly improved control over hysteresis, and the demonstration of bistability over a substantial range of strain will open new opportunities for applications of creases in sensors and responsive surfaces. This experimental system of a bilayer supported on a pre-stretched foundation provides great freedom to independently

tune the modulus, thickness and pre-stretch/compression of both the substrate and film layers. While the current study has concerned only a very small range of parameter space with small values of  $H_f/(H_f + H_s)$ , identical material properties for the film and substrate, and a narrow range of  $\varepsilon_0$ , we anticipate that the same approach will enable detailed studies of the rich landscape of behaviors in other regimes.

## Chapter 5

### Creases on the interface between two soft materials

#### 5.1 Introduction

Bonded materials with dissimilar properties are ubiquitous. They exist in composite materials [192], geological strata [193, 194], electronic devices [195], biological tissues [44, 196] and soft actuators [197]. In many cases, stresses arise due to differences in thermal expansion [198-200], chemical reactions [201], growth [44, 52], swelling [118], or mechanical pre-strains [202]. Such mismatches may cause buckling instabilities [7, 192, 200, 203], which can reduce the strength of structures [7, 192, 200, 203] and lead to debonding of the interfaces [198, 199, 204].

Interfacial instability has long been regarded as a bifurcation from a state of flat interface [7, 192, 200, 203]. For example, Biot [100, 205] studied two elastic materials compressed along a direction parallel to the interface. He predicted that the interface forms wrinkles at a critical compression, similar to the formation of wrinkles on the free surface of a soft solid [97]. These wrinkles have dynamic analogs: Stoneley waves on the interface between two materials [100, 206-208], and Rayleigh waves on the surface of a homogeneous material [208-210]. Wrinkles, however, have not been observed on surfaces of homogeneous elastic materials under compression; rather, creases have been observed [105, 112-114, 118]. A recent theory shows that surface wrinkles and surface creases are two types of instability, and the critical strain for the onset of surface wrinkles is higher than that for the onset of

surface creases [106]. Notably, these phenomena occur at rather large compressive strains. While hard elastic materials generally cannot be loaded to such large strains without fracture, soft materials such as gels and elastomers can easily be compressed to the point of instability.

Motivated by this recent understanding, in this chapter we reconsider the stability of the interface between two soft materials. Our theory and experiment show an analogous localized, large-strain instability, which we call interfacial creases (Figure 5.1). Wrinkles and creases are two types of bifurcation from the state of flat interface. While wrinkles bifurcate by a deformation nonlocal in space and infinitesimal in amplitude, creases bifurcate by a deformation local in space and large in amplitude. In this regard, the wrinkling instability is of the same type as buckling of columns and plates, while the creasing instability is reminiscent of cracking, cavitation, shear banding, and phase transformation. Upon initiation, an interfacial crease corresponds to a field scaled by a single length scale. The critical strain is independent of this length scale and is scale-free. We calculate the critical conditions for the onset of the interfacial creases and find that, just like their surface counterparts, interfacial creases always form at lower compression than interfacial wrinkles. We show that interfacial creases are V-shaped. The presence of two materials prevents the interface from self-contact, but the tip of an interfacial crease is singular. Because the interface does not enter self-contact, the analysis of interfacial creases is simplified compared to that of surface creases. We demonstrate the existence of interfacial creases by experiments with hydrogels. By using differential swelling of two types of gels, we can form interfacial creases and surface creases independently.

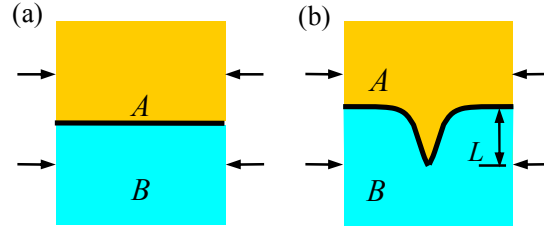


Figure 5.1 Materials A and B are bonded to each other along a flat interface. Subject to a compressive strain, the interface may either remain flat (a), or form creases (b).

## 5.2 Analysis and simulations

### 5.2.1 Interfacial creases under applied strain

We study the initiation of interfacial creases by comparing two states of equilibrium subject to the same applied strain (Figure 5.1). In the state of flat interface, the field in either material is homogeneous, and the elastic energy of the state is denoted by  $U_0$ . In the creased state, one point of the interface is prescribed with a downward displacement  $L$ , and the elastic energy of the state is denoted  $U$ . The magnitude of the displacement  $L$  is arbitrary, so long as it is much smaller than any other length in the boundary-value problem (e.g., the thickness and width of the block used in computation). Once  $L$  is prescribed, the creased state is determined by a boundary-value problem of large deformation. The two states of equilibrium differ by a deformation of large amplitude, but the difference is localized in a small region scaled by the length  $L$ . The two materials are taken to be incompressible and neo-Hookean, with shear moduli  $G_A$  and  $G_B$ . We begin with the case that pre-strains are absent, and the block is compressed to reduce its width under plane strain conditions. The applied strain  $\varepsilon$  is defined as the reduction in the width of the block divided by the width of

the block in the undeformed state. Dimensional considerations dictate that the energy of the creased state should differ from that of the flat state by

$$U - U_0 = G_B L^2 f(\varepsilon, G_B / G_A). \quad (5.1)$$

As indicated, the dimensionless number  $f$  is a function of the applied strain and the ratio of the shear moduli. The scaling relation (5.1) generalizes the result for surface creases [107].

Without loss of generality, we assume that  $G_A < G_B$ . We expect that interfacial creases form by growing into the stiffer material (B). In the absence of applied strain, the energy of the state of flat interface vanishes, but the energy of the creased state is positive, so that the state of flat interface is stable. When a sufficiently large compressive strain is applied, the crease elongates the interface, so that the crease reduces energy in material B, but increases energy in material A. Because  $G_A < G_B$ , the crease can reduce the total elastic energy in the two materials. For a fixed ratio  $G_B / G_A$ , the function  $f(\varepsilon, G_B / G_A)$  decreases monotonically with the applied strain  $\varepsilon$ . An interfacial crease sets in when the creased state has the same energy as the flat state, namely,

$$f(\varepsilon, G_B / G_A) = 0. \quad (5.2)$$

This condition gives the critical strain for the onset of interfacial crease,  $\varepsilon_c$ , as a function of the modulus ratio,  $G_B / G_A$ .

The critical condition (5.2) for the onset of interfacial crease is independent of any length scale. This scale-free behavior results from two considerations. First, the prescribed displacement  $L$  is assumed to be small compared to other lengths in the boundary-value problem, such as the thickness and width of the block used in the calculation. The flat state differs from the creased state by a deformation localized within a region scaled with  $L$ .

Consequently, only the length  $L$  enters (5.1), and no length appears in the critical condition (2). Second, the theory of elasticity does not have any material-defined length scale. The situation would be different if we accounted for the interfacial tension  $\gamma$  between the two materials. The interfacial tension, together with the elastic modulus  $G$ , would provide a length scale, the elastocapillary length  $\gamma/G$ . This length scale can vary across many orders of magnitude depending on the material system, but typical values for elastomer/elastomer interfaces are  $\gamma \sim 1 - 10$  mN/m and  $G \sim 100$  kPa, while for gel/gel interfaces they are  $\gamma \sim 0.1 - 1$  mN/m and  $G \sim 10$  kPa, in both cases yielding  $\gamma/G \sim 10 - 100$  nm. Incorporating interfacial tension will cause the tip of an interfacial crease to be rounded on a length scale of  $\gamma/G$ , rather than being infinitely sharp. Interfacial tension would also provide a barrier against the initiation of interfacial creases, just as in the case of surface creases, thus requiring the application of a small amount of overstrain to drive crease nucleation [138]. For simplicity, however, we ignore here the effects of interfacial tension and consider only elastic contributions, which is appropriate for understanding fully formed creases for samples much thicker than  $\gamma/G$ .

In the above description, the creased state is determined by a boundary-value problem of large deformation, and the prescribed displacement  $L$  specifies the length scale. This particular way of specifying a length scale, however, does not affect the critical strain for the onset of the crease. Upon initiation, the creased state is scaled by one length, independent of how the length is specified.

We use the finite element software ABAQUS to solve the boundary-value problem of the creased state, from the reference state of flat interface to the current state of a prescribed

displacement  $L$  (Figure 5.2). Analysis of this type has also been used in our previous work on surface creases [107]. Due to symmetry, only half of a crease is simulated. The materials deform under plane-strain conditions, and element type CPE4H is used. Compare the creased state and the flat state subject to the same applied strain  $\varepsilon$ . Their energy difference  $U - U_0$  is plotted as a function of the applied strain  $\varepsilon$  for a fixed value of the modulus ratio  $G_B/G_A = 5$ . When  $\varepsilon < 0.512$ , the state of flat interface has a lower elastic energy than the creased state. When  $\varepsilon > 0.512$ , the state of flat interface has a higher elastic energy than the creased state. The strain  $\varepsilon_c = 0.512$  is identified as the critical condition for the onset of the interfacial crease.

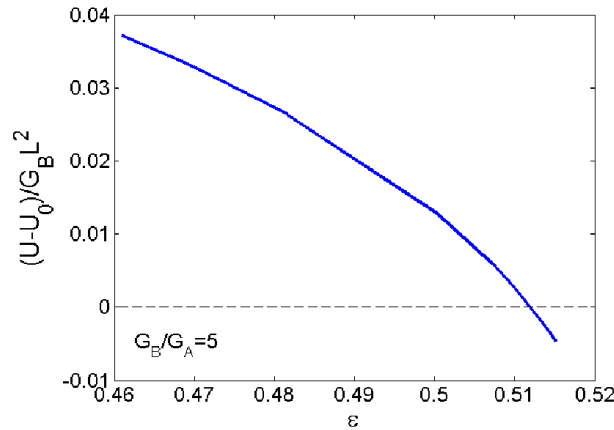


Figure 5.2 The energy difference between the creased state  $U$  and the flat state  $U_0$  plotted as a function of the applied strain  $\varepsilon$  for a fixed value of the modulus ratio  $G_B/G_A = 5$ . When  $\varepsilon = 0.512$ , the energy of the creased state is equal to the energy of the flat state, and  $\varepsilon = 0.512$  is identified as the critical condition for the onset of the interfacial crease.

We use another finite element method to simulate the growth of an interfacial crease (Figure 5.3). In the reference state, two materials A and B are bonded with a flat interface (Figure 5.3a). We make use of the symmetry condition, and only simulate the right half of a crease. After a crease initiates, its growth does depend on the size of the block used in the calculation. Here the two materials in the reference state have the same thickness  $H$ , and the

lateral size of the simulation box (corresponding to half of the spacing between creases) is set to be  $W = H$ , close to what is observed in our experiments. To seed the crease, a small defect is prescribed on the left end of the interface. The size of the defect is much smaller than the thickness of either material, but is large compared to the size of the surrounding mesh. An image of a region in the vicinity of the defect, with depth  $D$  and angle  $\alpha$ , is shown in Figure 5.3b. In the current state, a horizontal displacement is applied on the boundary on the right (Figure 5.3c). The top and bottom boundaries are constrained to remain planar, so that they cannot form surface creases. The boundary on the left is a plane of mirror symmetry. The two materials are compressed in the horizontal direction and expand in the vertical direction, while the depth of the crease,  $L$ , evolves as a function of the applied displacement.

The depth of the crease is plotted as a function of the applied strain (Figure 5.4). The depth of the crease remains nearly zero below the critical strain, and begins to grow when the applied strain is beyond the critical value about  $\varepsilon_c = 0.512$ . The crease is seeded with defects of different depths  $D$  and angles  $\alpha$ . Meshes with different size are used as well: mesh 1 uses 18 elements along the defect; mesh 2 uses 36 elements along the defect. So long as a defect is small compared to the thickness of each material, but large compared to the size of surrounding mesh, the depth and the angle of the defect and the mesh size have a negligible effect on the critical strain for the onset of the crease and subsequent growth of the crease.

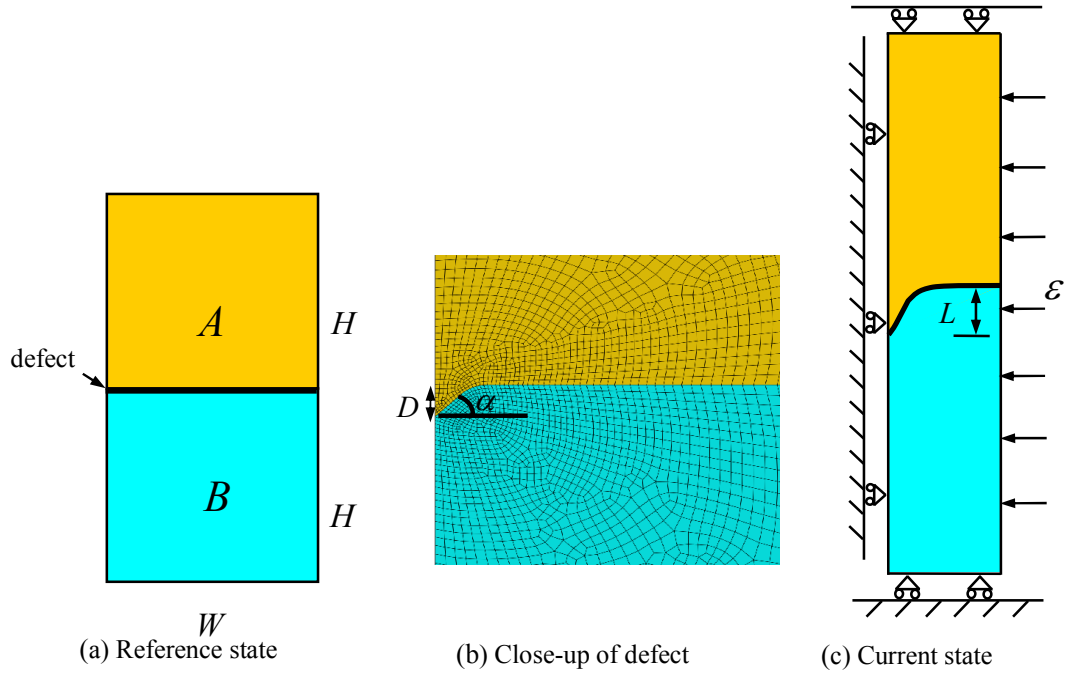


Figure 5.3 Finite element model. (a) In the reference state, two materials A and B are bonded with a flat interface. A small defect is prescribed on the left end of the interface. (b) An image of a region in the vicinity of the defect, with depth  $D$  and angle  $\alpha$ . (c) In the current state, the two materials are compressed in the horizontal direction and expand in the vertical direction, while the depth of the crease,  $L$ , evolves as a function of the applied displacement.

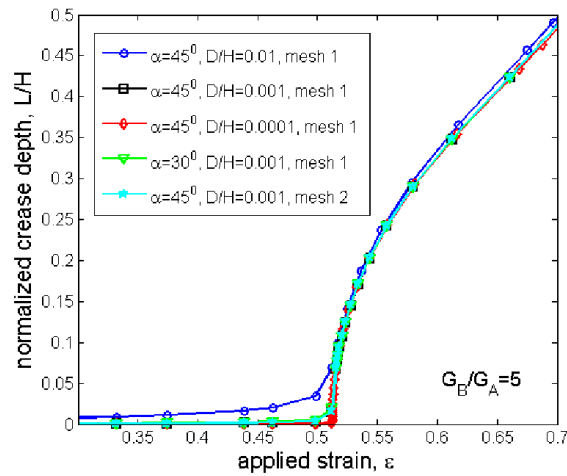


Figure 5.4 The depth of the crease is plotted as a function of the applied strain. The crease is seeded with defects of different depths  $D$  and angles  $\alpha$ . Mesh 1 uses 18 elements along the defect, and mesh 2 uses 36 elements along the defect.

The elastic energy is a function of the applied strain (Figure 5.5). Let  $U_0$  be the

energy in the two materials in the state of flat interface, and  $U_F$  be the energy in the two materials calculated by using the finite element method of simulating crease growth. When the applied strain  $\varepsilon < 0.512$ , the interface remains flat, and the total elastic energy is the same as that in the two materials in the state of flat interface  $U_F/U_0 = 1$ . When  $\varepsilon > 0.512$ , a crease forms, reducing the total elastic energy below that in the two materials in the state of flat interface,  $U_F/U_0 < 1$ . Consequently, we identify  $\varepsilon = 0.512$  as the critical strain for the onset of creases, which is consistent with the result by the method of prescribing a length scale (Figure 5.2). After an interfacial crease forms, the elastic energy of the bottom material  $U_B$  decreases while the elastic energy of the top material  $U_A$  increases. Since the bottom material is stiffer than the top material, the decrease in elastic energy of the bottom material is larger than the increase in the energy of the top material. Consequently, the interfacial crease reduces the total energy  $U_F$ .

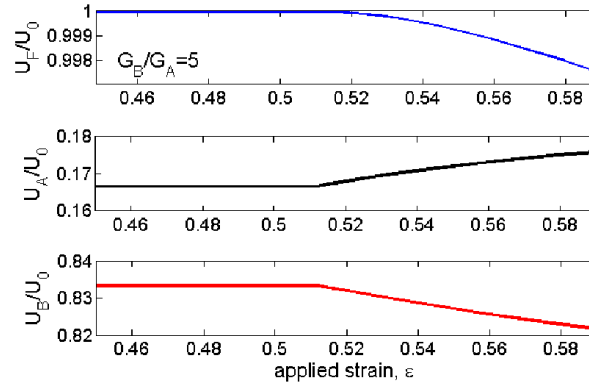


Figure 5.5 Energy in both materials,  $U_F$ , energy in material A,  $U_A$ , and energy in material B,  $U_B$  are plotted as functions of the applied strain. Each energy is normalized by the energy in the two materials in the state of flat interface,  $U_0$ .

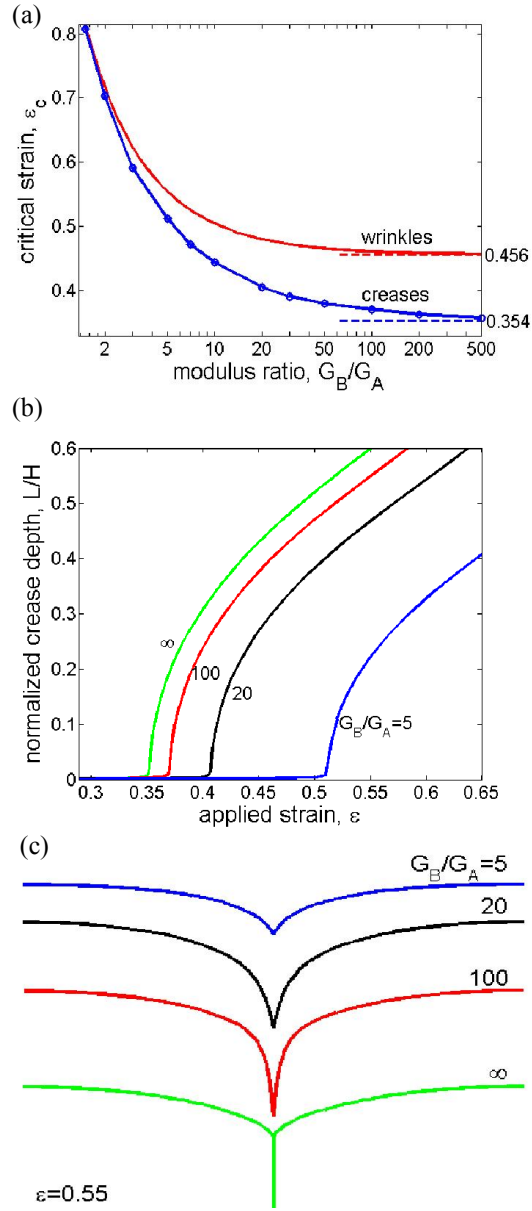


Figure 5.6 Interfacial creases under applied strain. (a) The critical strain for the onset of creases as a function of the ratio of the shear modulus,  $G_B/G_A$ . Also plotted is the critical strain for the onset of wrinkles. (b) The depth of a crease as a function of the applied strain for several values of  $G_B/G_A$ . (c) Shapes of creased interfaces at applied strain  $\epsilon = 0.55$ , for several values of the modulus ratio.

Similarly, we can simulate the initiation and growth of interfacial creases for other modulus ratios. As expected, the critical strain for the onset of interfacial crease decreases as the modulus ratio  $G_B/G_A$  increases (Figure 5.6a). In the limit  $G_B/G_A \rightarrow \infty$ , the critical

strain for the onset of an interfacial crease recovers that of a surface crease,  $\varepsilon_c = 0.354$  [106, 107]. In the limit  $G_B/G_A \rightarrow 1$ , the two materials are elastically homogeneous, and an interfacial crease will not form under any compressive strain, so that  $\varepsilon_c \rightarrow 1$ . Also plotted in Figure 5.6a is the critical strain for the onset of interfacial wrinkles. While the onset of interfacial creases is determined by a boundary-value problem of large deformation, the onset of interfacial wrinkles is determined by a boundary-value problem of infinitesimal deformation superimposed on a known large deformation [100, 205]; see Section 5.3 for more details. For any value of modulus ratio, the interfacial crease sets in at a critical strain lower than the interfacial wrinkles.

Figure 5.6b shows the evolution of interfacial crease depth with the applied strain for different modulus ratios. The limit  $G_B/G_A \rightarrow \infty$  corresponds to a surface crease. At a lower value of  $G_B/G_A$ , material A retards the onset of the crease, and the interfacial crease is shallower than the surface crease under the same applied strain. The calculated shapes of the creased interfaces are V-shaped (Figure 5.6c). Under the same strain  $\varepsilon = 0.55$ , the interfacial crease is deeper for a larger value of  $G_B/G_A$ , and asymptotically approaches the shape of a surface crease with self-contact as  $G_B/G_A \rightarrow \infty$ .

### 5.2.2 Interfacial creases under both applied strain and pre-strains

We next study interfacial creases under both pre-strains and applied strains (Figure 5.7). Prior to bonding, material B is subject to pre-stretches  $\lambda_1^{pre}$  and  $\lambda_2^{pre}$ , while material A is undeformed (Figure 5.7a, b). The pre-stretches are defined as the current length divided by the original length, with subscripts 1 and 2 indicating the coordinate directions in the plane

of the interface. After bonding, both materials are subject to applied stretches  $\lambda_1$  and  $\lambda_2$ , which can be controlled independently of the pre-stretches  $\lambda_1^{pre}$  and  $\lambda_2^{pre}$  (Figure 5.7c). Both materials are taken to be incompressible,  $\lambda_1^{pre}\lambda_2^{pre}\lambda_3^{pre}=1$  and  $\lambda_1\lambda_2\lambda_3=1$ .

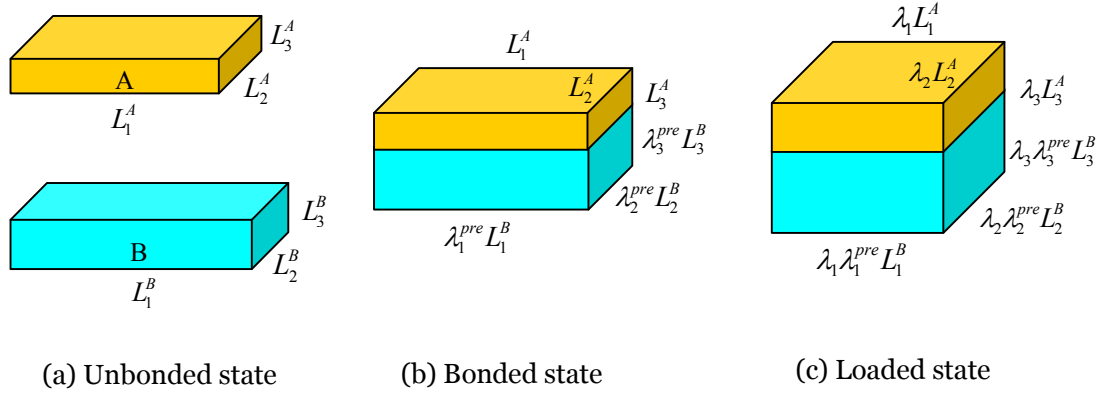


Figure 5.7 Two materials with bonding on the interface under both pre-strains and applied strains. (a) In the unbonded state, both materials are stress-free. (b) In the bonded state, material B is subject to pre-stretches  $\lambda_1^{pre}$ ,  $\lambda_2^{pre}$  and  $\lambda_3^{pre}$ , and material A is stress-free. (c) In the loaded state, the bilayer is subject to applied stretches  $\lambda_1$ ,  $\lambda_2$  and  $\lambda_3$ .

For the same reason stated above, the energy in the creased state differs from that in the flat state by  $U - U_0 = G_B L^2 f$ , but  $f$  now depends on five dimensionless parameters:  $\lambda_1, \lambda_2, \lambda_1^{pre}, \lambda_2^{pre}, G_B / G_A$ . A further analysis, however, indicates that the critical condition for the onset of interfacial creases depends on three combined parameters:

$$f\left(\lambda_1 \sqrt{\lambda_2}, \lambda_1^{pre} \sqrt{\lambda_2^{pre}}, G_B / G_A \lambda_2^{pre}\right) = 0 \quad (5.3)$$

This result is obtained as follows.

In analyzing creases, we assume that the materials deform under the generalized plane strain conditions (Figure 5.7c). The deformation gradient is invariant with respect to axis 2 and takes the form

$$\mathbf{F} = \begin{bmatrix} F_{11} & 0 & F_{13} \\ 0 & \lambda_2 & 0 \\ F_{31} & 0 & F_{33} \end{bmatrix}. \quad (5.4)$$

The free energy density of material A is

$$W_A = \frac{G_A}{2} F_{iK} F_{iK} + \frac{G_A}{2} \lambda_2^2. \quad (5.5)$$

Each repeated index implies a sum over 1 and 3. Consider an intermediate state in which material A is stretched along the three axes by  $(\lambda_2^{-1/2}, \lambda_2, \lambda_2^{-1/2})$ . Using this intermediate state as a new reference state, the deformation gradient in the plane of axes 1 and 3 is  $\hat{F}_{iK} = \lambda_2^{1/2} F_{iK}$ .

Rewrite the free energy density as

$$W_A = \frac{G_A}{2\lambda_2} \hat{F}_{iK} \hat{F}_{iK} + \frac{G_A}{2} \lambda_2^2. \quad (5.6)$$

The free energy density in material B is

$$W_B = \frac{G_B}{2} F_{iK} F_{K\alpha}^{pre} F_{iL} F_{L\alpha}^{pre} + \frac{G_B}{2} (\lambda_2 \lambda_2^{pre})^2. \quad (5.7)$$

Write  $\hat{F}_{K\alpha}^{pre} = (\lambda_2^{pre})^{1/2} F_{K\alpha}^{pre}$ , so that

$$W_B = \frac{G_B}{2\lambda_2 \lambda_2^{pre}} \hat{F}_{iK} \hat{F}_{K\alpha}^{pre} \hat{F}_{iL} \hat{F}_{L\alpha}^{pre} + \frac{G_B}{2} (\lambda_2 \lambda_2^{pre})^2. \quad (5.8)$$

Because  $\lambda_2$  and  $\lambda_2^{pre}$  are prescribed constants, the last terms in (5.6) and (5.8) do not contribute to the energy difference between the creased state and the flat state. The first terms in (5.6) and (5.8) describe the energy change from the intermediate states to the current states, with plane strain deformation  $\hat{F}_{iK}$  in material A and plane strain deformation and pre-stretches  $\hat{F}_{iK} \hat{F}_{K\alpha}^{pre}$  in material B. Consequently, the deformation under generalized plane strain conditions correspond to the deformation under plane strain conditions, with the effective shear moduli  $G_A / \lambda_2$  and  $G_B / \lambda_2 \lambda_2^{pre}$  for the two materials.

Thus we show that the critical condition for the onset of creases depends on three

dimensionless parameters:  $\lambda_1\sqrt{\lambda_2}, \lambda_1^{pre}\sqrt{\lambda_2^{pre}}, G_B/G_A\lambda_2^{pre}$ . This result generalizes the critical condition for the onset of surface creases [107]. The same conclusion holds for the critical condition for the onset of wrinkles. Similar combinations of parameters have been identified in an independent analysis of wrinkles in film-substrate structures [170].

The critical condition for the onset of interfacial creases is calculated using finite element method. We write a user-defined material subroutine UMAT to include the pre-stretches in the free energy function. For a given value of  $G_B/G_A\lambda_2^{pre}$ , the critical condition is represented by a curve in the plane spanned by parameters  $\lambda_1\sqrt{\lambda_2}$  and  $\lambda_1^{pre}\sqrt{\lambda_2^{pre}}$  (Figure 5.8a). Below the curve interfacial creases form, and above the curve interfacial creases do not form. The condition for the onset of surface creases corresponds to the limit  $G_B/G_A\lambda_2^{pre} \rightarrow \infty$ . The critical condition for the onset of wrinkles is plotted in a similar diagram (Figure 5.8b); see Section 5.3 for details. For a given value of  $G_B/G_A\lambda_2^{pre}$ , the curve for interfacial creases always lies above the one for interfacial wrinkles. This result predicts that interfacial creases will form, rather than interfacial wrinkles.

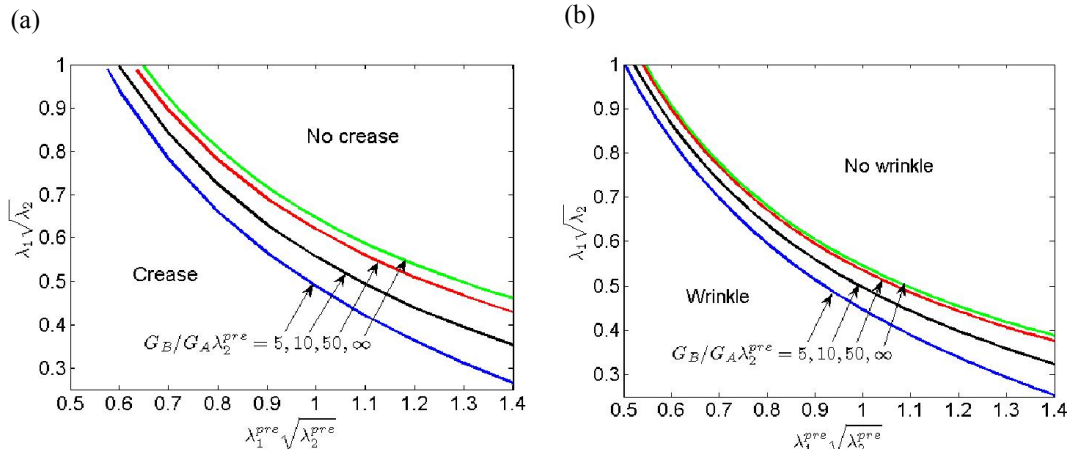


Figure 5.8 (a) The critical condition for the onset of interfacial creases. (b) The critical condition for the onset of interfacial wrinkles.

### 5.3 Linear perturbation analysis for the onset of interfacial wrinkles

We calculate the critical condition for the onset of interfacial wrinkles by using the small-perturbation method described by Biot [100, 205]. Additional results are obtained here to account for pre-stretches. The analysis relies on the theory of finite deformation of an elastic body. The reference state is taken to be the bonded state, where the bottom material is pre-stretched, while the top material is undeformed (Figure 5.7b). Label a material particle in the body by its coordinate  $\mathbf{X}$  when the body is in the reference state. In the deformed state, the material particle moves to a place of coordinate  $\mathbf{x}$ . The function  $\mathbf{x}(\mathbf{X})$  describes the deformation of the body. The deformation gradient is

$$F_{iK} = \frac{\partial x_i(\mathbf{X})}{\partial X_K}. \quad (5.9)$$

The nominal stress  $s_{iK}$  satisfies the conditions of equilibrium

$$\frac{\partial s_{iK}}{\partial X_K} = \mathbf{0}. \quad (5.10)$$

The interface between materials A and B coincides with the plane  $X_3 = 0$ . Across the interface, both the displacement and traction are continuous:

$$x_i^A = x_i^B, \quad (5.11)$$

$$s_{i3}^A = s_{i3}^B. \quad (5.12)$$

Each material is characterized by the Helmholtz free energy as a function of the deformation gradient,  $W(\mathbf{F})$ . The nominal stress relates to the deformation gradient by

$$s_{iK} = \frac{\partial W(\mathbf{F})}{\partial F_{iK}}. \quad (5.13)$$

The materials are taken to be incompressible:

$$\det(\mathbf{F})=1. \quad (5.14)$$

The materials are described by the neo-Hookean model. For material A, the free energy is

$$W_A(\mathbf{F}) = \frac{G_A}{2} F_{iK} F_{iK} - (\det \mathbf{F} - 1) \Pi, \quad (5.15)$$

where  $\Pi$  is the Lagrange multiplier used to enforce incompressibility. In general the Lagrange multiplier is inhomogeneous, and should be solved as a part of the problem. The material model (5.13) becomes

$$s_{iK}^A = G_A F_{iK} - \Pi H_{iK}, \quad (5.16)$$

where  $\mathbf{H} = \mathbf{F}^{-T}$ . In the reference state (Figure 5.7b), material B is pre-stretched to a homogeneous state with deformation gradient:

$$\mathbf{F}^{pre} = \begin{bmatrix} \lambda_1^{pre} & 0 & 0 \\ 0 & \lambda_2^{pre} & 0 \\ 0 & 0 & \lambda_3^{pre} \end{bmatrix}. \quad (5.17)$$

The material B is also taken to be incompressible,  $\det \mathbf{F}^{pre} = \lambda_1^{pre} \lambda_2^{pre} \lambda_3^{pre} = 1$ . For material B, the net deformation gradient between the current state and the undeformed state is  $F_{iK} F_{K\alpha}^{pre}$ , and the free energy is

$$W_B = \frac{G_B}{2} F_{iK} F_{K\alpha}^{pre} F_{iL} F_{L\alpha}^{pre} - (\det \mathbf{F} - 1) \Pi. \quad (5.18)$$

The material model (5.13) becomes

$$s_{iK}^B = G_B F_{K\alpha}^{pre} F_{L\alpha}^{pre} F_{iL} - \Pi H_{iK}. \quad (5.19)$$

We next perturb from the state of finite deformation (Figure 5.7c), of displacement  $x_i^0(\mathbf{X})$ , deformation gradient  $F_{iK}^0(\mathbf{X})$  and nominal stress  $s_{iK}^0(\mathbf{X})$ . In particular, the deformation gradient of this state is prescribed by the applied stretches:

$$\mathbf{F}^0 = \begin{bmatrix} \lambda_1 & 0 & 0 \\ 0 & \lambda_2 & 0 \\ 0 & 0 & \lambda_3 \end{bmatrix}. \quad (5.20)$$

The corresponding field of displacement is  $\mathbf{x}^0 = \mathbf{F}^0 \mathbf{X}$ . This state of finite deformation is then perturbed by a state of infinitesimal deformation  $\tilde{\mathbf{x}}(\mathbf{X})$ . We write the perturbed state as  $\mathbf{x} = \mathbf{x}^0(\mathbf{X}) + \tilde{\mathbf{x}}(\mathbf{X})$ . The other fields are similarly perturbed. Both state  $\mathbf{x}^0(\mathbf{X})$  and the state  $\mathbf{x}^0(\mathbf{X}) + \tilde{\mathbf{x}}(\mathbf{X})$  satisfy the same governing equations (5.9)-(5.19). Equations (5.9)-(5.12) reduce to equations for the fields of perturbation:

$$\tilde{F}_{iK} = \frac{\partial \tilde{x}_i(\mathbf{X})}{\partial X_K}, \quad (5.21)$$

$$\frac{\partial \tilde{s}_{iK}}{\partial X_K} = 0, \quad (5.22)$$

$$\tilde{x}_i^A = \tilde{x}_i^B, \quad (5.23)$$

$$\tilde{s}_{i3}^A = \tilde{s}_{i3}^B. \quad (5.24)$$

The condition of incompressibility (5.14) is perturbed as

$$H_{iK}^0 \tilde{F}_{iK} = 0, \quad (5.25)$$

where  $\mathbf{H}^0 = \mathbf{F}^{0-T}$ . Expanding (5.16) in the Taylor series at  $\mathbf{F}^0$  and keeping only the linear term, we obtain that

$$\tilde{s}_{iK}^A = (G_A \delta_{ij} \delta_{KL} + \Pi^0 H_{iL}^0 H_{jK}^0) \tilde{F}_{jL} - H_{iK}^0 \tilde{\Pi}. \quad (5.26)$$

Similarly perturbing (5.19), we obtain that

$$\tilde{s}_{iK}^B = (G_B F_{K\alpha}^{pre} F_{L\alpha}^{pre} \delta_{ij} + \Pi^0 H_{iL}^0 H_{jK}^0) \tilde{F}_{jL} - H_{iK}^0 \tilde{\Pi}. \quad (5.27)$$

Inserting (5.21), (5.26) and (5.27) into (5.22), we obtain that

$$(G_A \delta_{ij} \delta_{KL} + \Pi^0 H_{iL}^0 H_{jK}^0) \frac{\partial^2 \tilde{x}_j(\mathbf{X})}{\partial X_K \partial X_L} - H_{iK}^0 \frac{\partial \tilde{\Pi}(\mathbf{X})}{\partial X_K} = 0, \quad (5.28)$$

$$(G_B F_{K\alpha}^{pre} F_{L\alpha}^{pre} \delta_{ij} + \Pi^0 H_{iL}^0 H_{jK}^0) \frac{\partial^2 \tilde{x}_j(\mathbf{X})}{\partial X_K \partial X_L} - H_{iK}^0 \frac{\partial \tilde{\Pi}(\mathbf{X})}{\partial X_K} = 0, \quad (5.29)$$

for material A and B respectively. For a given field  $x_i^0(\mathbf{X})$ , (5.25), (5.28), and (5.29) define a

set of linear, homogeneous partial differential equations for the fields of perturbation,  $\tilde{x}_i(\mathbf{X})$  and  $\tilde{\Pi}(\mathbf{X})$ . The displacement and the traction are continuous across the interface. Consequently, the fields of perturbation  $\tilde{x}_i(\mathbf{X})$  and  $\tilde{\Pi}(\mathbf{X})$  are governed by an eigenvalue problem. The characteristic equation of this eigenvalue problem defines the critical condition for the onset of wrinkles. Following an analysis similar to that of Biot [100, 205], we obtain the critical condition for the onset of interfacial wrinkles:

$$\left[ \frac{\lambda_2^{pre} G_A}{G_B} \left( \frac{\lambda_3}{\lambda_1} + 1 \right) + \left( \frac{\lambda_3 \lambda_3^{pre}}{\lambda_1 \lambda_1^{pre}} + 1 \right) \right] \left[ \frac{\lambda_2^{pre} G_A}{G_B} \left( \frac{\lambda_1}{\lambda_3} + 1 \right) + \left( \frac{\lambda_1 \lambda_1^{pre}}{\lambda_3 \lambda_3^{pre}} + 1 \right) \right] - \left[ \frac{\lambda_2^{pre} G_A}{G_B} \left( 1 - \frac{\lambda_3}{\lambda_1} \right) - \left( 1 - \frac{\lambda_3 \lambda_3^{pre}}{\lambda_1 \lambda_1^{pre}} \right) \right]^2 = 0. \quad (5.30)$$

This condition is plotted in Figure 5.8b. When  $\lambda_1^{pre} = \lambda_2^{pre} = \lambda_3^{pre} = 1$ , the condition recovers Biot's solution [100, 205], and is plotted in Figure 5.6a.

## 5.4 Experimental results

We perform experiments to show the existence of interfacial creases. In one experiment, two hydrogels are confined between glass slides (Figure 5.9). The two gels are bonded to each other, but are not bonded to the glass slides. The colored gel is stiffer than the colorless gel. The former has a polymer network containing fixed charges, while the latter has an uncharged network (Figure 5.9a). After preparation, the two gels are nearly stress-free, and the interface is flat (Figure 5.9b). When placed in water and allowed to swell, the charged gel is subject to compressive stress due to its inability to expand laterally, leading to the formation of interfacial creases (Figure 5.9c). The uncharged gel swells negligibly, so that the top surface does not form surface creases.

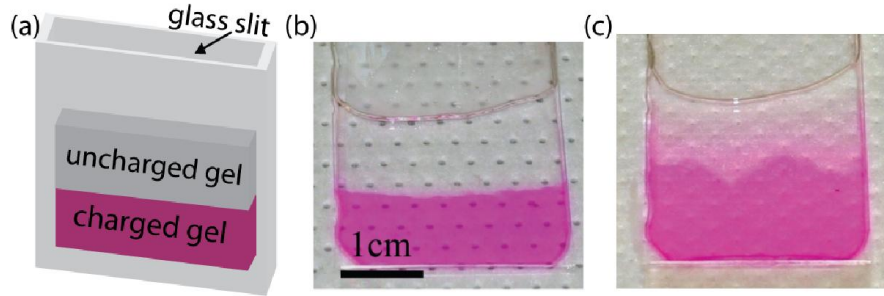


Figure 5.9 Creases formed on the interface between two hydrogels. (a) A schematic of the experimental setup. Confined in a 1 mm thick glass slit are two gels, one with a charged network and the other with unchanged network. The gels are bonded to each other, but are not bonded to the glass. (b) After the preparation, the two hydrogels are relatively dry and stress-free, and the interface is flat. (c) When soaked in water, the charged gel swells much more than the uncharged gel, so that creases form on the interface between the two gels, but not on the free surface of the uncharged gel.

A second experiment is performed to compare interfacial creases and surface creases (Figure 5.10). A charged gel of thickness  $H_2 = 6 - 8 \mu\text{m}$  is attached on a glass substrate. A portion of the gel is then covered with an uncharged gel of thickness  $H_1 = 76 \mu\text{m}$  (Figure 5.10a). When immersed in a phosphate buffered saline solution containing 274 mM sodium chloride, both gels swell slightly and generate in-plane equi-biaxial compressive stresses, but the compression is insufficient to cause either surface or interfacial creases. Deionized water is then added drop by drop to reduce the concentration of the saline solution, so that the charged gel swells more and the uncharged gel swells negligibly (as characterized by fluorescence confocal microscopy). When the swelling ratio of the charged gel reaches  $H_2'/H_2 = 2.4 \pm 0.1$ , the uncovered portion of the charged gel forms surface creases, while the interface between the two gels remains flat (Figure 5.10b, d). This critical swelling ratio for the onset of surface creases is in good agreement with previous reports [112]. When the swelling ratio is increased to  $H_2''/H_2 = 3.3 \pm 0.1$ , the covered region of the gel forms interfacial creases (Figure 5.10c, e). At the same degree of swelling, the interfacial creases are shallower than surface creases, as shown by the cross-sectional confocal images in the insets of Figure

5.10e. Both surface and interfacial creases show a spacing of  $\sim 20\mu\text{m}$ , or roughly 2.5 – 3 times  $H_2$ . The gel of uncharged network swells negligibly, and its surface remains flat.

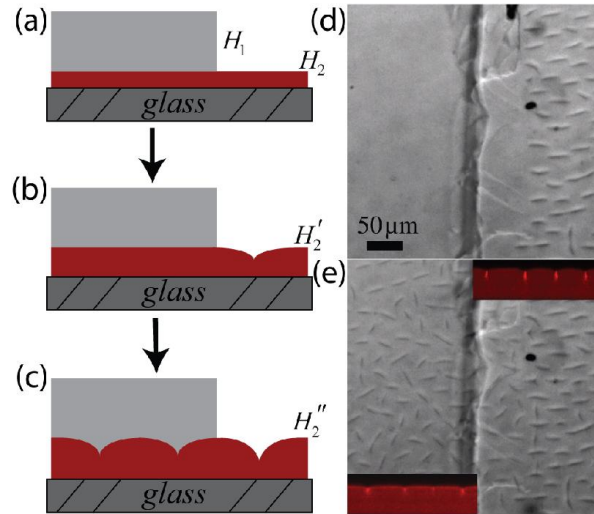


Figure 5.10 A comparison of surface creases and interfacial creases. (a) A charged gel is attached to a glass substrate, and is partially covered by an uncharged gel. (b) Cross-sectional schematic and (d) top-view micrograph when the charged gel swells by  $H_2'/H_2 = 2.4$ . Creases form on the free surface of the charged gel, while the interface between the gels remains flat. (c) Cross-sectional schematic and (e) top-view micrograph when the charged gel swells by  $H_2''/H_2 = 3.3$ . Creases also form on the interface. The creases on the interface have a smaller depth than the creases on the surface, as shown by the cross-sectional confocal images in the insets.

Further details of the two experiments can be found in Section 5.5. While these experimental observations qualitatively agree with our theoretical predictions, quantitative comparison between experiments and calculations would require that constitutive behavior of the gels be characterized with precision and used in the calculations. This task is beyond the scope of the present work.

## 5.5 Experimental methods

### 5.5.1 Experiment with hydrogels confined in a glass slit

A glass slit, thickness 1 mm and width 28 mm, is constructed by gluing glass slides together (Figure 5.9). The inner surfaces of the slit are treated with trimethylchlorosilane to reduce adhesion of the gels to the glass surfaces. A charged gel layer is first prepared by loading the slit with an aqueous pre-gel solution containing 700 mM *N*-isopropyl-acrylamide, 660 mM sodium acrylate and 45 mM *N,N'*-methylenebisacrylamide. Gelation is initiated by adding 1  $\mu$ L of 10% w/w ammonium persulfate aqueous solution as the initiator and 0.3  $\mu$ L *N,N,N',N'*-tetramethylethylenediamine as the catalyst into 200  $\mu$ L of freshly degassed pre-gel solution immediately prior to loading the chamber. To stain the charged gel, a small amount ( $3.2 \times 10^{-5}$  mmol) of a Rhodamine B-labeled methacrylate is incorporated into the 200  $\mu$ L pre-gel solution. Next, a softer uncharged gel is prepared on top of the charged gel using the same procedure as above, but with a pre-gel solution containing 701 mM acrylamide and 19 mM *N,N'*-methylenebisacrylamide. Some interpenetration of the second gel into the existing charged gel does occur, and helps to bond the materials together, but based on the relatively rapid speed of gelation ( $\sim 20$  min), this length-scale is small compared to the  $\sim 1$  cm dimensions of the gels. The contrast in modulus between the gels is not known, but based simply on the relative crosslinker concentrations, the charged gel should be at least  $\sim 2.4$ -fold stiffer than the uncharged gel [211]. Following gelation, this confined gel sample is soaked in deionized water for 3 weeks to reach swelling equilibrium, and the shape of the interface is recorded using a digital camera.

### **5.5.2 Experiment with thin layers of gels on a glass substrate**

This experiment uses a photo-crosslinkable poly(*N*-isopropylacrylamide-co-sodium

acrylate-co-acrylamidobenzophenone) polymer described in previous reports [112, 212]. A glass cover slip substrate is pretreated with [3-(methacryloxy)-propyl]trichlorosilane to provide covalently anchoring, and then a copolymer film is solution cast from chloroform to yield a film thickness of  $H_2 = 6 - 8 \mu\text{m}$ , followed by crosslinking by exposure to 365 nm UV light. A much softer uncharged gel is next formed by loading a freshly prepared de-gassed aqueous pre-gel solution (containing 701 mM acrylamide and 19 mM  $N,N'$ -methylenebisacrylamide; prepared as above) between the substrate-attached photo-crosslinked polymer film and a clean cover slip, and allowing 20 min for polymerization to proceed. The uncharged gel film thickness  $H_1 = 76 \mu\text{m}$  is defined using Kapton 300HN films (DuPont) as spacers. To prevent swelling of the photo-crosslinked poly( $N$ -isopropylacrylamide) film by the pre-gel solution, the neutral gel is formed at 70 °C. Following polymerization, the cell is cooled to room temperature and the glass slides are separated. The surface-attached gel bilayer is then transferred to a phosphate buffered saline swelling solution containing 274 mM sodium chloride. Deionized water is then added drop-wise to dilute the swelling solution and thus increase the swelling ratio of the charged gel, while the formation of creases is monitored in situ using either an upright optical microscope (Zeiss AxioTech Vario) in reflected-light differential interference contrast mode or a laser scanning confocal fluorescence microscope (Zeiss). Based on a previous report, we estimate the Young's modulus of the uncharged gel to be  $\sim 5$  kPa [213], while that of the charged gel is estimated to be several hundred kPa based on the density of photo-crosslinking groups in the copolymer.

## 5.6 Summary

We present calculations and experiments to show that an interface between two soft materials under compression can form creases. A creased state deviates from a state of flat interface by a deformation large in amplitude and local in space. The critical condition for the onset of interfacial creases is scale-free. This critical condition is calculated in terms of elastic moduli, pre-stretches and applied stretches by allowing deviation from a flat state with a large deformation. By contrast, a wrinkled state deviates from a state of flat interface by a deformation infinitesimal in amplitude and nonlocal in space. The critical condition for the onset of interfacial wrinkles is calculated by a small-perturbation method. In all cases studied, the critical conditions for the onset of interfacial creases are reached before those for the onset of interfacial wrinkles.

## Chapter 6

### The formation of wrinkles or creases in bilayers

#### 6.1 Introduction

Soft materials, such as elastomers, gels and living tissues, are often under compression due to forces, swelling, and growth. When the compression exceeds some critical strain, the soft materials undergo elastic instability, forming, e.g., wrinkles and creases [3, 10, 12]. Elastic instability of various kinds has been used in engineering to fabricate stretchable electronics [13], measure material properties [22], tune adhesion [31, 32], change wettability [35], and control surface chemistry [39]. Wrinkles and creases also provide forms and functions in nature, such as formation of fingerprints [50], invagination of embryos [51], development of guts [52], folding of brains [56-58] and morphogenesis of viruses [64] and plants [65-72].

Wrinkles and creases are two distinct types of instability [106]. Wrinkles deviate from the flat state by a field of infinitesimal strain in a finite region, whereas a crease deviates from the flat state by a field of large strain in an infinitesimal region (Figure 6.1). To determine the critical strain for the onset of wrinkles, a field of infinitesimal strain is superimposed upon the flat state [78, 85, 97, 103]. This superimposed field linearizes the field equations around the flat state of finite deformation, leading to an eigenvalue problem. By contrast, the critical strain for the onset of a crease cannot be determined by linearization around the flat state, but can be determined by allowing the surface to form a localized

region of self-contact.

Engineering systems and living tissues often involve layered materials of dissimilar elastic moduli [52, 56, 57, 214-216]. Several special cases have been well studied. For a stiff thin film on a compliant thick substrate, the critical strain for the onset of wrinkles is smaller than that for the onset of creases, and wrinkles are observed in experiments [3, 10, 12, 76, 81]. For a homogeneous material, the critical strain for the onset of wrinkles is larger than that for the onset of creases, and creases are observed in experiments [105-107, 112-114, 118, 127, 130]. For layered materials of comparable thicknesses and moduli, the critical strain for the onset of wrinkles can be either smaller or larger than that for the onset of creases [99, 122, 170-172]. It is tempting to expect a layered material to form wrinkles if the critical strain for the onset of wrinkles is smaller than that for the onset of creases, or vice versa.

This expectation turns out to be wrong. In many cases, the bifurcation points themselves do not predict the behavior of a layered material. Rather, we need to construct bifurcation diagrams. We illustrate our findings using bilayers of dissimilar materials (Figure 6.1). Even for a bilayer with a critical strain for the onset of wrinkles much lower than that for the onset of creases, we find that a subcritical crease exists near the critical strain for the onset of wrinkles. We show that such a subcritical bifurcation can lead to channeling creases and snapping creases, at strains much below that for the onset of creases in a homogeneous material.

We analyze the critical conditions for the onset of wrinkles in bilayers by using the linear perturbation method (Section 6.2). We simulate the initiation and growth of creases by using the finite element method (Section 6.3). In particular, we use the Riks method to

simulate subcritical creases. We construct a plane using the ratio of the elastic moduli and the ratio of thicknesses as coordinates. In this plane, the conditions of equal critical strains for the onset of wrinkles and creases form a curve. The curve, however, as mentioned above, does not demarcate whether wrinkles or creases will form. Rather, we show that bilayers of moduli and thicknesses near this boundary can have complex bifurcation diagrams, leading to, for example, bilayers to form creases even when the critical strain for the onset of wrinkles is much lower than that for the onset of creases (Section 6.4).

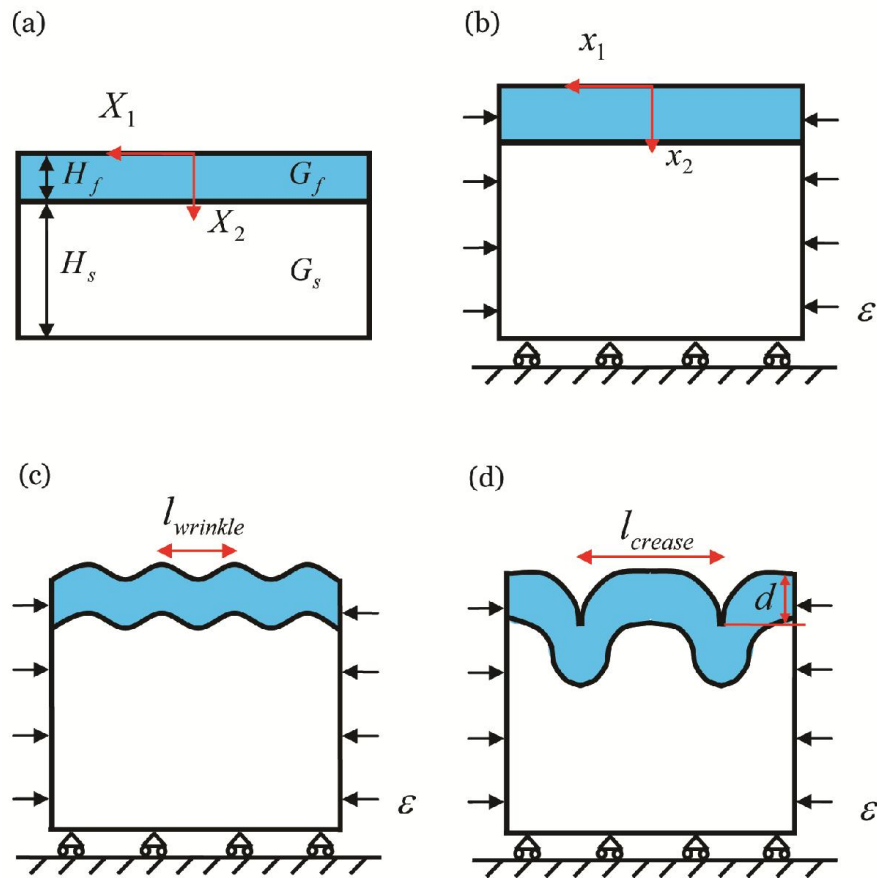


Figure 6.1 A bilayer subject to compression may form wrinkles or creases. (a) A bilayer in the undeformed state. The surface of the film is set as  $X_2 = 0$ , and the axis of  $X_2$  goes towards the substrate. (b) The bilayer subject to homogeneous compression. (c) The formation of wrinkles with wavelength  $l_{wrinkle}$ . (d) The formation of creases with spacing  $l_{crease}$ .

## 6.2 Linear perturbation analysis for wrinkles

Consider a bilayer of a film and a substrate, with thicknesses  $H_f$  and  $H_s$  in the undeformed state (Figure 6.1a). The two materials are taken to be neo-Hookean, with shear moduli  $G_f$  and  $G_s$ . Perfect bonding between the film and substrate is assumed. The bilayer is subject to homogeneous compression. The top of the film is traction-free. The bottom of the substrate is fixed in vertical direction, and is traction-free in horizontal direction (Figure 6.1b).

### 6.2.1 Governing equations and their incremental forms

Here we formulate the governing equations and their incremental forms of a bilayer subject to an applied compression. Choose the stress-free state before compression as the reference, and name every material particle by its coordinate  $\mathbf{X}$  in the reference state. After the deformation, each particle  $\mathbf{X}$  moves to the current position  $\mathbf{x}(\mathbf{X})$ . The deformation gradient is defined as

$$F_{iK} = \frac{\partial x_i(\mathbf{X})}{\partial X_K}. \quad (6.1)$$

We model both layers of the bilayer structure as the incompressible neo-Hookean material with the free energy function

$$W(\mathbf{F}) = \frac{G}{2} F_{iK} F_{iK} - \pi(\det \mathbf{F} - 1), \quad (6.2)$$

where  $G$  is the shear modulus, and  $\pi(\mathbf{X})$  is the Lagrange multiplier to enforce the constraint of incompressibility  $\det \mathbf{F} = 1$ . The nominal stress  $s_{iK} = \partial W(\mathbf{F}) / \partial F_{iK}$  can be calculated as

$$s_{iK} = GF_{iK} - \pi H_{iK}, \quad (6.3)$$

where  $\mathbf{H} = \mathbf{F}^{-T}$ . In equilibrium, the nominal stress satisfies that

$$\frac{\partial s_{iK}}{\partial X_K} = \mathbf{0}, \quad (6.4)$$

inside the body. The boundary conditions are

$$s_{iK} N_K = 0, \quad (6.5)$$

on the free surface of the film  $X_2 = 0$  with  $N_K$  the normal direction of the surface in the reference state, and

$$s_{1K} N_K = 0 \quad \text{and} \quad x_2 = X_2, \quad (6.6)$$

on the bottom of the substrate  $X_2 = h_f + h_s$ . On the interface of the film and substrate  $X_2 = h_f$ , the continuity of the displacement and traction needs to be satisfied

$$(s_{iK}^f - s_{iK}^s) N_K = 0 \quad \text{and} \quad x_i^f = x_i^s, \quad (6.7)$$

where the superscripts  $f$  and  $s$  represent film and substrate respectively.

The above governing equations are perturbed in the current state with the independent variable  $\mathbf{x}$ , the coordinate in the current state. The displacement associated with the perturbation is written as  $\mathbf{u}(\mathbf{x}) = \dot{\mathbf{x}}(\mathbf{X})$ , and the perturbation of the deformation gradient becomes [108, 217]

$$L_{ij}(\mathbf{x}) = \frac{\partial u_i(\mathbf{x})}{\partial x_j} = H_{jK} \dot{F}_{iK}. \quad (6.8)$$

The condition of incompressibility becomes [108, 217]

$$L_{ii} = 0. \quad (6.9)$$

Write the stress-stretch relation (6.3) and the equilibrium equation (6.4) in the incremental forms, and we get [108, 217]

$$\dot{s}_{iK}F_{jK} = GF_{jK}F_{pK}L_{ip} + \pi L_{ji} - \dot{\pi}\delta_{ij}, \quad (6.10)$$

$$\frac{\partial \dot{s}_{iK}F_{jK}}{\partial x_j} = 0. \quad (6.11)$$

The boundary conditions (6.5) and (6.6) in the incremental form are

$$\begin{aligned} \dot{s}_{iK}F_{jK}n_j &= 0, \\ \dot{s}_{1K}F_{jK}n_j &= 0 \quad \text{and} \quad u_2 = 0, \end{aligned} \quad (6.12)$$

with  $n_j$  the normal direction of the surface in the current state, and the continuity condition (6.7) becomes

$$\left( \dot{s}_{iK}^f F_{jK}^f - \dot{s}_{iK}^s F_{jK}^s \right) n_j = 0 \quad \text{and} \quad u_i^f = u_i^s. \quad (6.13)$$

Governing equations (6.9-6.11), together with the boundary conditions (6.12) and (6.13) constitute an incremental boundary value problem.

### 6.2.2 Eigenvalue problem

The onset of wrinkles corresponds to the existence of a non-trivial solution to the incremental boundary value problem, which is an eigenvalue problem.

Before the formation of wrinkles, the bilayer is subject to uniform compression in direction 1, with the deformation gradient  $\mathbf{F} = \text{diag}[\lambda_1, 1/\lambda_1, \lambda_3, \lambda_3]$  in both the film and substrate, where the incompressibility has been imposed. The deformation in direction 3,  $\lambda_3$ , is determined by the boundary condition in direction 3. For example, for a plane strain condition  $\lambda_3 = 1$ , while for a uniaxial compression  $\lambda_3 = 1/\sqrt{\lambda_1}$ . Wrinkles are assumed to form parallel to direction 3 at a critical compression, as shown in the Figure 6.1b, with  $\lambda_3$  intact. Separated solutions exist for the incremental boundary value problem with the

perturbation in the following form

$$\begin{cases} u_1 = f_1(x_2)\sin kx_1, \\ u_2 = f_2(x_2)\cos kx_1, \\ \dot{\pi} = f_3(x_2)\cos kx_1, \end{cases} \quad (6.14)$$

where  $f_i$  ( $i=1,2,3$ ) are three unknown functions, and  $k$  is the wave number in the current state, which relates the wave number in the reference state  $K$  by  $k = K / \lambda_1$ .

Insert equation (6.14) into the equilibrium equation (6.11) and the incompressibility condition (6.9), with using the stress-stretch relation (6.10). Three ordinary differential equations are obtained for the three unknown functions  $f_i(x_2)$  ( $i=1,2,3$ ). Eliminate  $f_1$  and  $f_3$ , and we get a single equation for  $f_2$

$$\lambda_1^{-2}\lambda_3^{-2}f_2^{(4)} - (\lambda_1^2 + \lambda_1^{-2}\lambda_3^{-2})k^2f_2^{(2)} + k^4\lambda_1^2f_2 = 0, \quad (6.15)$$

where  $f_2^{(i)}$  means the  $i$ th derivative of  $f_2$  with respect to  $x_2$ . The general solution to (6.15) is

$$f_2^i(x_2) = A_i e^{kx_2} + B_i e^{-kx_2} + C_i e^{kx_2\lambda_1^2\lambda_3} + D_i e^{-kx_2\lambda_1^2\lambda_3}, \quad (6.16)$$

where  $i=f,s$  corresponds to the solution in the film and substrate, and  $A_i, B_i, C_i$  and  $D_i$  are eight unknown constants.  $f_1^i$  and  $f_3^i$  can be calculated correspondingly

$$\begin{aligned} f_1^i(x_2) &= -A_i e^{kx_2} + B_i e^{-kx_2} - C_i \lambda_1^2 \lambda_3 e^{kx_2\lambda_1^2\lambda_3} + D_i \lambda_1^2 \lambda_3 e^{-kx_2\lambda_1^2\lambda_3}, \\ f_3^i(x_2) &= G_i k (\lambda_1^{-2}\lambda_3^{-2} - \lambda_1^2) (A_i e^{kx_2} - B_i e^{-kx_2}) \end{aligned} \quad (6.17)$$

The eight boundary conditions (6.12) and (6.13) are

$$\begin{aligned} \dot{s}_{2K}^f F_{2K}^f &= 0 \quad \text{and} \quad \dot{s}_{1K}^f F_{2K}^f = 0 \quad \text{at} \quad x_2 = 0, \\ \dot{s}_{2K}^f F_{2K}^f &= \dot{s}_{2K}^s F_{2K}^s, \quad \dot{s}_{1K}^f F_{2K}^f = \dot{s}_{1K}^s F_{2K}^s, \quad u_1^f = u_1^s \quad \text{and} \quad u_2^f = u_2^s \quad \text{at} \quad x_2 = H_f / \lambda_1 \lambda_3, \\ \dot{s}_{1K}^s F_{2K}^s &= 0 \quad \text{and} \quad u_2^s = 0 \quad \text{at} \quad x_2 = (H_f + H_s) / \lambda_1 \lambda_3. \end{aligned} \quad (6.18)$$

Inserting (6.16) and (6.17) into the eight boundary conditions, we obtain eight linear algebraic equations for the eight unknown constants.

$$\mathbf{A}[A_f, B_f, C_f, D_f, A_s, B_s, C_s, D_s]^T = 0, \quad (6.19)$$

where the  $8 \times 8$  matrix  $\mathbf{A}$  can be written as a function of dimensionless parameters  $G_f/G_s$ ,  $H_s/H_f$ ,  $KH_f$ ,  $\lambda_1$  and  $\lambda_3$ ,  $\mathbf{A} = \mathbf{A}(G_f/G_s, H_s/H_f, KH_f, \lambda_1, \lambda_3)$ . The detailed expression of  $\mathbf{A}$  is given in Appendix B.

The existence of the a non-trivial solution to the incremental boundary value problem requires

$$\det \mathbf{A} = 0, \quad (6.20)$$

which gives the critical stretch  $\lambda_1 = \lambda_c$  for wrinkle initiation under certain  $G_f/G_s$ ,  $H_s/H_f$ ,  $KH_f$  and a given state of strain  $\lambda_3$ . By maximizing  $\lambda_c$  with respect to different modes  $KH_f$ , we find the mode which happens first  $K_m$  and the maximal critical stretch  $\lambda_m$ . The corresponding critical strain and minimal strain are defined as  $\varepsilon_c = 1 - \lambda_c$  and  $\varepsilon_m = 1 - \lambda_m$  respectively. The maximal stretch  $\lambda_m$  and minimal strain  $\varepsilon_m$  only depend on the modulus ratio  $G_f/G_s$ , thickness ratio  $H_s/H_f$  and the state of strain  $\lambda_3$ .

We further notice that for an arbitrary constant  $\lambda_3$ , if we replace the variable  $\lambda_1$  by  $\lambda_1/\sqrt{\lambda_3}$  in the function  $\mathbf{A} = \mathbf{A}(G_f/G_s, H_s/H_f, KH_f, \lambda_1, \lambda_3)$ , equation (6.20) recovers the one under plane strain condition. This means under a generalized plane strain condition with an arbitrary  $\lambda_3$ , the critical stretch, and thus the maximal stretch, relates to the ones of plane strain condition  $\lambda_c^{PE}$  and  $\lambda_m^{PE}$  by

$$\lambda_c^{PE} = \sqrt{\lambda_3} \lambda_c \quad \text{and} \quad \lambda_m^{PE} = \sqrt{\lambda_3} \lambda_m, \quad (6.21)$$

and  $K_m$  is independent on  $\lambda_3$ , although  $k_m = K_m/\lambda_m$  depends on  $\lambda_3$ . Relation similar to (6.21) was also pointed out in [107, 140, 170].

### 6.2.3 Critical condition for the onset of wrinkles

Here the results of the critical strain and wavelength for the onset of wrinkles under different modulus ratios and thickness ratios are presented. As an example, we show the results of the uniaxial compression condition, and the critical condition of wrinkle formation under an arbitrary strain condition can be converted by (6.21).

The critical strain  $\varepsilon_c$  always decreases first and then increases as the nominal wavelength  $L_{wrinkle}$  normalized by  $H_f$  increases, with  $L_{wrinkle} = 2\pi/K$  (Figure 6.2). Bending the film penalizes the modes with short wavelengths, while stretching the substrate penalizes the modes with long wavelengths. Thus, wrinkles with intermediate wavelength can form under the lowest strain,  $\varepsilon_m$ . When the film is very stiff and thin, like the case where a thin metal film is on the top of a thick polymeric substrate,  $\varepsilon_m$  can be smaller than 1%. In general,  $\varepsilon_m$  increases with the decrease of the modulus ratio  $G_f/G_s$  or the thickness ratio  $H_s/H_f$ .

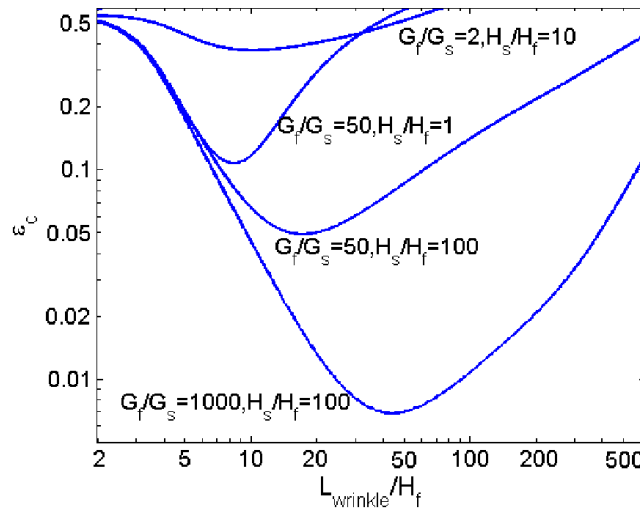


Figure 6.2 The critical strain  $\varepsilon_c$  for the onset of wrinkles as a function of the wavelength for several ratios of shear moduli and thicknesses. For each curve, the critical strain reaches a minimum for wrinkles of certain wavelength.

For a fixed thickness ratio  $H_s/H_f$ , the minimal critical strain  $\varepsilon_m$  monotonically decreases with the increase of the modulus ratio  $G_f/G_s$  (Figure 6.3a). When  $G_f/G_s=1$ , the bilayer becomes one layer and  $\varepsilon_m$  reaches the Biot strain under the uniaxial compression condition 0.556 [97]. When the film is much stiffer and thinner than the substrate, a nonlinear theory modeling both the film and substrate as linear elastic materials and the film as a von Karman plate can predict the critical strain and wavelength of wrinkles reasonably well [76-78, 85, 102, 103]. The critical strains obtained by the nonlinear theory for  $H_s/H_f=1000$  are plotted with blue circles for comparison [77]. When  $G_f/G_s$  is large, for instance  $G_f/G_s=1000$ , the minimal critical strain  $\varepsilon_m$  for the nonlinear theory overlaps with the result for neo-Hookean material, because when  $H_s/H_f$  and  $G_f/G_s$  are both large, the critical strain is smaller than 1% and linear elasticity is applicable. When  $G_f/G_s$  is small, for instance  $G_f/G_s=2$ , the assumption of linear elasticity overestimates  $\varepsilon_m$  for around 0.05. Under a fixed thickness ratio  $H_s/H_f$ , normalized nominal wavelength  $L_{wrinkle}^m/H_f$  mostly increases with modulus ratio  $G_f/G_s$  (Figure 6.3b). However, when  $H_s/H_f=0.2$ , at around  $G_f/G_s=10$ ,  $L_{wrinkle}^m/H_f$  increases, decreases and then increases again with  $G_f/G_s$ . This is due to two competing factors: with the increase of  $G_f/G_s$ , larger current wavelength becomes more energetically preferential, while the minimal strain  $\varepsilon_m$  decreases. Therefore, the nominal wavelength as the ratio of the current wavelength to the maximal stretch shows non-monotonic dependence on  $G_f/G_s$ . Under fixed  $G_f/G_s$ ,  $\varepsilon_m$  decreases with  $H_s/H_f$  (Figure 6.3c), since it is easier to bend a thinner film and the wrinkling configuration is preferential under lower strain. However, the nominal wavelength  $L_{wrinkle}^m/H_f$  is smaller for smaller  $H_s/H_f$  (Figure 6.3d), since a thin substrate strongly

suppresses wrinkles with long wavelength. When  $H_s/H_f$  is large enough, both  $\varepsilon_m$  and  $L_{wrinkle}^m/H_f$  reach a plateau, and do not vary with the further increase of  $H_s/H_f$ , which represents the limiting case of a thin film on a thick substrate.

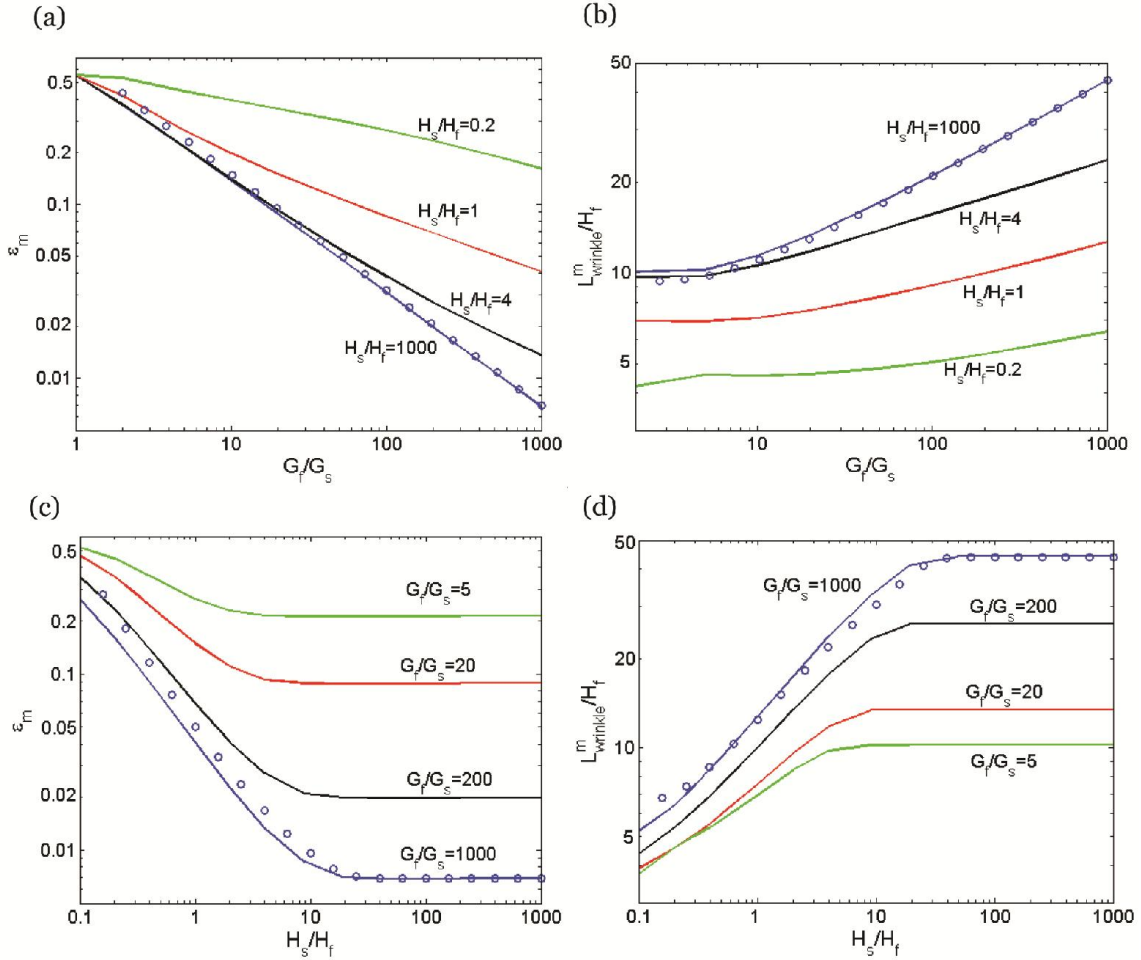


Figure 6.3 The minimal critical strain  $\varepsilon_m$  and its corresponding wavelength  $L_{wrinkle}^m/h_f$  depend on the ratios of moduli and thicknesses. The solid curves are obtained when both materials are modeled as neo-Hookean solids. The circles correspond to approximate solutions when both materials are modeled as linearly elastic solids, and the film is modeled as a von Karman plate [77].

Figure 6.4a and b show the contour plot of  $\varepsilon_m$  and  $L_{wrinkle}^m/H_f$  in the plane with the axes of  $H_s/H_f$  and  $G_f/G_s$ . The minimal strains depend on whether the structure deforms under the uniaxial stress conditions or the plane strain conditions. In Figure 6.4a,

$\varepsilon_m^{Uni}$  is the minimal strain under uniaxial compression condition, while  $\varepsilon_m^{PE}$  is the corresponding value under plane strain condition. When both  $H_s/H_f$  and  $G_f/G_s$  are larger,  $\varepsilon_m$  is smaller. The line marked by ' $\varepsilon_m^{Uni} = 0.44, \varepsilon_m^{PE} = 0.35$ ' represents the conditions when the critical strain for the onset of creases coincides with that of wrinkles. Above this boundary of equal critical strain (shown in pink), the onset of wrinkles is under a strain smaller than the onset of creases. Below this boundary (shown in purple), the onset of wrinkles is under a strain larger than the onset of creases. In Figure 6.4b, the nominal wavelengths  $L_{wrinkle}^m/H_f$  are independent of the type of deformation. When both  $H_s/H_f$  and  $G_f/G_s$  are larger,  $L_{wrinkle}^m/H_f$  is larger.

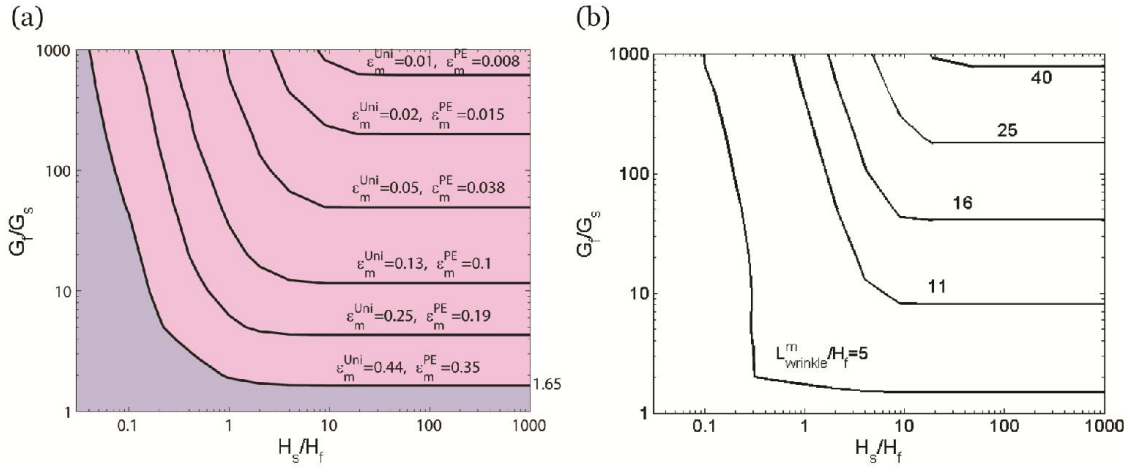


Figure 6.4 The critical conditions for the onset of wrinkles represented in the plane with the axes of  $G_f/G_s$  and  $H_s/H_f$ . (a) The contour plots of the minimal critical strain under the uniaxial stress conditions or the plane strain conditions. The curve marked by ' $\varepsilon_m^{Uni} = 0.44, \varepsilon_m^{PE} = 0.35$ ' represents the conditions when the critical strain for the onset of creases coincides with that of the onset of wrinkles. Above this curve (shown in pink), the critical strain for the onset of wrinkles is smaller than that of creases. Below this curve (shown in purple), the critical strain for the onset of wrinkles is larger than that of creases. (b) The corresponding nominal wavelengths are independent of the type of deformation.

### 6.3 Subcritical and supercritical creases

We know in a homogeneous material, creases are supercritical if they form under purely elasticity and the bottom of the material is kept flat. However, creases become subcritical, if surface energy is large enough [138] or the material is free-standing [139]. Moreover, a bilayer with same moduli of the film and substrate but substrate pre-compressed can also form subcritical creases [173]. In this section, we use finite element method to study the initiation and growth of creases in a bilayer. We find that in a bilayer, creases could be either supercritical or subcritical.

The commercial finite element software ABAQUS is utilized to simulate creases. We implement both the film and substrate as incompressible neo-Hookean materials. We assume creases form periodically, and the spacing between two neighboring creases is two times the total thickness of the film and substrate, which is similar to experimental observations [113, 173]. Reflection symmetry of creases is assumed so that we only simulate half of a crease and the simulation box has the size of  $(H_s + H_f) \times (H_s + H_f)$ . Symmetry condition is prescribed on the left boundary, and the other three boundary conditions are applied as sketched in Figure 6.1b. We simulate plane strain compression of the bilayer. Element type CPE4H is used. In order to break the translational symmetry of the surface, a small defect (size as small as  $10^{-3}$  of the film thickness) is prescribed at the top left corner. The defect is small enough so that its effect on the critical strain is eliminated. On the other hand, to resolve the field close to the defect, mesh size close to the defect is made much smaller than the defect size. In order to simulate subcritical creases, static Riks method is implemented to solve the boundary value problem [189]. After the initiation of a crease, the

crease tip folds up and forms self-contact. Because the combination of contact and Riks method makes the convergence difficult, a thick layer with extremely low shear modulus (1/200 of the film shear modulus) is added on the top of the film to prevent self-contact [173]. The top of the extremely compliant layer is confined to be flat so that instability only happens on the interface between the film and the compliant layer. As shown in [140], the interfacial crease asymptotically approaches the surface crease when the modulus of the compliant layer is much smaller than that of the film.

We simulate creases in bilayer structures for different ratios of moduli and thicknesses. We find the creases can be subcritical or supercritical (Figure 6.5a). Supercritical creases tend to form in a bilayer with thicker and more compliant film, while subcritical creases tend to form in a bilayer with thinner and stiffer film.

Figure 6.5b is a bifurcation diagram of a supercritical crease, where the applied strain represents the loading parameter, and the depth of the crease (defined in Figure 6.1d) represents the state of the system. The flat state becomes unstable and creases initiate at strain 0.35 under plane strain condition and 0.44 under uniaxial condition. With further increase of strain, the crease gradually grows deeper (Figure 6.5b). The pink curve marked by  $G_f/G_s = 1.05$  in Figure 6.5d, and the pink curve marked by  $H_s/H_f = 0.2$  in Figure 6.5e show typical dependence of crease depth as a function of strain for supercritical creases. Here because of the existence of the extremely compliant layer, the snapping forward strain  $\varepsilon_F$  is increased slightly to around 0.36.

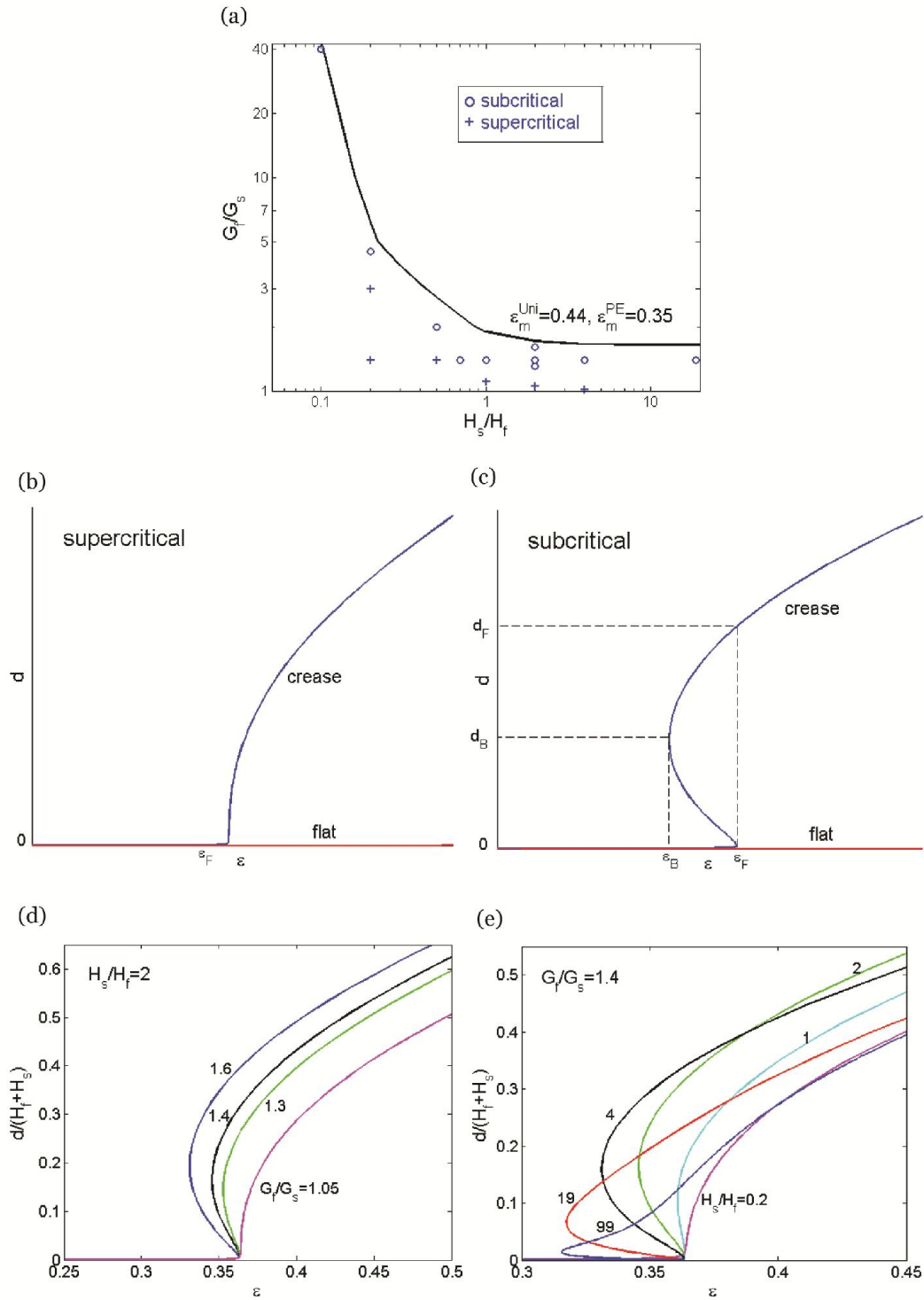


Figure 6.5 The formation of creases in bilayers of various ratios of moduli and thicknesses. (a) Below the solid curve, the critical strain for the onset of wrinkles is larger than that of creases. Creases in a bilayer can be subcritical or supercritical. (b) Bifurcation diagram of a supercritical crease, where the applied strain represents the loading parameter, and the depth of the crease represents the state of the system. (c) Bifurcation diagram of a subcritical crease. (d) and (e) Calculated bifurcation diagrams for bilayers of some ratios of moduli and thicknesses.

Figure 6.5c is a bifurcation diagram of a subcritical crease. When the strain is smaller than the snapping backward strain  $\varepsilon_B$ , the flat state with  $d = 0$  is the only solution to the boundary value problem. When the strain is larger than the snapping forward strain  $\varepsilon_F$ , the crease state with a finite depth is the only solution to the boundary value problem. When the strain is in between the snapping forward and snapping backward strains  $\varepsilon_B < \varepsilon < \varepsilon_F$ , both the flat state and the deep crease state are the solutions to the boundary value problem, and can co-exist. Figure 6.5d and e show the dependence of crease depth on external strain for subcritical creases under plain strain condition. The snapping backward strain  $\varepsilon_B$  varies with  $H_s/H_f$  and  $G_f/G_s$ , while the snapping forward strain  $\varepsilon_F$  is a constant. The snapping forward happens when the critical strain of crease initiation is satisfied on the top of the film. Since the deformation in a bilayer structure is homogeneous before the initiation of creases, the snapping forward strain is 0.35 under plane strain condition and 0.44 under uniaxial condition.

When  $H_s/H_f = 2$ , creases are supercritical if  $G_f/G_s$  is small enough (Figure 6.5d). With the increase of  $G_f/G_s$  the snapping backward strain decreases, and therefore the hysteresis increases. The snapping forward and backward depths ( $d_F$  and  $d_B$  as defined in Figure 6.5c) also increases with  $G_f/G_s$ . When  $G_f/G_s = 1.4$ , the depth-strain curve varies dramatically with  $H_s/H_f$  (Figure 6.5e). When  $H_s/H_f = 0.2$ , the curve is monotonic, and the crease is supercritical. With the increase of  $H_s/H_f$ , creases become subcritical, and the hysteresis increases. However, the crease snapping forward and backward depths normalized by the total thickness  $H_s + H_f$ ,  $d/(H_s + H_f)$ , increases and then decreases with the increase of  $H_s/H_f$ . We can see that creases tend to be more subcritical when the

substrate is more compliant and thicker. When  $G_f/G_s \rightarrow \infty$ , the bilayer approaches the limit of a free standing homogeneous material [139].

#### 6.4 Diagram of wrinkles and creases

In this section, we construct a diagram of different bifurcation behavior (Figure 6.6). By comparing the critical strains for the onset of wrinkles and creases, we find a boundary of equal critical strain (Figure 6.4a, Figure 6.5a and the middle black line in Figure 6.6). Since the critical condition of crease initiation (for supercritical creases) or snapping forward (for subcritical creases) under different loading conditions satisfies the same relation as the critical condition of wrinkle initiation, equation (6.21) [107], this phase boundary is independent of loading condition. From the phase diagram, we can see that creases tend to set in for more compliant and thicker films. Especially, when  $G_f/G_s < 1.65$ , creases always form earlier than wrinkles, no matter how large the thickness  $H_s/H_f$  ratio is. This was also predicted in [99] when the authors studied instability in a bilayer with infinite substrate, and this condition is close to the critical condition when wrinkles in a bilayer structure become unstable [170]. When  $H_s/H_f$  reaches around 10, with the further increase of  $H_s/H_f$ , the phase boundary keeps flat, which means the thin film limit is reached. It is tempting to expect that the boundary demarcates regions in which wrinkles or creases form.

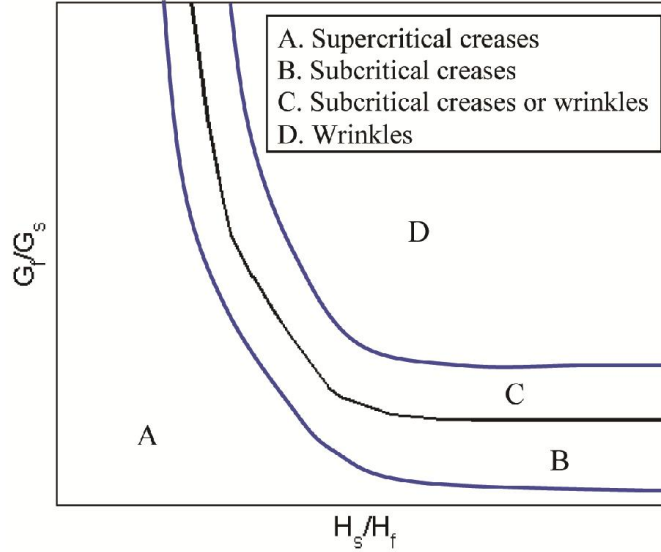


Figure 6.6 On the plane of the axes  $G_f/G_s$  and  $H_s/H_f$ , approximate regions are marked for various types of bifurcation behavior.

However, we found remarkably rich bifurcation behavior. On the left of equal critical strain curve (shown in purple in Figure 6.4a), we further find a boundary of two different bifurcation behavior, the left curve in Figure 6.6, on the left of which creases are supercritical (type A), while on the right of which creases are subcritical (type B). As a result, supercritical creases tend to form for thicker and more compliant films, while subcritical creases tend to form for thinner and stiffer films. Figure 6.7a shows simulation result of a type A bifurcation for  $G_f/G_s=1.4$  and  $H_s/H_f=0.2$ , where the applied strain  $\varepsilon$  represents the loading parameter, and the total elastic energy  $U$  normalized by the total elastic energy for the flat state  $U_0$ ,  $U/U_0$ , represents the state of the system. The red flat line  $U/U_0=1$  represents the flat state. For a supercritical crease,  $U$  becomes smaller than  $U_0$  after the formation of the crease (blue curve in Figure 6.7a). The minimal strain for the initiation of wrinkles  $\varepsilon_m$  (represented by the green diamond in Figure 6.7a) is higher than the critical strain for the

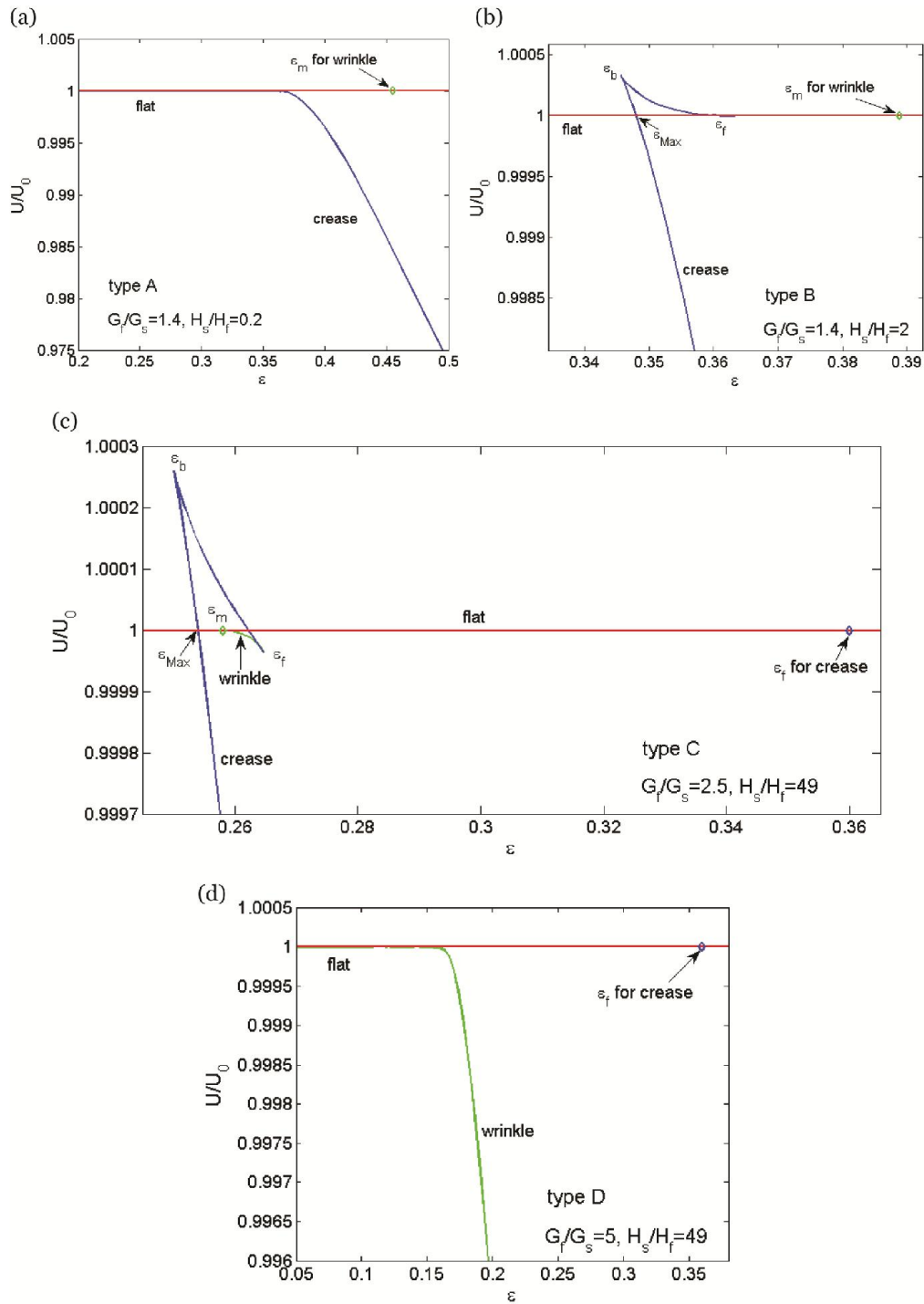


Figure 6.7 Several types of bifurcation diagrams for bilayers of various ratios of moduli and thicknesses. (a) Critical strain for the onset of creases is smaller than that for the onset of wrinkles, and creases are supercritical. (b) Critical strain for the onset of creases is smaller than that for the onset of wrinkles, and creases are subcritical. (c) Critical strain for the onset of wrinkles is smaller than that for the onset of creases, but larger than the Maxwell strain  $\epsilon_{Max}$ . Supercritical wrinkles form, and then snap into creases. Or subcritical creases form from the flat state. (d) Critical strain for the onset of wrinkles is smaller than the Maxwell strain  $\epsilon_{Max}$ . Supercritical wrinkles form.

initiation of creases. Figure 6.7b shows a type B bifurcation for  $G_f/G_s=1.4$  and  $H_s/H_f=2$ . Similarly, the red line  $U/U_0=1$  represents the flat state. The blue curve represents the solution of a crease. For a subcritical crease, the Maxwell strain  $\varepsilon_{Max}$  is defined as the critical strain when the energy of the deep crease state is the same as the flat state. When a flat surface is loaded without perturbations to strain  $\varepsilon_{Max} < \varepsilon < \varepsilon_F$ , the surface can still keep flat, but creases can channel through from the edge of the sample. Similarly, when a sample with deep creases is unloaded without perturbations to strain  $\varepsilon_B < \varepsilon < \varepsilon_{Max}$ , deep creases can still exist, but they can shrink by channeling from the edge. The green diamond represents the critical condition for the initiation of wrinkles, which is also higher than the snapping forward strain  $\varepsilon_F$ .

When the minimal strain for the initiation of wrinkles  $\varepsilon_m$  is smaller than the snapping forward strain of the subcritical creases  $\varepsilon_F$ , but larger than the Maxwell strain  $\varepsilon_{Max}$ ,  $\varepsilon_{Max} < \varepsilon_m < \varepsilon_F$ , the energy bifurcation diagram for  $G_f/G_s=2.5$  and  $H_s/H_f=49$  is shown in Figure 6.7c as an example (type C in Figure 6.6). The red line  $U/U_0=1$  represents the flat state. The green line existing between strains  $\varepsilon_m$  and  $\varepsilon_F$  represents the solution of wrinkles. The blue line represents the solution of creases. When the sample is subject a critical compression, we expect the formation of channeling creases if channeling is allowed through the boundary. However, if channeling is eliminated, we expect to see simultaneous wrinkles. Those wrinkles can further channel to creases with perturbations, or snap to creases with further increase of the strain. This explains why in [99] the authors observed creases experimentally under higher  $G_f/G_s$  than predicted by their theory, which only considers supercritical creases. The blue diamond represents the critical strain for the

initiation of wrinkles on the flat surface. We notice the critical strain for the initiation of creases with the facilitation of wrinkles is much lower than 0.35. When the critical strain for the initiation of wrinkles is even smaller than the Maxwell strain  $\varepsilon_{Max}$  of the subcritical creases, wrinkles are observed (type D in Figure 6.6). Those wrinkles may still channel to creases under a larger strain. Therefore, wrinkles tend to set in for stiffer and thinner films. Figure 6.7d shows an example of the type D bifurcation diagram for  $G_f/G_s = 5$  and  $H_s/H_f = 49$ . The green curve represents the wrinkle solution. The elastic energy  $U$  becomes smaller than  $U_0$  when the strain is larger than the initiation strain of wrinkles  $\varepsilon_m$ . The critical strain for the initiation of creases on a flat surface, represented by a blue diamond, is higher.

## 6.5 Summary

In this chapter, we study wrinkle and crease instability in bilayers. We study wrinkles in a bilayer with finite thickness of the substrate by the linear perturbation method. We simulate creases in a bilayer structure by finite element method, and find several new types of bifurcation behavior. The ratio of the elastic moduli and that of the thicknesses define a plane, and by comparing the onset conditions for wrinkles and creases, we find a curve of equal critical strain in that plane. Far below the curve when the critical strain for the onset of creases is much lower than that for the onset of wrinkles, the supercritical creases form. Right below the curve when the critical strain for the onset of creases is slightly lower than that for the onset of wrinkles, creases are subcritical and can channel into the bilayers at the Maxwell strain. Far above the equal critical strain curve, when the critical strain for the onset

of wrinkles is much lower than that for the onset of creases, wrinkles form. Right above the curve, even when the critical strain for the onset of creases is higher than that for the onset of wrinkles, subcritical creases can still channel at the Maxwell strain, which could be much lower than the critical strain for the onset of creases in a homogeneous material, as long as the Maxwell strain is lower than the critical strain for the initiation of wrinkles. When the Maxwell strain is higher than the critical strain for the initiation of wrinkles, wrinkles form first, but a further compression causes the strain at the troughs of the wrinkles to be high enough to initiate creases, and wrinkles transit to creases subcritically.

## **Chapter 7**

# **Role of substrate pre-stretch in post-wrinkling bifurcations**

### **7.1 Introduction**

Wrinkles form when a thin stiff film supported on a soft substrate is compressed beyond a critical strain. When the compression is slightly above the critical strain, the wrinkles are periodic. The wavelength of the wrinkles is determined by a balance between the deformation of the substrate, which favors short wavelengths, and the bending of the film, which favors long wavelengths [10, 76]. By controlling the onset and evolution of wrinkles in a number of different material systems, researchers have demonstrated a wide range of applications. These include the fabrication of materials with changeable wetting [34-37], adhesive [8, 31, 32], and optical properties [37, 40, 41], the measurement of mechanical characteristics [14, 22-26] of thin films and soft substrates, and the use of wrinkles as templates for self-assembly [27-29], in microfluidic [19-21], photovoltaic [16-18] and flexible electronic devices [13-15, 218], and for alignment of cultured cells [29, 30, 219].

When compressed sufficiently far beyond the onset of wrinkling, however, new deformation modes may appear, with characteristics that depend sensitively on the details of the substrate response [147]. For a thin elastic film supported on a viscous substrate, wrinkles lose their periodicity and transition to localized folds once the displacement applied approaches one third of the initial wrinkling wavelength [74, 151]. The transition to localized

deformation may even lead to the fracture of the film [220]. For an elastomeric foundation, wrinkles lose their initial periodicity through the emergence of sub-harmonic modes due to nonlinear contributions to the elastic response of the substrate [82, 149]. Typically, a progression from wrinkles to a period-doubled state is observed, followed by a period-quadrupled state, and finally the formation of self-contacting folds [95, 145, 147]. The emergence of sub-harmonic spatial modes in this context is analogous to appearance of temporal sub-harmonics for a non-linear oscillator [145].

In light of the key role played by the substrate in driving post-wrinkling bifurcations, it follows that this behavior should be highly sensitive to the state of the substrate, for example the presence of a compressive or tensile pre-stress. In spite of this expectation, however, only a limited number of studies along these lines have been conducted. In particular, Hutchinson and co-workers have predicted the emergence of localized ridges as a different type of post-wrinkling bifurcation for large substrate pre-tension from numerical modeling [75, 155]. The application of in-plane pre-tension causes a softening of the outward deflection of the substrate relative to the inward deflection and hence promotes the formation of ridges. Conversely, the application of in plane pre-compression stiffens outward deflection of the substrate relative to inward, favoring the formation of folds. While a few experiments have indicated the emergence of ridges [155-157] or other modes of strain localization [99] with pre-tension, the level of agreement with theory remains unclear. Further, there has been little work focused on the case of substrate pre-compression. Thus, there remains much to understand about how post-wrinkling behavior depends on substrate pre-stretch.

The critical importance of a pre-stretched substrate is demonstrated by the simple experimental result shown in Figure 7.1. Using an approach that will be described in detail below, a soft elastomeric substrate is subjected to: (a) a tensile pre-stretch, (b) no pre-stretch, or (c) a compressive pre-stretch, prior to formation of the stiff skin. At the same applied nominal film strain, the resulting morphologies vary dramatically. With substrate pre-tension, the surface remains uniformly wrinkled; with no pre-strain, it shows the clear emergence of a sub-harmonic (period-doubled) mode; and with pre-compression, it shows a highly irregular ‘chaotic’ pattern. The aim of the study in this chapter is to establish, through a combination of experiments and simulations, how substrate pre-stretch alters the onset and evolution of post-wrinkling modes as well as to understand the chaotic emergence of different sub-harmonic modes by adopting a general method to study symmetry breaking from a periodic structure.

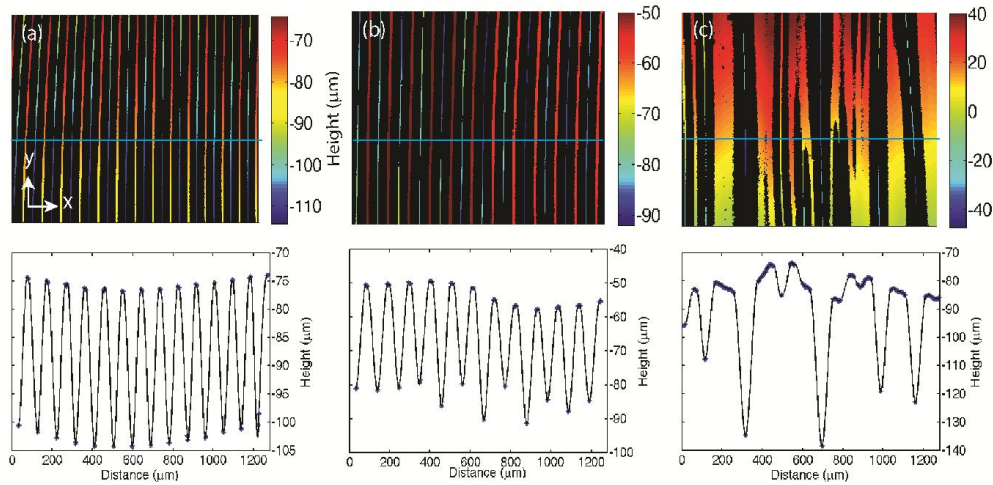


Figure 7.1 Optical profilometry is used to characterize the surface profiles of films at similar nominal strains  $\epsilon_f$  on substrates with varying amounts of pre-stretch  $\lambda_o$ . (a) At  $\epsilon_f = 0.16$  and  $\lambda_o = 1.3$ , uniform wrinkles are observed. (b) At  $\epsilon_f = 0.17$  and  $\lambda_o = 1.0$ , period doubling has just begun to emerge. (c) At  $\epsilon_f = 0.15$  and  $\lambda_o = 0.7$ , ‘chaotic’ post-wrinkling is found.

## 7.2 Methods

### 7.2.1 Experimental setup

Our experiments rely on an elastic trilayer system modified from a recently described approach (Figure 7.2) [173]. A 400- $\mu\text{m}$ -thick soft (shear modulus  $\mu_s = 12.5$  kPa) poly(dimethylsiloxane) (PDMS) substrate is attached to a 1-mm-thick stiffer ( $\mu = 260$  kPa) PDMS mounting layer that has been uniaxially stretched to an initial length  $L_o$ . This bilayer is then partially released, or stretched further, to a new length  $L$ , placing the substrate under a pre-stretch  $\lambda_o = L/L_o$ . The importance of the mounting layer is that it allows for the substrate to be loaded under pre-compression without undergoing macroscopic buckling. Next, the surface is exposed to UV/ozone, which converts the top layer of the PDMS substrate into a gradient-modulus silicate film with an effective film thickness of 3-8  $\mu\text{m}$  that shows excellent adhesion to the substrate [221]. We consider the film to be stress free at this point, although we note the possibility for a slight residual stress due to mismatches in thermal expansion and/or oxidation-induced changes in volume. A subsequent partial release of the mounting layer to length  $l$  now places the bilayer under compression, which we characterize in terms of the nominal strain applied to the film  $\varepsilon_f = (L-l)/L$ . The subsequent wrinkling and post-wrinkling behavior of the surface as a function of applied strain is then characterized by *in situ* optical profilometry. Using a defect in the wrinkling pattern as a point of reference, we track the same region while increasing the compressive strain in the film.

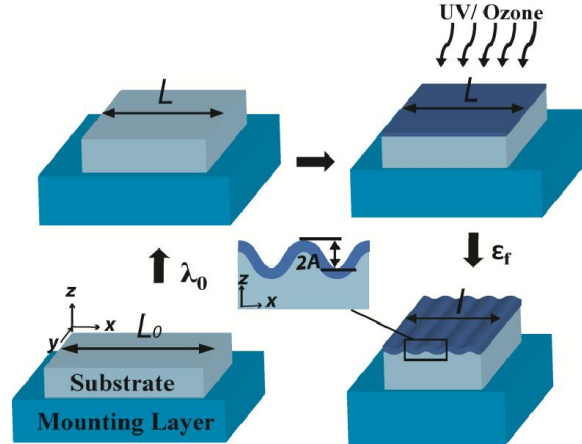


Figure 7.2 A schematic of the experimental procedure. An elastomeric substrate is attached to a pre-stretched mounting layer, deformed to  $\lambda_0$ , and exposed to UV/O<sub>3</sub> to form a stiff film layer. The stiff film is compressed with strain  $\epsilon_f$  by partially releasing the mounting layer.

### 7.2.2 Experimental details

A trilayer system was used to independently vary the compression applied to the substrate and the silicate film. A silica reinforced vinyl-terminated polydimethylsiloxane (PDMS) mounting layer (DMS-V31S15, Gelest Inc.) with a shear modulus 260 kPa and thickness 1 mm was uniaxially pre-stretched on a stretcher. A pre-cured substrate with thickness of approximately 400  $\mu\text{m}$  composed of a PDMS elastomer (Sylgard 184, Dow Corning) with a 50:1 weight ratio of base to crosslinker (shear modulus 12.5 kPa based on dynamic mechanical analysis) was attached to the pre-stretched mounting layer using a thin (2-5  $\mu\text{m}$  thick) layer of uncured PDMS with the same composition as the substrate. This bilayer assembly was placed in an oven at 60  $^{\circ}\text{C}$  for 4 h to bond the layers, and then allowed to cool to room temperature over 30 min before deforming the mounting layer to put the substrate under a pre-stretch  $\lambda_0$ . The substrate was left at  $\lambda_0$  for 30 min before being placed

in a UV/O<sub>3</sub> cleaner for 25 min to convert the surface of the PDMS substrate into a stiffer oxide layer. For each sample, we determined the amplitudes and spacings between at least seven neighboring wrinkles from optical profilometry. The oxide films were found to have effective thicknesses of 3-8 μm and shear moduli of 620 kPa – 3.8 MPa as determined by fitting the dependence of the wrinkle amplitude and wavelength on film strain for samples with no substrate pre-stretch via the classical buckling equations as described by Stafford and co-workers [22, 23]. For any given sample, the respective uncertainties in these quantities were less than 0.6 μm and 50 kPa; the large ranges determined for different samples therefore presumably reflect slight differences in sample position within the UV/O<sub>3</sub> cleaner. However, as the film modulus is larger than the substrate modulus by a factor of 50 – 300, this variation should not play a significant role in the observed behavior. Compression was applied to the trilayer by relaxing the pre-stretch of the mounting layer.

Optical profilometry (Zygo NewView 7300) was used for in-situ characterization of the height profiles of the sample surfaces using MetroPro 8.3.2 software. The 5x and 10x lenses were utilized as well as the stitch application to characterize a large area of the sample. At high film strains only the data points from the crest and trough could be imaged due to the steep angles of the surface; a spline was used to fill in the missing segments of the surface profiles in Figure 7.1 and Figure 7.6. Laser scanning confocal fluorescence microscopy (Zeiss LSM 510 Meta) was used to characterize the shape of the wrinkles. Fluorescent labeling of the substrate was accomplished by adding 4.5 μg of fluorescein-o-acrylate in 1,4-dioxane per 1 g of PDMS prior to curing. During imaging, a refractive index matching fluid consisting of 72% glycerol and 28% water (weight percent) was used along with a 25x variable immersion

lens. Several two-dimensional frames were taken and manually stitched together by aligning peaks and troughs of the wrinkles to cover a larger area of the sample.

### 7.2.3 Finite element simulations

The commercial finite element software ABAQUS was used to computationally study the effect of pre-stretch on post-wrinkling bifurcations. The substrate was uniaxially pre-stretched and then the film-substrate bilayer compressed under plane strain. Both the film and substrate were modeled as incompressible neo-Hookean materials, and the free energy of neo-Hookean material with a pre-stretch was implemented by a user-defined subroutine UMAT. For all the simulations except Figure 7.3, the modulus ratio of the film to substrate was set to 50, and the thickness ratio of the bilayer to the film was chosen as 50, both of which roughly match the experimental conditions. To break the symmetry of the surface during compression, the first and second eigenmodes obtained by a linear perturbation step were introduced as initial imperfections with very small amplitudes (roughly 1/2000 times the film thickness).

We call the wrinkle wavelength  $l_w$ . When we simulate the critical strain for period doubling (Figures 7.3 and 7.5), the simulation sample length is chosen as  $l_w$ . To understand chaotic period multiplication (Figures 7.8-7.13), we calculate the energy of different periodic states: wrinkling with the initial periodicity, period doubling, tripling and quadrupling. To realize these different periodicities, we simulate samples with lengths  $l_w/2$ ,  $l_w$ ,  $3l_w/2$  and  $2l_w$  respectively. Symmetry condition is added on one boundary and uniform strain is applied on the other boundary. Static method is used for all the simulations.

## 7.3 Results

### 7.3.1 Effect of substrate pre-stretch on period doubling

We plot measured amplitudes for several different levels of pre-strain ( $\lambda_o = 0.7 - 1.2$ ) in Figure 7.3 (black triangles). The amplitude associated with a given feature on the surface is defined as half of the average out-of-plane displacement between a given ‘trough’ and its two neighboring ‘crests’. For each sample, at least seven features are measured. The critical strain for wrinkling varied for different samples between 0.03-0.05, while the wrinkle wavelength was  $l_w = 100 - 160 \mu\text{m}$ . This degree of variability is apparently due to slight differences in the position of the sample relative to the UV light source during oxidation. Using the approach of Stafford and co-workers [22], the effective thicknesses of the silicate layers are estimated for each sample with no substrate pre-stretch as  $h_f = 3 - 8 \mu\text{m}$ , with shear moduli of  $\mu_f = 620 \text{ kPa} - 3.8 \text{ MPa}$ , corresponding to modulus mismatch values ( $\mu_f/\mu_s$ ) of 50 - 300. These large ranges in effective film thickness and modulus are the result of variations between different samples. However, as shown by Cao and Hutchinson, the modulus mismatch does not affect the critical strain for post-wrinkling bifurcations if the mismatch is above 10 [75].

In the wrinkle regime, the amplitudes are nearly homogeneous, as can be seen from the small amount of scatter in Figure 7.3 (standard deviations in wrinkle amplitudes are typically less than  $1 \mu\text{m}$ ), and grow with increasing strain. However, at a sufficiently large value of  $\varepsilon_f$ , a post-wrinkling bifurcation is observed in which some wrinkles grow in amplitude while their neighbors shrink. As seen in Figure 7.3a-c, pre-stretches from  $\lambda_o = 1.0 - 1.2$  show a clean bifurcation corresponding to a period doubled state, as shown by Brau

et al. for the case of  $\lambda_o = 1$  [145]. We denote the strain at which this first post-wrinkling bifurcation is observed as  $\epsilon_{pw}$ , identified in practice as the point at which the standard deviation of wrinkle amplitudes show a dramatic increase. For the case of  $\lambda_o = 1$ , we verified that the period doubling bifurcation showed no apparent hysteresis from initial loading, to unloading, and subsequent reloading (Figure 7.4), suggesting that plastic deformation plays little if any role in this process.

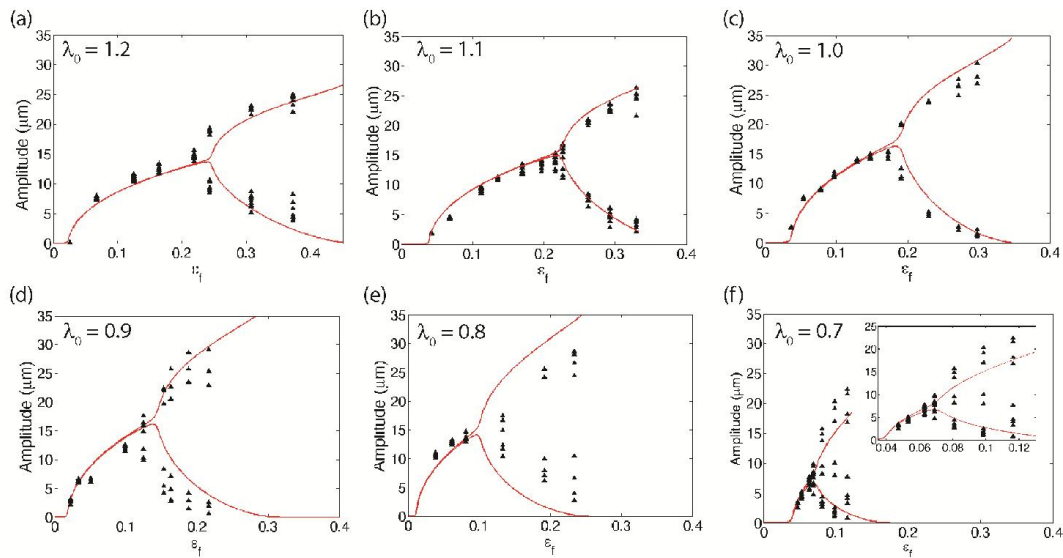


Figure 7.3 Bifurcation curves of the wrinkle amplitude as a function of film strain for substrates pre-stretched to  $\lambda_o =$  (a) 1.2, (b) 1.1, (c) 1.0, (d) 0.9, (e) 0.8 and (f) 0.7. The experimental data (black triangles) reveal a gradual shift of the bifurcation point as well as an increase in distribution of amplitudes past  $\epsilon_{pw}$  with a decrease in  $\lambda_o$ . Simulations (red lines) show good agreement with the experimental data.

For  $\lambda_o = 1$  (Figure 7.3c), we measure a value of  $\epsilon_{pw} = 0.18$ , which is in good agreement with the values reported by Brau et al. of 0.17 - 0.20 for a true bilayer system [145]. When the substrate is under slight pre-tension, the period-doubled bifurcation shifts to higher strains but remains otherwise qualitatively similar; at  $\lambda_o = 1.2$  we measure  $\epsilon_{pw} = 0.23$  for the sample characterized in Figure 7.3a and at  $\lambda_o = 1.1$  we measure  $\epsilon_{pw} = 0.22$  for the sample in Figure 7.3b. Under slight pre-compression the bifurcation occurs at lower film strain; at  $\lambda_o = 0.9$

and  $\lambda_0 = 0.8$  (Figure 7.3d-e), we find  $\epsilon_{pw} = 0.11$  and  $\epsilon_{pw} = 0.10$ , respectively. While a clear bifurcation into a bimodal collection of larger and smaller amplitudes can still be seen in this case, consistent with period doubling, the spread in amplitudes for each population is larger than for  $\lambda_0 = 1$  and  $\lambda_0 = 1.2$ .

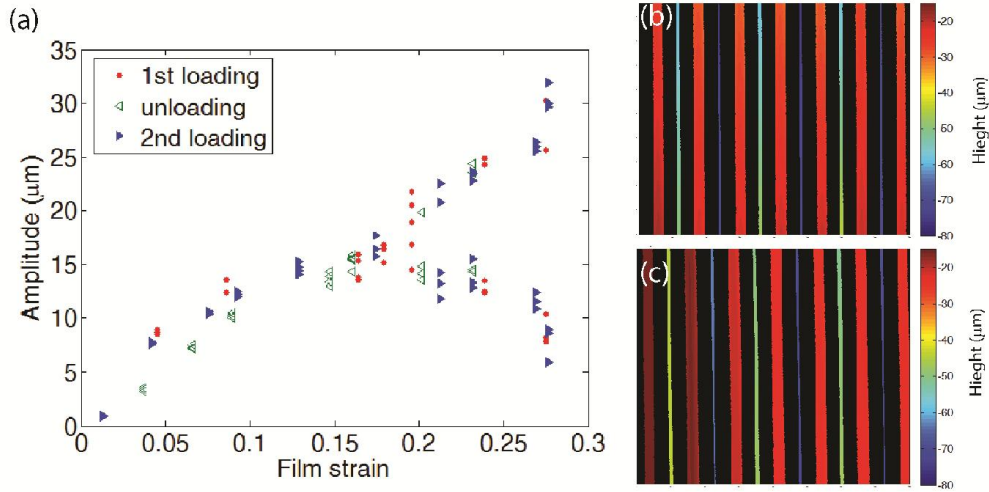


Figure 7.4 (a) Bifurcation curves for  $\lambda_0 = 1.0$  show no detectable hysteresis from the first loading cycle to unloading and subsequent reloading. Optical profilometry images of the surface (b) during the first loading at a film strain of 0.24, and (c) during the second loading at a film strain of 0.23.

This non-uniformity becomes dramatically more pronounced for a film on a substrate with a larger pre-compression,  $\lambda_0 = 0.7$  (Figure 7.3f). In this case, a clean bifurcation is lost, replaced instead by the emergence of a broad spread of amplitudes at a strain of  $\epsilon_{pw} = 0.06$ , which is only slightly above the critical strain for wrinkling,  $\epsilon_w = 0.04$ . The transition from regular wrinkles to irregular, or ‘chaotic’, structures occur over such a small range of strain that when plotted on the same scale as the other samples in Figure 7.3a-e, the distinction between wrinkling and post-wrinkling is completely obscured; however, the inset to Figure 7.3f shows that indeed a narrow range of regular wrinkling can be discerned.

To better understand these effects, we model the system using the commercial finite element software ABAQUS. Both the film and substrate are taken to be incompressible

neo-Hookean materials. For a ratio of the film to substrate modulus of only 50 – 300, as studied here, the maximum strain in the film can be as large as  $\sim 0.20$  in our simulations. Thus, it is necessary to use a non-linear hyperelastic model for both the film and substrate. However, as the range of strains is still modest, the neo-Hookean model should provide a reasonable description of both materials. The substrate is uniaxially pre-stretched while the film/substrate bilayer is subsequently compressed under plane strain, which is similar to the condition in the experiments. To simulate the period doubled state, we choose a unit cell of width  $l_w$ , the wrinkle wavelength. Symmetry is maintained across one boundary and uniform strain is applied on the other boundary. A small amplitude initial imperfection is introduced to break the translational symmetry of the surface. More details about the simulations of the period doubled state will be discussed below. When compressive strain is incrementally applied, the surface initially remains flat and then forms wrinkles after a critical strain. With further increase in strain, the wrinkle amplitude grows but the nominal wavelength does not change. After a second critical strain, wrinkles lose their original periodicity through a supercritical period-doubling bifurcation. We record the second critical strain as  $\epsilon_{pw}$ .

In Figure 7.3, we plot the simulation results for wrinkle amplitudes with different substrate pre-stretches as red lines. From the experimentally measured wrinkle wavelength, and the dependence of wrinkle amplitude on strain, we estimate the film thickness by fitting the classical buckling equations [22], as before. For the effective film modulus, however, we make use of the theoretical prediction that takes into account substrate pre-stretch and assumes infinite substrate thickness [75]. The modulus ratios of the film to substrate estimated in this fashion are (a) 120, (b) 200, (c) 50, (d) 130, (e) 225 and (f) 35, while the

film thickness are (a) 5.8  $\mu\text{m}$ , (b) 6.0  $\mu\text{m}$ , (c) 8.0  $\mu\text{m}$ , (d) 6.6  $\mu\text{m}$ , (e) 5.5  $\mu\text{m}$  and (f) 7.8  $\mu\text{m}$ . In the simulations, we choose a modulus ratio to match the experimental value for each plot. The ratio of the total thickness to the film thickness is fixed at a representative value 50 in all cases, since the ratio has no effect on the wrinkling and post-wrinkling as long as the substrate is much thicker than the film, and can be treated as infinite. As seen in Figure 7.3, the simulations generally agree well with the experimental results, in terms of both the location of the post-wrinkling bifurcation and the subsequent evolution of amplitudes. The agreement of the cases with pre-tension in the substrate is slightly better than with pre-compression. A possible reason is the competition between different post-wrinkling bifurcation modes, which clearly influences the behavior at large pre-compression, as we discuss further below.

Figure 7.5 shows the dependence of  $\varepsilon_{pw}$  on  $\lambda_o$ , obtained from finite element simulations and experiments on at least 3 different samples at each  $\lambda_o$ . In this simulation and the remainder of the chapter, the ratio of the film modulus to substrate modulus is fixed as 50, since  $\varepsilon_{pw}$  is almost independent of the modulus ratio as long as the modulus ratio is larger than 10 [75]. The ratio of the total thickness to the film thickness is also fixed as 50, which is large enough for the thickness of the substrate to be considered as infinite. When there is no pre-stretch in the substrate,  $\varepsilon_{pw}$  is calculated to be around 0.18, which matches the experimental value of  $0.18 \pm 0.02$ . A monotonic increase in  $\varepsilon_{pw}$  with  $\lambda_o$  is seen: pre-compression in the substrate decreases  $\varepsilon_{pw}$ , while pre-tension increases  $\varepsilon_{pw}$ . Under pre-tension, e.g.  $\lambda_o = 1.2$ , the finite element result of  $\varepsilon_{pw} = 0.26$  agrees well with that from experiments ( $0.27 \pm 0.07$ ). Under pre-compression, e.g. at  $\lambda_o = 0.7$ , the respective

experimental and simulation results of  $\varepsilon_{pw} = 0.05 \pm 0.02$  and  $0.06$  are again in agreement. Overall, the simulations in Figures 7.3 and 7.5 show almost quantitative agreement with experimental data, and the qualitative trend of  $\varepsilon_{pw}$  monotonically and strongly increasing with  $\lambda_0$  over this range of substrate pre-stretch is clear in both cases.

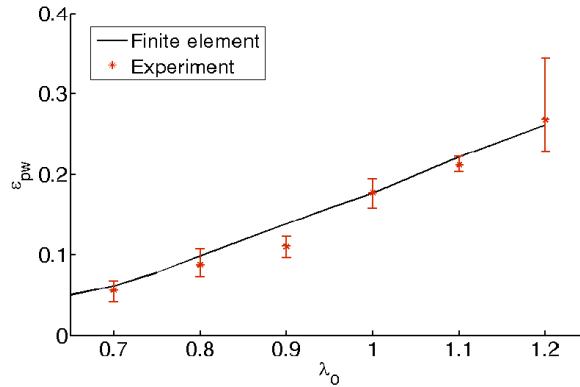


Figure 7.5 The critical film strain for post-wrinkling bifurcation  $\varepsilon_{pw}$  is plotted against the substrate pre-stretch  $\lambda_0$ . The solid line represents finite element results and the solid symbols represent experimental results, with the error bars corresponding to minimum/maximum values for at least 3 samples. As pre-stretch increases, the film strain required for post-wrinkling bifurcation increases.

### 7.3.2 Chaotic period multiplication under large substrate pre-compression

We next consider the irregularity of amplitudes observed during post-wrinkling bifurcation for substrates under pre-compression. In Figure 7.6, we compare in detail the evolution of surface topography with increasing film strain for samples with  $\lambda_0 = 1.0$  and  $0.7$ . Color maps of the surface profiles are shown over large areas of the sample (Figure 7.6a-c, e-g), along with line profiles (Figure 7.6d, h) at the locations indicated. The profiles are taken at nearly the same position on each sample, and plotted with an x-axis normalized by  $(1 - \varepsilon_f)$  to vertically align each crest and trough so that its evolution with film strain can be easily observed.

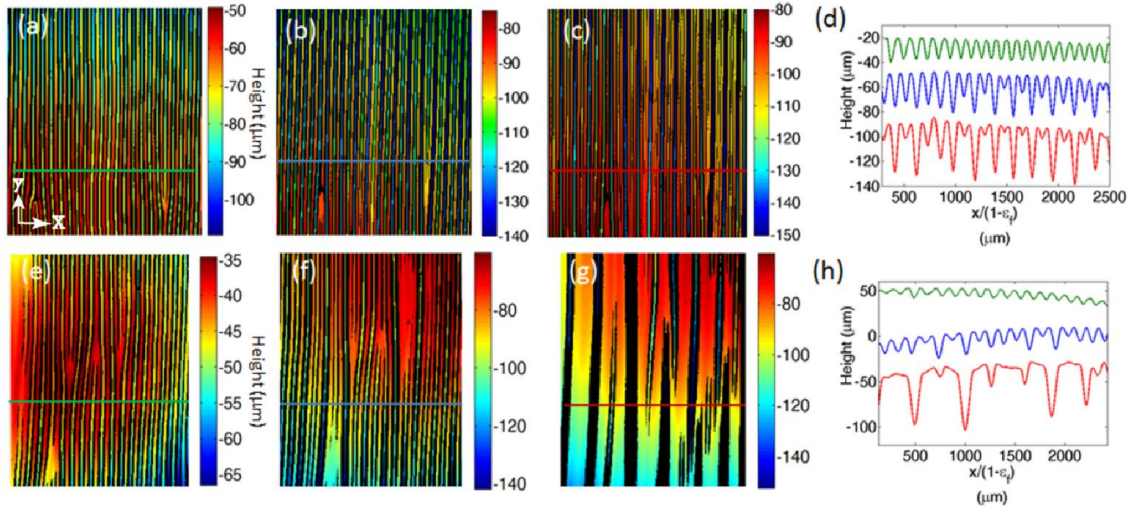


Figure 7.6 The surface profile of a sample with pre-stretch 1.0 at film strains of (a) 0.083, (b) 0.16, (c) 0.23. (d) One-dimensional profiles at the locations indicated by the solid lines in (a-c). The surface profile of a sample with pre-stretch 0.7 at film strains of (e) 0.045, (f) 0.063 and (g) 0.11. (h) One-dimensional profiles at the locations indicated by the solid lines in (e-g).

With no pre-stretch, the sample evolves from the wrinkled state (green trace in Figure 7.6d) at  $\varepsilon_f = 0.083$  to a period-doubled state at  $\varepsilon_f = 0.16$  (blue trace) and a period-quadrupled state at  $\varepsilon_f = 0.23$  (red trace). The amplitudes evolve in a fairly regular fashion across the entire sample, except in regions close to a defect in the wrinkling pattern (i.e., as seen to the lower left of Figures 7.6a-c and correspondingly to the left side of the traces in Figure 7.6d).

With a pre-compression of  $\lambda_0 = 0.7$ , however, dramatically different behavior is observed. A regular wrinkle pattern is first observed, as seen for  $\varepsilon_f = 0.045$  (Figure 7.6e, green trace in Figure 7.6h), but rapidly evolves into a set of deep features with irregular spacing by  $\varepsilon_f = 0.11$  (Figure 7.6g, red trace in Figure 7.6h). Examination of the behavior at intermediate strains, e.g. at  $\varepsilon_f = 0.063$  suggests that this pattern emerges through the competition between multiple different sub-harmonic modes with periodicities of 2, 3, and 4 times the fundamental wrinkle mode. In other words, some regions show behavior locally

characteristic of period doubling (two troughs that grow in depth separated by one that becomes more shallow), while others show characteristics of period tripling (deep troughs separated by two shallow troughs) and quadrupling (separation by three shallow troughs).

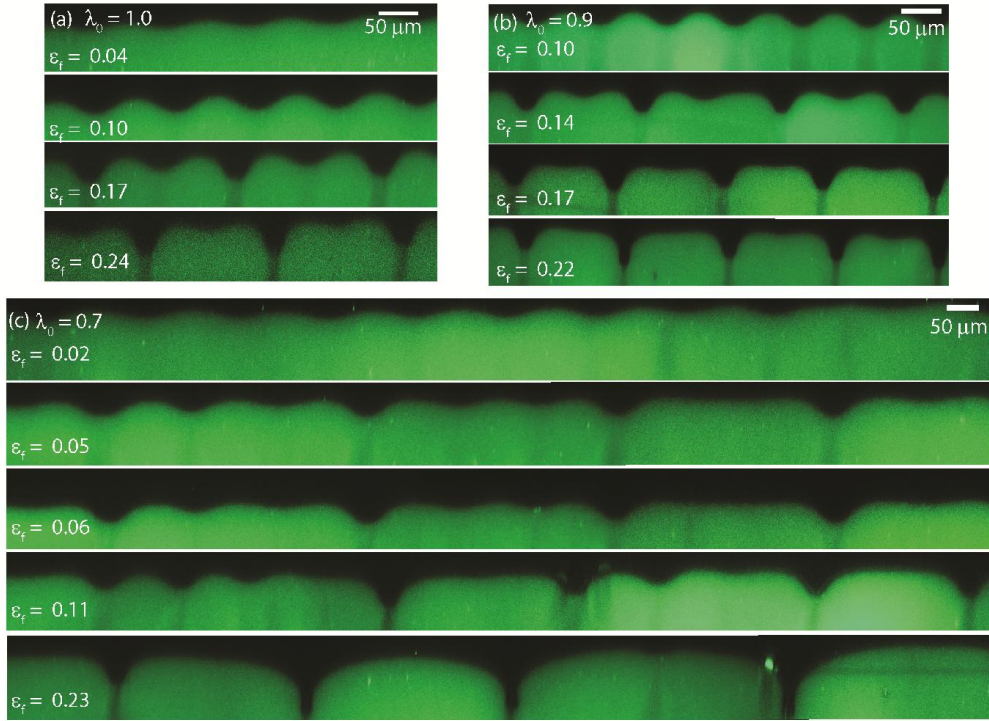


Figure 7.7 Laser scanning confocal fluorescence cross-sections of compressed bilayers with substrate pre-compression of  $\lambda_0 =$  (a) 1.0, (b) 0.9, and (c) 0.7, showing the emergence of post-wrinkling modes with increasing nominal film compression  $\varepsilon_f$ .

Similar behavior can be observed by using laser scanning confocal fluorescence microscopy to characterize samples with fluorescently labeled substrates. With no substrate pre-stretch (Figure 7.7a), regular wrinkles first develop at  $\varepsilon_f = 0.04$ , then grow in amplitude before period doubling takes place at  $\varepsilon_f = 0.17$ . When the substrate is under a small amount of pre-compression,  $\lambda_0 = 0.9$  (Figure 7.7b), wrinkles first give way to a shallow period doubled state at  $\varepsilon_f = 0.14$ , and by  $\varepsilon_f = 0.17$ , the sample is well past the onset of period doubling, with the amplitude of the diminishing wrinkles approaching zero. By  $\varepsilon_f = 0.22$ , the bilayer with  $\lambda_0 = 0.9$  has already transitioned to the period quadrupled state; whereas for  $\lambda_0$

$= 1.0$ , the sample remains in the period doubled state even at a slightly higher film strain of 0.24. With larger pre-compression,  $\lambda_0 = 0.7$  (Figure 7.7c), wrinkles form but are soon followed by a ‘chaotic’ surface pattern with shallow regions of the period doubled, period tripled and period quadrupled states. Interestingly, this behavior shows variability across the transverse direction of the sample, as seen in Figure 7.6g. We suspect this behavior arises because different regions of the sample spontaneously break the symmetry of the wrinkle pattern in different ways, leading to the presence of ‘domain boundaries’ where one set of deep features meets another, mismatched set. However, further study is required to better understand this process.

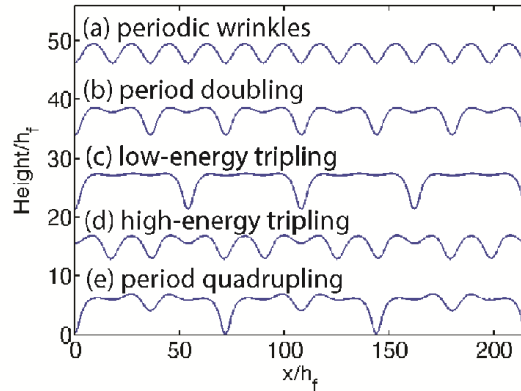


Figure 7.8 Various post-wrinkling bifurcations obtained by finite element simulation. (a) Wrinkles maintaining the initial periodicity. (b) Period doubling. (c) Low-energy tripling. (d) High-energy tripling. (e) Period quadrupling. The film strain is  $\epsilon_f = 0.11$  and the substrate pre-stretch is  $\lambda_0 = 0.7$ .

The emergence of such chaotic behavior can be anticipated based on the analogy to the nonlinear oscillator [145, 222-224], which is well-known to show chaotic behaviors in certain regimes. However, to provide a better understanding of the driving force in the current system, we use finite element methods to compare the energies of the different sub-harmonic modes. To enable such comparisons at equivalent levels of compression, we employ simulation cells with several different sizes, boundary conditions, and initial

imperfections, to enforce different symmetries on the post-wrinkled states. For example, Figure 7.8 shows simulated surface height profiles for different modes at a constant film strain of  $\varepsilon_f = 0.11$  and pre-stretch of  $\lambda_o = 0.7$ : wrinkling that maintains the initial periodicity (Figure 7.8a), period doubling (Figure 7.8b), low-energy tripling (Figure 7.8c), high-energy tripling (Figure 7.8d) and period quadrupling (Figure 7.8e).

To enforce the initial wrinkle period to be conserved throughout the application of the strain, as in Figure 7.8a, we simulate a unit cell with half the nominal wrinkle wavelength  $l_w/2$ . One boundary of the unit cell is chosen at a trough of the wrinkles and the other is chosen at the neighboring peak. We apply reflection symmetry on one boundary and uniform strain on the other boundary, so that both boundaries are kept flat. The corresponding energy per wavelength  $l_w$  is calculated and called  $U_1$ .

To study the bifurcation from a periodic wrinkled state to a period-doubled state (Figure 7.8b), we use a unit cell of width  $l_w$ . We can position the boundaries of the unit cell in two ways: at the troughs of two neighboring wrinkles (Figure 7.9b), or at the peaks (Figure 7.9c). The simulations start with a nearly flat surface with small amplitude (1/2000 times the film thickness) prescribed imperfections, shown in Figure 7.9b and c greatly magnified in amplitude for visual clarity. In both cases, symmetry condition is applied on one boundary and uniform strain is applied on the other boundary. Our simulations indicate that the first choice of boundaries (Figure 7.9b) leads to period-doubling at the critical strain  $\varepsilon_{pw}$ , and we call the energy per wavelength  $l_w$  of this configuration  $U_2$ . By contrast, for the second choice of boundaries, the system retains the initial wrinkle periodicity and does not undergo period doubling.

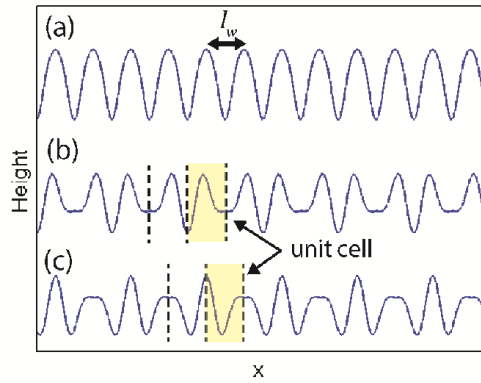


Figure 7.9 Simulating bifurcation from a periodic wrinkled state to a period-doubled state. (a) The wrinkled state with period  $l_w$ . The finite element simulations use unit cells of width  $l_w$  of two types. (b) A unit cell with boundaries at the troughs of neighboring wrinkles bifurcates into the period-doubled state at a critical strain  $\epsilon_{pw}$ . (c) The other type of unit cell with boundaries at the peaks of neighboring wrinkles remains in the periodic wrinkled state and does not bifurcate. The simulations start with a nearly flat surface with prescribed imperfections shown in (b) and (c). For visual clarity, the amplitude of the imperfections has been greatly magnified.

To study the bifurcation to a period-tripled state (Figure 7.8c and d), we use a unit cell of width  $3l_w/2$ , which allows for period-tripling but prevents period-doubling. There is only one choice for placing the boundaries of the unit cell, with one boundary at a trough and the other boundary at a peak of the wrinkles (Figure 7.10a). Again, we apply symmetry condition and uniform strain to the two boundaries. The period-tripled state can lead to two modes (Figure 7.8c and d), which are selected through the initially prescribed small amplitude imperfections, as shown in Figure 7.10b and c. In one mode of period tripling, of the three neighboring troughs, one becomes deeper and the other two become shallower (Figure 7.8c and 7.10b). In the other mode of period tripling, of the neighboring troughs, one becomes shallower and the other two become deeper (Figure 7.8d and 7.10c). We call the energy per wavelength  $l_w$  of both modes  $U_3$ . Figure 7.10d plots the difference in the energies between the two tripling modes and the doubling mode,  $U_3-U_2$ , as a function of the film strain for a pre-stretch of  $\lambda_0 = 0.7$ . We

normalize the energies by  $\mu_s l_w h_f$ , where  $h_f$  is the thickness of the film. The mode in Figure 7.10b has a lower energy than the mode in Figure 7.10c, and thus for the remainder of the chapter, we only consider the former, lower energy, mode of period tripling. Remarkably, this low-energy tripling mode has a lower energy than the period-doubling mode at sufficiently large film strains—a point to which we will return below.

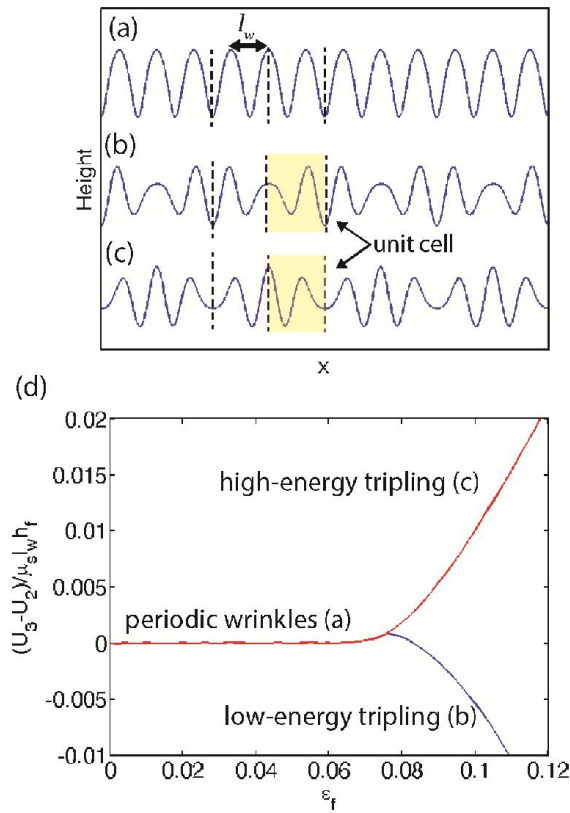


Figure 7.10 Simulating bifurcation from a periodic wrinkled state to a period-tripled state. (a) The wrinkled state with period  $l_w$ . The finite element simulation uses a unit cell of width  $3l_w/2$ , with one boundary at a trough and the other boundary at a peak. This unit cell leads to two modes of period tripling. (b) In one mode, of the three neighboring troughs, one becomes deeper and the other two become shallower. (c) In the other mode, one becomes shallower and the other two become deeper. The simulations start with a nearly flat surface with prescribed imperfections shown in (b) and (c), where the amplitude has been greatly magnified. (d) The difference in the energies of the tripling and doubling modes,  $U_3 - U_2$ , as a function of the film strain. The pre-stretch is  $\lambda_0 = 0.7$ . The mode in (b) has a lower energy than the mode in (c). Furthermore, the mode in (b) has a lower energy than the period-doubled state beyond a critical film strain, but the mode in (c) always has a higher energy than the period-doubled state.

To study the bifurcation to a period quadrupled state (Figure 7.8e), we use a unit cell of width  $2l_w$ , which allows both period doubling and quadrupling. Similar to period doubling, we can choose the boundaries of the unit cell in two ways: at two troughs (Figure 7.11b) or at two peaks (Figure 7.11c). Moreover, similar to period tripling, there can be more than one mode of the period-quadrupled states even when the boundary of the unit cell is chosen. Here, we will not go into details regarding these different modes, but instead focus on the mode of quadrupling corresponding to that observed in experiments (Figure 7.8e), which is selected by the prescribed imperfections shown in Figure 7.11b. In this case the system first undergoes period doubling, followed by period quadrupling, and we denote the energy per wavelength  $l_w$  as  $U_4$ .

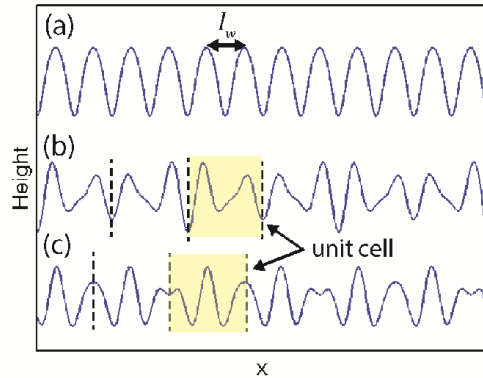


Figure 7.11 Simulating bifurcation from a periodic wrinkled state to a period-quadrupled state. (a) The wrinkled state with period  $l_w$ . (b) The finite element simulation uses a unit cell of width  $2l_w$ , with boundaries at two troughs of the wrinkles. With the initial prescribed imperfections shown in (b), magnified in amplitude for clarity, the system undergoes period quadrupling at a critical strain after period doubling. (c) If the boundaries are chosen at the peaks of the wrinkles, period quadrupling cannot happen.

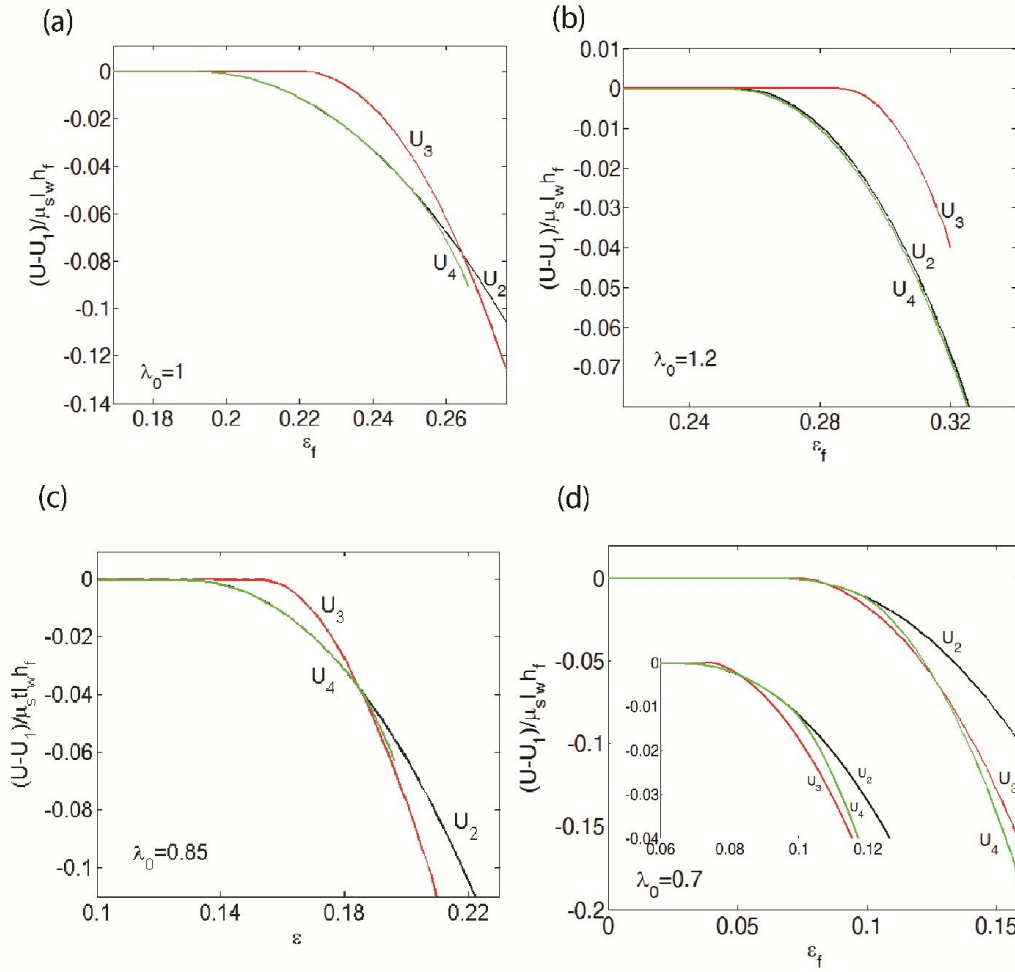


Figure 7.12 The normalized energy of the period-doubled state  $U_2$ , tripled state  $U_3$ , and quadrupled state  $U_4$  relative to the energy of the periodic wrinkled state  $U_1$ . The pre-stretch in the substrate is (a)  $\lambda_0 = 1.0$ , (b)  $\lambda_0 = 1.2$ , (c)  $\lambda_0 = 0.85$  and (d)  $\lambda_0 = 0.7$ . The inset in (d) shows a magnification of the region of  $\varepsilon_f = 0.06 - 0.13$ .

In Figure 7.12a-d, we plot the normalized energy by which each of the configurations  $U_2$ ,  $U_3$ ,  $U_4$  differ from the wrinkled state  $U_1$ , as a function of the applied strain  $\varepsilon_f$ . When a given curve falls below 0, the corresponding type of period multiplication is energetically favorable, with the lowest energy curve representing the ground state. As seen in Figure 7.12a for no pre-stretch, the system remains in the wrinkled state and thus all of the curves stay at an energy of 0, until a strain of  $\varepsilon_f = 0.19$ . Beyond this point, the curves for  $U_2$  and  $U_4$  become negative, corresponding to the period-doubled state. At a strain of  $\varepsilon_f = 0.25$ , the

curve for  $U_4$  becomes lower in energy than  $U_2$ , corresponding to the period-quadrupled state. Over this range of strain, the energy  $U_3$  remains above both  $U_2$  and  $U_4$ , and thus period tripling is energetically disfavored. These findings are in excellent agreement with our experiments at  $\lambda_0 = 1.0$ , as well as previous work, showing clean period doubling and period quadrupling bifurcations [95, 145, 147].

The pre-tensioned substrate stabilizes both the wrinkled and period-doubled states, as seen in Figure 7.12b for  $\lambda_0 = 1.2$ . Here, the onset of period doubling is delayed until  $\varepsilon_f = 0.25$ , while over the range of strain studied (up to  $\varepsilon_f = 0.32$ ) period quadrupling is not observed at all, and  $U_3$  remains well above  $U_2$ . The simulation results show excellent agreement with our experimental findings that period doubling is shifted to higher strains when there is pre-tension in the substrate and no period quadrupling is observed over the range of  $\varepsilon_f$  studied.

In contrast, the pre-compressed substrate de-stabilizes both the wrinkled and period-doubled states compared to the period-tripled and quadrupled states (Figure 7.12c and d). As seen in Figure 7.12c for  $\lambda_0 = 0.85$ , the curve for  $U_2$  falls below zero at a strain of 0.13, only slightly before  $U_3$  does, at 0.15. The period-tripled state  $U_3$  then falls below  $U_2$  and  $U_4$  at a strain of 0.18. As seen in Figure 7.12d for  $\lambda_0 = 0.7$ , the curves for  $U_2$  and  $U_3$  fall below zero at very similar strains ( $\varepsilon_f = 0.07 - 0.08$ ). The period-quadrupled state  $U_4$  falls below  $U_2$  at only slightly higher strain ( $\varepsilon_f = 0.10$ ), and remains very close to  $U_3$  for larger strains. Because period doubling, tripling and quadrupling all happen at strains close to the formation of wrinkles, wrinkles are still very shallow, and the energies of each of these subharmonic modes in the range of  $\varepsilon_f = 0.07 - 0.10$  are very close to each other. The inset of

Figure 7.12d magnifies the energies in this region of strain.

We further illustrate the effect of pre-stretch by plotting the difference between  $U_3$  and  $U_2$  for several values of  $\lambda_0$  (Figure 7.13). The pre-compressed substrate greatly reduces the energy difference between the period-tripled state and the period-doubled state. Presumably, this similarity in energy means that the presence of defects or even slight spatial variations in material properties would lead to local biases in favor of a given sub-harmonic mode, thus yielding a globally chaotic behavior. The prediction from the simulation is qualitatively in very good agreement with our experimental observations.

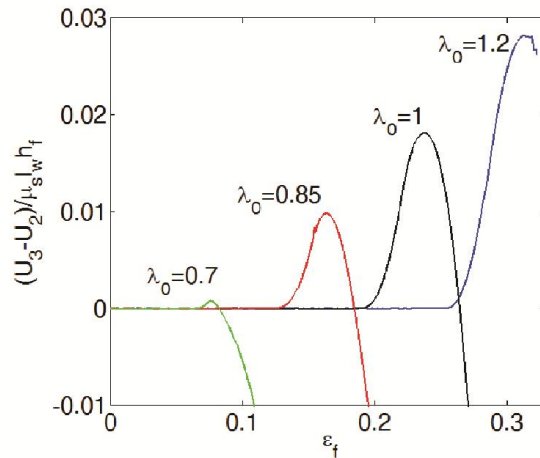


Figure 7.13 The difference in energy between the period-tripled state  $U_3$  and the period-doubled state  $U_2$  for different values of the substrate pre-stretch  $\lambda_0$ .

## 7.4 Summary

Our study reveals the strong effect of substrate pre-stretch on post-wrinkling bifurcations. Pre-stretch shifts the critical strain for period doubling: modest amounts of pre-tension are found to stabilize wrinkles to higher strains, while modest pre-compression promotes the emergence of sub-harmonic modes at lower strains. For large substrate

pre-compression, a new type of spatially chaotic behavior is found. A newly developed computational approach allows for the study of symmetry breaking from a periodic structure by the emergence of different sub-harmonic modes through the prescription of different simulation cell sizes, initial imperfections, and boundary conditions. The computational results reveal that energies of the different subharmonic modes become similar when the substrate is pre-compressed, thus eliminating the preference for a clean sequence of period doubling and quadrupling bifurcations. We anticipate that substrate pre-stretch will be an important parameter in future efforts to control the morphologies of wrinkled and post-wrinkled surfaces.

## **Chapter 8**

# **Ridge localizations and networks under equi-biaxial loading**

### **8.1 Introduction**

The intriguing buckling patterns exhibited by bilayer systems composed of a thin stiff film bonded to a thick elastomeric substrate have been studied extensively in recent years both experimentally and theoretically. Under compression, the film is constrained by the substrate and buckles with a wavelength that is usually large compared to the film thickness yet small compared to substrate thickness. The most common patterns observed are the sinusoidal wrinkle mode when compression in one direction is dominant [22], and the herringbone mode [82, 86] and the labyrinth mode [81, 82, 86] under states of equi-biaxial compression.

This chapter is part of the ongoing research effort in the soft materials community to produce and manipulate specific buckling patterns [99, 156]. Most of the previous work has focused on buckling patterns of bilayer systems under small compression. Recent work, however, has demonstrated that large compression of a bilayer system can engender other surface patterns such as period-doubling [145] and folding [74, 146], opening the way for the creation of a wider array of surface patterns. These post-wrinkling modes involve the large strain behavior of the substrate and geometrical nonlinearity of the films in an essential way.

The focus of this chapter is on the post-wrinkling modes discovered most recently,

the ridge localization mode. While folds and creases protrude into the substrate, the ridge is a large amplitude localization that pushes out from the substrate. This mode should be characterized as localization because the large amplitude of the ridge is fed by flattening the nearby wrinkle undulations resulting in ridges that are separated from each other by expanses of relatively flat film. Thus, a distinct feature of the transition from wrinkles to ridges is the abrupt increase of spacing from crest to crest. The ridge localization was predicted to occur [75], and has been observed experimentally [99, 148, 155, 156], only when a relatively large pre-stretch is imposed on the elastomeric substrate prior to film attachment. Controlled incremental release of the pre-stretch of the thick substrate then imposes compression on the film which drives buckling. The large substrate pre-stretch favors the formation of the ridge mode [75]. The buckling pattern reported in this chapter consists of localized ridge lines separated by relatively flat patches of film. Exploitation of high pre-stretch produces these new high aspect convex structures which have potential for expanding the range of surface morphologies for applications such as smart adhesion [32], hydrophobic surfaces [15, 34, 35], and templates for micro-patterning [225].

This chapter features a method for applying equi-biaxial pre-stretch and release and thereby complements recent related work on ridge formation which has primarily been limited to uniaxial or plane strain pre-stretch [75, 99, 148, 155]. The present chapter also highlights the underlying characteristics and nature of ridges, including emergence and evolution aspects, which are still unclear due to the highly non-linear behavior of the system caused by high pre-stretch. For the system and approach employed here delamination [99, 226, 227] and cracking [90] of the thin film, which often accompany wrinkling instabilities,

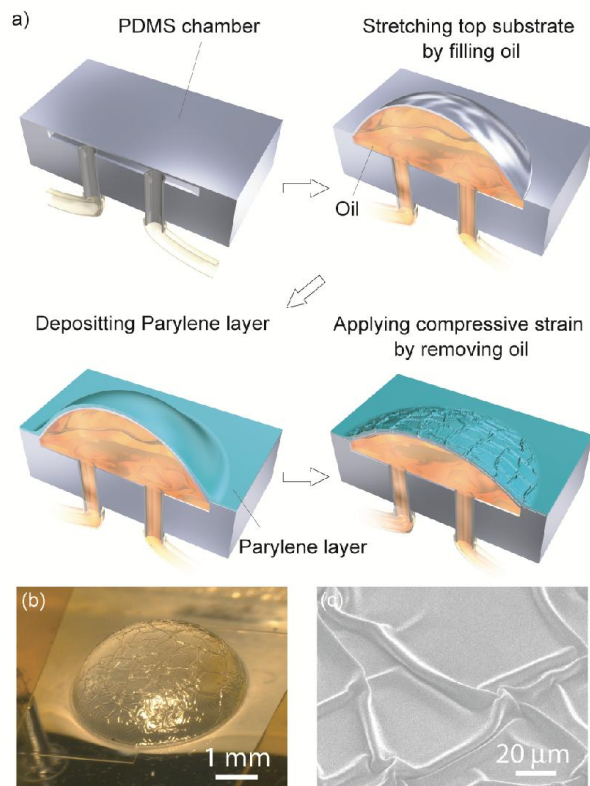
have been avoided.

The transition to the ridge buckling morphology is studied in a bilayer system comprised of a thin stiff film attached to a relatively thick compliant substrate. The substrate is subject to a large equi-biaxial pre-stretch prior to film attachment and then the bilayer is incrementally unloaded producing equi-biaxial compression in the film. The experiments are carried out using a specially designed micro-fluidic loading system. The system enables equi-biaxial pre-stretch and incremental compression simply by changing pressure inside the micro-fluidic chamber as used in [228], while more conventional loading systems [86, 156] require well-synchronized control of mechanical stretchers. Because mechanical stretchers are not employed, our method can simultaneously handle several systems at the scale of 1cm within the film deposition cavity, whose space is often limited. Using this system, we clearly captured transitions from wrinkles to localized ridges and formation of a ridge network surrounding flattened regions. In particular, the experiments reveal the evolution of the ridge structure which involves propagation of individual ridges to form a network. The influence on the geometry of the ridge is explored by varying the pre-stretch and the thickness of the thin film. Further, finite element simulations have been carried out to obtain conditions for localized ridge formation and propagation. Unlike sinusoidal or herringbone wrinkles, the ridge is a finite amplitude mode, and the wrinkle to ridge transition is subcritical as described more fully in conjunction with the simulations. As the pre-stretch is released, once a ridge forms, it grows and saturates to a height comparable to its width.

## **8.2 Experimental results**

Figure 8.1a illustrates the method of preparing the highly pre-stretched substrate. A chamber capped by a flat layer of the elastomeric substrate material, Polydimethylsiloxane (PDMS), is formed. The substrate layer is then stretched by filling the chamber with oil. With the pressure inside the chamber held constant, an organic polymer material, Parylene-C, is deposited on the surface to form the film. Prior to deformation the PDMS substrate layer has a thickness in the range,  $h_s = 50 \mu\text{m}$  to  $300 \mu\text{m}$  and a shear modulus,  $\mu_s \sim 0.33 \text{ MPa}$ . The Parylene film (thickness  $h_f$  from  $85 \text{ nm}$  to  $1.3 \mu\text{m}$  thick, shear modulus  $\mu_f \sim 0.58 \text{ GPa}$ ) is stress-free as deposited. The stress-strain curves of PDMS and Parylene are given in Appendix Figure C.1, and the detail of the fabrication is available in Appendix C.1. The equi-biaxial pre-stretch  $\lambda_0$  attained in the central region of the substrate is defined as the ratio of the length after stretch  $L$  to the original length  $L_0$ ,  $\lambda_0 = L/L_0$ . An equi-biaxial compressive strain,  $\varepsilon$ , is exerted on the film in the central region when oil is released incrementally from the chamber. The compressive strain is defined as  $\varepsilon = 1 - l/L$  where the current length is  $l$ .

Compared methods such as thermal expansion [81] and swelling [82, 83, 229, 230] for inducing equi-biaxial strain, the present method can induce pre-stretch greater than 1.5 and the magnitude of the pre-stretch can be readily adjusted by controlling the pressure inside the chamber. The thickness of the substrate is selected to be at least 50 times that of the film, and the film is about 2000 times stiffer than the substrate. The radius of the chamber is 2 mm, and the effect on the instability due to the curvature of the chamber is considered to be negligible (discussed in Appendix C.1).



Figures 8.1 (a) Schematic illustration showing the preparation of the highly pre-stretched bilayer system using micro-fluidics. (b) Image of the experimental setup: Compressive strain is applied by reducing the oil inside the chamber and a ridge structure emerges on the surface. (c) SEM image of the ridge structure: the localized convex structure is observed concomitantly with a flattening of the neighboring film surface.

Figures 8.1b and c show the typical morphology of the surface with ridges. Figure 8.1b shows an overview of an experimental setup taken by a microscope at point in the release process where ridges have formed with the chamber still substantially inflated. Figure 8.1c shows an image of Scanning Electron Microscopy of a surface of another sample. This figure reveals localized ridges separated by extensive unbuckled regions. Unlike a typical wrinkle or herringbone buckling pattern [82, 86] which fills the entire surface of the film, a ridge is localized with extensive regions on both sides of the ridge being almost flat. Furthermore, unlike creases and folds [74, 146] which protrude into the substrate, ridges push upward from the substrate. These and other aspects of the ridge mode will be discussed

in further detail later in the chapter.

The scale of the ridges depends on the film thickness  $h_f$ . In Figure 8.1b, with  $h_f \sim 1 \mu\text{m}$ , the width of the ridges is  $\sim 50 \mu\text{m}$ , while in Figure 8.1c, with  $h_f \sim 100 \text{ nm}$ , the width of the ridges is  $\sim 5 \mu\text{m}$ . In neither of these cases has the Parylene thin film delaminated from the PDMS substrate (a cross-sectional view is available in Appendix Figure C.2). The pre-stretch and compressive strain in the central region are estimated by measuring the height of the chamber at each stage of inflation or deflation, and the non-uniformity of the pre-stretch of the system is considered to be negligible; see Appendix Figure C.3 for more details.

An overview description of one experiment is now presented. As the equi-biaxial compression in the film is increased by slowly releasing oil from chamber, wrinkles first form and then, with further compression, wrinkles give way to ridges as seen in Figure 8.2. In this experiment,  $h_f = 100 \text{ nm}$ ,  $h_s = 50 \mu\text{m}$  and the substrate has been pre-stretched to  $\lambda_0 = 1.59$ . For this system, dimpled wrinkles, reflecting the equi-biaxial compressive stress experienced by the film, cover the surface at  $\varepsilon \cong 0.05$  (Figures 8.2a and b). As the compressive strain experienced by the film is further increased the dimples become more like wrinkles (Figures 8.2c) and then, by  $\varepsilon = 0.066$ , the transition to ridge-like features is evident (Figures 8.2d and e). At  $\varepsilon = 0.066$ , ridges are observed to advance flattening neighboring regions under conditions when no oil is released from the chamber such that the overall compression in the system is nominally fixed (Figure 8.2f). As will be shown later, the critical compressive strain for ridge formation is only slightly above that for the wrinkle pattern, and in the present study it has not been possible to experimentally resolve the

difference between the two critical strains.

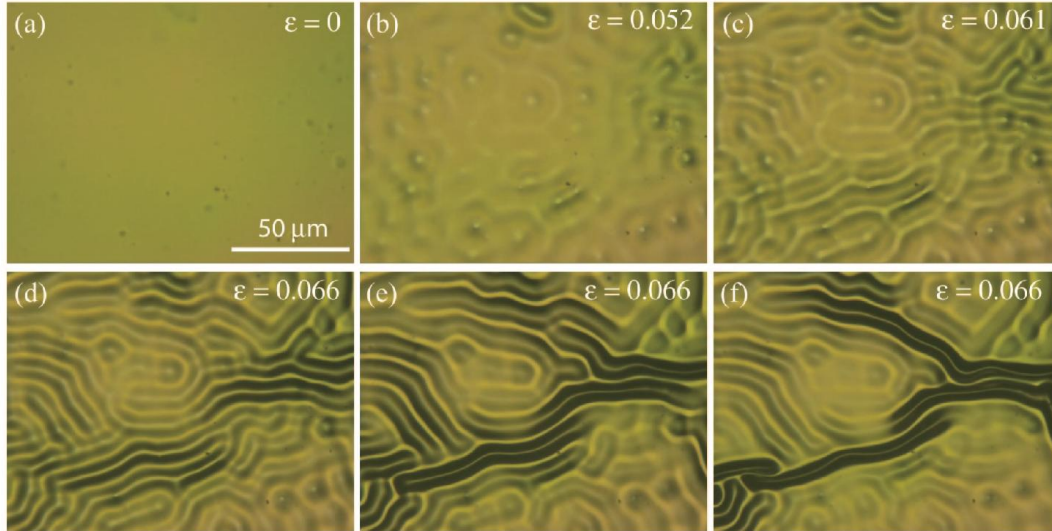


Figure 8.2 Wrinkle to ridge transition. (a) In its initial state the surface of the chamber is flat. (b) With compressive strain, the dimpled wrinkle pattern is engendered on the surface. (c) With increase of the compressive strain, the dimpled wrinkle pattern transforms into the wrinkle pattern. (d) With further compression, some peaks of the wrinkles increase their height and ridges are nucleated. (e, f) Under essentially the same applied compression, ridges can propagate and flatten neighboring surfaces.

Further experimental details on the development and evolution of a ridge network are presented in Figure 8.3. For this experiment, the substrate is pre-stretched to a larger value,  $\lambda_0 = 1.85$ , enhancing ridge formation and the ensuing ridge network. In this case,  $h_f = 85 \text{ nm}$  and  $h_s = 50 \mu\text{m}$ . As shown in Figure 8.3a, unconnected ridges are first formed with wrinkles appearing perpendicular to the ridges. With the increase of compression, new ridges nucleate and propagate perpendicularly to existing ones until they become blocked by a pre-existing ridge (Figure 8.3b and c). A network of ridges is created; the few wrinkles still present illustrate clearly the distinction between wrinkles and ridges. With the further increase of compression, the network grows denser (Figure 8.3d and e) until there is no space for new ridges to be nucleated and the network saturates (Figure 8.3f). The evolution seen here for the ridge pattern is similar to the evolution of folds in a compressive bilayer

without pre-stretch reported in [146].

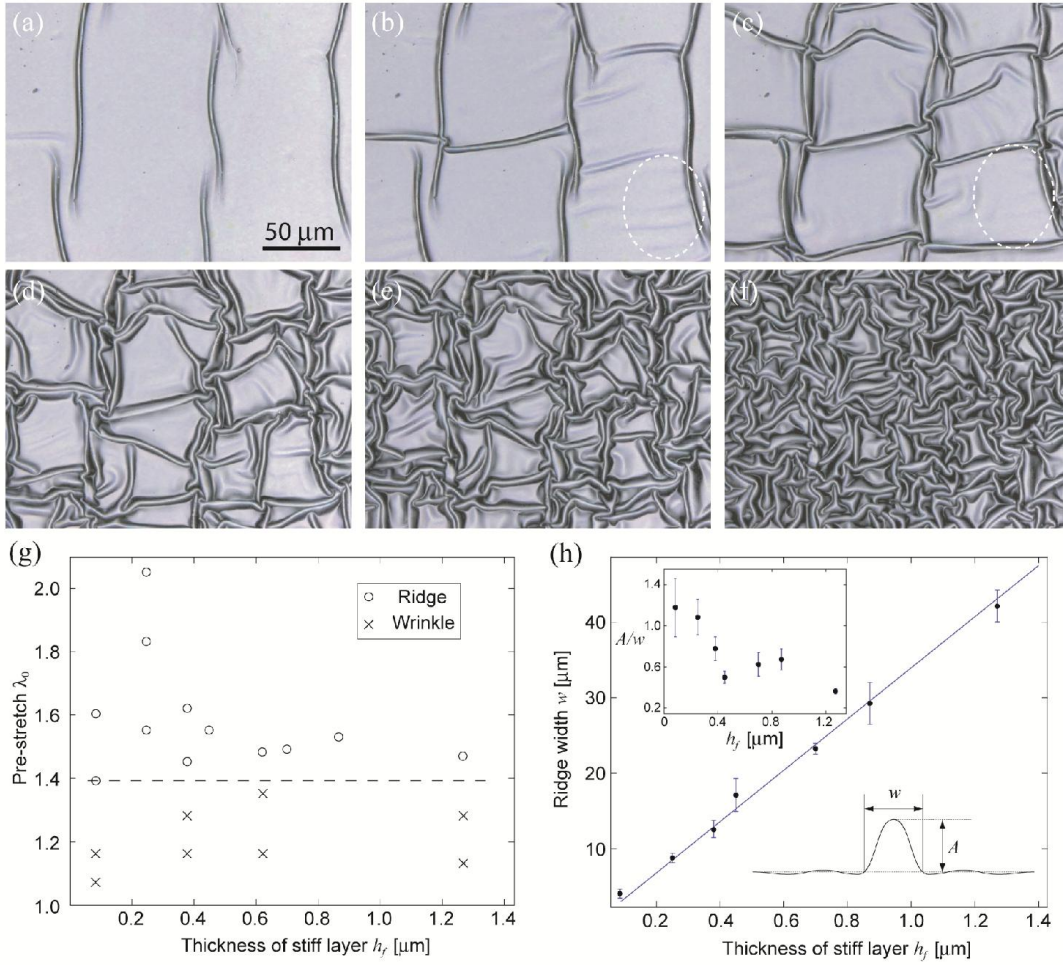


Figure 8.3 The formation of the ridge network: (a) In compression, unconnected ridges first appear. (b-c) With the further increase of the compression, new ridges nucleate perpendicular to the existing ridges. As marked with the dashed circles, wrinkled regions emerge before ridge nucleation and become flattened after the formation of the ridge. (d-e) With even further increase of the compression, the network grows denser, and (f) finally is completely packed. (g) Phase diagram of wrinkle/ridge mode. Ridge structure appears with the pre-stretch  $\lambda_0 > 1.4$ . (h) Relationship between stiff film thickness and width of the ridge. Fitting curve is  $w = 34h_f$ . Relationship between height/width ratio

$A/w$  of a ridge and stiff film thickness  $h_f$  is embedded.

The dependence of the geometry of the ridge and the threshold pre-stretch  $\lambda_c$  required for the formation of a ridge has been measured by systems with seven different

thicknesses of the Parylene film ranging from  $h_f = 85 \text{ nm}$  (with  $h_s = 50 \text{ }\mu\text{m}$ ) to  $h_f = 1.3 \text{ }\mu\text{m}$  (with  $h_s = 300 \text{ }\mu\text{m}$ ). For a given pre-stretch,  $\lambda_0$ , the compressive strain  $\varepsilon$  is increased by release of the pre-stretch and the surface of the bilayer is carefully examined to see the buckling patterns that emerge and, in particular, whether ridges form. The phase diagram of wrinkle/ridge is plotted in Figure 8.3g. The threshold pre-stretch is approximately  $\lambda_c = 1.4$  for ridge formation—that is, for smaller pre-stretches ridges are not observed and for larger pre-stretches they are observed. The threshold appears to be independent of the thickness of the stiff film, consistent with what is expected on dimensional grounds for thick substrates. For cases in which ridges are formed, the width  $w$  and the height  $A$  of the ridges (as defined in the inset of Figure 8.3h) are also measured and plotted in Figure 8.3h. The measurements presented in the Figure 8.3h have been taken for cases in Figure 8.3g in which the pre-stretch  $\lambda_0$  is between 1.4 and 1.6. The width  $w$  is proportional to the film thickness  $h_f$ , and for the stiffness ratio of the present film/substrate system the experimental results are fitted by  $w = 34 h_f$ . If one imagines a ridge to be the localization of a single wrinkle, one would expect the ridge width  $w$  to be the same order as the wavelength of the wrinkle  $l_w$ . In [75], the wavelength of a wrinkled linear elastic film on a neo-Hookean substrate subject to an equi-biaxial pre-stretch  $\lambda_0$  is  $l_w = 2\pi h_f \left( 2\mu_f \lambda_0 / \left( 3\mu_s (1 + \lambda_0^3) \right) \right)^{1/3}$ . With  $\mu_f / \mu_s = 1750$  and  $\lambda_0 = 1.5$ , one finds  $l_w = 46 h_f$ , which is on the same order as the experimentally measured wavelength in Figure 8.3h. In all of these cases, the ratio of the ridge height  $A$  to its width  $w$ ,  $A/w$  (inset of Figure 8.3h) is significantly larger than the amplitude/wavelength ratio of the conventional wrinkle at these compressive strains, i.e.,  $\sim 0.1$ .

### 8.3 Finite element simulations

Numerical simulations employing the commercial finite element software, ABAQUS, have been carried out to study and quantify the conditions for ridge formation. These simulations go well beyond the initial plane strain studies [75], where ridges were first discovered theoretically. In addition to systematically exploring the effect of equi-biaxial pre-stretch on ridge formation, we have investigated the mechanics by which the ridges propagate. Simulation details can be found in Appendix C.1, and details on the mechanics of ridge formation and propagation can be found in Chapter 9.

To break the translational symmetry of the flat surface and initiate wrinkles, a very small initial imperfection in the form of a slight surface waviness is introduced. The formation of wrinkles and ridges is simulated under a generalized plane strain condition in the 1-2 plane (as defined in Figure 8.4a) with an equi-biaxial pre-stretch  $\lambda_0$  in the substrate and the subsequent equi-biaxial compressive strain  $\varepsilon$  applied to both film and substrate. In keeping with generalized plane strain, the overall strains in the 1-3 directions are equi-biaxial, but the displacements caused by the wrinkles or by ridges relative to the equi-biaxial flat state are subject to the constraint of plane strain. The plane strain constraint limits wrinkling and ridging to one-dimensional entities—the dimple mode seen in Figure 8.2 and the 2D ridge pattern in Figure 8.3 are excluded. Nevertheless, the essence of ridge formation is captured within the constraint adopted. Both film and substrate are modeled as incompressible neo-Hookean materials. Ridges grow at the expense of neighboring wrinkles and, therefore, to simulate ridge localization the width of the computational model must be at least several times the wrinkle wavelength. In the present simulation, this width is

$L \cong 10l_w$ . By making use of symmetry, only half of this length is simulated, and as shown in

Figure 8.4a, the symmetric condition is set at the left boundary.

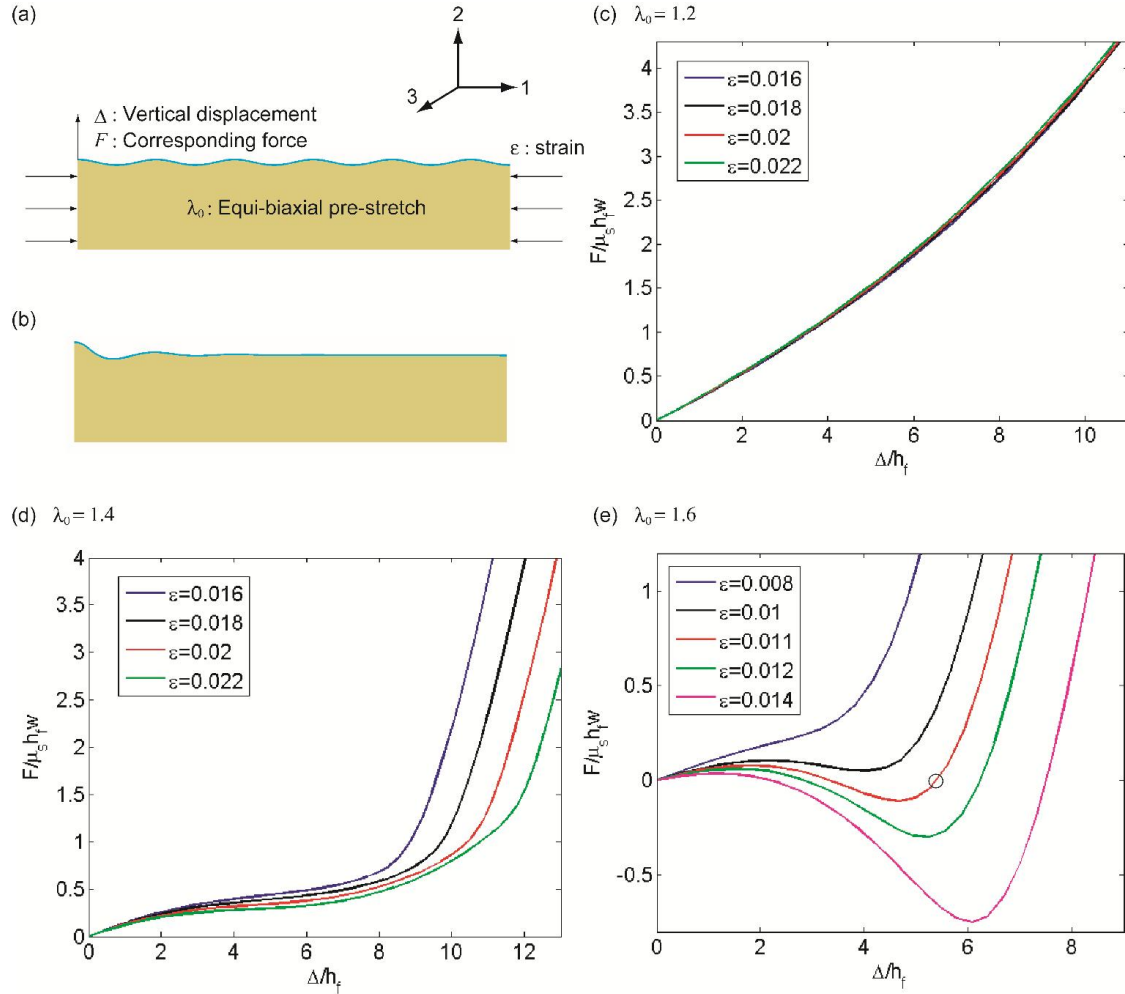


Figure 8.4 Finite element simulation results. (a) is a simulation result showing wrinkles under equi-biaxial strain  $\varepsilon = 0.011$  and pre-stretch  $\lambda_0 = 1.6$  in the substrate. (b) is a simulation result showing the large amplitude ridge state under the same loading condition as (a). In (a) and (b), the blue color shows the thin film and the yellow brown color shows the substrate. The  $F - \Delta$  curves are obtained for various fixed strains for equi-biaxial pre-stretch (c)  $\lambda_0 = 1.2$ , (d)  $\lambda_0 = 1.4$ , and (e)  $\lambda_0 = 1.6$  with  $\mu_f / \mu_s = 2000$  and  $(h_f + h_s) / h_f = 50$ .

When  $\varepsilon$  reaches a critical strain denoted by  $\varepsilon_w$ , wrinkles start to form in the 1-direction with wavelength  $l_w$ . The computed values of  $\varepsilon_w$  and  $l_w$  are in close agreement with predictions of the classical bifurcation results for wrinkling [75]. As the applied

compression is further increased, the wrinkle amplitudes increase but the nominal wrinkle wavelength does not change.

We have found that the wrinkle to ridge transition is unstable (subcritical in the language of bifurcation theory) such that a wrinkle snaps dynamically to a ridge with a much larger amplitude. Conventional quasi-static simulations fail for such phenomena and special numerical techniques are required, such as the arc-length method [173, 189] or dynamic simulations. We have developed the following quasi-static technique to probe for the existence of a ridge and found it to be systematic and reliable. As depicted in Figure 8.4a, under the fixed overall strain  $\varepsilon$ , an additional vertical displacement  $\Delta$  is imposed on the peak of the wrinkle at the left boundary. The associated reaction force  $F(\Delta)$  is computed. The system remains stable when the additional vertical displacement  $\Delta$  is prescribed, and this allows large displacement equilibrium states to be discovered wherever  $F = 0$ . If a state with  $F = 0$  is found when  $\Delta$  is non-zero, then that state can exist (without an external force) at the strain  $\varepsilon$  although it may be stable or unstable. An example of this state is shown in Figure 8.4b. The ridge seen in Figure 8.4b (at  $F = 0$ ) is clearly a localized mode in sense that the amplitudes of the wrinkles neighboring it have diminished significantly.

Figures 8.4c-e show the  $F - \Delta$  relation under different fixed strains  $\varepsilon$  for three pre-stretches,  $\lambda_0 = 1.2, 1.4$ , and  $1.6$ , in the substrate. The shear modulus ratio of the film to the substrate  $\mu_f / \mu_s$  has been taken to be 2000, slightly larger than that of the experimental system for simplicity, and the thickness ratio of the bilayer to the film is set to be 50 so that the substrate can be considered much thicker than the film. When  $\lambda_0 = 1.2$ , the critical condition for wrinkle initiation is approximately  $\varepsilon_w \cong 0.0022$ . As shown in Figure

8.4c, when the strain  $\varepsilon$  is fixed at 0.016,  $F$  sharply increases with  $\Delta$  and  $F$  does not become zero. In fact, for all of the fixed strains  $\varepsilon$ , from 0.016 to 0.022, the  $F-\Delta$  curves almost overlap. The behavior for a larger pre-stretch,  $\lambda_0 = 1.6$ , is dramatically different. For small applied compression,  $\varepsilon = 0.008$ ,  $F$  increases monotonically with  $\Delta$  (Figure 8.4e). However, for larger  $\varepsilon$ , the  $F-\Delta$  curves become non-monotonic:  $F$  increases, decreases and then increases again with  $\Delta$ . Above a critical value of  $\varepsilon$ , the  $F-\Delta$  curve intersects the  $\Delta$ -axis at three points: the origin, which represents the wrinkle state; the middle point, which represents an unstable medium amplitude ridge; and the point on the right, which represents a stable large amplitude ridge. This plot clearly shows the large amplitude nature of ridges. Figure 8.4a shows the simulation result of wrinkles for  $\varepsilon = 0.011$  when  $\lambda_0 = 1.6$ . Figure 8.4b shows the simulation result for the stable large amplitude ridge for the same strain and pre-stretch (as indicated by a circle in Figure 8.4e). The additional film length needed to form the ridge is obtained by flattening neighboring wrinkles, and it is this feature which gives rise to localization. At the intermediate pre-stretch,  $\lambda_0 = 1.4$ , the  $F-\Delta$  relation is strongly nonlinear. However, even at  $\varepsilon = 0.03$  (not shown in Figure 8.4d),  $F$  does not become zero at non-zero  $\Delta$ . To conclude, our simulations suggest that the threshold value of pre-stretch for ridges to form is slightly larger than  $\lambda_0 = 1.4$ . This is in general agreement with the experimental observations reported in Figure 8.3g.

Additional simulations have been performed to show the evolution of the ridges by a pseudo-dynamic simulation (Figure 8.5). Again, an initial imperfection consisting of a slight waviness is introduced to trigger the initiation of the wrinkles. The bilayer is loaded equi-biaxially with an equi-biaxial pre-stretch  $\lambda_0 = 1.6$  in the substrate. The modulus ratio

and thickness ratio are the same as Figure 8.4.

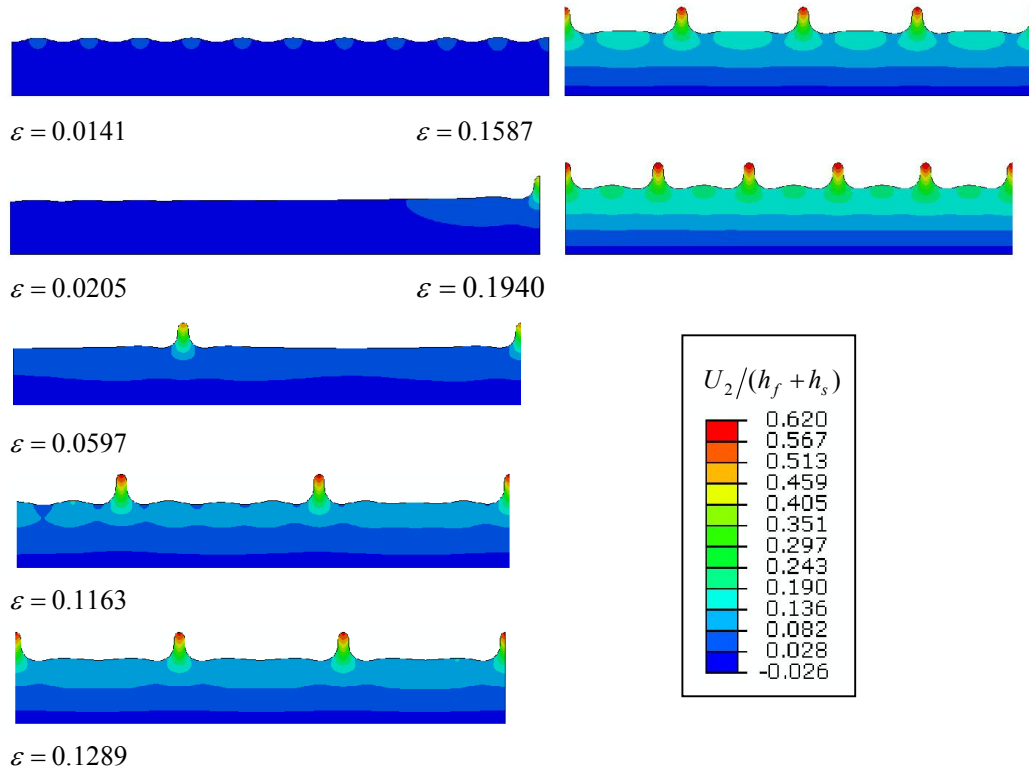


Figure 8.5 Evolution of the morphology of the film-substrate bilayer at different equi-biaxial strains  $\varepsilon$  revealing the progression to wrinkles and then to ridges. The color bar represents the normalized vertical displacement  $U_2/(h_f + h_s)$ . The parameters used in the simulation are as followings:

$$\lambda_0 = 1.6, \quad \mu_f / \mu_s = 2000, \quad \text{and} \quad (h_f + h_s) / h_f = 50.$$

With a gradual compression increase, well defined wrinkles first form. When the compression  $\varepsilon$  increases to about 0.0185, a ridge initiates and snaps to a state with finite amplitude. As noted earlier, the ridge forms at the expense of neighboring wrinkles. The ridge quickly grows to a saturated height when  $\varepsilon$  reaches around 0.0205. With the further increase of compression, more ridges form. However, the height of previously formed ridges changes relatively little with increasing compression consistent with the notion of a saturated height. For  $\varepsilon = 0.1163$ , the ratio of the height of the ridges to the film thickness predicted for

this system is around  $A/h_f = 24$ , and the ratio of the width of the ridges to the nominal film thickness is around  $w/h_f = 29$ , such that  $A/w = 0.83$ . These characteristic length scales of the ridges and the evolution of their behavior predicted by simulations are in reasonable general agreement with the experiments. The experimental measured width to film thickness ratio in Figure 8.3h is about 15% higher than the prediction. While the theoretical height to thickness ratio is within the range of the experimental results in Figure 8.3h, the experimental measurements display considerably more variation. In part, this can be explained by the fact that there is some dependence of the ridge amplitude on the applied strain after it is formed. In addition, there may be some influence of the finite thickness of the substrate on  $A/w$ , which is not accounted for in the numerical simulations, because the height of the ridge is comparable to the substrate thickness in the experiment. The main discrepancy between simulation and experiment is the critical strain for the initiation of wrinkles and ridges—simulations predict somewhat lower critical strains than those measured experimentally. In previous work [231], residual stress in Parylene film has been noted. For the present system, the residual tensile strain in the Parylene film on PDMS substrate has been measured as  $\sim 1\%$  (Appendix Figure C.4). The applied compression  $\varepsilon$  has to overcome any residual tensile strain in the film, and it is believed that this accounts for the discrepancy mentioned above.

## 8.4 Summary

To summarize, the evolution of the buckling patterns of bilayer film-substrate systems has been studied for systems having a large equi-biaxial pre-stretch in the substrate.

A micro-fluidics chamber has been designed for carrying out the experiments. The pre-stretch in the substrate is tuned by varying the volume of the oil in the PDMS chamber, and the compressive strain is applied to the bilayer system by diminishing the volume of oil. Transitions from wrinkles to ridges and the formation and evolution of ridge networks are clearly captured. Ridges are a highly localized deformation mode resulting in flattening of the film in its vicinity. Details of ridge formation and geometry have been studied by varying the pre-stretch and the thickness of the thin film. Finite element simulations have been carried out to reveal the highly nonlinear character of ridges and to quantify conditions for their formation. The wrinkle to ridge transition is unstable, or subcritical, and the ridge amplitudes are much larger than those of the wrinkles. The simulations qualitatively capture the experimental results in all respects and reproduce most aspects quantitatively with reasonable success. The ability of the present system to attain high pre-stretch enriches the scope for exploring surface instability patterns of bilayer systems. The ridge mode has higher aspect ratios than the wrinkle mode and a ridge network consists of isolated patches of flat surface surrounded by ridges. It is hoped that our method will open a new way to create and improve the properties of functional surfaces, such as hydrophobicity, adhesion and micro-patterning.

## Chapter 9

# Mechanics of ridge formation and propagation

### 9.1 Introduction

When a stiff thin film supported by a compliant thick substrate is compressed to a critical strain, the flat surface loses stability and forms periodic wrinkles [81, 96]. Instead of considering wrinkles as a failure mode and suppress them, people have creatively developed various applications of wrinkles, such as fabricating stretchable electronics [13], measuring mechanical properties [22], assembling particles [27, 28], changing optical properties [37, 40], and tuning surface adhesion and wettability [31, 32, 34, 35]. The reversibility of elastic deformations is widely appreciated, so that in all those applications people can repeatedly cycle between the flat and the wrinkle states. People also studied different morphology of wrinkles, such as sinusoidal, herringbone, checkerboard and hexagonal modes [81, 82, 85], under different loading conditions, such as uniaxial and biaxial compression [83], and try to control the deterministic order of wrinkles [84, 86].

After the formation of wrinkles, if the compressive strain is further increased sufficiently, new bifurcation modes can happen: wrinkles double their periodicity and finally form localized folds [74, 95, 145-147, 151]. It turns out that post-wrinkling bifurcations highly depend on the stress state of the substrate [232]. If the substrate is subject to a tensile pre-stretch, wrinkles are stabilized and the period doubles at a lower strain [158, 232]. Therefore, wrinkles can grow to a high aspect ratio [158]. If the substrate is subject to a mild

pre-compression, wrinkles are destabilized and the period doubles at a lower strain [232]. If the substrate is subject to a large pre-compression of around 0.3 strain, the wrinkle period multiplies chaotically [232].

It is further found that if the substrate is subject to a sufficiently large pre-tension, a different mode of post-wrinkling bifurcation, localized ridge mode, happens [75, 99, 155-157]. One in every several wrinkles grows to large amplitude to form ridges, and leave the neighboring wrinkles flattened. Although both folds and ridges are localized, their morphologies look very different. Folds grow inwards and fold up the surface, while ridges grow outwards and lift up the surface. The various post-wrinkling behaviors can be explained by the highly nonlinear elasticity of the substrate [155]. A pre-tension of the substrate favors the occurrence of outward deflections of the surface, while a pre-compression favors inward deflections [155]. Ridge instability was first found and predicted by a numerical simulation [75], and then was observed in experiments [99, 155-157]. Large aspect ratio of the ridge instability facilitates its applications in reversible wettability tuning and cells alignment [156].

Another localized surface instability that has been widely studied is crease [73, 106]. When a homogeneous soft material is compressed to a critical value, creases, instead of wrinkles, form on the surface [105, 112-114, 118]. A crease folds up the surface and forms self-contact with a sharp tip. While wrinkles have infinitesimal strain deviating from the flat state, creases have finite strain deviating from the flat state [73, 106]. Creases are supercritical (stable bifurcation) if they form under purely elasticity and the bottom of the material is kept flat [107]. However, creases become subcritical (unstable bifurcation), if

surface energy is large enough [138] or the bottom of the material has a stress-free boundary [139]. Moreover, a bilayer with same modulus of the film and substrate but substrate pre-compressed can also form subcritical creases [173]. Subcritical creases can propagate perpendicular to the loading direction, or called channel, under a fixed strain [138, 173].

It has been shown that the wrinkle to ridge transition is also subcritical—that is the transition is unstable and wrinkles dynamically snap to ridges [157]. However, the detailed mechanics of the formation and propagation of ridges has not been studied. In this chapter, we use the finite element method to study the formation, propagation, hysteresis and geometry of ridges. To simulate the unstable wrinkle to ridge transition, we develop two numerical ways: static force-displacement method and pseudo-dynamic loading-unloading method. We carefully analyze the distributions of strain and energy density of ridges and wrinkles in order to understand the deformation mechanism of ridges.

## 9.2 Formation and propagation of ridges

We study the formation and propagation of ridges in a film/substrate bilayer. In the undeformed state, the substrate (represented by green color) has a length  $L_0$ , and the film (represented by red color) has a length  $L$  (Figure 9.1a). The substrate is pre-stretched to length  $L$ , with the pre-stretch defined as  $\lambda_0 = L/L_0$ , and bonded together with the stress-free film (Figure 9.1b). In the bonded state, the thicknesses of the film and substrate are  $h_f$  and  $h_s$  respectively. Then the bilayer is compressed together to the current length  $l$ , with the strain defined as  $\varepsilon = (L-l)/L$  (Figure 9.1c). Both the film and substrate are

considered as incompressible neo-Hookean materials, with modulus  $\mu_f$  and  $\mu_s$  respectively (Figure 9.1a).

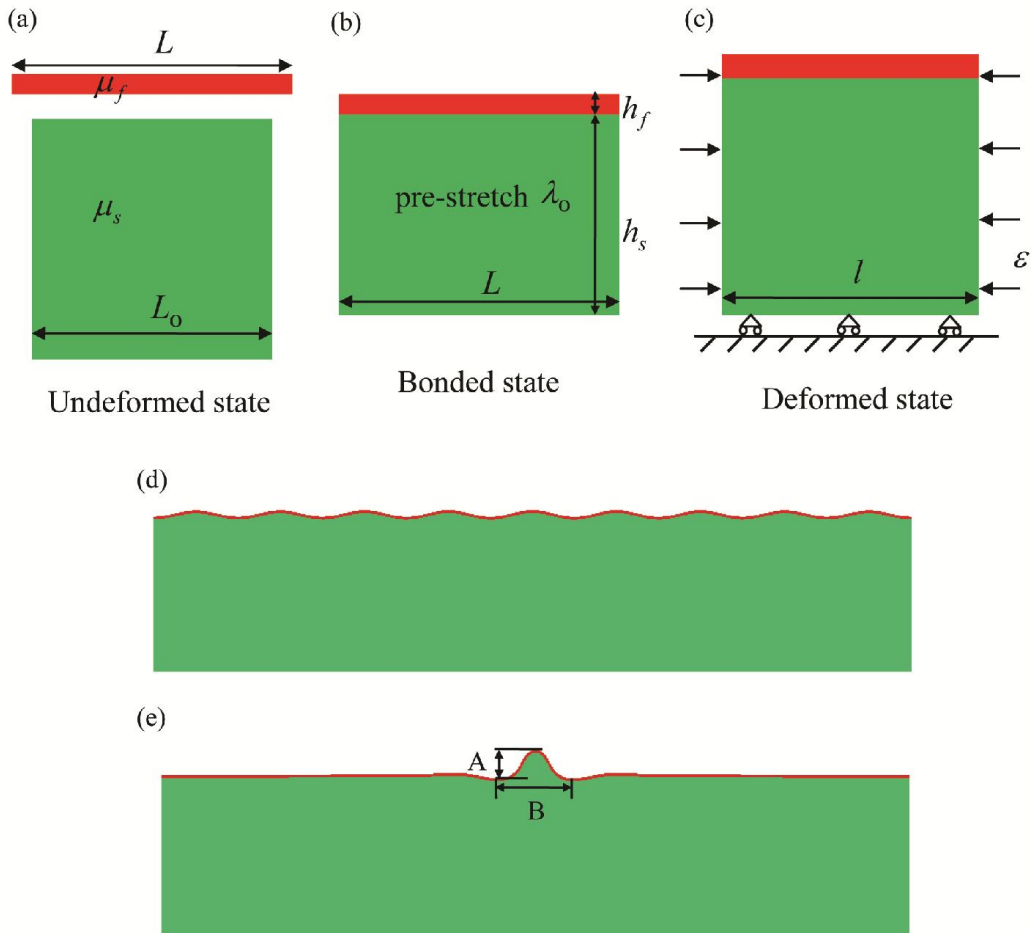


Figure 9.1 A film/substrate bilayer in different states. (a) In the undeformed state, the film has a length  $L_0$  and modulus  $\mu_f$ , while the substrate has a length  $L$  and modulus  $\mu_s$ . (b) In the bonded state, the substrate is pre-stretched to length  $L$ , with pre-stretch  $\lambda_0$ , and bonded with the stress-free film. (c) In the deformed state, both the film and substrate are compressed together to strain  $\epsilon$ . (d) A simulation result of wrinkles at the snapping backward strain  $\epsilon_b$ . (e) A simulation result of a localized ridge at the snapping forward strain  $\epsilon_f$ . The green color represents the substrate, while the red color represents the film.

When the compressive strain  $\epsilon$  is small, the surface is flat and both the film and substrate are subject to a homogeneous deformation. When  $\epsilon$  reaches a critical value  $\epsilon_w$ ,

wrinkles set in (Figure 9.1d). If  $\lambda_0$  is a sufficiently large tensile stretch, with the further increase of  $\varepsilon$ , ridges set in when  $\varepsilon$  is sufficiently large (Figure 9.1e). The wrinkle to ridge transition is an unstable transition, with wrinkles snapping into ridges. Special numerical techniques are usually needed to simulate those subcritical transitions, and here we develop two ways to simulate ridges.

### 9.2.1 Static force-displacement method

We use finite element software ABAQUS to simulate the formation and growth of ridges. Here we consider a plane strain pre-stretch and plane strain compression. We first carry out a linear perturbation analysis to identify the critical strain of wrinkle initiation  $\varepsilon_w$  and the critical wavelength  $l_w$ . We then simulate a static process of compression, with the critical wrinkle mode obtained by the linear perturbation times a very small amplitude factor (0.01 of the film thickness) introduced as the imperfection to break the translational symmetry of the sample. Wrinkles form when the sample is compressed to strain  $\varepsilon_w$ . With the further increase of the strain, the amplitude of wrinkles become larger, but the number of wrinkles does not change. Under the fixed strain  $\varepsilon > \varepsilon_w$ , an additional vertical displacement  $\Delta$  is added on a peak of wrinkles, and the reaction force  $F$  and the total elastic energy of the sample  $W$  are computed as a function of  $\Delta$  (Figure 9.2a).

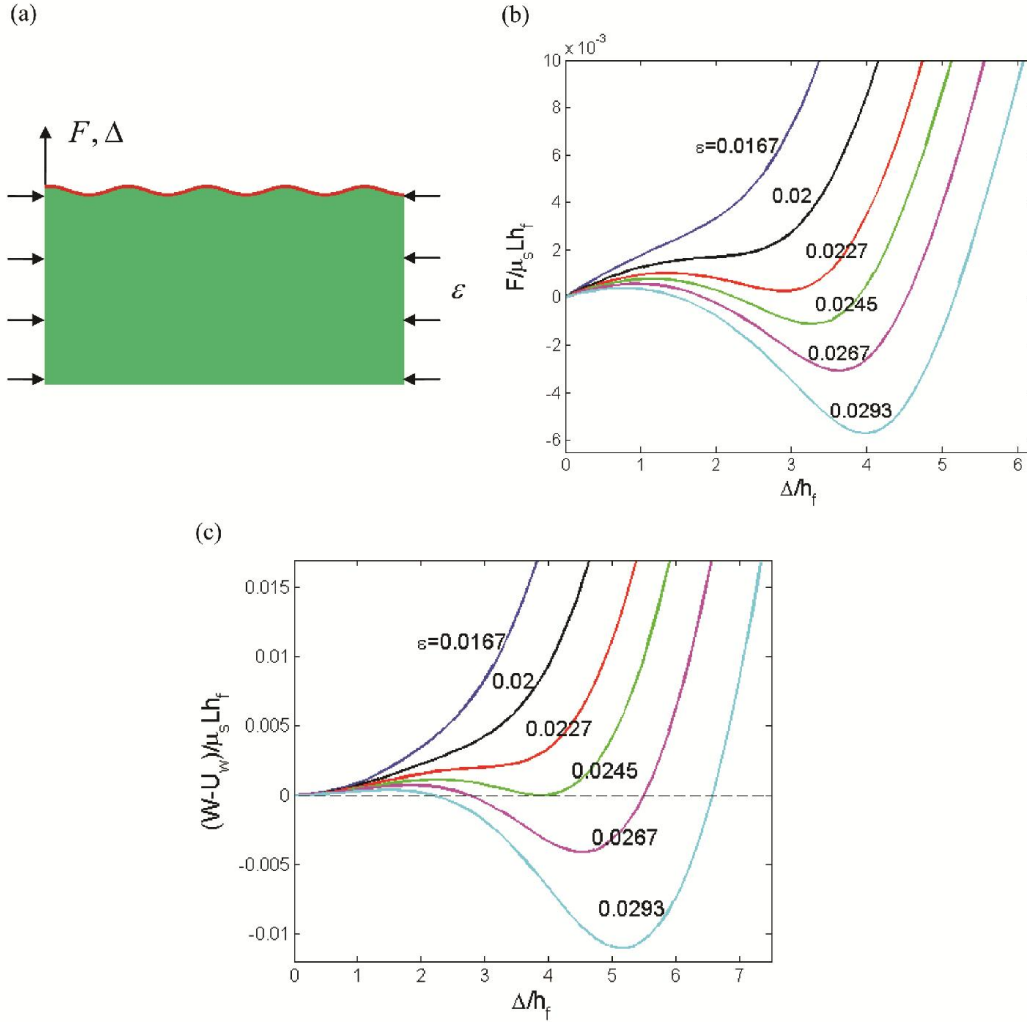


Figure 9.2 The computation results by using the static force-displacement method. (a) A schematic of the method. A film/substrate bilayer is subject to a strain  $\varepsilon > \varepsilon_w$ , and wrinkles form. Under the fixed strain  $\varepsilon$ , an additional vertical displacement  $\Delta$  is added on the peak of a wrinkle, and the reaction force  $F$  and the total elastic energy of the sample  $W$  are computed. (b) The reaction force  $F$  as a function of the vertical displacement  $\Delta$  with pre-stretch  $\lambda_0 = 2$  under different fixed strains  $\varepsilon$ . (c) The elastic energy subtracting the elastic energy of the wrinkled state  $W - U_w$  as a function of the vertical displacement  $\Delta$  with the same pre-stretch and strains as (b).

In order to simulate the localization or a ridge, the sample length  $L$  has to be several times of the wrinkle wavelength  $l_w$ . As an example, here we choose  $L = 9l_w$ . We assume the symmetry of a ridge, so that we only need to simulate half of it. As shown in Figure 9.2a, the reflection symmetry boundary condition is added to the left boundary and the displacement  $\Delta$  is added on the left most peak. Uniform horizontal displacement is

added on the right boundary, and no vertical displacement is allowed on the bottom boundary (Figure 9.1c). Here we set the thickness ratio as  $(h_f + h_s)/h_f = 200$ . As long as the thickness of the substrate is much larger than that of the film, and much larger than the amplitude of the ridge, the thickness ratio does not affect the critical condition for the formation of wrinkles and ridges. Both the film and substrate are modeled as incompressible neo-Hookean material. The pre-stretch of the substrate is implemented in a user-defined material subroutine UMAT. As an example, here we choose  $\mu_f / \mu_s = 1000$ , and the critical strain for wrinkle initiation is around  $\varepsilon_w = 0.0093$ .

Figure 9.2b plots the reaction force  $F$  normalized by  $\mu_s L h_f$  as a function of the vertical displacement  $\Delta$  normalized by  $h_f$  with pre-stretch  $\lambda_0 = 2$  under different fixed strains  $\varepsilon$ . When  $\varepsilon$  is small, the  $F-\Delta$  curve is monotonic, and  $F$  is only zero when  $\Delta$  is zero. With the increase of  $\varepsilon$ , the  $F-\Delta$  curve starts to be non-monotonic. When  $\varepsilon$  is larger than a critical value,  $F$  reaches zero at a finite  $\Delta$ . If a state with zero  $F$  is found when  $\Delta$  is non-zero, that state can exist (without an external force) at the strain  $\varepsilon$ , which means an equilibrium solution, although the state may be stable or unstable. With the further increase of  $\varepsilon$ , the  $F-\Delta$  curve has three intersections with the  $\Delta$ -axis. The intersection in the origin means the solution of the wrinkle state, the right most intersection means the solution of the stable ridge state with a large amplitude, and the intersection in between means the unstable ridge with a intermediate amplitude.

Figure 9.2c plots the dependence of the elastic energy  $W$  subtracting the elastic energy of the wrinkle state  $U_w$ , normalized by  $\mu_s L h_f$ , as a function of the vertical displacement  $\Delta$  normalized by  $h_f$  with the same pre-stretch and strains as Figure 9.2b.

When  $\varepsilon$  is small, the  $F-\Delta$  curve is monotonic in Figure 9.2b, and the wrinkle state with zero  $\Delta$  is the only energy minimum in Figure 9.2c. With the increase of  $\varepsilon$ , there starts to be another energy minimum at a non-zero  $\Delta$ . The three intersections of a  $F-\Delta$  curve with the  $\Delta$ -axis in Figure 9.2b correspond to the two energy minima and one energy maximum in Figure 9.2c. Especially, when  $\varepsilon = 0.0245$ , the two energy minima have the same value, and this strain is defined as the Maxwell strain  $\varepsilon_{Max}$ . When  $\varepsilon > \varepsilon_{Max}$ , the energy of the ridge state with a large amplitude is smaller than that of the wrinkle state.

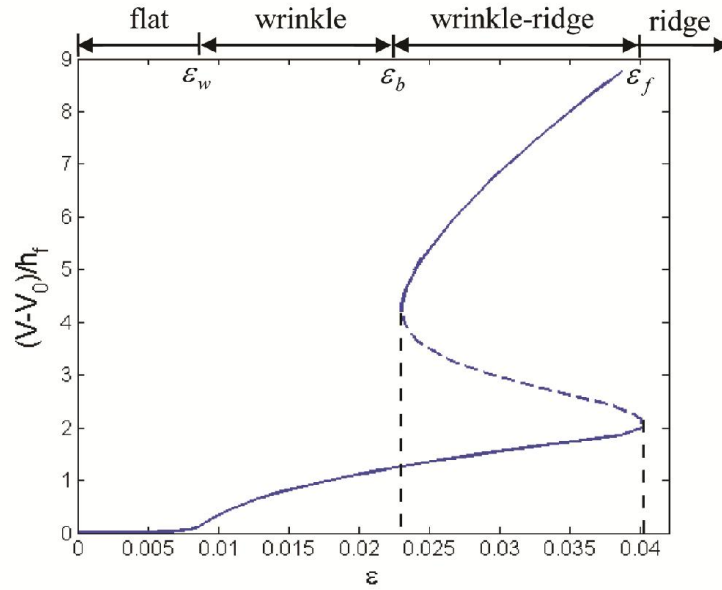


Figure 9.3 Vertical displacement  $V$  of the ridge peak, subtracting the vertical displacement of the homogeneous deformation  $V_0$ , for all the equilibrium states as a function of  $\varepsilon$ .

In Figure 9.3, we plot the vertical displacement  $V$  of the ridge peak (top left corner of the sample), subtracting the vertical displacement of the homogeneous deformation  $V_0$ , for all the equilibrium states as a function of  $\varepsilon$  obtained by the computations described in Figure 9.2. When  $\varepsilon < \varepsilon_w$ ,  $V - V_0 = 0$  and the surface keeps flat. When  $\varepsilon_w < \varepsilon < \varepsilon_b$ , with  $\varepsilon_b$  the snapping backward strain of ridges, wrinkles form and the wrinkle state is the only

equilibrium state. When  $\varepsilon_b < \varepsilon < \varepsilon_f$ , with  $\varepsilon_f$  the snapping forward strain of ridges, there are three equilibrium states, which are the wrinkle state and the stable ridge state with a large amplitude (shown by the solid lines), and the unstable ridge state with an intermediate amplitude (shown by the dashed line). When  $\varepsilon > \varepsilon_f$ , the ridge state with large amplitude becomes the only equilibrium state. The snapping forward and backward strains obtained by the simulations are  $\varepsilon_f = 0.040$  and  $\varepsilon_b = 0.023$  respectively.

In Figure 9.4a, we plot the elastic energy  $U$  of the stable equilibrium states subtracting the elastic energy of the flat state  $U_0$  as a function of  $\varepsilon$ . The wrinkle state is represented by the blue line and the ridge state is represented by the red line. When  $\varepsilon < \varepsilon_w$ ,  $U = U_0$ . When  $\varepsilon > \varepsilon_w$ , the wrinkle state has an elastic energy lower than the flat state. When  $\varepsilon > \varepsilon_b$ , the ridge solution starts to exist, and its energy is also lower than the flat state. However, the energy difference between the wrinkle and ridge states is small compared to their difference from the flat state. To further demonstrate the energy difference between the wrinkle state and the ridge state, in Figure 9.4b, we plot the energy subtraction of the ridge and wrinkle states  $U_r - U_w$  as a function of  $\varepsilon$ . The ridge state has a higher energy than the wrinkle state  $U_r - U_w > 0$  when the strain is lower than the Maxwell condition  $\varepsilon < \varepsilon_{Max}$ , while the ridge state has a lower energy  $U_r - U_w < 0$  when  $\varepsilon > \varepsilon_{Max}$ .

So far, we have obtained all the equilibrium solutions under different given strains  $\varepsilon$ , and have known their energetics and stability. In experiments, we expect to see the formation of wrinkles supercritically at strain  $\varepsilon_w$ . With the further increase of the strain to  $\varepsilon > \varepsilon_{Max}$ , the energy of the ridge state is lower than that of the wrinkle state. We expect ridges nucleate at the edge of the sample, and propagate — that is wrinkles transit to ridges

by channeling. If channeling is eliminated and the surface of the sample has few defects, we expect wrinkles can exist until the strain  $\varepsilon = \varepsilon_f$ , and then dynamically snap to ridges.

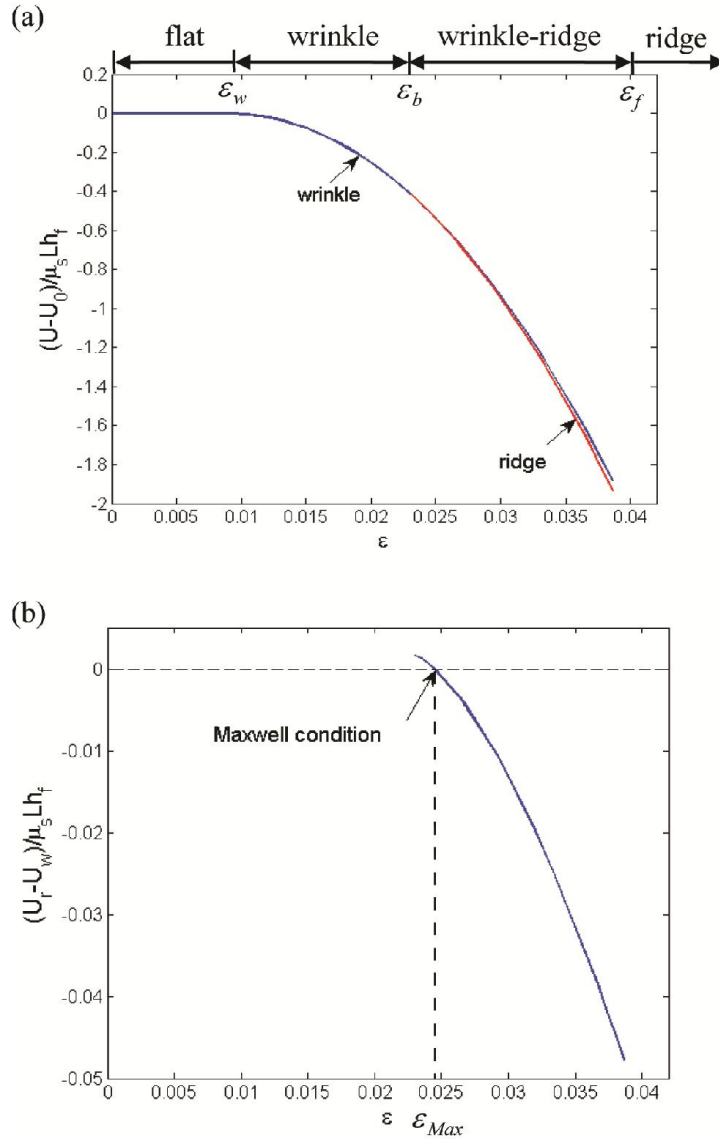


Figure 9.4 (a) Elastic energy  $U$  of the stable equilibrium states subtracting the elastic energy of the flat state  $U_0$  as a function of  $\varepsilon$ . The wrinkle state is represented by the blue line and the ridge state is represented by the red line. (b) Energy difference between the ridge state and the wrinkle states  $U_r - U_w$ . At the Maxwell strain  $\varepsilon_{Max}$ , the ridge state and the wrinkle state have the same energy  $U_r = U_w$ .

### 9.2.2 Pseudo-dynamic loading-unloading method

Next, we use a pseudo-dynamic loading-unloading method to study the wrinkle to ridge transition. We take the same sample size and boundary conditions as the static force-displacement method. Similar to the static method, a linear perturbation analysis is done first and then the critical wrinkle mode is introduced as imperfection of the compression simulation. In the pseudo-dynamic method, we still run a static step but allow numerical stabilization, which can capture the snap through processes between the wrinkle state and the ridge state. The damping factor is set as 0.0002.

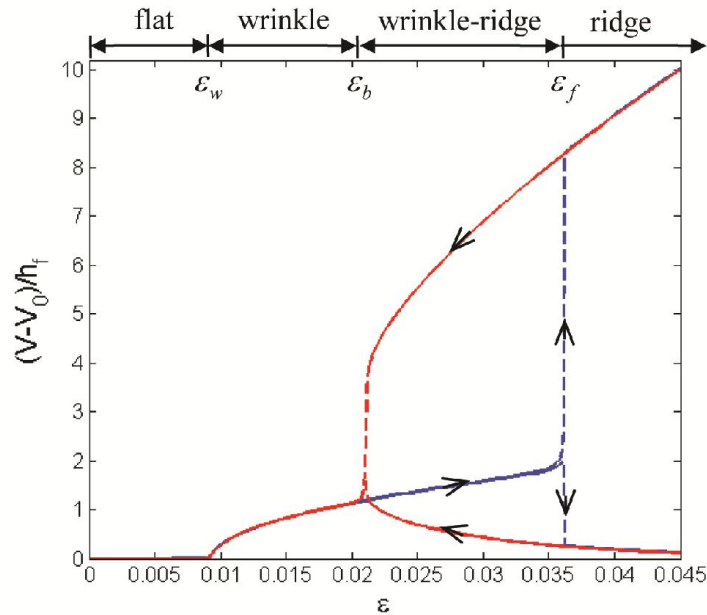


Figure 9.5 The vertical displacements  $V$  of the peaks of the ridge and its neighboring wrinkle as a function of strain  $\varepsilon$ . The blue line represents loading while the red line represents unloading, with arrows showing the direction of the paths. During the loading, wrinkles snap to a ridge, and therefore the two displacements bifurcate, at the snapping forward strain  $\varepsilon_f$ . During the unloading, the ridge snaps back to wrinkles, and therefore the two displacements converge to the same value, at the snapping backward strain  $\varepsilon_b$ .

The sample with pre-stretch  $\lambda_0 = 2$  is first compressed to a strain larger than the snapping forward strain  $\varepsilon > \varepsilon_f$ , and then unloaded to the bonded state. The vertical displacements  $V$  of the peaks of the ridge and its neighboring wrinkle are recorded in

Figure 9.5 as a function of strain  $\varepsilon$ . The blue lines represent loading while the red lines represent unloading, with arrows showing the direction of the paths. During the loading, the sample keeps flat under strain  $\varepsilon < \varepsilon_w$ , and forms wrinkles under strain  $\varepsilon_w < \varepsilon < \varepsilon_f$ . The vertical displacements of the peak of the ridge and its neighboring wrinkle coincide before strain reaches  $\varepsilon_f$ . At the snapping forward strain  $\varepsilon_f$ , wrinkles become dynamically unstable, and snap to a localized ridge, with the original period broken. The snapping process is represented by dashed lines. The  $V - \varepsilon$  curve bifurcate:  $V$  of the ridge peak snaps to a large value, while  $V$  of the neighboring wrinkle peak snaps to a small value, which means the formation of a large amplitude ridge with the neighboring wrinkles flattened. With the further increase of the strain,  $V$  of the ridge peak keeps increasing, while  $V$  of the neighboring wrinkle peak keeps decreasing. During the unloading, when  $\varepsilon > \varepsilon_f$ , the unloading curves overlap the loading curve. However, the sample still stays in the ridge state when  $\varepsilon < \varepsilon_f$  until the snapping backward strain  $\varepsilon_b$ . At the snapping backward strain  $\varepsilon_b$ , the ridge state snaps back to the wrinkle state. A large hysteresis between strains  $\varepsilon_f$  and  $\varepsilon_b$  is created during loading and unloading. Afterwards, the unloading curves of the two displacements overlap, and coincide with the loading curves. All the equilibrium solutions obtained by the pseudo-dynamic method show good agreement with the static method. The snapping forward strain and the snapping backward strain obtained by this method are  $\varepsilon_f = 0.0361$  and  $\varepsilon_b = 0.0212$  respectively, which are close to the values obtained by the static method. The main reason of the discrepancy could be the numerical damping of the pseudo-dynamic method. Figure 9.1d shows the simulation result of the wrinkle state at  $\varepsilon_b$ . Figure 9.1e shows the simulation result of the ridge state at  $\varepsilon_f$ . Only top

one-fourth of the samples are shown, and the bottom parts undergo a homogeneous deformation.

We further exam the energetics of the loading and unloading processes. We calculate the elastic energies the loading and unloading processes, and their difference  $U_L - U_{UL}$  as a function of strain  $\varepsilon$  is plotted in Figure 9.6a. When  $\varepsilon < \varepsilon_b$  or  $\varepsilon > \varepsilon_f$ , the loading and unloading follow the same deformation path, and therefore their energies coincide  $U_L - U_{UL} = 0$ . However, when  $\varepsilon_b < \varepsilon < \varepsilon_f$ , there is hysteresis between the loading and unloading. The loading curve represents the wrinkle state, while the unloading curve represents the ridge state. Therefore, the energy difference between the loading and unloading in strain  $\varepsilon_b < \varepsilon < \varepsilon_f$  is essentially the energy difference between the wrinkle and ridge states. The values obtained by this method are close to the ones obtained by the static method. We can obtain the Maxwell condition by checking the point when  $U_L - U_{UL}$  reaches zero in strain  $\varepsilon_b < \varepsilon < \varepsilon_f$ . Figure 9.6b further amplifies the region close to the Maxwell condition, illustrated by a square in Figure 9.6a. The Maxwell strain obtained by this method is  $\varepsilon_{Max} = 0.0222$ , which is close to the value obtained by the static method. When  $\varepsilon < \varepsilon_{Max}$ , the wrinkle state has a lower energy, while when  $\varepsilon > \varepsilon_{Max}$ , the ridge state has a lower energy. Figure 9.6c shows the simulation result of the ridge state at the Maxwell condition  $\varepsilon_{Max}$ . Only top one-fourth of the sample is shown, and bottom part undergoes a homogeneous deformation.

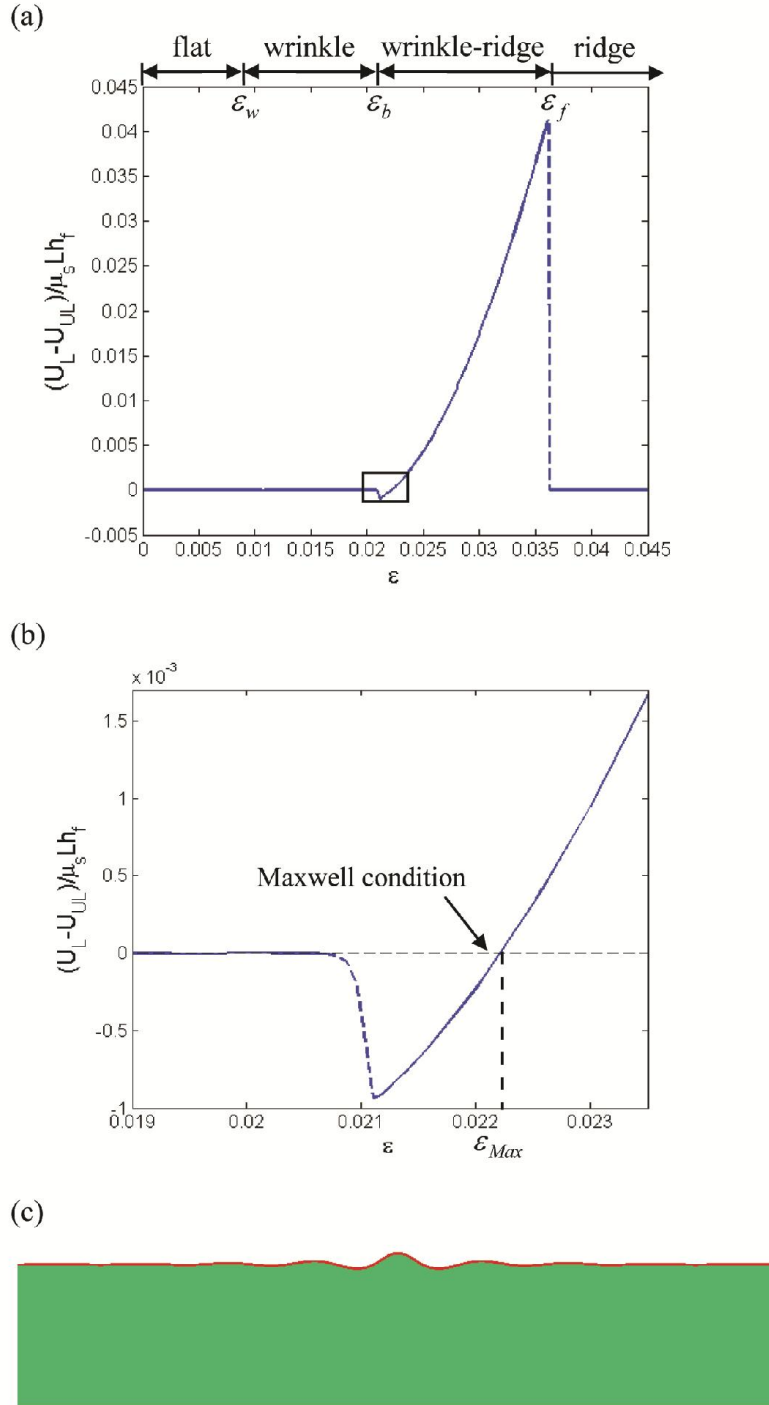


Figure 9.6 (a) The elastic energy difference between the loading and unloading states  $U_L - U_{UL}$  as a function of strain  $\epsilon$ . When  $\epsilon_b < \epsilon < \epsilon_f$ , this is essentially the energy difference between the wrinkle state and the ridge state. The Maxwell condition is defined by the point when  $U_L - U_{UL}$  reaches zero in strain  $\epsilon_b < \epsilon < \epsilon_f$ . (b) The amplification of the region close to the Maxwell condition of (a). (c) Simulation result of the ridge state at the Maxwell condition  $\epsilon_{Max}$ .

The pseudo-dynamic loading-unloading method can reproduce all the stable equilibrium solutions obtained by the static force-displacement method. Although, the introduction of the numerical dissipation in the pseudo-dynamic method may slightly affect the critical conditions of ridges, the pseudo-dynamic method is more efficient. In order to obtain all  $\varepsilon_b$ ,  $\varepsilon_f$  and  $\varepsilon_{Max}$  of a wrinkle to ridge transition, only one simulation is needed by the pseudo-dynamic method, while multiple simulations are needed by the static method. Therefore, all the results we present in Section 9.3 will be based on the pseudo-dynamic method.

### 9.2.3 Verification of the two methods

We verify the two simulation methods here by tuning the parameters of simulations. In all the simulations above, we assume the spacing of ridges is 9 times of the wrinkle wavelength  $L = 9l_w$ . In Figure 9.7a, we change the spacing of ridges for the case with  $\mu_f / \mu_s = 1000$ ,  $(h_f + h_s) / h_f = 200$  and  $\lambda_0 = 2$ . and see how this affects the critical condition of ridges. The Maxwell strain  $\varepsilon_{Max}$  decreases with the increase of the ridge spacing for both the static and pseudo-dynamic methods. However, the decrease goes more slowly when the spacing is larger, and we expect a plateau of  $\varepsilon_{Max}$  will be reached when the spacing is sufficiently large. When the ratio of ridge spacing to wrinkle wavelength increases from 6 to 9,  $\varepsilon_{Max}$  decreases for more than 0.5%. However, when the ratio of ridge spacing to wrinkle wavelength increases from 9 to 18,  $\varepsilon_{Max}$  decreases for less than 0.5%. Therefore, in considering the balance between the efficiency and accuracy, we think  $L = 9l_w$  is a reasonable choice of the ridge spacing, and we will also do so for the results below.

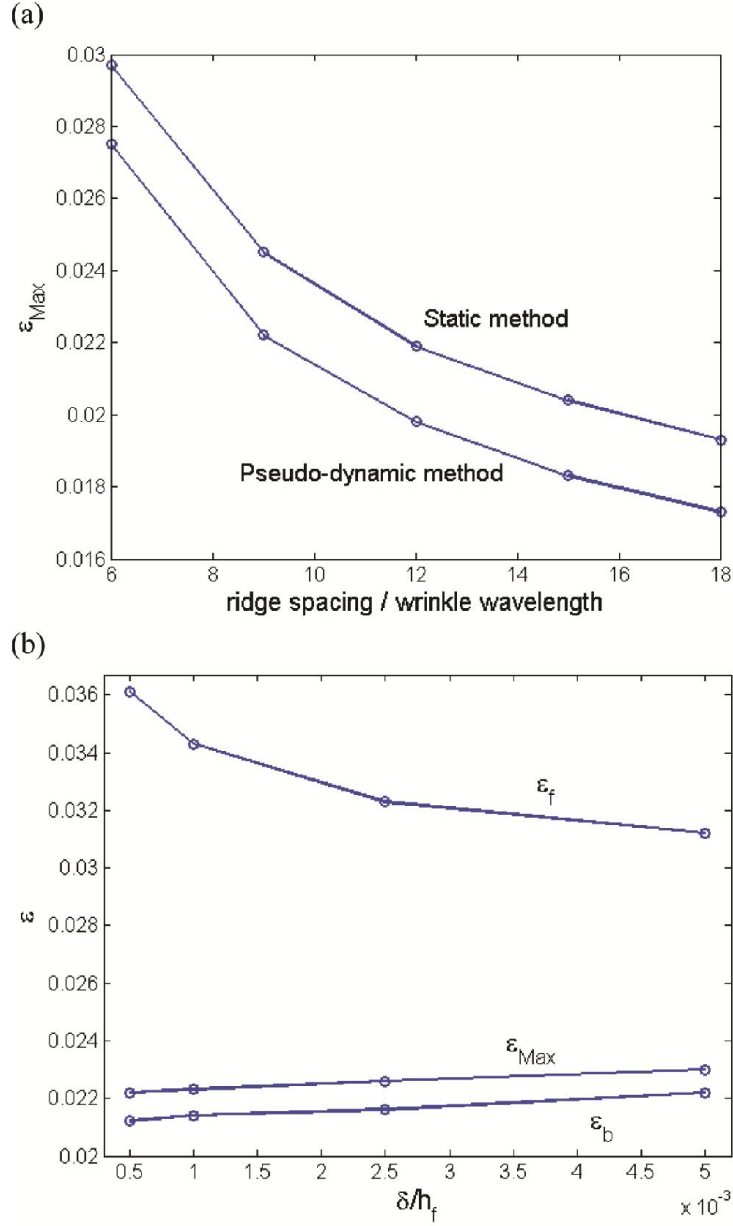


Figure 9.7 (a) Effect of the ridge spacing in the simulations on the Maxwell strain  $\varepsilon_{Max}$ . (b) Effect of the imperfection size  $\delta$  on the snapping forward strain  $\varepsilon_f$ , the Maxwell strain  $\varepsilon_{Max}$  and the snapping backward strain  $\varepsilon_b$  in pseudo-dynamic method.

In Figure 9.7b, we study the effect of the size of imperfection on the critical conditions of ridges obtained by the pseudo-dynamic method. It is well known that unstable bifurcations are highly sensitive to imperfections [233, 234]. In the pseudo-dynamic simulations, since we have to guarantee that the left most half period of wrinkle forms a half

ridge so that we only need to simulate half of the sample, besides the critical wrinkle mode (first eigenmode), we also add the second eigenmode as the initial imperfection to break the periodicity of wrinkles. We take the following form of the initial imperfection:  $\delta \times \text{mode1} + \delta/2 \times \text{mode2}$ , with  $\delta$  the amplitude of the first eigenmode. Figure 9.7b shows that the snapping forward strain  $\varepsilon_f$  decreases dramatically with  $\delta$ , while the Maxwell strain  $\varepsilon_{Max}$  and the snapping backward strain  $\varepsilon_b$  only slightly increase with  $\delta$ . All the results obtained by the pseudo-dynamic method elsewhere are based on  $\delta/h_f = 5e-4$ . For the simulations by the static method, we do not expect this effect, because the system always remains stable when we add the vertical displacement  $\Delta$ .

### 9.3 Deformation mechanism and geometry of ridges

In this section, we carefully analyze the strain and energy density distributions in the wrinkle and ridge states in order to understand the deformation mechanism and geometry of ridges. We also study the effect of pre-stretch on the critical conditions of wrinkle and ridge formation.

In Figure 9.8, we plot the elastic energy differences between the loading and unloading  $U_L - U_{UL}$  in the film and substrate respectively in the strain range  $\varepsilon_b < \varepsilon < \varepsilon_f$ , where the wrinkle and ridge states can coexist, for the case with  $\mu_f/\mu_s = 1000$ ,  $(h_f + h_s)/h_f = 200$  and  $\lambda_0 = 2$ . The energy difference  $U_L - U_{UL}$  is essentially the energy difference between the wrinkle state and the ridge state. The sum of these two energy differences is the total energy difference of the whole sample shown in Figure 9.6a. In this strain range, the elastic energy of the film is always higher in the wrinkle state than the ridge

state, while the elastic energy of the substrate is higher in the wrinkle state when the strain is high, but is lower in the wrinkle state when the strain is low. Therefore, at strain  $\varepsilon = \varepsilon_f$ , by forming a ridge, the elastic energies of both the film and substrate decrease.

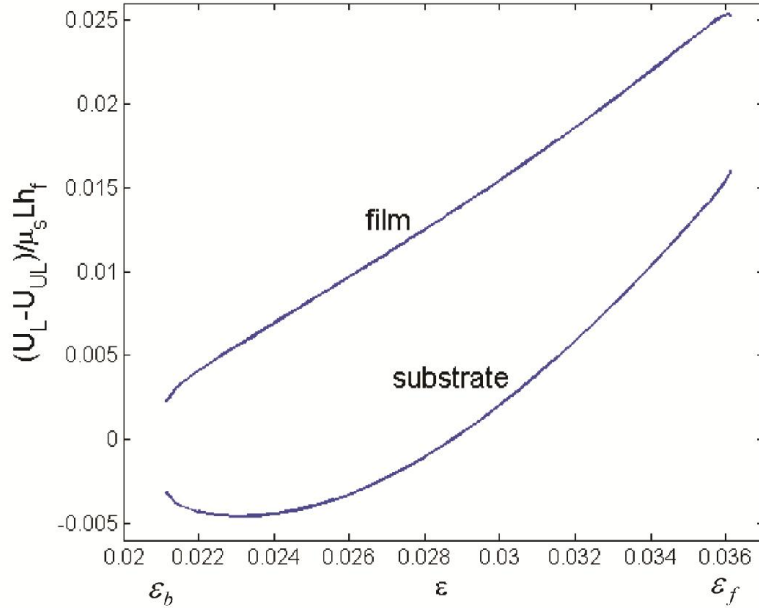


Figure 9.8 The elastic energy differences between the loading and unloading  $U_L - U_{UL}$  in the film and substrate in the strain range  $\varepsilon_b < \varepsilon < \varepsilon_f$ , with  $\mu_f / \mu_s = 1000$ ,  $(h_f + h_s) / h_f = 200$  and  $\lambda_0 = 2$ .

Now we take a closer look at the strain and energy distributions in the substrate (Figure 9.9) and film (Figure 9.10). Figure 9.9a and b show respectively the distribution of the elastic energy density  $\psi$  and the logarithmic strain in the compression direction  $e_{11}$  in the substrate at strain  $\varepsilon = \varepsilon_f = 0.0361$  for the ridge state with  $\mu_f / \mu_s = 1000$ ,  $(h_f + h_s) / h_f = 200$  and  $\lambda_0 = 2$ . Far away from the ridge peak, the sample sustains a homogeneous deformation. Therefore the blue-green color in the far field in Figure 9.9a represents the energy level of a homogeneous deformation of the substrate under the pre-stretch and the external strain. Similarly, the brown-yellow color in the far field in Figure 9.9b represents the homogeneous logarithmic strain level in the substrate. Since the

substrate is highly pre-stretched in the bonded state, the far field is subject to a large tensile strain. However, due to the formation of the ridge,  $e_{11}$  dramatically decreases in the region below the ridge peak, represented by yellow, green and blue colors (Figure 9.9b). In the blue region,  $e_{11}$  even has a large negative value. Therefore, as shown in Figure 9.9a, the elastic energy density in a dumbbell-shaped region below the ridge peak, represented by blue colors, is much smaller than the value in the far field. As a penalty, the energy density in a wing-shaped region, represented by red, yellow and green colors, is higher than the far field. All the elements of the mesh have a square shape in the bonded state. We can see from the shape of the elements that the top of the substrate close to the wing-shaped region is highly sheared in order to accommodate the ridged shape of the film. As a comparison, Figure 9.9c shows the distribution of the elastic energy density  $\psi$  in the substrate for the wrinkle state under the same strain  $\varepsilon = \varepsilon_f$ . The energy is lower in the peaks of the wrinkles, while higher in the troughs of the wrinkles. The energy maximum in the wrinkle state is lower than the ridge state, but the energy minimum in the wrinkle state is much higher than the ridge state. Due to the high non-linearity of the neo-Hookean model under large pre-stretch, the localized ridge mode reduces the total energy from the wrinkle state.

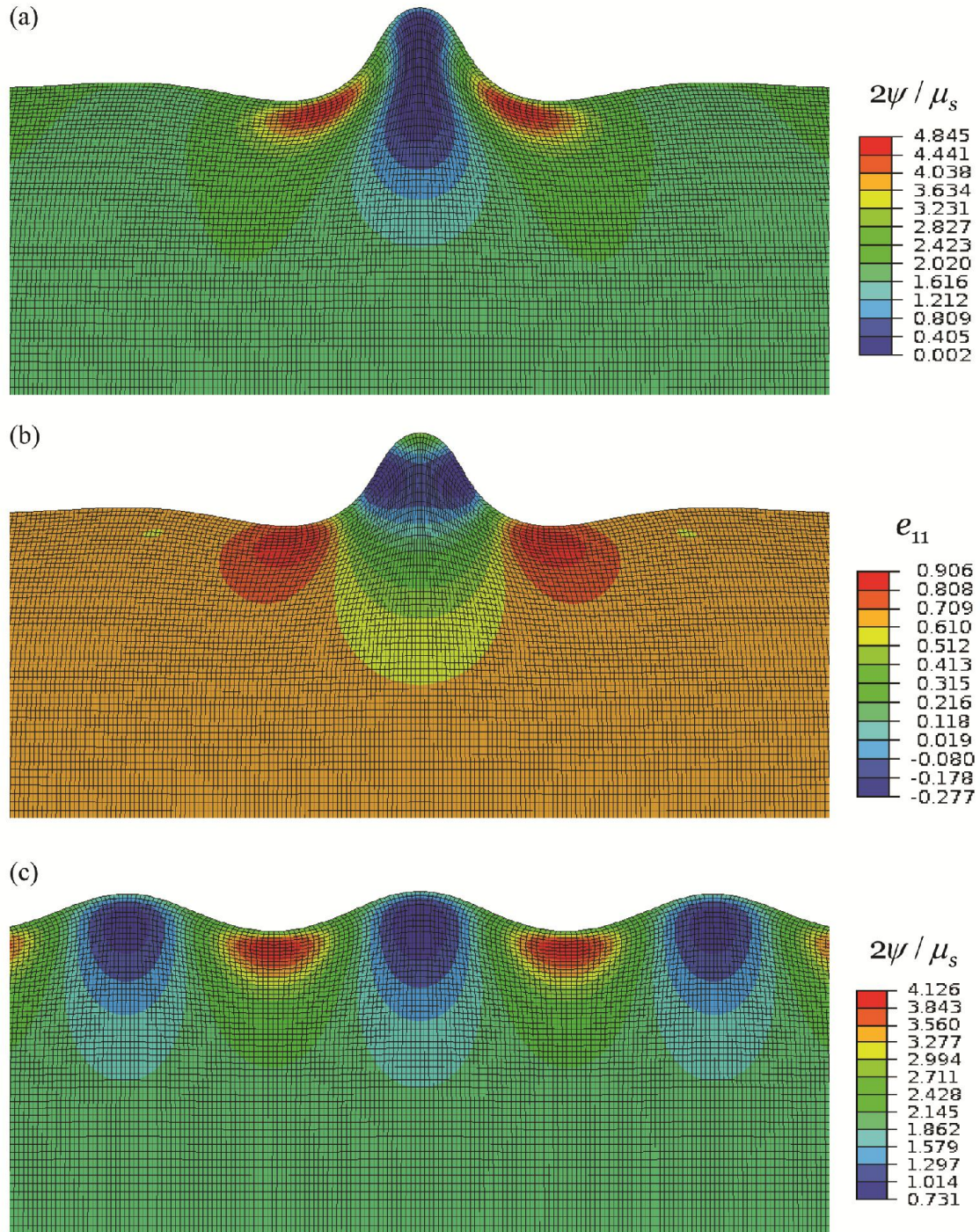


Figure 9.9 The distribution of (a) elastic energy density  $\psi$  and (b) logarithmic strain in the compression direction  $e_{11}$  in the substrate at strain  $\varepsilon = \varepsilon_f = 0.0361$  for the ridge state with  $\mu_f / \mu_s = 1000$ ,  $(h_f + h_s) / h_f = 200$  and  $\lambda_0 = 2$ . (c) The distribution of elastic energy density  $\psi$  in the substrate for the wrinkle state at the same strain and pre-stretch as (a).

Figure 9.10a and b show the distributions of the maximal principal logarithmic strain  $e_{\max}$  in the film in the ridge and wrinkle states respectively at strain  $\varepsilon = \varepsilon_f$ . For an incompressible neo-Hookean material under a plane strain loading,  $e_{\max}$  monotonically increases with  $\psi$ . Similar to the situation in the substrate (Figure 9.9), the maximal value of  $e_{\max}$  in the ridge state is higher than the wrinkle state, while the minimal value of  $e_{\max}$  in the ridge state is lower than the wrinkle state. By forming a localized ridge, although the peak of the ridge has a much higher  $e_{\max}$  than the peak of the wrinkles, the other parts are flattened in the ridge state and have lower  $e_{\max}$ . The total elastic energy in the film reduces by forming a ridge.

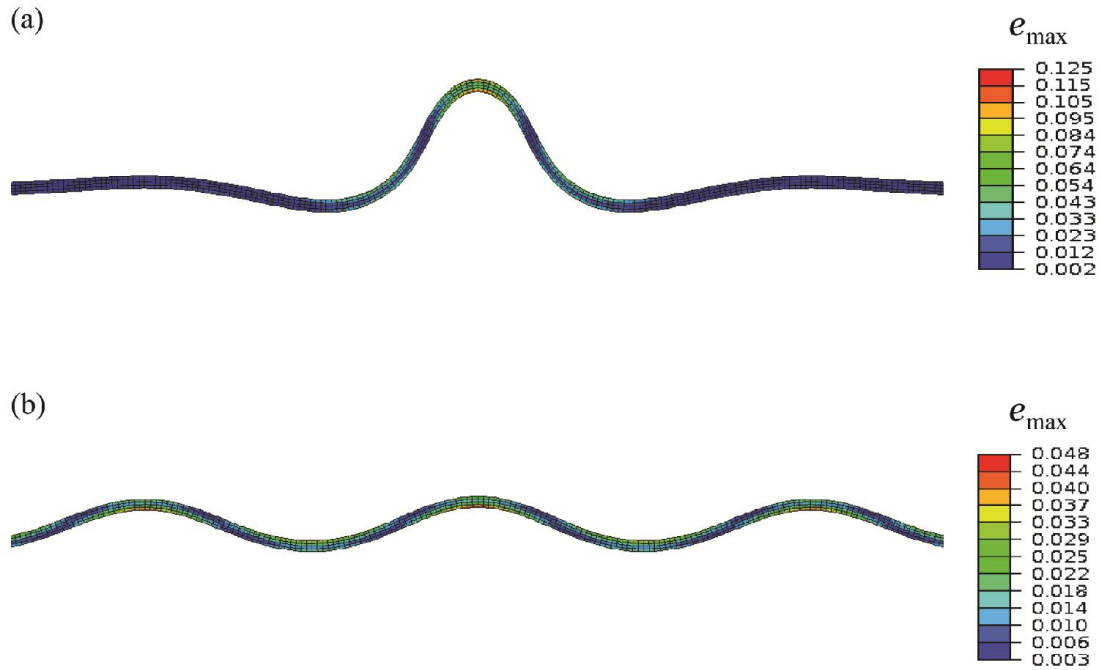


Figure 9.10 The distributions of the maximal principal logarithmic strain  $e_{\max}$  in the film in the (a) ridge state and (b) wrinkle state at strain  $\varepsilon = \varepsilon_f = 0.0361$  with  $\mu_f/\mu_s = 1000$ ,  $(h_f + h_s)/h_f = 200$  and  $\lambda_0 = 2$ .

We further check the ridge state at strain  $\varepsilon = 0.045 > \varepsilon_f$ , where a stable wrinkle state no longer exists (Figure 9.11). The ridge has a larger height and smaller width, as defined in

Figure 9.1e, compared to the ridge state at strain  $\varepsilon = \varepsilon_f = 0.0361$  (Figure 9.9a and b). This shape change makes the maximal compressive logarithmic strain  $e_{11}$  in the substrate even larger (more negative) (Figure 9.11b). The maximal energy density becomes smaller than the one at strain  $\varepsilon = \varepsilon_f$ , while the minimal energy density becomes slightly larger (Figure 9.11a).

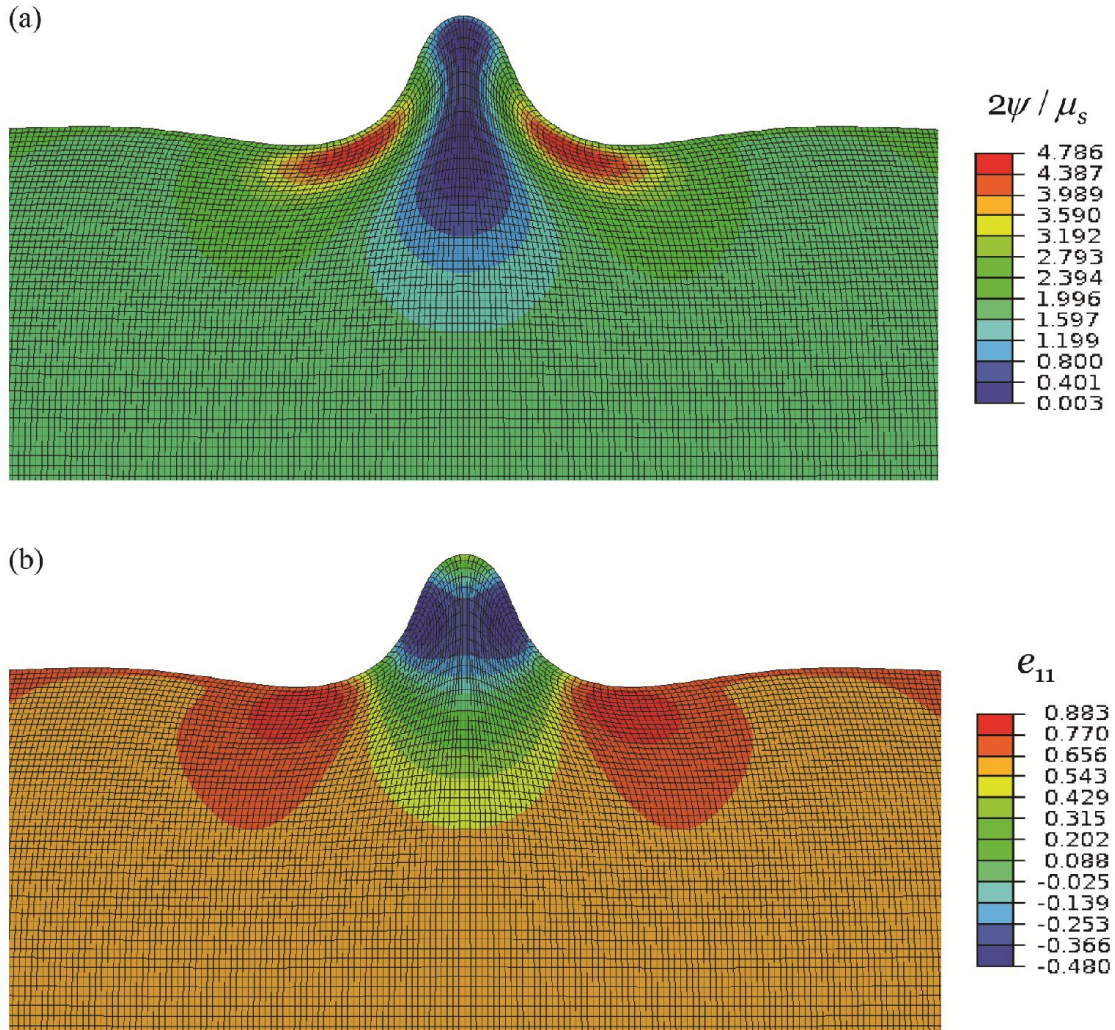


Figure 9.11 The distributions of (a) elastic energy density  $\psi$  and (b) logarithmic strain in the compression direction  $e_{11}$  in the substrate at strain  $\varepsilon = 0.045$  for the ridge state with  $\mu_f / \mu_s = 1000$ ,  $(h_f + h_s) / h_f = 200$  and  $\lambda_0 = 2$ .

Figure 9.12 plots the width  $B$  and height  $A$  of the ridge, as defined in Figure 9.1e, as a function of strain  $\varepsilon$ . For the condition  $\mu_f / \mu_s = 1000$ ,  $(h_f + h_s) / h_f = 200$  and  $\lambda_0 = 2$ ,

the critical wrinkle wavelength is  $l_w = 33.3h_f$ . The width of the ridge is comparable to the wrinkle wavelength. The height of the ridge is smaller than the width, but still much larger than the thickness of the film. With the increase of strain  $\varepsilon$ , the height increases, to accommodate which, the width decreases. When the strain  $\varepsilon$  is large, the width and height of the ridge are on the same order of magnitude. Therefore, the ridge has large amplitude, in contrast to shallow wrinkles.

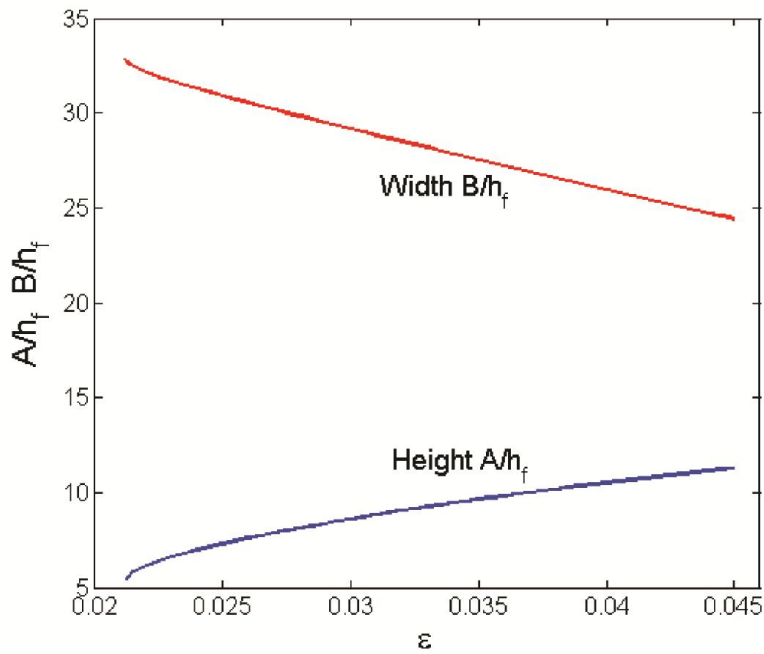


Figure 9.12 The width  $B$  and height  $A$  of the ridge as a function of strain  $\varepsilon$ . With the increase of  $\varepsilon$ , the height increases, to accommodate which, the width decreases.

Figure 9.13 studies the effect of pre-stretch  $\lambda_0$  on the critical conditions of ridges and wrinkles (Figure 9.13a), and the width and height of ridges (Figure 9.13b). As shown in Figure 9.13a, the critical strain for the initiation of wrinkles  $\varepsilon_w$  increases slightly with the increase of  $\lambda_0$ . The snapping backward strain  $\varepsilon_b$  and the Maxwell strain  $\varepsilon_{Max}$  of ridges slightly decreases with  $\lambda_0$ , while the snapping forward strain  $\varepsilon_f$  dramatically decreases with  $\lambda_0$ . Therefore, the hysteresis size decreases with  $\lambda_0$ . As shown in Figure 9.13b, the

snapping forward width  $B$  and height  $A$  of the ridge decrease dramatically with  $\lambda_0$ , while the snapping backward width and height vary slightly with  $\lambda_0$ .

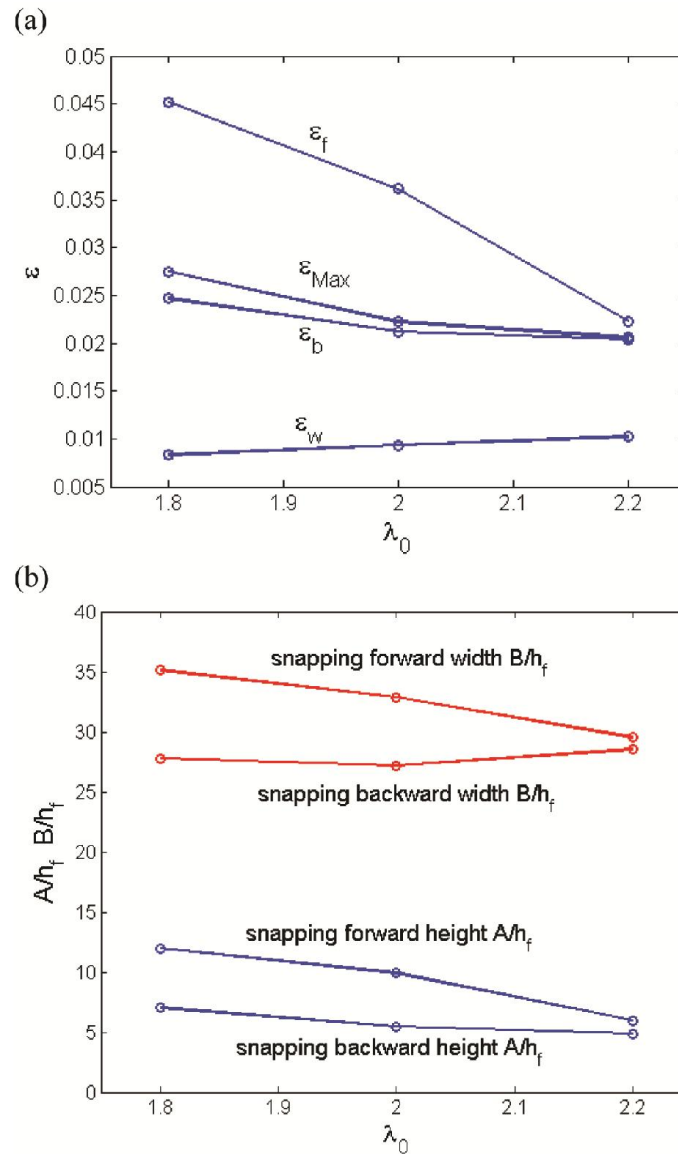


Figure 9.13 (a) The dependence of the critical conditions of wrinkle initiation  $\varepsilon_w$ , snapping backward strain  $\varepsilon_b$ , Maxwell strain  $\varepsilon_{Max}$  and the snapping forward strain  $\varepsilon_f$  of ridges on pre-stretch  $\lambda_0$ . (b) The dependence of the width and height of ridges on pre-stretch  $\lambda_0$ .

## 9.4 Summary

In this chapter, we study the mechanics of the formation and propagation of localized ridge instability by finite element analysis. Subject to a critical compression, a film/substrate bilayer with substrate under high tensile pre-stretch forms wrinkles first. With the further increase of the compression, wrinkles can transit to localized ridges by lifting up the peaks in every several wrinkles. The wrinkle to ridge transition is subcritical — that is unstable, and wrinkles dynamically snap to ridges. We develop two numerical ways to study ridges: static force-displacement method and pseudo-dynamic loading-unloading method. We can obtain all the stable equilibrium solutions to the boundary value problem under different given strain by both methods. Therefore, we can find the snapping backward strain  $\varepsilon_b$ , the Maxwell strain  $\varepsilon_{Max}$  and the snapping forward strain  $\varepsilon_f$  of ridges. We further analyze the strain and energy distributions of the wrinkle and ridge states in order to understand the deformation mechanism of ridges. We find that under a sufficiently large strain the ridge state reduced the energy in both the film and substrate compared to the wrinkle state. Ridges have a high aspect ratio, which facilitates their applications in reversible control of wettability and adhesion.

## Chapter 10

### Conclusions

Mechanical instabilities are ubiquitous in nature and daily life. In the engineering field, mechanical instabilities were thought to be failure modes of materials, but now people start to develop various creative applications of mechanical instabilities. Moreover, because of the high stretchability of soft materials, new types of highly nonlinear instabilities were realized.

Motivated by this emerging field, this thesis has explored different types of mechanical instabilities: creases, wrinkles, folds, and ridges. This thesis has studied mechanical instabilities in materials with different properties and structures, proposed understandings of the deformation mechanisms of different types of mechanical instabilities, designed structures to realize a better control of the formation and disappearance of mechanical instabilities, and shown new types of mechanical instabilities.

We started with studying creases in homogeneous materials. We first studied creases in soft tissues generated by constrained growth. We adopted the model of growth that factors the deformation gradient into a growth tensor and an elastic deformation tensor, and showed that the critical conditions for the onset of creases take a remarkably simple form. The critical conditions were illustrated with tubes of tissues growing either inside a rigid shell or outside a rigid core. Furthermore, deep creases in a tube of tissues were simulated by using the finite element method, and the number of creases in the tube was estimated by minimizing the free energy. We then studied creases in strain-stiffening materials by the

finite element method. We found that for a solid that stiffens steeply at large strains, as the compression increases, the surface is initially smooth, then forms creases, and finally becomes smooth again. For a solid that stiffens steeply at small strains, creases never form and the surface remains smooth for all levels of compression. We also obtained the critical conditions for the formation of wrinkles in strain-stiffening materials by a linear perturbation method. When the surface does become unstable, we find that creases always set in at a lower compression than wrinkles. Our findings may shed light in developing crease-resistant materials.

Since the conditions for the formation and disappearance of creases had so far been poorly controlled, we then designed a soft elastic bilayer, with similar moduli of the two layers but the substrate pre-compressed, and showed that it can snap between the flat and creased states repeatedly, with hysteresis. The strains at which the creases form and disappear are highly reproducible, and are tunable over a large range, through variations in the level of pre-compression applied to the substrate and the thickness ratio of the two layers. We conducted both numerical simulations and experiments, and showed that they agree very well with each other. The introduction of bistable flat and creased states and hysteretic switching is an important step to enable applications of crease instability.

Next we showed that an interface between two soft materials under compression can form creases, a type of bifurcation distinct from wrinkles. While creases bifurcate from a state of flat interface by a deformation localized in space and large in amplitude, wrinkles bifurcate from a state of flat interface by a deformation nonlocal in space and infinitesimal in amplitude. The interfacial creases set in at a lower critical compression than interfacial

wrinkles, but higher than surface creases. The condition for the onset of interfacial creases is scale-free, and was calculated in terms of elastic moduli, pre-strains and applied strains. Our experimental observations verified the theoretical predictions.

Then we studied the formation of wrinkles or creases in bilayers. We constructed a diagram of the formation of wrinkles and creases in a bilayer, and found several new types of bifurcation behavior when the moduli and the thicknesses of the film and substrate are comparable. We studied initiation of wrinkles by the linear perturbation method and initiation and growth of creases by the finite element method. We found creases tend to set in for more compliant and thicker films, while wrinkles tend to set in for stiffer and thinner films. When the modulus ratio of the film to substrate is smaller than a critical value 1.65, creases always form earlier than wrinkles. When the film and substrate have comparable moduli, creases could be subcritical or supercritical. Creases can also form from wrinkles by channeling at a much lower strain than the critical strain for the onset of creases in a homogeneous material.

We further studied the post-wrinkling bifurcations. We demonstrated that pre-stretched substrates not only show substantial shifts in the critical strain for the onset of post-wrinkling bifurcations, but also exhibit qualitatively different post-wrinkled states. In particular, we reported on the stabilization of wrinkles in films on pre-tensioned substrates and the emergence of 'chaotic' morphologies in films on pre-compressed substrates.

When the pre-stretch in the substrate is a sufficiently large tensile stretch, we demonstrated a different type of post-wrinkling bifurcation, localized ridges. The evolution of ridge localizations and networks was realized by incremental release of a large equi-biaxial

substrate pre-stretch in a microfluidic device. We found the wrinkle to ridge transition is subcritical. Ridges only form when the equi-biaxial pre-stretch is larger than 1.4. We further studied the mechanics of ridge formation and propagation. We developed two numerical ways to study ridges: static force-displacement method and pseudo-dynamic loading-unloading method, both of which allow us to find all the stable equilibrium solutions to the boundary value problem under different given strains, including the flat, wrinkle and ridge states. We obtained the snapping forward strain, snapping backward strain, and Maxwell strain of wrinkle to ridge transitions. We found the formation of a localized ridge can reduce the energy in both the film and substrate compared to the wrinkle state by protruding the surface out and releasing the pre-tension in the substrate.

Mechanical instability in soft materials is an emerging field. It is hoped that this thesis provides insight into the fundamental understanding of the different types of instability modes and contributes to the new applications of mechanical instabilities.

## Bibliography

- [1] E. Sharon, M. Marder, H. L. Swinney, Leaves, flowers and garbage bags: Making waves, *American Scientist*, 2004, 92 (3): 254-261.
- [2] H. Vandeparre, M. Pineirua, F. Brau, B. Roman, J. Bico, C. Gay, W. Z. Bao, C. N. Lau, P. M. Reis, P. Damman, Wrinkling hierarchy in constrained thin sheets from suspended graphene to curtains, *Physical Review Letters*, 2011, 106 (22): 224301.
- [3] B. Li, Y. P. Cao, X. Q. Feng, H. J. Gao, Mechanics of morphological instabilities and surface wrinkling in soft materials: A review, *Soft Matter*, 2012, 8 (21): 5728-5745.
- [4] H. Vandeparre, S. Gabriele, F. Brau, C. Gay, K. K. Parker, P. Damman, Hierarchical wrinkling patterns, *Soft Matter*, 2010, 6 (22): 5751-5756.
- [5] E. Chater, J. W. Hutchinson, On the propagation of bulges and buckles, *Journal of Applied Mechanics-Transactions of the ASME*, 1984, 51 (2): 269-277.
- [6] S. Krylov, B. R. Ilic, D. Schreiber, S. Seretensky, H. Craighead, The pull-in behavior of electrostatically actuated bistable microstructures, *Journal of Micromechanics and Microengineering*, 2008, 18 (5): 055026.
- [7] Y. Hu, A. Hiltner, E. Baer, Buckling in elastomer/plastic/elastomer 3-layer films, *Polymer Composites*, 2004, 25 (6): 653-661.
- [8] S. Yang, K. Khare, P. C. Lin, Harnessing surface wrinkle patterns in soft matter, *Advanced Functional Materials*, 2010, 20 (16): 2550-2564.
- [9] C. M. Chen, S. Yang, Wrinkling instabilities in polymer films and their applications, *Polymer International*, 2012, 61 (7): 1041-1047.

- [10] J. Genzer, J. Groenewold, Soft matter with hard skin: From skin wrinkles to templating and material characterization, *Soft Matter*, 2006, 2 (4): 310-323.
- [11] E. P. Chan, A. J. Crosby, Fabricating microlens arrays by surface wrinkling, *Advanced Materials*, 2006, 18 (24): 3238-3242.
- [12] X. Chen, J. Yin, Buckling patterns of thin films on curved compliant substrates with applications to morphogenesis and three-dimensional micro-fabrication, *Soft Matter*, 2010, 6 (22): 5667-5680.
- [13] D. Y. Khang, H. Q. Jiang, Y. Huang, J. A. Rogers, A stretchable form of single-crystal silicon for high-performance electronics on rubber substrates, *Science*, 2006, 311 (5758): 208-212.
- [14] D. Y. Khang, J. A. Rogers, H. H. Lee, Mechanical buckling: Mechanics, metrology, and stretchable electronics, *Advanced Functional Materials*, 2009, 19 (10): 1526-1536.
- [15] S. Lee, S. Kim, T. T. Kim, Y. Kim, M. Choi, S. H. Lee, J. Y. Kim, B. Min, Reversibly stretchable and tunable terahertz metamaterials with wrinkled layouts, *Advanced Materials*, 2012, 24 (26): 3491-3497.
- [16] D. J. Lipomi, B. C. K. Tee, M. Vosgueritchian, Z. N. Bao, Stretchable organic solar cells, *Advanced Materials*, 2011, 23 (15): 1771-1775.
- [17] M. S. White, M. Kaltenbrunner, E. D. Glowacki, K. Gutnichenko, G. Kettlgruber, I. Graz, S. Aazou, C. Ulbricht, D. A. M. Egbe, M. C. Miron, Z. Major, M. C. Scharber, T. Sekitani, T. Someya, S. Bauer, N. S. Sariciftci, Ultrathin, highly flexible and stretchable LEDs, *Nature Photonics*, 2013, 7 (10): 811-816.
- [18] J. B. Kim, P. Kim, N. C. Pegard, S. J. Oh, C. R. Kagan, J. W. Fleischer, H. A. Stone, Y. L.

- Loo, Wrinkles and deep folds as photonic structures in photovoltaics, *Nature Photonics*, 2012, 6 (5): 327-332.
- [19] Y. F. Mei, D. J. Thurmer, F. Cavallo, S. Kiravittaya, O. G. Schmidt, Semiconductor sub-micro-/nanochannel networks by deterministic layer wrinkling, *Advanced Materials*, 2007, 19 (16): 2124-2128.
- [20] S. Chung, J. H. Lee, M. W. Moon, J. Han, R. D. Kamm, Non-lithographic wrinkle nanochannels for protein preconcentration, *Advanced Materials*, 2008, 20 (16): 3011-3016.
- [21] K. Khare, J. H. Zhou, S. Yang, Tunable open-channel microfluidics on soft poly(dimethylsiloxane) (PDMS) substrates with sinusoidal grooves, *Langmuir*, 2009, 25 (21): 12794-12799.
- [22] C. M. Stafford, C. Harrison, K. L. Beers, A. Karim, E. J. Amis, M. R. Vanlandingham, H. C. Kim, W. Volksen, R. D. Miller, E. E. Simonyi, A buckling-based metrology for measuring the elastic moduli of polymeric thin films, *Nature Materials*, 2004, 3 (8): 545-550.
- [23] J. Y. Chung, A. J. Nolte, C. M. Stafford, Surface wrinkling: A versatile platform for measuring thin-film properties, *Advanced Materials*, 2011, 23 (3): 349-368.
- [24] E. A. Wilder, S. Guo, S. Lin-Gibson, M. J. Fasolka, C. M. Stafford, Measuring the modulus of soft polymer networks via a buckling-based metrology, *Macromolecules*, 2006, 39 (12): 4138-4143.
- [25] J. Huang, M. Juskiewicz, W. H. de Jeu, E. Cerda, T. Emrick, N. Menon, T. P. Russell, Capillary wrinkling of floating thin polymer films, *Science*, 2007, 317 (5838): 650-653.

- [26] J. A. Howarter, C. M. Stafford, Instabilities as a measurement tool for soft materials, *Soft Matter*, 2010, 6 (22): 5661-5666.
- [27] C. H. Lu, H. Mohwald, A. Fery, A lithography-free method for directed colloidal crystal assembly based on wrinkling, *Soft Matter*, 2007, 3 (12): 1530-1536.
- [28] A. Schweikart, A. Fery, Controlled wrinkling as a novel method for the fabrication of patterned surfaces, *Microchimica Acta*, 2009, 165 (3-4): 249-263.
- [29] A. Chen, D. K. Lieu, L. Freschauf, V. Lew, H. Sharma, J. X. Wang, D. Nguyen, I. Karakikes, R. J. Hajjar, A. Gopinathan, E. Botvinick, C. C. Fowlkes, R. A. Li, M. Khine, Shrink-film configurable multiscale wrinkles for functional alignment of human embryonic stem cells and their cardiac derivatives, *Advanced Materials*, 2011, 23 (48): 5785-5791.
- [30] M. Guvendiren, J. A. Burdick, Stem cell response to spatially and temporally displayed and reversible surface topography, *Advanced Healthcare Materials*, 2013, 2 (1): 155-164.
- [31] P. C. Lin, S. Vajpayee, A. Jagota, C. Y. Hui, S. Yang, Mechanically tunable dry adhesive from wrinkled elastomers, *Soft Matter*, 2008, 4 (9): 1830-1835.
- [32] E. P. Chan, E. J. Smith, R. C. Hayward, A. J. Crosby, Surface wrinkles for smart adhesion, *Advanced Materials*, 2008, 20 (4): 711-716.
- [33] Y. Rahmawan, C.-M. Chen, S. Yang, Recent advances in wrinkle-based dry adhesion, *Soft Matter*, 2014, 10 (28): 5028-5039.
- [34] J. Y. Chung, J. P. Youngblood, C. M. Stafford, Anisotropic wetting on tunable micro-wrinkled surfaces, *Soft Matter*, 2007, 3 (9): 1163-1169.

- [35] P. C. Lin, S. Yang, Mechanically switchable wetting on wrinkled elastomers with dual-scale roughness, *Soft Matter*, 2009, 5 (5): 1011-1018.
- [36] D. Y. Xia, L. M. Johnson, G. P. Lopez, Anisotropic wetting surfaces with one-dimensional and directional structures: Fabrication approaches, wetting properties and potential applications, *Advanced Materials*, 2012, 24 (10): 1287-1302.
- [37] S. G. Lee, D. Y. Lee, H. S. Lim, D. H. Lee, S. Lee, K. Cho, Switchable transparency and wetting of elastomeric smart windows, *Advanced Materials*, 2010, 22 (44): 5013-5017.
- [38] C. J. Rand, A. J. Crosby, Friction of soft elastomeric wrinkled surfaces, *Journal of Applied Physics*, 2009, 106 (6): 064913.
- [39] J. Kim, J. Yoon, R. C. Hayward, Dynamic display of biomolecular patterns through an elastic creasing instability of stimuli-responsive hydrogels, *Nature Materials*, 2010, 9 (2): 159-164.
- [40] P. Kim, Y. H. Hu, J. Alvarenga, M. Kolle, Z. G. Suo, J. Aizenberg, Rational design of mechano-responsive optical materials by fine tuning the evolution of strain-dependent wrinkling patterns, *Advanced Optical Materials*, 2013, 1 (5): 381-388.
- [41] E. Lee, M. L. Zhang, Y. Cho, Y. Cui, J. Van der Spiegel, N. Engheta, S. Yang, Tilted pillars on wrinkled elastomers as a reversibly tunable optical window, *Advanced Materials*, 2014, 26 (24): 4127-4133.
- [42] B. Kolaric, H. Vandeparre, S. Desprez, R. A. L. Vallee, P. Damman, In situ tuning the optical properties of a cavity by wrinkling, *Applied Physics Letters*, 2010, 96 (4): 043119.
- [43] D. P. Holmes, A. J. Crosby, Snapping surfaces, *Advanced Materials*, 2007, 19 (21):

3589-3593.

- [44] M. Basan, J. F. Joanny, J. Prost, T. Risler, Undulation instability of epithelial tissues, *Physical Review Letters*, 2011, 106 (15): 158101.
- [45] B. Li, F. Jia, Y. P. Cao, X. Q. Feng, H. J. Gao, Surface wrinkling patterns on a core-shell soft sphere, *Physical Review Letters*, 2011, 106 (23): 234301.
- [46] A. Goriely, R. Vandiver, On the mechanical stability of growing arteries, *IMA Journal of Applied Mathematics*, 2010, 75 (4): 549-570.
- [47] Y. Forterre, J. M. Skotheim, J. Dumais, L. Mahadevan, How the venus flytrap snaps, *Nature*, 2005, 433 (7024): 421-425.
- [48] L. Jin, S. Cai, Z. Suo, Creases in soft tissues generated by growth, *Europhysics Letters*, 2011, 95 (6): 64002.
- [49] M. A. Wyczalkowski, Z. Chen, B. A. Filas, V. D. Varner, L. A. Taber, Computational models for mechanics of morphogenesis, *Birth Defects Research Part C-Embryo Today-Reviews*, 2012, 96 (2): 132-152.
- [50] M. Kucken, A. C. Newell, A model for fingerprint formation, *Europhysics Letters*, 2004, 68 (1): 141-146.
- [51] L. Pauchard, Y. Couder, Invagination during the collapse of an inhomogeneous spheroidal shell, *Europhysics Letters*, 2004, 66 (5): 667-673.
- [52] T. Savin, N. A. Kurpios, A. E. Shyer, P. Florescu, H. Y. Liang, L. Mahadevan, C. J. Tabin, On the growth and form of the gut, *Nature*, 2011, 476 (7358): 57-62.
- [53] E. Hannezo, J. Prost, J. F. Joanny, Instabilities of monolayered epithelia: Shape and structure of villi and crypts, *Physical Review Letters*, 2011, 107 (7): 078104.

- [54] A. E. Shyer, T. Tallinen, N. L. Nerurkar, Z. Y. Wei, E. S. Gil, D. L. Kaplan, C. J. Tabin, L. Mahadevan, Villification: How the gut gets its villi, *Science*, 2013, 342 (6155): 212-218.
- [55] M. Ben Amar, F. Jia, Anisotropic growth shapes intestinal tissues during embryogenesis, *Proceedings of the National Academy of Sciences of the United States of America*, 2013, 110 (26): 10525-10530.
- [56] D. P. Richman, R. M. Stewart, J. W. Hutchinson, V. S. Caviness, Mechanical model of brain convolitional development, *Science*, 1975, 189 (4196): 18-21.
- [57] S. Budday, C. Raybaud, E. Kuhl, A mechanical model predicts morphological abnormalities in the developing human brain, *Scientific reports*, 2014, 4 5644.
- [58] P. V. Bayly, L. A. Taber, C. D. Kroenke, Mechanical forces in cerebral cortical folding: A review of measurements and models, *Journal of the Mechanical Behavior of Biomedical Materials*, 2014, 29 568-581.
- [59] M. Ben Amar, C. Chatelain, P. Ciarletta, Contour instabilities in early tumor growth models, *Physical Review Letters*, 2011, 106 (14): 148101.
- [60] W. Yang, T. C. Fung, K. S. Chian, C. K. Chong, Instability of the two-layered thick-walled esophageal model under the external pressure and circular outer boundary condition, *Journal of Biomechanics*, 2007, 40 (3): 481-490.
- [61] B. Li, Y. P. Cao, X. Q. Feng, S. W. Yu, Mucosal wrinkling in animal antra induced by volumetric growth, *Applied Physics Letters*, 2011, 98 (15): 153701.
- [62] B. Li, Y. P. Cao, X. Q. Feng, H. J. Gao, Surface wrinkling of mucosa induced by volumetric growth: Theory, simulation and experiment, *Journal of the Mechanics and Physics of Solids*, 2011, 59 (4): 758-774.

- [63] D. E. Moulton, A. Goriely, Possible role of differential growth in airway wall remodeling in asthma, *Journal of Applied Physiology*, 2011, 110 (4): 1003-1012.
- [64] J. Lidmar, L. Mirny, D. R. Nelson, Virus shapes and buckling transitions in spherical shells, *Physical Review E*, 2003, 68 (5): 051910.
- [65] J. Dumais, C. R. Steele, New evidence for the role of mechanical forces in the shoot apical meristem, *Journal of Plant Growth Regulation*, 2000, 19 (1): 7-18.
- [66] H. Y. Liang, L. Mahadevan, The shape of a long leaf, *Proceedings of the National Academy of Sciences of the United States of America*, 2009, 106 (52): 22049-22054.
- [67] H. Y. Liang, L. Mahadevan, Growth, geometry, and mechanics of a blooming lily, *Proceedings of the National Academy of Sciences of the United States of America*, 2011, 108 (14): 5516-5521.
- [68] S. Armon, E. Efrati, R. Kupferman, E. Sharon, Geometry and mechanics in the opening of chiral seed pods, *Science*, 2011, 333 (6050): 1726-1730.
- [69] P. D. Shipman, A. C. Newell, Phyllotactic patterns on plants, *Physical Review Letters*, 2004, 92 (16): 168102.
- [70] J. Dervaux, M. Ben Amar, Morphogenesis of growing soft tissues, *Physical Review Letters*, 2008, 101 (6): 068101.
- [71] E. Katifori, S. Alben, E. Cerda, D. R. Nelson, J. Dumais, Foldable structures and the natural design of pollen grains, *Proceedings of the National Academy of Sciences of the United States of America*, 2010, 107 (17): 7635-7639.
- [72] J. Yin, Z. X. Cao, C. R. Li, I. Sheinman, X. Chen, Stress-driven buckling patterns in spheroidal core/shell structures, *Proceedings of the National Academy of Sciences of*

- the United States of America*, 2008, 105 (49): 19132-19135.
- [73] E. Hohlfeld, Creasing, post-bifurcations and the spontaneous breakdown of scale invariance, PhD thesis, Harvard University, Cambridge, MA, 2008.
- [74] L. Pocivavsek, R. Dellsy, A. Kern, S. Johnson, B. H. Lin, K. Y. C. Lee, E. Cerda, Stress and fold localization in thin elastic membranes, *Science*, 2008, 320 (5878): 912-916.
- [75] Y. P. Cao, J. W. Hutchinson, Wrinkling phenomena in neo-hookean film/substrate bilayers, *Journal of Applied Mechanics-Transactions of the ASME*, 2012, 79 (3): 031019.
- [76] E. Cerda, L. Mahadevan, Geometry and physics of wrinkling, *Physical Review Letters*, 2003, 90 (7): 074302.
- [77] Z. Y. Huang, W. Hong, Z. Suo, Nonlinear analyses of wrinkles in a film bonded to a compliant substrate, *Journal of the Mechanics and Physics of Solids*, 2005, 53 (9): 2101-2118.
- [78] X. Chen, J. W. Hutchinson, Herringbone buckling patterns of compressed thin films on compliant substrates, *Journal of Applied Mechanics-Transactions of the ASME*, 2004, 71 (5): 597-603.
- [79] K. D. Danov, P. A. Kralchevsky, S. D. Stoyanov, Elastic langmuir layers and membranes subjected to unidirectional compression: Wrinkling and collapse, *Langmuir*, 2010, 26 (1): 143-155.
- [80] K. Efimenko, M. Rackaitis, E. Manias, A. Vaziri, L. Mahadevan, J. Genzer, Nested self-similar wrinkling patterns in skins, *Nature Materials*, 2005, 4 (4): 293-297.
- [81] N. Bowden, S. Brittain, A. G. Evans, J. W. Hutchinson, G. M. Whitesides, Spontaneous

- formation of ordered structures in thin films of metals supported on an elastomeric polymer, *Nature*, 1998, 393 (6681): 146-149.
- [82] S. Cai, D. Breid, A. J. Crosby, Z. Suo, J. W. Hutchinson, Periodic patterns and energy states of buckled films on compliant substrates, *Journal of the Mechanics and Physics of Solids*, 2011, 59 (5): 1094-1114.
- [83] D. Breid, A. J. Crosby, Effect of stress state on wrinkle morphology, *Soft Matter*, 2011, 7 (9): 4490-4496.
- [84] J. Yin, J. L. Yague, D. Eggenpieler, K. K. Gleason, M. C. Boyce, Deterministic order in surface micro-topologies through sequential wrinkling, *Advanced Materials*, 2012, 24 (40): 5441-5446.
- [85] B. Audoly, A. Boudaoud, Buckling of a stiff film bound to a compliant substrate - Part I: Formulation, linear stability of cylindrical patterns, secondary bifurcations, *Journal of the Mechanics and Physics of Solids*, 2008, 56 (7): 2401-2421.
- [86] P.-C. Lin, S. Yang, Spontaneous formation of one-dimensional ripples in transit to highly ordered two-dimensional herringbone structures through sequential and unequal biaxial mechanical stretching, *Applied Physics Letters*, 2007, 90 (24): 241903.
- [87] E. Cerda, K. Ravi-Chandar, L. Mahadevan, Thin films - wrinkling of an elastic sheet under tension, *Nature*, 2002, 419 (6907): 579-580.
- [88] A. Takei, F. Brau, B. Roman, J. Bico, Stretch-induced wrinkles in reinforced membranes: From out-of-plane to in-plane structures, *Europhysics Letters*, 2011, 96 (6): 64001.
- [89] V. Nayyar, K. Ravi-Chandar, R. Huang, Stretch-induced stress patterns and wrinkles

- in hyperelastic thin sheets, *International Journal of Solids and Structures*, 2011, 48 (25-26): 3471-3483.
- [90] A. L. Volynskii, S. Bazhenov, O. V. Lebedeva, N. F. Bakeev, Mechanical buckling instability of thin coatings deposited on soft polymer substrates, *Journal of Materials Science*, 2000, 35 (3): 547-554.
- [91] Y. W. Wong, S. Pellegrino, Wrinkled membranes Part I: Experiments, *Journal of Mechanics of Materials and Structures*, 2006, 1 (1): 3-25.
- [92] P. Ciarletta, M. Destrade, A. L. Gower, Shear instability in skin tissue, *Quarterly Journal of Mechanics and Applied Mathematics*, 2013, 66 (2): 273-288.
- [93] M. Destrade, M. D. Gilchrist, J. A. Motherway, J. G. Murphy, Bimodular rubber buckles early in bending, *Mechanics of Materials*, 2010, 42 (4): 469-476.
- [94] M. Destrade, A. N. Annaidh, C. D. Coman, Bending instabilities of soft biological tissues, *International Journal of Solids and Structures*, 2009, 46 (25-26): 4322-4330.
- [95] J. Y. Sun, S. M. Xia, M. W. Moon, K. H. Oh, K. S. Kim, Folding wrinkles of a thin stiff layer on a soft substrate, *Proceedings of the Royal Society A-Mathematical Physical and Engineering Sciences*, 2012, 468 (2140): 932-953.
- [96] J. L. Nowinski, Surface instability of a half-space under high two-dimensional compression, *Journal of the Franklin Institute*, 1969, 288 (5): 367-376.
- [97] M. A. Biot, Surface instability of rubber in compression, *Applied Scientific Research*, 1963, 12 168-182.
- [98] M. A. Biot, *Mechanics of incremental deformations*, John Wiley & Sons, New York, 1965.

- [99] Q. M. Wang, X. H. Zhao, Phase diagrams of instabilities in compressed film-substrate systems, *Journal of Applied Mechanics-Transactions of the ASME*, 2013, 81 (5): 051004.
- [100] M. A. Biot, Interfacial instability in finite elasticity under initial stress, *Proceedings of the Royal Society A-Mathematical Physical and Engineering Sciences*, 1963, 273 (1352): 340-344.
- [101] J. Groenewold, Wrinkling of plates coupled with soft elastic media, *Physica A*, 2001, 298 (1-2): 32-45.
- [102] H. Q. Jiang, D. Y. Khang, J. Z. Song, Y. G. Sun, Y. G. Huang, J. A. Rogers, Finite deformation mechanics in buckled thin films on compliant supports, *Proceedings of the National Academy of Sciences of the United States of America*, 2007, 104 (40): 15607-15612.
- [103] J. Song, H. Jiang, Z. J. Liu, D. Y. Khang, Y. Huang, J. A. Rogers, C. Lu, C. G. Koh, Buckling of a stiff thin film on a compliant substrate in large deformation, *International Journal of Solids and Structures*, 2008, 45 (10): 3107-3121.
- [104] B. Li, S. Q. Huang, X. Q. Feng, Buckling and postbuckling of a compressed thin film bonded on a soft elastic layer: A three-dimensional analysis, *Archive of Applied Mechanics*, 2010, 80 (2): 175-188.
- [105] A. N. Gent, I. S. Cho, Surface instabilities in compressed or bent rubber blocks, *Rubber Chemistry and Technology*, 1999, 72 (2): 253-262.
- [106] E. Hohlfeld, L. Mahadevan, Unfolding the sulcus, *Physical Review Letters*, 2011, 106 (10): 105702.

- [107] W. Hong, X. H. Zhao, Z. G. Suo, Formation of creases on the surfaces of elastomers and gels, *Applied Physics Letters*, 2009, 95 (11): 111901.
- [108] S. Q. Cai, K. Bertoldi, H. M. Wang, Z. G. Suo, Osmotic collapse of a void in an elastomer: Breathing, buckling and creasing, *Soft Matter*, 2010, 6 (22): 5770-5777.
- [109] W. H. Wong, T. F. Guo, Y. W. Zhang, L. Cheng, Surface instability maps for soft materials, *Soft Matter*, 2010, 6 (22): 5743-5750.
- [110] T. Tallinen, J. S. Biggins, L. Mahadevan, Surface sulci in squeezed soft solids, *Physical Review Letters*, 2013, 110 (2): 024302.
- [111] W. Hong, F. Gao, Crease instability on the surface of a solid, in: X. Chen (Ed.) *Mechanical self-assembly*, Springer, New York, 2013, 111-130.
- [112] V. Trujillo, J. Kim, R. C. Hayward, Creasing instability of surface-attached hydrogels, *Soft Matter*, 2008, 4 (3): 564-569.
- [113] S. Q. Cai, D. Y. Chen, Z. G. Suo, R. C. Hayward, Creasing instability of elastomer films, *Soft Matter*, 2012, 8 (5): 1301-1304.
- [114] A. Ghatak, A. L. Das, Kink instability of a highly deformable elastic cylinder, *Physical Review Letters*, 2007, 99 (7): 076101.
- [115] S. Mora, M. Abkarian, H. Tabuteau, Y. Pomeau, Surface instability of soft solids under strain, *Soft Matter*, 2011, 7 (22): 10612-10619.
- [116] B. Xu, D. Chen, R. C. Hayward, Mechanically gated electrical switches by creasing of patterned metal/elastomer bilayer films, *Advanced Materials*, 2014, 26 (25): 4381-4385.
- [117] T. Tanaka, Kinetics of phase transition in polymer gels, *Physica A*, 1986, 140 (1-2):

261-268.

- [118] T. Tanaka, S. T. Sun, Y. Hirokawa, S. Katayama, J. Kucera, Y. Hirose, T. Amiya, Mechanical instability of gels at the phase transition, *Nature*, 1987, 325 (6107): 796-798.
- [119] J. Yoon, J. Kim, R. C. Hayward, Nucleation, growth, and hysteresis of surface creases on swelled polymer gels, *Soft Matter*, 2010, 6 (22): 5807-5816.
- [120] M. Guvendiren, J. A. Burdick, S. Yang, Solvent induced transition from wrinkles to creases in thin film gels with depth-wise crosslinking gradients, *Soft Matter*, 2010, 6 (22): 5795-5801.
- [121] O. Ortiz, A. Vidyasagar, J. Wang, R. Toomey, Surface instabilities in ultrathin, cross-linked poly(n-isopropylacrylamide) coatings, *Langmuir*, 2010, 26 (22): 17489-17494.
- [122] J. Dervaux, Y. Couder, M. A. Guedeau-Boudeville, M. Ben Amar, Shape transition in artificial tumors: From smooth buckles to singular creases, *Physical Review Letters*, 2011, 107 (1): 018103.
- [123] J. Dervaux, M. Ben Amar, Mechanical instabilities of gels, *Annual Review of Condensed Matter Physics*, 2012, 3 311-332.
- [124] M. Arifuzzaman, Z. L. Wu, T. Kurokawa, A. Kakugo, J. P. Gong, Swelling-induced long-range ordered structure formation in polyelectrolyte hydrogel, *Soft Matter*, 2012, 8 (31): 8060-8066.
- [125] W. Barros, E. N. de Azevedo, M. Engelsberg, Surface pattern formation in a swelling gel, *Soft Matter*, 2012, 8 (32): 8511-8516.

- [126] A. Pandey, D. P. Holmes, Swelling-induced deformations: A materials-defined transition from macroscale to microscale deformations, *Soft Matter*, 2013, 9 (23): 5524-5528.
- [127] F. Weiss, S. Cai, Y. Hu, M. K. Kang, R. Huang, Z. Suo, Creases and wrinkles on the surface of a swollen gel, *Journal of Applied Physics*, 2013, 114 073507.
- [128] N. Zalachas, S. Q. Cai, Z. G. Suo, Y. Lapusta, Crease in a ring of a pH-sensitive hydrogel swelling under constraint, *International Journal of Solids and Structures*, 2013, 50 (6): 920-927.
- [129] J. Kim, Morphological analysis of crease patterns formed on surface-attached hydrogel with a gradient in thickness, *Journal of Applied Polymer Science*, 2014, 131 (13): 40482.
- [130] Q. M. Wang, L. Zhang, X. H. Zhao, Creasing to cratering instability in polymers under ultrahigh electric fields, *Physical Review Letters*, 2011, 106 (11): 118301.
- [131] Q. M. Wang, X. F. Niu, Q. B. Pei, M. D. Dickey, X. H. Zhao, Electromechanical instabilities of thermoplastics: Theory and in situ observation, *Applied Physics Letters*, 2012, 101 (14): 141911.
- [132] Q. M. Wang, X. H. Zhao, Creasing-wrinkling transition in elastomer films under electric fields, *Physical Review E*, 2013, 88 (4): 042403.
- [133] H. S. Park, Q. M. Wang, X. H. Zhao, P. A. Klein, Electromechanical instability on dielectric polymer surface: Modeling and experiment, *Computer Methods in Applied Mechanics and Engineering*, 2013, 260 40-49.
- [134] B. Xu, R. C. Hayward, Low-voltage switching of crease patterns on hydrogel surfaces,

*Advanced Materials*, 2013, 25 (39): 5555-5559.

- [135] Q. Wang, D. Robinson, X. Zhao, On-demand hierarchical patterning with electric fields, *Applied Physics Letters*, 2014, 104 (23): 231605.
- [136] J. Yoon, P. Bian, J. Kim, T. J. McCarthy, R. C. Hayward, Local switching of chemical patterns through light-triggered unfolding of creased hydrogel surfaces, *Angewandte Chemie-international Edition*, 2012, 51 (29): 7146-7149.
- [137] P. Gabriel, Y. Fukahori, A. G. Thomas, J. J. C. Busfield, FEA modeling of schallamach waves, *Rubber Chemistry and Technology*, 2010, 83 (4): 358-367.
- [138] D. Y. Chen, S. Q. Cai, Z. G. Suo, R. C. Hayward, Surface energy as a barrier to creasing of elastomer films: An elastic analogy to classical nucleation, *Physical Review Letters*, 2012, 109 (3): 038001.
- [139] E. Hohlfeld, L. Mahadevan, Scale and nature of sulcification patterns, *Physical Review Letters*, 2012, 109 (2): 025701.
- [140] L. Jin, D. Chen, R. C. Hayward, Z. Suo, Creases on the interface between two soft materials, *Soft Matter*, 2014, 10 (2): 303-311.
- [141] K. Saha, J. Kim, E. Irwin, J. Yoon, F. Momin, V. Trujillo, D. V. Schaffer, K. E. Healy, R. C. Hayward, Surface creasing instability of soft polyacrylamide cell culture substrates, *Biophysical Journal*, 2010, 99 (12): 94-96.
- [142] E. P. Chan, J. M. Karp, R. S. Langer, A "self-pinning" adhesive based on responsive surface wrinkles, *Journal of Polymer Science Part B-Polymer Physics*, 2011, 49 (1): 40-44.
- [143] P. Shivapooja, Q. Wang, B. Orihuela, D. Rittschof, G. P. Lopez, X. Zhao, Bioinspired

- surfaces with dynamic topography for active control of biofouling, *Advanced Materials*, 2013, 25 (10): 1430-1434.
- [144] L. Pocivavsek, B. Leahy, N. Holten-Andersen, B. Lin, K. Y. C. Lee, E. Cerda, Geometric tools for complex interfaces: From lung surfactant to the mussel byssus, *Soft Matter*, 2009, 5 (10): 1963-1968.
- [145] F. Brau, H. Vandeparre, A. Sabbah, C. Poulard, A. Boudaoud, P. Damman, Multiple-length-scale elastic instability mimics parametric resonance of nonlinear oscillators, *Nature Physics*, 2011, 7 (1): 56-60.
- [146] P. Kim, M. Abkarian, H. A. Stone, Hierarchical folding of elastic membranes under biaxial compressive stress, *Nature Materials*, 2011, 10 (12): 952-957.
- [147] F. Brau, P. Damman, H. Diamant, T. A. Witten, Wrinkle to fold transition: Influence of the substrate response, *Soft Matter*, 2013, 9 (34): 8177-8186.
- [148] Y. Ebata, A. B. Croll, A. J. Crosby, Wrinkling and strain localizations in polymer thin films, *Soft Matter*, 2012, 8 (35): 9086-9091.
- [149] B. Audoly, Localized buckling of a floating elastica, *Physical Review E*, 2011, 84 (1): 011605.
- [150] A. B. Croll, A. J. Crosby, Pattern driven stress localization in thin diblock copolymer films, *Macromolecules*, 2012, 45 (9): 4001-4006.
- [151] D. P. Holmes, A. J. Crosby, Draping films: A wrinkle to fold transition, *Physical Review Letters*, 2010, 105 (3): 038303.
- [152] B. D. Leahy, L. Pocivavsek, M. Meron, K. L. Lam, D. Salas, P. J. Viccaro, K. Y. C. Lee, B. Lin, Geometric stability and elastic response of a supported nanoparticle film,

- Physical Review Letters*, 2010, 105 (5): 058301.
- [153] P. M. Reis, F. Corson, A. Boudaoud, B. Roman, Localization through surface folding in solid foams under compression, *Physical Review Letters*, 2009, 103 (4): 045501.
- [154] H. Diamant, T. A. Witten, Compression induced folding of a sheet: An integrable system, *Physical Review Letters*, 2011, 107 (16): 164302.
- [155] J. Zang, X. Zhao, Y. Cao, J. W. Hutchinson, Localized ridge wrinkling of stiff films on compliant substrates, *Journal of the Mechanics and Physics of Solids*, 2012, 60 (7): 1265-1279.
- [156] C. Cao, H. F. Chan, J. Zang, K. W. Leong, X. Zhao, Harnessing localized ridges for high-aspect-ratio hierarchical patterns with dynamic tunability and multifunctionality, *Advanced Materials*, 2014, 26 (11): 1763-1770.
- [157] A. Takei, L. Jin, J. W. Hutchinson, H. Fujita, Ridge localizations and networks in thin films compressed by the incremental release of a large equi-biaxial pre-stretch in the substrate, *Advanced Materials*, 2014, 26 (24): 4061-4067.
- [158] Y. C. Chen, A. J. Crosby, High aspect ratio wrinkles via substrate prestretch, *Advanced Materials*, 2014, 26 (32): 5626-5631.
- [159] B. Li, Y.-P. Cao, X.-Q. Feng, Growth and surface folding of esophageal mucosa: A biomechanical model, *Journal of Biomechanics*, 2011, 44 (1): 182-188.
- [160] J. Dervaux, M. Ben Amar, Buckling condensation in constrained growth, *Journal of the Mechanics and Physics of Solids*, 2011, 59 (3): 538-560.
- [161] M. Ben Amar, A. Goriely, Growth and instability in elastic tissues, *Journal of the Mechanics and Physics of Solids*, 2005, 53 (10): 2284-2319.

- [162] B. R. Wiggs, C. A. Hrousis, J. M. Drazen, R. D. Kamm, On the mechanism of mucosal folding in normal and asthmatic airways, *Journal of Applied Physiology*, 1997, 83 (6): 1814-1821.
- [163] C. A. Hrousis, B. J. R. Wiggs, J. M. Drazen, D. M. Parks, R. D. Kamm, Mucosal folding in biologic vessels, *Journal of Biomechanical Engineering-Transactions of the ASME*, 2002, 124 (4): 334-341.
- [164] Y. P. Cao, J. W. Hutchinson, From wrinkles to creases in elastomers: The instability and imperfection-sensitivity of wrinkling, *Proceedings of the Royal Society A-Mathematical Physical and Engineering Sciences*, 2012, 468 (2137): 94-115.
- [165] E. K. Rodriguez, A. Hoger, A. D. McCulloch, Stress-dependent finite growth in soft elastic tissues, *Journal of Biomechanics*, 1994, 27 (4): 455-467.
- [166] R. Skalak, S. Zargaryan, R. K. Jain, P. A. Netti, A. Hoger, Compatibility and the genesis of residual stress by volumetric growth, *Journal of Mathematical Biology*, 1996, 34 (8): 889-914.
- [167] R. Skalak, Growth as a finite displacement field, in: D.E. Carlson, R.T. Shield (Eds.) *Proceedings of the IUTAM Symposium on Finite Elasticity*, Martinus Nijhoff Publishers, Lehigh University, 1980: 347-355.
- [168] D. E. Moulton, A. Goriely, Circumferential buckling instability of a growing cylindrical tube, *Journal of the Mechanics and Physics of Solids*, 2011, 59 (3): 525-537.
- [169] E. Hohlfeld, Coexistence of scale-invariant states in incompressible elastomers, *Physical Review Letters*, 2013, 111 (18): 185701.
- [170] J. W. Hutchinson, The role of nonlinear substrate elasticity in the wrinkling of thin

- films, *Philosophical Transactions of the Royal Society A-Mathematical Physical and Engineering Sciences*, 2013, 371 (1993): 20120422.
- [171] M. Z. Diab, T. Zhang, R. K. Zhao, H. J. Gao, K. S. Kim, Ruga mechanics of creasing: From instantaneous to setback creases, *Proceedings of the Royal Society A-Mathematical Physical and Engineering Sciences*, 2013, 469 (2157): 20120753.
- [172] Z. G. Wu, N. Bouklas, R. Huang, Swell-induced surface instability of hydrogel layers with material properties varying in thickness direction, *International Journal of Solids and Structures*, 2013, 50 (3-4): 578-587.
- [173] D. Chen, L. Jin, Z. Suo, R. C. Hayward, Controlled formation and disappearance of creases, *Materials Horizons*, 2014, 1 (2): 207-213.
- [174] Y. C. Fung, *Biomechanics: Material properties of living tissues*, Springer, New York 1993.
- [175] L. R. G. Treloar, *The physics of rubber elasticity* (third edition), Clarendon Press, Oxford, 1975.
- [176] A. N. Gent, A new constitutive relation for rubber, *Rubber Chemistry and Technology*, 1996, 69 (1): 59-61.
- [177] G. A. Holzapfel, *Nonlinear solid mechanics: A continuum approach for engineering*, John Wiley & Sons, Chichester, 2000.
- [178] A. N. Stroh, Dislocations and cracks in anisotropic elasticity, *Philosophical Magazine*, 1958, 3 (30): 625-646.
- [179] Z. G. Suo, Singularities interfaces and cracks in dissimilar anisotropic media, *Proceedings of the Royal Society A-Mathematical Physical and Engineering Sciences*,

- 1990, 427 (1873): 331-358.
- [180] Z. Suo, M. Ortiz, A. Needleman, Stability of solids with interfaces, *Journal of the Mechanics and Physics of Solids*, 1992, 40 (3): 613-640.
- [181] G. F. Carrier, M. Krook, C. E. Pearson, Functions of a complex variable: Theory and technique, Hod Books, Ithaca, 1983.
- [182] G. A. Holzapfel, Biomechanics of soft tissue, in: J. Lemaitre (Ed.), *The handbook of materials behavior models, Volume III, Multiphysics behaviors*, Academic Press, Boston, 2001: 1049-1063.
- [183] M. G. Dunn, F. H. Silver, D. A. Swann, Mechanical analysis of hypertrophic scar tissue: Structural basis for apparent increased rigidity, *Journal of Investigative Dermatology*, 1985, 84 (1): 9-13.
- [184] Y.-L. Pi, M. Bradford, B. Uy, In-plane stability of arches, *International Journal of Solids and Structures*, 2002, 39 (1): 105-125.
- [185] P. Yang, R. M. Baker, J. H. Henderson, P. T. Mather, In vitro wrinkle formation via shape memory dynamically aligns adherent cells, *Soft Matter*, 2013, 9 (18): 4705-4714.
- [186] H. Lee, C. Xia, N. X. Fang, First jump of microgel; actuation speed enhancement by elastic instability, *Soft Matter*, 2010, 6 (18): 4342-4345.
- [187] C. Keplinger, T. Li, R. Baumgartner, Z. Suo, S. Bauer, Harnessing snap-through instability in soft dielectrics to achieve giant voltage-triggered deformation, *Soft Matter*, 2012, 8 (2): 285-288.
- [188] Q. Wang, M. Tahir, J. Zang, X. Zhao, Dynamic electrostatic lithography: Multiscale on-demand patterning on large-area curved surfaces, *Advanced Materials*, 2012, 24

- (15): 1947-1951.
- [189] E. Riks, The application of newton's method to the problem of elastic stability, *Journal of Applied Mechanics-Transactions of the ASME*, 1972, 39 (4): 1060-1065.
- [190] J. He, G. H. Xu, Z. Suo, Experimental determination of crack driving forces in integrated structures, *AIP Conference Proceedings*, 2004, 741 (1): 3-14.
- [191] A. N. Gent, Adhesion and strength of viscoelastic solids. Is there a relationship between adhesion and bulk properties, *Langmuir*, 1996, 12 (19): 4492-4496.
- [192] C. Mueller, A. Gorius, S. Nazarenko, A. Hiltner, E. Baer, Single fiber microbuckling in a model composite, *Journal of Composite Materials*, 1996, 30 (17): 1912-1921.
- [193] G. B. Brietzke, A. Cochard, H. Igel, Importance of bimaterial interfaces for earthquake dynamics and strong ground motion, *Geophysical Journal International*, 2009, 178 (2): 921-938.
- [194] A. N. Guz, V. N. Chekhov, Problems of folding in the earth's stratified crust, *International Applied Mechanics*, 2007, 43 (2): 127-159.
- [195] Y. G. Sun, J. A. Rogers, Inorganic semiconductors for flexible electronics, *Advanced Materials*, 2007, 19 (15): 1897-1916.
- [196] P. B. Noble, A. R. West, R. A. McLaughlin, J. J. Armstrong, S. Becker, P. K. McFawn, J. P. Williamson, P. R. Eastwood, D. R. Hillman, D. D. Sampson, H. W. Mitchell, Airway narrowing assessed by anatomical optical coherence tomography in vitro: Dynamic airway wall morphology and function, *Journal of Applied Physiology*, 2010, 108 (2): 401-411.
- [197] I. Tokarev, S. Minko, Stimuli-responsive hydrogel thin films, *Soft Matter*, 2009, 5 (3):

511-524.

- [198] J. S. Wang, A. G. Evans, Effects of strain cycling on buckling, cracking and spalling of a thermally grown alumina on a nickel-based bond coat, *Acta Materialia*, 1999, 47 (2): 699-710.
- [199] D. R. Mumm, A. G. Evans, I. T. Spitsberg, Characterization of a cyclic displacement instability for a thermally grown oxide in a thermal barrier system, *Acta Materialia*, 2001, 49 (12): 2329-2340.
- [200] S. H. Im, R. Huang, Ratcheting-induced wrinkling of an elastic film on a metal layer under cyclic temperatures, *Acta Materialia*, 2004, 52 (12): 3707-3719.
- [201] K. J. Zhao, M. Pharr, Q. Wan, W. L. Wang, E. Kaxiras, J. J. Vlassak, Z. G. Suo, Concurrent reaction and plasticity during initial lithiation of crystalline silicon in lithium-ion batteries, *Journal of the Electrochemical Society*, 2012, 159 (3): A238-A243.
- [202] J. S. Huang, J. Liu, B. Kroll, K. Bertoldi, D. R. Clarke, Spontaneous and deterministic three-dimensional curling of pre-strained elastomeric bi-strips, *Soft Matter*, 2012, 8 (23): 6291-6300.
- [203] M. I. Darby, V. N. Kanellopoulos, Theory of fiber buckling in carbon-fiber reinforced-plastics, *Journal of Physics D-Applied Physics*, 1987, 20 (3): 298-302.
- [204] S. R. Choi, J. W. Hutchinson, A. G. Evans, Delamination of multilayer thermal barrier coatings, *Mechanics of Materials*, 1999, 31 (7): 431-447.
- [205] M. A. Biot, Continuum theory of stability of embedded layer in finite elasticity under initial stress, *Quarterly Journal of Mechanics and Applied Mathematics*, 1964, 17 (1):

17-22.

- [206] R. Stoneley, Elastic waves at the surface of separation of two solids, *Proceedings of the Royal Society A-Mathematical Physical and Engineering Sciences*, 1924, 106 (738): 416-428.
- [207] D. M. Barnett, J. Lothe, S. D. Gavazza, M. J. P. Musgrave, Considerations of the existence of interfacial (stoneley) waves in bonded anisotropic elastic half-spaces, *Proceedings of the Royal Society A-Mathematical Physical and Engineering Sciences*, 1985, 402 (1822): 153-166.
- [208] D. M. Barnett, Bulk, surface, and interfacial waves in anisotropic linear elastic solids, *International Journal of Solids and Structures*, 2000, 37 (1-2): 45-54.
- [209] L. Rayleigh, On waves propagated along the plane surfaces of an elastic solid, *Proceedings of the London Mathematical Society*, 1885, 1 (1): 4-11.
- [210] K. Worden, Rayleigh and lamb waves - basic principles, *Strain*, 2001, 37 (4): 167-172.
- [211] S. P. Obukhov, M. Rubinstein, R. H. Colby, Network modulus and superelasticity, *Macromolecules*, 1994, 27 (12): 3191-3198.
- [212] J. Kim, J. A. Hanna, M. Byun, C. D. Santangelo, R. C. Hayward, Designing responsive buckled surfaces by halftone gel lithography, *Science*, 2012, 335 (6073): 1201-1205.
- [213] E. Sultan, A. Boudaoud, The buckling of a swollen thin gel layer bound to a compliant substrate, *Journal of Applied Mechanics-Transactions of the ASME*, 2008, 75 (5): 051002.
- [214] D. H. Kim, N. S. Lu, R. Ma, Y. S. Kim, R. H. Kim, S. D. Wang, J. Wu, S. M. Won, H. Tao, A. Islam, K. J. Yu, T. I. Kim, R. Chowdhury, M. Ying, L. Z. Xu, M. Li, H. J. Chung,

- H. Keum, M. McCormick, P. Liu, Y. W. Zhang, F. G. Omenetto, Y. G. Huang, T. Coleman, J. A. Rogers, Epidermal electronics, *Science*, 2011, 333 (6044): 838-843.
- [215] C. Keplinger, J. Y. Sun, C. C. Foo, P. Rothmund, G. M. Whitesides, Z. G. Suo, Stretchable, transparent, ionic conductors, *Science*, 2013, 341 (6149): 984-987.
- [216] M. Kolle, A. Lethbridge, M. Kreysing, J. J. Baumberg, J. Aizenberg, P. Vukusic, Bio-inspired band-gap tunable elastic optical multilayer fibers, *Advanced Materials*, 2013, 25 (15): 2239-2245.
- [217] R. W. Ogden, Non-linear elastic deformation, Dover Publications, New York, 1997.
- [218] J. A. Rogers, T. Someya, Y. Huang, Materials and mechanics for stretchable electronics, *Science*, 2010, 327 (5973): 1603-1607.
- [219] K. Anselme, P. Davidson, A. M. Popa, M. Giazzon, M. Liley, L. Ploux, The interaction of cells and bacteria with surfaces structured at the nanometre scale, *Acta Biomaterialia*, 2010, 6 (10): 3824-3846.
- [220] R. Huang, H. Yin, J. Liang, J. C. Sturm, K. D. Hobart, Z. Suo, Mechanics of relaxing SiGe islands on a viscous glass, *Acta Mechanica Sinica*, 2002, 18 (5): 441-456.
- [221] J. Song, D. Tranchida, G. J. Vancso, Contact mechanics of uv/ozone-treated PDMS by AFM and JKR testing: Mechanical performance from nano- to micrometer length scales, *Macromolecules*, 2008, 41 (18): 6757-6762.
- [222] R. M. May, Simple mathematical-models with very complicated dynamics, *Nature*, 1976, 261 (5560): 459-467.
- [223] J. Testa, J. Pérez, C. Jeffries, Evidence for universal chaotic behavior of a driven nonlinear oscillator, *Physical Review Letters*, 1982, 48 (11): 714-717.

- [224] R. C. Hilborn, *Chaos and nonlinear dynamics: An introduction for scientists and engineers*, Oxford university press, Oxford, 2000.
- [225] C. Badre, J. P. Chapel, S. Yang, Selective dry and reversible transfer-printing of nanoparticles on top of PDMS wrinkles, *Soft Matter*, 2011, 7 (21): 9886-9889.
- [226] D. Vella, J. Bico, A. Boudaoud, B. Roman, P. M. Reis, The macroscopic delamination of thin films from elastic substrates, *Proceedings of the National Academy of Sciences of the United States of America*, 2009, 106 (27): 10901-10906.
- [227] J. Zang, S. Ryu, N. Pugno, Q. Wang, Q. Tu, M. J. Buehler, X. Zhao, Multifunctionality and control of the crumpling and unfolding of large-area graphene, *Nature Materials*, 2013, 12 (4): 321-325.
- [228] M. Staykova, D. P. Holmes, C. Read, H. A. Stone, Mechanics of surface area regulation in cells examined with confined lipid membranes, *Proceedings of the National Academy of Sciences of the United States of America*, 2011, 108 (22): 9084-9088.
- [229] M. Guvendiren, S. Yang, J. A. Burdick, Swelling-induced surface patterns in hydrogels with gradient crosslinking density, *Advanced Functional Materials*, 2009, 19 (19): 3038-3045.
- [230] D. Breid, A. J. Crosby, Curvature-controlled wrinkle morphologies, *Soft Matter*, 2013, 9 (13): 3624-3630.
- [231] S. Dabral, J. Vanetten, X. Zhang, C. Applett, G. R. Yang, P. Ficalora, J. F. McDonald, Stress in thermally annealed parylene films, *Journal of Electronic Materials*, 1992, 21 (10): 989-994.

- [232] A. Auguste, L. Jin, Z. Suo, R. C. Hayward, The role of substrate pre-stretch in post-wrinkling bifurcations, *Soft Matter*, 2014, 10 (34): 6520-6529.
- [233] B. Budiansky, J. W. Hutchinson, Dynamic buckling of imperfection-sensitive structures, in: H. Gortler (Ed.) *Proceedings of the Eleventh International Congress of Applied Mechanics*, Springer-Verlag, Munich, Germany, 1964: 637-651.
- [234] A. M. A. van der Heijden, W. T. Koiter's elastic stability of solids and structures, Cambridge University Press, New York, 2009.
- [235] P. Wang, J. M. Shim, K. Bertoldi, Effects of geometric and material nonlinearities on tunable band gaps and low-frequency directionality of phononic crystals, *Physical Review B*, 2013, 88 (1): 014304.
- [236] W. Wilson, An explanation for the onset of mechanically induced cartilage damage, PhD thesis, Technische Universiteit Eindhoven, Eindhoven, 2005.
- [237] G. G. Stoney, The tension of metallic films deposited by electrolysis, *Proceedings of the Royal Society A-Mathematical Physical and Engineering Sciences*, 1909, 82 (553): 172-175.
- [238] X. Feng, Y. Huang, A. Rosakis, On the Stoney formula for a thin film/substrate system with nonuniform substrate thickness, *Journal of Applied Mechanics*, 2007, 74 (6): 1276-1281.

# Appendix

## Appendix A Supporting information for Chapter 3

### A.1 Implementation of the Gent material in ABAQUS

We implement the Gent model in the finite element software ABAQUS by writing a user-defined material subroutine, UMAT. We use a compressible form of the Gent free energy density [235]

$$\psi = -\frac{\mu}{2} J_{\text{lim}} \log\left(1 - \frac{J_1}{J_{\text{lim}}}\right) - \mu \log(J) + \left(\frac{K}{2} - \frac{\mu}{J_{\text{lim}}}\right) (J-1)^2, \quad (\text{A.1})$$

where  $J = \det(\mathbf{F})$  and the parameter  $K$  is the bulk modulus. The last two terms in (A.1) is the energy density related to a volume change, and they are non-zero when  $J \neq 1$ . The incompressible Gent material (3.6) can be recovered in the limit,  $K/\mu \rightarrow \infty$ .

In the user subroutine UMAT, the Cauchy stress tensor  $\boldsymbol{\sigma}$ , defined as  $\boldsymbol{\sigma} = \frac{1}{J} \frac{\partial \psi}{\partial \mathbf{F}} \mathbf{F}^T$ , is implemented as

$$\sigma_{ij} = \frac{\mu J^{-1}}{1 - J_1/J_{\text{lim}}} F_{iK} F_{jK} + \left(2 \left(\frac{K}{2} - \frac{\mu}{J_{\text{lim}}}\right) (J-1) - \frac{\mu}{J}\right) \delta_{ij}. \quad (\text{A.2})$$

The fourth order Jacobian tensor  $\mathbf{D}$  is defined as

$$\delta(J\sigma_{ij}) = JD_{ijmn} (\delta F_{mK} H_{nK} + \delta F_{nK} H_{mK})/2, \quad (\text{A.3})$$

which can be calculated as [236]

$$D_{ijmn} = \left( \sigma_{ij} H_{nK} + \frac{\delta \sigma_{ij}}{\delta F_{nK}} \right) F_{mK}. \quad (\text{A.4})$$

For a Gent material, it can be derived that

$$\begin{aligned} \frac{\delta\sigma_{ij}}{\delta F_{nK}} = & \frac{\mu J^{-1}}{1 - J_1 / J_{\text{lim}}} (\delta_{in} F_{jK} + \delta_{jn} F_{iK}) + \frac{2\mu J_{\text{lim}}^{-1} J^{-1}}{(1 - J_1 / J_{\text{lim}})^2} F_{iL} F_{jL} F_{nK} \\ & + \left( \left( J \left( K - \frac{2\mu}{J_{\text{lim}}} \right) + \frac{\mu}{J} \right) \delta_{ij} - \frac{\mu J^{-1}}{1 - J_1 / J_{\text{lim}}} F_{iL} F_{jL} \right) H_{nK}. \end{aligned} \quad (\text{A.5})$$

Substituting (A.2) and (A.5) into (A.4), we can calculate the Jacobian tensor.

In the ABAQUS subroutine UMAT, we need to implement the Cauchy stress tensor (A.2), the Jacobian tensor (A.4), and the free energy density (A.1). The UMAT checks how far the state is from the limiting stretch for every material particle in every increment to ensure that the state stays within the limit  $J_1 = J_{\text{lim}}$ . We implement this requirement in the UMAT as follows. The calculation is conducted incrementally. After the UMAT finishes the calculation at a given increment, if  $J_{\text{lim}} - J_1 < 1e-3$ , the UMAT abandons the original increment, and attempts the calculation again with an increment half of the original one. Then the UMAT checks the criterion  $J_{\text{lim}} - J_1 < 1e-3$  again. The UMAT attempts to satisfy the criterion  $J_{\text{lim}} - J_1 < 1e-3$  for a maximal times, say 5 times; if not, the UMAT aborts the simulation.

## A.2 Tangent moduli $\mathbf{C}$ and matrices $\mathbf{A}$ , $\mathbf{Q}$ and $\mathbf{L}$ of the Gent materials

When the material is specified as an incompressible Gent material with free energy as shown in (3.6), according to (3.17), we obtain the tensor of tangent moduli:

$$C_{iKjL} = \frac{\mu}{1 - J_1 / J_{\text{lim}}} \delta_{ij} \delta_{KL} + \frac{2\mu J_{\text{lim}}^{-1}}{(1 - J_1 / J_{\text{lim}})^2} F_{iK}^0 F_{jL}^0 + \Pi H_{iL}^0 H_{jK}^0. \quad (\text{A.6})$$

The field of finite deformation before perturbation is under a homogeneous plane strain condition, and the principal stretches are in the directions coinciding with  $X_1, X_2$  and  $X_3$ .

Consequently,  $\mathbf{F}^0 = \text{diag}(\lambda, 1, \lambda^{-1})$ ,  $\mathbf{H}^0 = \text{diag}(\lambda^{-1}, 1, \lambda)$ . The hydrostatic pressure  $\Pi^0$  is

determined by the boundary condition  $s_{33}=0$ , and according to (3.7), we get

$\Pi^0 = \mu\lambda^{-2}/(1-J_1/J_{\text{lim}})$ . The tangent moduli reduce to the following nonzero elements:

$$C_{1111} = \frac{\mu(1+\lambda^{-4})}{1-J_1/J_{\text{lim}}} + \frac{2\mu\lambda^2 J_{\text{lim}}^{-1}}{(1-J_1/J_{\text{lim}})^2}, \quad C_{2222} = \frac{\mu(1+\lambda^{-2})}{1-J_1/J_{\text{lim}}} + \frac{2\mu J_{\text{lim}}^{-1}}{(1-J_1/J_{\text{lim}})^2},$$

$$C_{3333} = \frac{2\mu}{1-J_1/J_{\text{lim}}} + \frac{2\mu\lambda^{-2} J_{\text{lim}}^{-1}}{(1-J_1/J_{\text{lim}})^2}, \quad (\text{A.7})$$

$$C_{1212} = C_{2121} = C_{1313} = C_{3131} = C_{3232} = C_{2323} = \frac{\mu}{1-J_1/J_{\text{lim}}}, \quad (\text{A.8})$$

$$C_{1122} = C_{2211} = \frac{2\mu\lambda J_{\text{lim}}^{-1}}{(1-J_1/J_{\text{lim}})^2}, \quad C_{1133} = C_{3311} = \frac{2\mu J_{\text{lim}}^{-1}}{(1-J_1/J_{\text{lim}})^2},$$

$$C_{2233} = C_{3322} = \frac{2\mu\lambda^{-1} J_{\text{lim}}^{-1}}{(1-J_1/J_{\text{lim}})^2}, \quad (\text{A.9})$$

$$C_{2112} = C_{1221} = \frac{\mu\lambda^{-3}}{1-J_1/J_{\text{lim}}}, \quad C_{3113} = C_{1331} = \frac{\mu\lambda^{-2}}{1-J_1/J_{\text{lim}}},$$

$$C_{3223} = C_{2332} = \frac{\mu\lambda^{-1}}{1-J_1/J_{\text{lim}}}. \quad (\text{A.10})$$

Next we substitute (A.7)-(A.10) to the Stroh formalism. The complex numbers  $p_1$  and  $p_3$  are determined by (3.24), which is specialized to

$$\lambda^2 p^4 + g(\lambda)p^2 + \lambda^{-2} = 0, \quad (\text{A.11})$$

where

$$g(\lambda) = \frac{2}{J_{\text{lim}} - J_1} (\lambda^4 + \lambda^{-4} - 2) + \lambda^2 + \lambda^{-2}. \quad (\text{A.12})$$

The two roots with positive imaginary part of the above equation are

$$p_1 = i\sqrt{\frac{g(\lambda) + \sqrt{g(\lambda)^2 - 4}}{2\lambda^2}}, \quad p_3 = i\sqrt{\frac{g(\lambda) - \sqrt{g(\lambda)^2 - 4}}{2\lambda^2}}. \quad (\text{A.13})$$

The components of the matrices  $A_{i\alpha}$ ,  $Q_\alpha$  and  $L_{i\alpha}$  for the in-plane deformation are

$$A_{11} = p_1, \quad A_{13} = p_3, \quad A_{31} = -\lambda^{-2}, \quad A_{33} = -\lambda^{-2}; \quad (\text{A.14})$$

$$Q_1 = \frac{\mu \lambda p_1}{1 - J_1 / J_{\text{lim}}} \left[ (1 + p_1^2) + \frac{2}{J_{\text{lim}} - J_1} (\lambda^2 - \lambda^{-2}) \right],$$

$$Q_3 = \frac{\mu \lambda p_3}{1 - J_1 / J_{\text{lim}}} \left[ (1 + p_3^2) + \frac{2}{J_{\text{lim}} - J_1} (\lambda^2 - \lambda^{-2}) \right]; \quad (\text{A.15})$$

$$L_{11} = \frac{\mu}{1 - J_1 / J_{\text{lim}}} (p_1^2 - \lambda^{-4}), \quad L_{13} = \frac{\mu}{1 - J_1 / J_{\text{lim}}} (p_3^2 - \lambda^{-4}),$$

$$L_{31} = -\frac{\mu p_1}{1 - J_1 / J_{\text{lim}}} (g(\lambda) + \lambda^{-2} + \lambda^2 p_1^2), \quad L_{33} = -\frac{\mu p_3}{1 - J_1 / J_{\text{lim}}} (g(\lambda) + \lambda^{-2} + \lambda^2 p_3^2). \quad (\text{A.16})$$

## Appendix B Explicit expression of matrix **A** in Chapter 6

Here we give the explicit expression of the  $8 \times 8$  matrix **A** defined in (6.19).

$$A_{11} = \lambda_1^2 + \lambda_1^{-2} \lambda_3^{-2}, \quad A_{12} = -\lambda_1^2 - \lambda_1^{-2} \lambda_3^{-2}, \quad A_{13} = 2 / \lambda_3, \quad A_{14} = -2 / \lambda_3,$$

$$A_{15} = A_{16} = A_{17} = A_{18} = 0. \quad (\text{B.1})$$

$$A_{21} = A_{22} = 2, \quad A_{23} = A_{24} = 1 + \lambda_1^4 \lambda_3^2, \quad A_{25} = A_{26} = A_{27} = A_{28} = 0. \quad (\text{B.2})$$

$$A_{31} = (\lambda_1^2 + \lambda_1^{-2} \lambda_3^{-2}) e^{KH_f / (\lambda_1^2 \lambda_3)} G_f / G_s, \quad A_{32} = -(\lambda_1^2 + \lambda_1^{-2} \lambda_3^{-2}) e^{-KH_f / (\lambda_1^2 \lambda_3)} G_f / G_s,$$

$$A_{33} = 2e^{KH_f} G_f / (G_s \lambda_3), \quad A_{34} = -2e^{-KH_f} G_f / (G_s \lambda_3), \quad A_{35} = -(\lambda_1^2 + \lambda_1^{-2} \lambda_3^{-2}) e^{KH_f / (\lambda_1^2 \lambda_3)},$$

$$A_{36} = (\lambda_1^2 + \lambda_1^{-2} \lambda_3^{-2}) e^{-KH_f / (\lambda_1^2 \lambda_3)}, \quad A_{37} = -2e^{KH_f} / \lambda_3, \quad A_{38} = 2e^{-KH_f} / \lambda_3. \quad (\text{B.3})$$

$$A_{41} = 2e^{KH_f / (\lambda_1^2 \lambda_3)} G_f / G_s, \quad A_{42} = 2e^{-KH_f / (\lambda_1^2 \lambda_3)} G_f / G_s, \quad A_{43} = (1 + \lambda_1^4 \lambda_3^2) e^{KH_f} G_f / G_s,$$

$$A_{44} = (1 + \lambda_1^4 \lambda_3^2) e^{-KH_f} G_f / G_s, \quad A_{45} = -2e^{KH_f / (\lambda_1^2 \lambda_3)}, \quad A_{46} = -2e^{-KH_f / (\lambda_1^2 \lambda_3)},$$

$$A_{47} = -(1 + \lambda_1^4 \lambda_3^2) e^{KH_f}, \quad A_{48} = -(1 + \lambda_1^4 \lambda_3^2) e^{-KH_f}. \quad (\text{B.4})$$

$$A_{51} = -A_{55} = -e^{KH_f / (\lambda_1^2 \lambda_3)}, \quad A_{52} = -A_{56} = e^{-KH_f / (\lambda_1^2 \lambda_3)},$$

$$A_{53} = -A_{57} = -e^{KH_f} \lambda_1^2 \lambda_3, \quad A_{54} = -A_{58} = e^{-KH_f} \lambda_1^2 \lambda_3. \quad (\text{B.5})$$

$$A_{61} = -A_{65} = e^{KH_f / (\lambda_1^2 \lambda_3)}, \quad A_{62} = -A_{66} = e^{-KH_f / (\lambda_1^2 \lambda_3)},$$

$$A_{63} = -A_{67} = e^{KH_f}, \quad A_{64} = -A_{68} = e^{-KH_f}. \quad (\text{B.6})$$

$$A_{71} = A_{72} = A_{73} = A_{74} = 0, \quad A_{75} = 2e^{K(H_f+H_s)/(\lambda_1^2\lambda_3)}, \quad A_{76} = 2e^{-K(H_f+H_s)/(\lambda_1^2\lambda_3)},$$

$$A_{77} = (1 + \lambda_1^4 \lambda_3^2) e^{K(H_f+H_s)}, \quad A_{78} = (1 + \lambda_1^4 \lambda_3^2) e^{-K(H_f+H_s)}. \quad (\text{B.7})$$

$$A_{81} = A_{82} = A_{83} = A_{84} = 0, \quad A_{85} = e^{K(H_f+H_s)/(\lambda_1^2\lambda_3)}, \quad A_{86} = e^{-K(H_f+H_s)/(\lambda_1^2\lambda_3)},$$

$$A_{87} = e^{K(H_f+H_s)}, \quad A_{88} = e^{-K(H_f+H_s)}. \quad (\text{B.8})$$

## Appendix C Supporting information for Chapter 8

### C.1 Methods

*PDMS chamber fabrication:* 50  $\mu\text{m}$  or 300  $\mu\text{m}$  thick PDMS (Dow corning, Sylgard 184) substrate is spin coated on a glass substrate and cured for 2 hours at 75  $^\circ\text{C}$ . A PDMS micro-fluidics structure is also prepared using a silicon mold which has a concave circular part with a 2 mm diameter and holes for an inlet and outlet. The two components are bonded by applying oxygen plasma (20 W, 100 sccm, 20 Pa, 30 second) to both surfaces. The crosslinker/base ratio of PDMS is 1:10, and its shear modulus is 0.33 MPa. The PDMS chamber is inflated by filling Silicone oil (Shinetsu, HI-VAC-F-4), which is degassed for at least 2 hours before film deposition. The Parylene membrane is then deposited on the surface with a lab coater (Speciality Coating Systems, PDS2010). The shear modulus of Parylene is  $\sim 0.58$  GPa. Because it is difficult to measure the thickness of the film deposited on the hemispherical PDMS substrate, a glass substrate is also put into the deposition chamber and the Parylene layer is simultaneously deposited on the glass substrate under identical conditions. The thickness of the Parylene layer,  $h_f$ , is measured using the film on the glass substrate with a stylus profiler (KLA Tencor, D-120). The pre-stretch  $\lambda_0$  in the

central region of the substrate is estimated from the shape of the inflated chamber. The relation between the pre-stretch  $\lambda_0$  and the shape is calculated using the commercial software, ABAQUS (See, Appendix Figure C.3). The initial height of the chamber in the experiments in Figure 8.2 and 8.3 is 1.71 mm and 2.02 mm, which corresponds to the pre-stretches  $\lambda_0 = 1.59$  and 1.85 in the central region of the bilayer.

*Ridge geometry:* In the experiment in Figure 8.3h, the geometry of the ridge is measured by the same laser profiler used for Figure 8.3a-f. The measured thicknesses of the Parylene film are 85nm, 250nm, 380nm, 450nm, 700nm, 870nm and 1.3  $\mu\text{m}$ . For the sample with the 1.3  $\mu\text{m}$  film, the thickness of the PDMS substrate is 300  $\mu\text{m}$ ; for all the other samples, the thickness of the substrate is 50  $\mu\text{m}$ . According to [82], if the Poisson's ratios of the both materials  $\nu$  are identical, the effect of the radius of curvature of the chamber,  $R$ , on wrinkling is quantified by the following dimensionless parameter  $\Omega = 2\sqrt{1-\nu^2}(h_f/R)(\mu_f/3\mu_s)^{2/3}$ . In the present experimental set up, the maximum value of  $\Omega$  is  $\sim 0.1$  at  $h_f = 1.3 \mu\text{m}$ ,  $\nu = 0.5$  and  $R = 2.0 \text{ mm}$ . Here,  $R$  is considered to be of the same order of the radius of the chamber. This small value  $\Omega$  implies that curvature of surface of the bilayer has essentially no effect on the wrinkling and ridging behavior.

*Finite element simulations:* The finite element software, ABAQUS, was used to study the formation and growth of ridges. For both simulations shown in Figures 8.4 and 8.5, a linear perturbation simulation is first carried out to identify the critical strain of wrinkle initiation  $\varepsilon_w$  and the critical wavelength  $l_w$ . Then, the critical wrinkle mode with wavelength  $l_w$  times a very small amplitude factor (0.0001 of the total thickness of the film and substrate) is introduced as the initial imperfection to break the translational symmetry

for the simulations in Figure 8.4 and 8.5. Both the film and substrate are modeled as incompressible neo-Hookean materials, with shear modulus ratio of the film to substrate,  $\mu_f / \mu_s = 2000$ , and thickness ratio of the bilayer to film  $(h_f + h_s) / h_f = 50$ . In Figures 8.4 and 8.5, the equi-biaxial compression of the bilayer structure is simulated beginning with an equi-biaxial pre-stretch in the substrate. The formation of wrinkles and/or ridges is simulated under generalized plane strain, such that in any increment of loading, a 2D plane strain computation is made (in 1-2 plane as defined in Figure 8.4a) with invariance in the 3-direction. Overall equi-biaxial compression in the 1- and 3-direction is achieved incrementally in each loading step with the aid of a user-defined material subroutine. With an increment of the applied compressive strain  $\varepsilon$  in the 1-direction, the compression in the 3-direction is programmed to coincide with that in 1-direction. Equi-biaxial pre-stretch is also implemented in the user-defined material subroutine. In Figure 8.4, the length of the simulation region is  $L / h_f = 250$  for all pre-stretches,  $\lambda_0 = 1.2, 1.4, \text{ and } 1.6$ . In Figure 8.5, the length of the simulation region is  $L / h_f = 500$ . In Figure 8.4, the method which prescribes the vertical displacement at the ridge peak was used, as described above. For Figure 8.5, a pseudo-dynamic simulation method with numerical stabilization was employed to capture the snap-through process from wrinkles to ridges, with the damping factor set as 0.0002. In addition, a structured mesh technique was used.

## C.2 Supplementary figures

Figure C.1 Stress-strain curves of PDMS and Parylene

Stress-strain curves of PDMS (Figure C.1a) and Parylene (Figure C.1b) were measured with a force gauge (Instron, Instron 5865), which prescribes displacement and measures load. A PDMS strip with a width of 10 mm and a thickness of 300  $\mu\text{m}$  and a length of 30 mm was used to obtain the stress-strain curve of PDMS. To obtain the stress-strain curve of Parylene, a Parylene film of 2.4  $\mu\text{m}$  thickness was deposited on the PDMS strip, and then the stress-strain curve of the Parylene/PDMS bilayer system was measured. By using the bilayer system, plastic necking and cracking of the Parylene film can be avoided. By subtracting the contribution of the PDMS stiffness from the strain-stress curve of the bilayer system, the stress-strain curve of Parylene was obtained. From the curves, the Young's modulus of PDMS  $E_s$  and Parylene  $E_f$  are 1 MPa and 1.75 GPa, respectively. Considering both materials to be incompressible (Poisson's ratio  $\nu = 0.5$ ), one finds the shear moduli of PDMS  $\mu_s$  and Parylene  $\mu_f$  to be 0.33 MPa and 0.58 GPa, respectively.

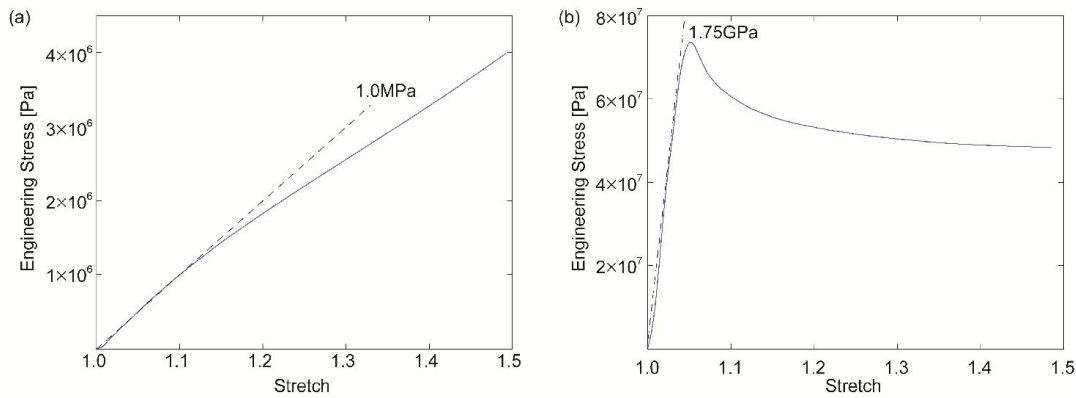


Figure C.2 Cross-sectional view

Liquid PDMS is filled in PDMS chamber, then Parylene film ( $\sim 800$  nm thick) is deposited on the surface. After the deposition, the liquid PDMS is slightly removed to induce the compressive strain. We leave the sample for 1 day at room temperature for solidification of

the liquid PDMS, and the sample is cut with a razor. The cross-section is observed with SEM. The Parylene film is not delaminated from the PDMS substrate, and the height and the width of the ridge is on the same order. The cross-section of Parylene film is highlighted with red line in the right image.

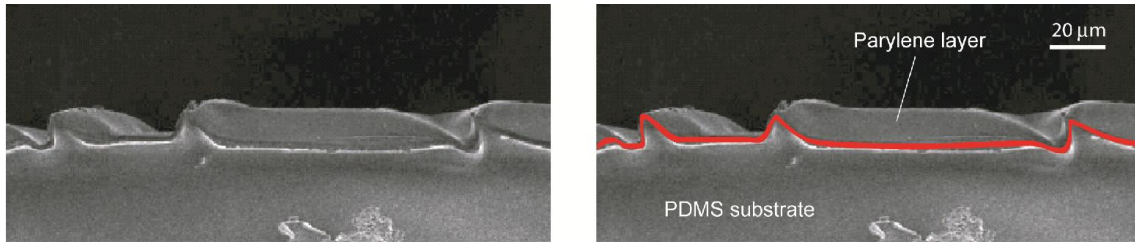


Figure C.3 Pre-stretch and compressive strain estimation by finite element simulations

We use the finite element software, ABAQUS, to relate the pre-stretch  $\lambda_0$ , compressive applied strain  $\varepsilon$  in the central region of the substrate to the PDMS chamber height, which is measured in the experiment. An axisymmetric simulation of a PDMS substrate with thickness  $50\mu\text{m}$  and radius  $2\text{mm}$  under pressure inflation is run to calculate the relation of the stretch  $\lambda$  in the middle of the chamber as a function of the height  $H$  (Figure C.3a). In the experiment of Figure 8.2, the height of the chamber before the deposition of Parylene film is  $H_0=1.71\text{ mm}$ , which corresponds to the pre-stretch  $\lambda_0=1.59$ . The shape of the chamber and vertical displacement  $U_2$  is shown in Figure C.3c. During the deflation of the PDMS chamber, the thickness of the Parylene is so small that it does not contribute significantly to the bending stiffness and the shape of the chamber. Therefore, the film is not accounted for in the simulation. The compressive strain  $\varepsilon$  is  $\varepsilon(H)=1-\lambda(H)/\lambda_0$ , and the  $\varepsilon-H$  relation is shown in Figure C.3b. The chamber height in Figure 8.2a-d is 1.71 mm, 1.60 mm, 1.58 mm and 1.57 mm, which corresponds to  $\varepsilon = 0, 0.052, 0.061$  and  $0.066$  respectively. In the

experiment of Figure 8.3h, the initial height of the PDMS chamber is set to be between 1.5 mm and 1.7 mm, which corresponds to the pre-stretch  $\lambda_0$  between 1.43 and 1.58. The central regions of the membrane in which wrinkles and ridges are measured typically have a radius of 100  $\mu\text{m}$  for Figure 8.2 and Figure 8.3a-f and of 500  $\mu\text{m}$  for Figure 8.3g and h. Within these regions there are less than 0.2% and 2.3 % variation in pre-stretch respectively due to the geometry of the chamber. Thus, the non-uniformity of the pre-stretch is considered to be negligible. The distribution of the pre-stretch  $\lambda_0$  obtained by ABAQUS is presented in Figure C.3d.

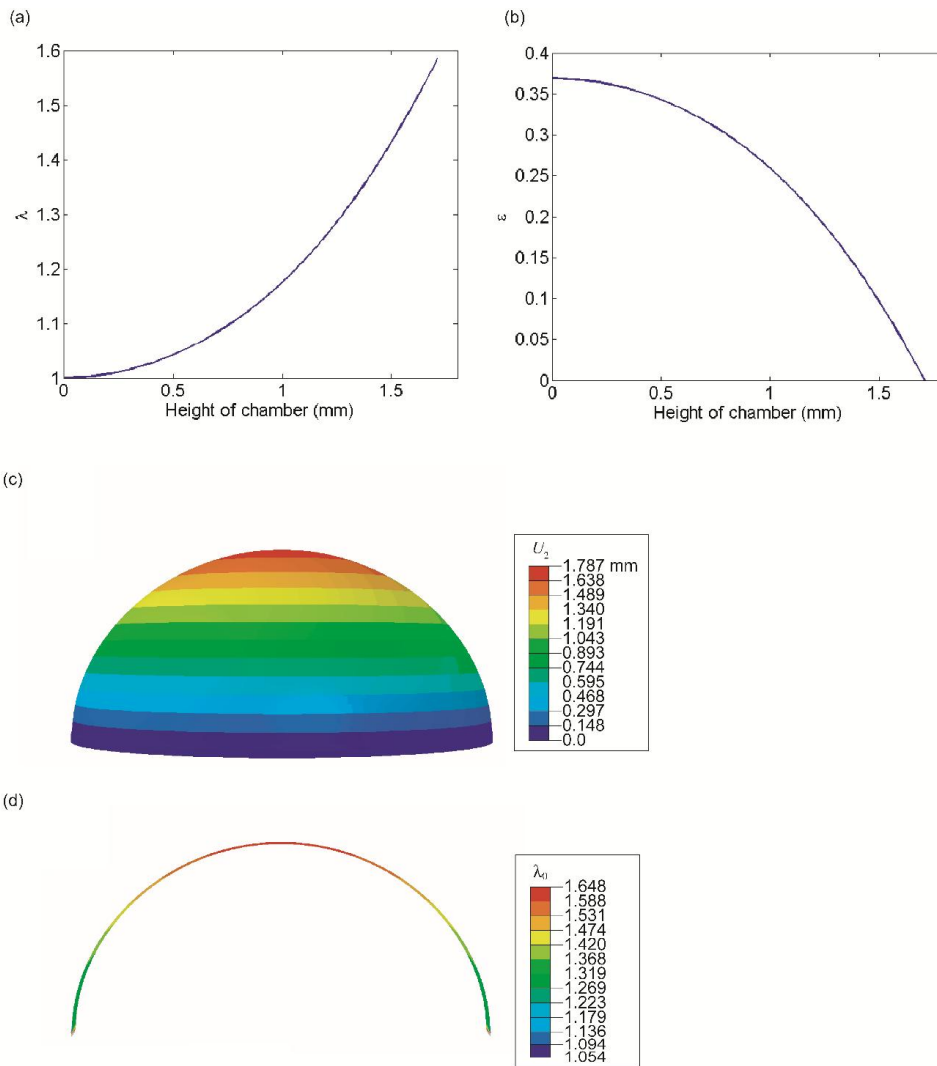


Figure C.4 Estimation of residual stress in Parylene film

To estimate the residual stress and strain in the Parylene film, the radius of curvature of a free-standing Parylene/PDMS strip has been measured. A 150 nm thick Parylene film is deposited onto a 250  $\mu\text{m}$  thick free-standing PDMS substrate, and a 8 mm x 30 mm strip is cut from the bilayer sample. The residual tensile stress in Parylene film gives rise to the curvature as shown below. The radius of curvature of short side is  $\rho = 19.0$  mm. Based on the Stoney formula [237, 238], the residual tensile stress  $\sigma_f$  and strain  $\varepsilon_f$  in Parylene film are given by  $\sigma_f = E_s h_s^2 / 6 h_f \rho (1 - \nu)$  and  $\varepsilon_f = (1 + \nu) \sigma_f / E_f$ . We obtain  $\sigma_f = 7.3 \text{ MPa}$  and  $\varepsilon_f = 0.63\%$ .

